The Dissertation Committee for Mehul Naginbhai Patel certifies that this is the approved version of the following dissertation:

Nanoparticles in Mesoporous Materials: Optical and Electrochemical Properties for Energy Storage Applications

Committee:

Keith P. Johnston, Supervisor

Keith J. Stevenson

Thomas E. Milner

Charles Buddie Mullins

Gyeong S. Hwang

Nanoparticles in Mesoporous Materials: Optical and Electrochemical Properties for Energy Storage Applications

by

Mehul Naginbhai Patel, B.E.

Dissertation

Presented to the Faculty of the Graduate School of
The University of Texas at Austin
in Partial Fulfillment
of the Requirements
for the Degree of

Doctor of Philosophy

The University of Texas at Austin
August, 2009

Dedication

To my parents

Acknowledgements

The completion of this dissertation was the result of interactions and discussions with many people. Foremost, I would like to thank my advisor, Dr. Keith P. Johnston, for his guidance and energy throughout my graduate studies. In addition, I would like to thank Dr. Keith J. Stevenson for providing fruitful ideas and discussions which contributed to this dissertation. Collaborating with Dr. Thomas E. Milner was helpful during my first years.

Thanks to the many co-authors who have contributed to the quality of this dissertation. Early guidance from Griffin Smith led to Chapter 2 (along with Jihoon Kim). Prof. Hiroshi Uchida who visited from Japan for one year helped lead to the possibility of Chapter 3, along with contributions from R. Alan May and Ryan D. Williams. Prof. Sheng Dai and Dr. Xiqing Wang contributed to Chapters 4 and 5. Thanks to Dr. Domingo Ferrer, Dr. Steven Swinnea, Dr. Aaron E. Saunders, Andrew T. Heitsch, Jaclyn Wiggins, and Brian Williams for their help in experiments.

I would like to thank the Cockrell School of Engineering at The University of Texas at Austin for their invaluable financial support by giving me the Engineering Doctoral Fellowship, contributed to by anonymous donors.

Special thanks to my group members Gaurav Gupta, Jasmine Tam, and Dan Slanac for insightful discussions and support. Thanks to my lunch group friends (Manas Shah, Landry Khounlavong, Gaurav Goel, and Amogh Prabhu) and to all my friends in Austin (the monkeybarrel) for their friendship.

Exceptional thanks to my parents, family, and Mohini for their support and encouragement.

Nanoparticles in Mesoporous Materials: Optical and Electrochemical Properties for Energy Storage Applications

Publication No._____________

Mehul Naginbhai Patel
The University of Texas at Austin, 2009

Supervisor: Keith P. Johnston

The design of nanoparticles in mesoporous supports is explored through synthetic strategies of electrophoretic deposition and electroless deposition with application towards energy storage. Electrophoretic deposition of nanoparticles into a mesoporous thin film is examined using charged nanocrystals in a low-permittivity solvent. To provide a basis for the deposition, the mechanism of particle charging in a low-permittivity solvent was studied. Dispersions of carbon black particles in toluene with an anionic surfactant were characterized using differential-phase optical coherence tomography with close electrode spacing to measure the electrophoretic mobility. The particle charge in concentrated dispersions was found to decrease as a function of increasing surfactant concentration. Partitioning of cations between the surfactant-laden particle surface and micelle cores in the double-layer was found to govern the dynamics of particle charging. Subsequently, charged Au nanocrystals were deposited by electrophoresis within perpendicular mesochannels of a TiO_2 support. High loadings of 21 wt% Au with good dispersion were achieved within the mesoporous TiO_2 support using electrophoretic deposition, which would otherwise be inhibited by the weak nanocrystal-support interaction. According to a modified Fokker-Planck equation, the mean penetration depth of a single nanocrystal inside of the perpendicular pores was found to be dependent on the electric field strength, electrophoretic mobility, pore diameter, nanocrystal size, and local deposition rate constant.

Nanocomposites for electrochemical capacitors were designed via electroless deposition of redox-active MnO_2 in a high surface area mesoporous carbon support. Disordered mesoporous carbon supports with a pore size of ~8 nm were used both in amorphous (AMC) and graphitic (GMC) form, with a ~1000-fold larger conductivity for GMC. High loadings of 30 wt% MnO_2 were achieved in the AMC in the form of ~1 nm thick domains, which were highly dispersed throughout the support. Oxidation of the GMC was necessary to facilitate wetting and deposition of the MnO_2 precursor in order to achieve high loadings of 35 wt% MnO_2 with ~1 nm thickness. High gravimetric MnO_2 pseudocapacitances of >500 F/g_{MnO2} were achieved at low loadings and low scan rate of 2 mV/s for both carbon supports. However, at high scan rates ≥100 mV/s, the MnO_2 pseudocapacitance is twofold larger for MnO_2/GMC, relative to MnO_2/AMC. Sodium ion diffusion throughout both MnO_2/AMC and MnO_2/GMC was shown to be facile. For the GMC versus AMC support, the higher MnO_2 pseudocapacitance is attributed to the higher electronic conductivity, which facilitates electron transport to the MnO_2 domains.

Table of Contents

List of Tables

List of Figures

Chapter 1

Introduction

With the demand for energy storage devices increasing, the push for novel materials with high power and energy densities is rising.[1-3] Currently, electrochemical capacitors (ECs) occupy a functional space between batteries and conventional capacitors with high power densities but low energy densities (0.1-10 Wh/kg) and are found in common items such as video recorders, car audio systems, and alarm clock radios.[2, 4, 5] While batteries have larger energy densities (10-100 Wh/kg), they typically have a short life span of ~1000 cycles, whereas ECs can be used for ~500000 cycles with minimal degradation and loss in capacity.[4, 6] Hence, there is intense interest in increasing the energy density of ECs for applications such as hybrid electric vehicle power systems for starting, lighting, and ignition, as well as for load leveling in commercial and industrial equipment.[6-8] Novel nanostructured materials, e.g. redox-active nanoparticles in mesoporous supports, will be crucial in raising the energy density of ECs. The ability to synthesize nanocomposites and understand charging behavior along with ion and electron transport will enable for better materials design to meet the energy demands of the future.

The design strategy to disperse nanoparticles in mesoporous supports is of interest to form nanocomposites with high accessibility of the nanoparticles for heterogeneous catalysis and electrochemical reactions, e.g. in ECs.[9] One method is by electroless deposition of nanoparticles in a mesoporous support. In this process, the support acts as a reducing agent to produce well dispersed nanoparticles, and the deposition can be controlled by varying the reaction time and concentration of reactants. An alternative technique for depositing nanoparticles in mesoporous supports is by electrophoretic deposition,[10-13] where presynthesized nanoparticles in either nonaqueous[14, 15] or aqueous solvents[16, 17] are guided in an electric field for deposition onto a support. Nonaqueous, or low-permittivity, solvents are favorable since many nanoparticle synthesis strategies utilize these solvents,[18] and both positive and negatively charged nanoparticles can be present simultaneously.[19, 20] High potentials can also be used without the problem of electrolysis or joule heating, which are prevalent in water at low potentials (<5 V).[21, 22] However, the charging mechanism is not fully clear in low-permittivity solvents, and developing an understanding of particle charging in low-permittivity solvents would enable for advancement of electrophoretic deposition of nanoparticles within mesoporous supports. Development of both electroless and electrophoretic deposition is important to form nanocomposites with highly active, accessible nanoparticles.

1.1 COLLOIDAL PARTICLE CHARGING IN LOW-PERMITTIVITY MEDIA

An abundance of nanoparticle synthesis techniques are performed in organic solvents to control the particle morphology and size.[18] Insight into the charging of these nanoparticles in nonaqueous solvents would be useful for understanding and developing a wide variety of applications including electrophoretic deposition of nanoparticles into mesoporous supports, ink-jet printing, liquid immersion development,[23, 24] electrophoretic displays,[25, 26] electrostatic lithography,[27] photoelectrophoresis,[28] electrorheological fluids,[29, 30] paints, and petroleum processing.[31, 32] With aqueous systems, colloidal charging and stabilization occur easily with dissociative surface groups or electrolytes playing a dominant role.[32] A fundamental understanding of the charging behavior of colloidal particles in low permittivity solvents would be advantageous for advancing these areas.

Electrostatic stabilization of colloids in low-permittivity solvents with a dielectric constant <5 generally requires additives such as polymers or surfactants to prevent ion paring.[33-43] The thermodynamics of ion separation for a 1:1 electrolyte are given by the Bjerrum length, the ratio between electrostatic interaction energy and thermal energy, as

$$l_B = \frac{e^2}{4\pi\varepsilon_r\varepsilon_0 k_B T} \tag{1.1}$$

where e is the elementary charge, ε_r is the dielectric constant (static permittivity), and ε_0 is the vacuum permittivity. For water, the dielectric constant is high ($\varepsilon_r \approx 80$), and l_B is quite small at 0.7 nm, which can be provided by water molecules hydrating the ions. However, for nonaqueous systems, the dielectric constant is much lower ($\varepsilon_r \approx 2$), and l_B is much larger at 28 nm. Hence in low-permittivity media, additives such as polymers, crown ethers, or micelles are needed to stabilize the ions in the double-layer (Fig. 1.1). These micelles (or charge carrying entities), which can be ~5 nm in size and easily solubilize small ions (<1 nm), are both positively and negatively charged in dynamic equilibrium with uncharged micelles as given by the charge fluctuation model.[44, 45] The colloid charge is balanced by ion transfer between the micelles in the double layer and colloid surface.

The electrophoretic mobility, μ, of colloids is much smaller in low-permittivity media compared to aqueous systems. The electrophoretic mobility, μ, is given by

$$\mu = \frac{\zeta \varepsilon_r \varepsilon_0 f(\kappa a)}{\eta} \tag{1.2}$$

where ζ is the zeta potential, κa is the reduced inverse Debye length, and η is the viscosity of the medium.[46] The value of $f(\kappa a)$ is determined mainly by the medium and size of the colloids. In aqueous systems $\kappa a >> 1$ and $f(\kappa a) = 1$ (Smoluchowski limit), while for nonaqueous systems $f(\kappa a) << 1$ and $f(\kappa a) = {}^2/_3$ (Hückel limit). Hence mobilities measured in nonaqueous systems are lower compared to their aqueous counterparts. The mobility is greatly reduced however from the dielectric constant which is ~40-fold lower for organic solvents compared to water. Only a limited number of techniques exist to adequately measure the mobility of particles in nonaqueous media.

One technique used to measure the electrophoretic mobility is using a light microscope and measuring the time is takes for a colloid to travel between fixed electrodes in an electric field, called visual microelectrophoresis. However, this can only be done for dilute dispersions of large particles to adequately identify the particles.[37] Laser Doppler electrophoresis (LDE) can be used to measured mobilities using the frequency shift of light of colloids that are sub-microscopic; however, the mobility of the colloids must be $>1\times10^{-9}$ m^2/Vs.[47, 48] An extension of LDE is phase analysis light scattering (PALS), which provides for a greater sensitivity to particle motion in an electric field.[49, 50] PALS uses changes in the phase angle to determine the velocity of the

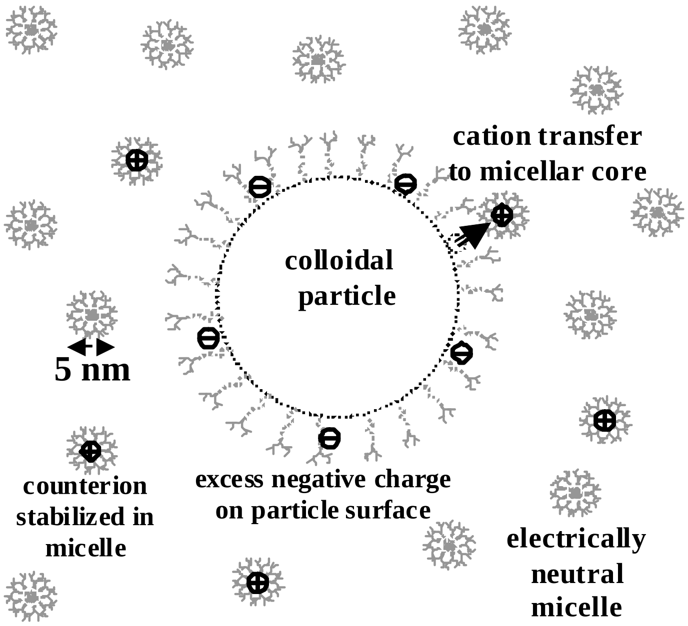

Figure 1.1: Schematic representation of negatively charged particle in the presence of charged and uncharged micelles in the large double-layer with charge transfer between the particle surface and micelles. (Adapted from Ryoo et al.[37])

particle in an electric field, which is 1000x more sensitive compared to LDE. However, with large electrode spacings (1-4 mm),[51] the small mobilities in low-permittivity media require large potentials,[52-54] which can lead to undesirable reactions[50] and instabilities.[55] Smaller potentials may be used instead with differential-phase optical coherence tomography (DP-OCT), which uses a broadband light source in a backscattering set-up, with close electrode spacing of 0.18 mm.[51, 56] Compared to techniques such as LDE and PALS, more turbid, concentrated colloidal dispersions can be analyzed using DP-OCT with a close electrode spacing since the sample volume is 10^4-fold smaller.[51]

Recently, TiO_2 particles in toluene with a sodium bis(2-ethyl-1-hexyl)sulfosuccinate (AOT) surfactant were studied using DP-OCT.[39, 51] Particles with different surface chemistries were compared, with a more hydrophilic surface giving a positive charge and a more hydrophobic surface giving a negative charge. The effect of surfactant concentration on the particle charge was also examined, and both surfaces exhibited the same behavior with a decreasing absolute surface charge with increasing surfactant concentration. The charging mechanism was shown to be based on partitioning of ions between the particle surface and surfactant micelles in the double-layer. Examination of other particles would be beneficial to determine if the charging mechanism can be applied on a more global scale.

1.2 DEPOSITION OF NANOPARTICLES INTO MESOPOROUS SUPPORTS

The deposition of nanoparticles in a mesoporous support can be done via multiple strategies. With an understanding of the charging mechanism of colloids in low permittivity solvents, nanocomposites can be formed via electrophoretic deposition of charged nanoparticles into a mesoporous support. Nanocomposites are of great interest for their application as magnetic, photonic, catalytic, sensor, and energy storage materials.[1, 57-59] Nanocrystal incorporation onto a mesoporous support can lead to enhanced optoelectronic and catalytic properties for the composite.[60] Nanocomposite films, composed of a porous TiO_2 support with metal nanocrystals, used for solar cells can lead to increased light harvesting efficiencies.[61] With control over the size of the metal nanocrystals, e.g. gold, the nanocrystals can act as capacitors for storing electrons for the metal oxide. This results in a shift in the Fermi level of the nanocrystal to equilibrate with the metal oxide leading to better charge separation with smaller nanocrystals having higher efficiencies.[61] Redox-active metal oxide nanoparticles on mesoporous carbon supports can lead to improved gravimetric capacitances.[62, 63] Addition of ~30 wt% MnO_2 nanoparticles on a high surface area carbon support led to a threefold increase in the gravimetric capacitance, relative to the bare carbon support, resulting from the high MnO_2 pseudocapacitance. Hence, the placement of nanoparticles within a mesoporous support to form nanocomposites is important for taking advantage of the nanoparticle properties.

One technique employed to prepare nanocomposite thin films with metal nanoparticles is precursor reduction inside a mesoporous thin film.[57, 64-67] In this technique, a mesoporous film is immersed in a metal ion precursor solution and sufficient time is allowed for the metal ions to diffuse throughout the film. The precursor is then reduced by various means such as heat treatment,[68] electrochemical deposition,[66, 69] or UV exposure.[70] Various nanocrystals such as Au, Pt, and Ag have been synthesized inside thin films with this technique. However, it is difficult to control the nanocrystal morphology and size and uniformity of dispersion; furthermore, the particles may grow until they block the pores as shown in Figure 1.2.

To overcome the difficulties in controlling the nanoparticle composition, size, and dispersion, an alternative approach has been developed to form composites of nanocrystals and mesoporous powders by infusing presynthesized nanocrystals into mesoporous supports.[71-73] The infusion has been driven by sonication[71] or by adding an anti-solvent, supercritical CO_2 to an organic solvent such as toluene.[72, 73] The $scCO_2$ strengthens the nanocrystal–mesoporous silica interaction leading to higher loadings.[72] This technique provides excellent control over the morphology of the mesoporous support as well as the nanocrystal size, shape, and composition for the purpose of achieving high catalytic activities and stabilities.[71, 73]

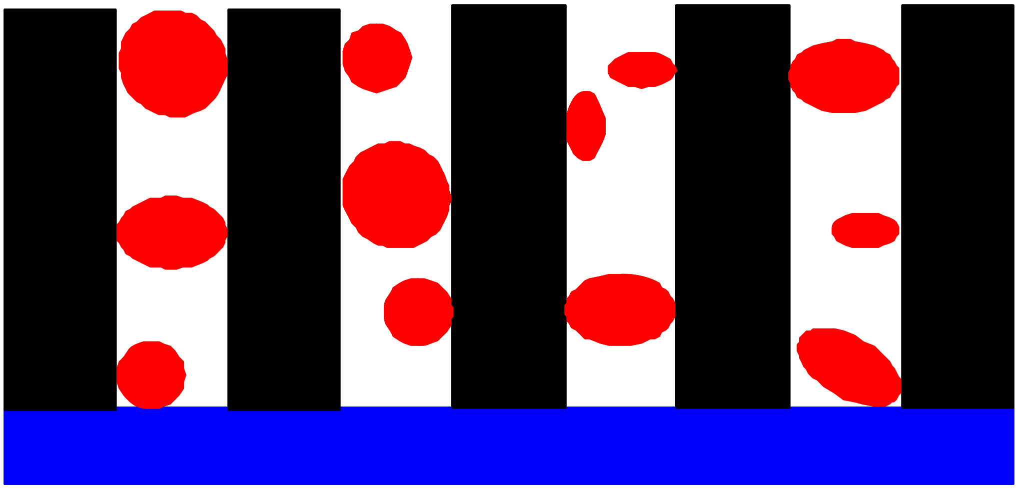

Figure 1.2: Illustration of pore blockage and non-uniform metal nanocrystal formation in mesoporous film with precursor reduction technique.

Recently the choice of the binding ligand on the nanocrystals was found to play a crucial role in achieving high loadings in mesoporous powders.[74] Strongly-bound ligands provide a protective covering around the nanocrystal inhibiting strong interactions from forming between the nanocrystal and mesoporous support.[75] Hence, an antisolvent such as $scCO_2$ was used to infuse nanocrystals inside of the mesoporous materials.[72, 73] Figure 1.3a shows a scanning transmission electron microscope (STEM) image of Ir nanocrystals loaded in mesoporous silica with 1.3 wt% Ir using $scCO_2$. The shiny white dots are the nanocrystals, the faint white lines are the pore walls, and the black lines are the pores. Using weakly-bound ligands, the nanocrystal support interaction increases as more of the bare metal is exposed, leading to high loadings through adsorption without the need for an antisolvent. Figure 1.3b shows a STEM image of FePt nanocrystals in mesoporous silica at 8 wt% FePt. Loadings reached as high as 14 wt% FePt in mesoporous silica using the weakly-binding oleic acid/oleylamine ligands.[74]

An alternative approach to design nanocomposite thin films is via electrophoretic deposition of presynthesized nanocrystals. With this technique, nanocrystals with strongly-bound or weakly-bound ligands can be deposited readily. Numerous studies have been performed with monolayer-like deposition on flat substrates such as carbon coated copper grids[76, 77] and ITO/glass.[16, 17] Metal nanocrystals such as Au, Pt, and Ir nanocrystals dispersed in organic solvents have been deposited on disordered 10–15 nm TiO_2 nanoparticles.[15, 78] These metal nanocrystal layers formed by electrophoretic deposition were thicker than those formed by Langmuir Blodgett, self-assembled monolayer, or adsorption techniques.[15] These films also exhibit nanoporosity with aggregation of the deposited gold nanocrystals. CdSe nanocrystals dispersed in an organic solvent, hexane, have also been electrophoretically deposited onto conducting planar substrates of gold to form thick films and line patterns.[14, 79, 80] Electrophoretic deposition produced more uniform films than dry casting or spin casting.

Very few studies report electrophoretic deposition of nanocrystals into mesoporous thin films. The pores of the film should be perpendicular to the substrate and aligned with the electric field (Fig. 1.4).[11, 12] Limmer et al. have infused small nanoclusters inside porous membranes such as track-etched polycarbonate or anodic

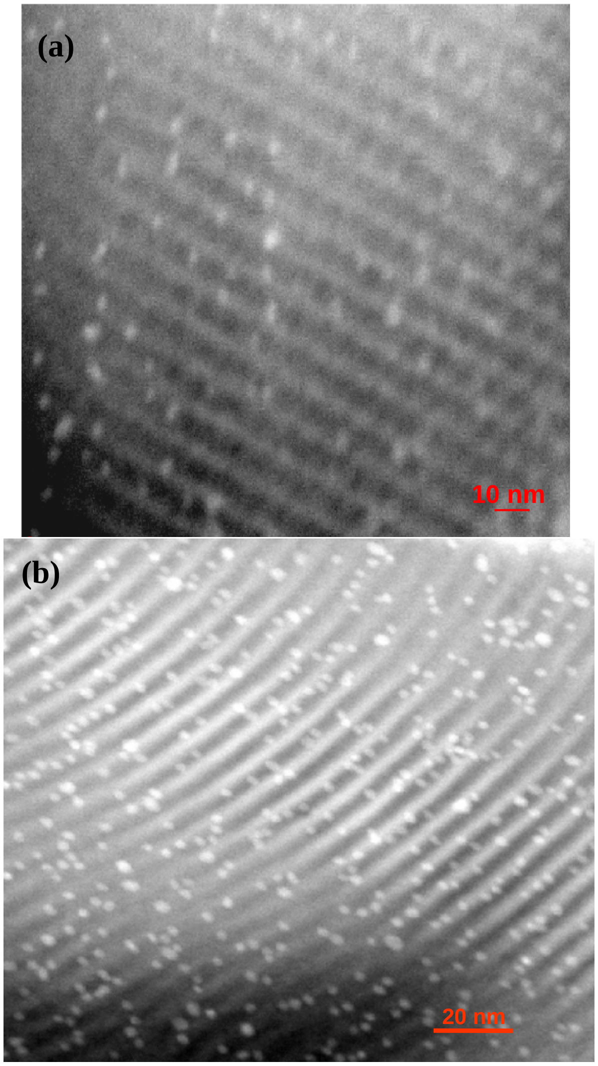

Figure 1.3: STEM images of (a) Ir–mesoporous silica composite with 1.3 wt% Ir and (b) FePt–mesoporous silica composite with 8 wt% FePt.

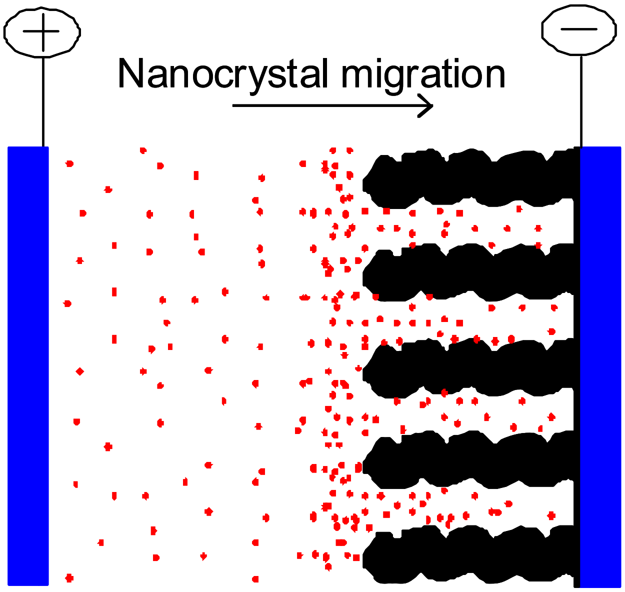

Figure 1.4: Schematic representation of electrophoretic deposition of nanocrystals inside of a mesoporous thin film electrode with pores aligned with electric field.

alumina with pore sizes of 100–200 nm and thicknesses to 10 μm.[13, 81-83] The nanoclusters completely fill the pores of the membranes and were heated to form nanowires. Zhang et al. used electrophoretic deposition to infuse 3 nm CdSe nanocrystals into thin polymer films (30–40 nm) with 15 nm pores.[10] In both of these studies, the pore to particle diameter was over 5; however, further tuning of this ratio to lower values would be important for mesoporous supports of <10 nm pores.

1.3 DEPOSITION OF REDOX-ACTIVE NANOPARTICLES IN MESOPOROUS CARBON FOR ELECTROCHEMICAL CAPACITORS

Nanocomposites of highly dispersed nanoparticles in mesoporous supports are of interest in a variety of practical applications, for example in energy storage. In addition to electrophoretic deposition, this dissertation also examines an electroless deposition technique, wherein the support acts as the reducing agent. The resultant nanocomposites have high surface areas and beneficial properties for electrochemical capacitors. Electrochemical double-layer capacitors (EDLCs), redox pseudocapacitors, ultracapacitors, and supercapacitors are commonly used names for ECs already used prevalently in digital cameras, cell phones, and circuit boards.[4, 8] More recent applications of ECs are in industrial equipment, transportation for starting, acceleration and regenerative braking, and in load leveling for smart grids, e.g., those which contain variable energy sources such as windmills and solar cells.[1, 6, 7] The higher specific power of these devices is ideally suited for the rapid storage and release of energy relative to most batteries, although their specific energy is somewhat lower (Fig. 1.5). However, the gravimetric capacitance and consequently, the energy and power densities of ECs may be increased by improving the design of material architectures to enhance electron transport and ion diffusion.[1, 3]

Electrochemical capacitors may store energy in the electric double-layer and by surface redox (Faradaic) reactions.[1, 84] For EDLCs, the capacitance is directly proportional to the surface area and indirectly proportional to the double-layer thickness,

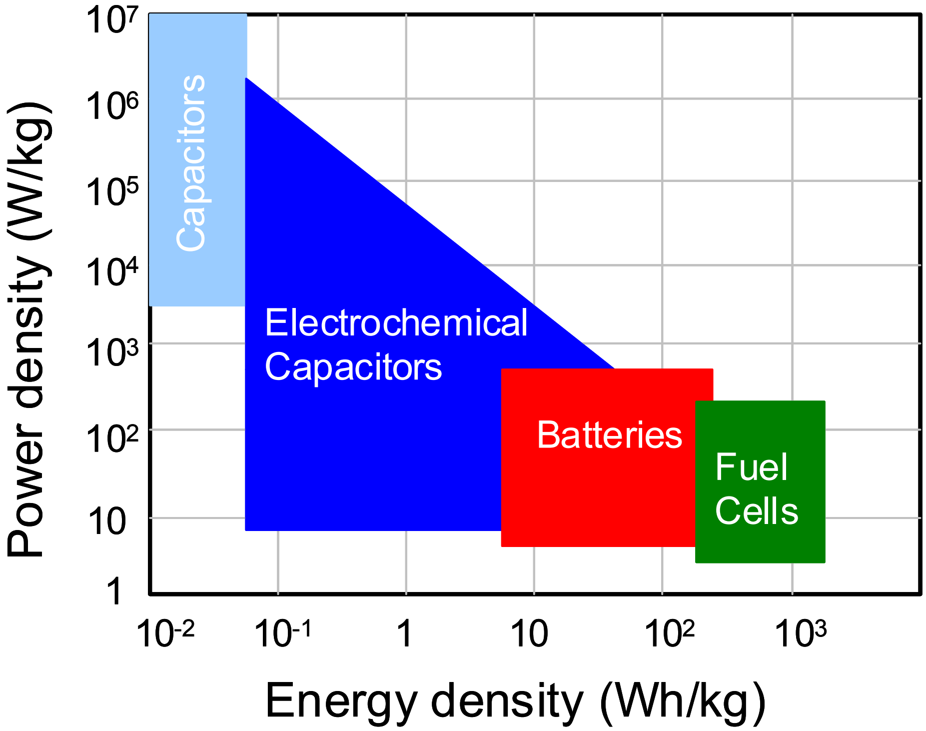

Figure 1.5: Ragone plot for energy storage and conversion devices. (Adapted from Kotz et al.[4])

which is typically on the order of ~1 nm.[5, 8, 84] For carbon-based EDLCs, the various allotropes, pore structure, surface area, and graphitic content can be manipulated to tailor the conductivity and gravimetric capacitance.[1, 85-98] Activated carbons with surface areas between 500 to 2500 m^2/g typically have a capacitance between 10 to 35 F/g.[5] The high surface area results predominantly from micropores (<2 nm), with some contribution from mesopores (2-50 nm) and little contribution from the macropores (>50 nm). Micropores are not favorable as they result in reduced ion flow throughout the porous structure.[85] Mesopores are sufficiently large for rapid ion transport [85] and for deposition of nanoparticles with pseudocapacitive behavior.[99] To achieve high capacitance at high scan rates, the electronic conductivity must also be sufficient to compliment rapid ion transport in the mesopores. Graphitic carbons possess carbon atoms arranged in highly ordered, stacked hexagonal rings giving high electrical conductivity.[88, 100] EDLCs composed of highly conductive carbon materials show minimal capacitance fade with increasing scan rates.[98, 101] The ability to design a support with a high surface area mesopores and high electronic conductivity would further enable enhancement in attaining high gravimetric capacitances at high scan rates.

The electric double-layer capacitance may be further increased by either surface functionalization or surface modification with redox-active sites that promote a surface redox pseudocapacitance.[1, 8, 84] Electrode materials for redox supercapacitors are typically conductive polymers or transition metal oxides such as ruthenium or manganese oxide.[1] Ruthenium oxide is an appealing material due to its high pseudocapacitance and high conductivity. Zheng et al. reported specific capacitance values as high as 720 F/g_{RuO2}.[102, 103] Many studies have been completed with different ruthenium oxide nanostructures synthesized such as thin films,[104] nanoparticles,[105] nanoneedles,[106] and nanotubes.[107] However a major deterrent for commercialization of ruthenium oxide is its high cost and low availability.[105] Manganese oxide, a low cost alternative with low toxicity and a high theoretical pseudocapacitance (1370 F/g_{MnO2}),[108] has been studied extensively for ECs.[108-126] High gravimetric pseudocapacitances are typically reported at 700 F/g_{MnO2}[114, 126] for thin films on conductive metal planar substrates. An atypically large value of ~1380 F/g_{MnO2}[109] was reported for MnO_2 porous particles deposited on conductive platinum foil. However, since MnO_2 is a mixed conductor, it is difficult to achieve a high pseudocapacitance at high rates, even when it is mixed with conductive agents such as activated carbon.[112] Combining the capacitance and electronic properties of a carbon support with a pseudocapacitive material such as MnO_2 can lead to higher energy density materials at high rates.

Novel nanocomposite redox pseudocapacitors may be designed by combining conductive, high surface area carbon materials with a redox-active transition metal oxide to increase the gravimetric capacitance. Manganese oxide has been deposited by electrodeposition and electroless deposition on various carbon supports.[62, 63, 99, 127-133] One emerging design strategy is to use mesoporous carbons as scaffolds for MnO_2 where the porous channels in the carbon support provide high surface area, and the conductive carbon scaffold facilitates electronic conductivity. Small nanoparticles or a conformal coating of MnO_2, no thicker than a few nm, may be grown within the mesopores of the highly conductive carbon to improve the utilization of the pseudocapacitive material.[1, 108] For an MnO_2 loading on the order of 30 wt.%, a uniform coating in 10 nm mesopores would correspond to a film thickness of ~1 nm. Thin MnO_2 films in conductive mesoporous supports with pore sizes of 5-10 nm would be favorable for rapid ion and electron transport to achieve high capacitance. Recent reports of MnO_x particles in high surface area carbon supports displayed large gravimetric capacitances.[62, 63, 99, 129, 134] Few studies have evaluated charge storage capacities at high scan rates (≥100mV/s). At higher scan rates, sloping profiles in the current-potential curves are often observed which suggests kinetic limitations due to sluggish ion and electron transport.[99, 134] Furthermore, typical MnO_2 modified carbons display substantial capacity fade and low faradaic efficiencies at high scan rates. With a high conductivity support, it would be desirable to tailor the architecture of the pores and the interface between the carbon and MnO_2 to achieve a high capacitance.

1.4 OBJECTIVES

This dissertation studies the design of nanocomposites of nanoparticles in mesoporous supports formed by both electrophoretic deposition and electroless deposition. Electrophoretic deposition is studied first for nanoparticles dispersed in low-permittivity solvents. A fundamental understanding of the charging mechanism of particles in low-permittivity solvents is presented as a basis for the study of electrophoretic deposition. Differential-phase optical coherence tomography is used to measure the electrophoretic mobilities to determine the particle charge. A charging mechanism is described for carbon black particles in a low-permittivity solvent (toluene) containing an anionic surfactant. The effect of surfactant concentration on the particle charge is studied and used to determine the charging mechanism, which is shown in terms of surfactant adsorption on the particle surface and preferential partitioning of cations from micelles in the double-layer to the particle surface. The understanding of particle charging in low-permittivity solvents is subsequently used to guide a study of electrophoretic deposition of nanoparticles into a mesoporous support. Charged gold nanocrystals are deposited into perpendicularly oriented mesochannels of a TiO_2 thin film. Electrophoretic deposition allows for high loadings to be achieved with presynthesized nanocrystals covered with strongly-bound ligands. Without an electrical field, the deposition would be inhibited by the weak nanocrystal-support interaction. A modified Fokker-Planck equation is used to model the mean penetration depth of a nanocrystal.

Electroless deposition is subsequently investigated to form redox-active metal oxide nanoparticle/mesoporous carbon composites of interest in electrochemical capacitors. Hybrid MnO_2/mesoporous carbon nanocomposites with ~8 nm pores are synthesized and characterized for MnO_2 pseudocapacitance and total gravimetric capacitance. High surface area disordered mesoporous carbon supports in both amorphous (AMC) and graphitic (GMC) form are used as sacrificial scaffolds to form MnO_2 nanoparticles. AMC allows for high loadings to be achieved easily, and the effect of loading on the pseudocapacitance and total gravimetric capacitance is studied at low and high scan rates. Diffusion of sodium ions throughout the MnO_2/AMC is examined to determine if the pore size is sufficient for ion flow. Graphitization of the mesoporous carbon support at a high heat treatment temperature leads to increased electronic conductivity of the support; however, pretreatment of the GMC via oxidation is required to achieve high loadings of MnO_2. The effect of MnO_2 loadings on capacitance is studied at low and high rates with much higher capacitance values achieved at high rates for the MnO_2/GMC, relative to the MnO_2/AMC. The AMC and GMC composites are compared to determine if ion or electron transport is limiting in achieving a high MnO_2 pseudocapacitance at high scan rates.

1.6 DISSERTATION OUTLINE

The first half of this dissertation focuses on the use of electrophoretic deposition in low-permittivity media for nanoparticle deposition in a mesoporous support. To provide a basis for the electrophoretic deposition studies, the charging mechanism of particles in low-permittivity solvent is first investigated, which is given in Chapter 2 with carbon black particles in toluene. The carbon black particles are electrostatically charged in toluene in the presence of sodium bis(2-ethyl-1-hexyl)sulfosuccinate (AOT) surfactant. Without surfactant, the carbon black particles settle after ~1 hr and show no charge; however with AOT surfactant, the carbon black particles become negatively charged and do not settle. Differential-phase optical coherence tomography (DP-OCT) is used to measure the electrophoretic mobilities of concentrated dispersions of carbon black particles. The close electrode spacing of 0.18 mm, i.e. small sample volume, allows for measurement of up to 1 wt% highly absorbing carbon black. The zeta potential ranged from -24 mV to -12 mV as the AOT concentration was increased from 1 to 100 mM. An electrostatic charging mechanism is discussed in terms of surfactant adsorption on the particle surface and micelles in the double-layer. Preferential partitioning of the hard sodium cation between the particle and double-layer determines the charge decrease with AOT concentration.

Given the understanding of particle charging in low-permittivity solvents from Chapter 2, Chapter 3 examines electrophoretic deposition of charged gold nanocrystals. The gold nanocrystals dispersed in chloroform are capped with dodecanethiol ligands, and loss of capping ligands is thought to leave an excess positive charge on the nanocrystal. The charged gold nanocrystals were electrophoretically deposited inside of perpendicular mesochannels of a TiO_2 support. High loadings up to 21 wt% Au were achieved in a short time of only 10 min using electrophoretic deposition compared with only ~5 wt% via adsorption over a 20 hr period. The ligand surface coverage and binding strength on the nanocrystal play a strong role in limiting the interaction between the nanocrystal and TiO_2 support. With this limitation, electrophoretic deposition provides a driving force to achieve high nanoparticle loadings. The mean penetration depth of a single nanocrystal is modeled using a modified Fokker-Planck equation. The nanocrystal penetration depth inside of the perpendicular pores is found to be dependent on the electric field strength, electrophoretic mobility, pore diameter, nanocrystal size, and local deposition rate constant.

To compliment the study of electrophoretic deposition of presynthesized charged nanoparticles in Chapter 3, electroless deposition is used in Chapter 4 and 5 to form redox-active metal oxide nanoparticles in a mesoporous support. These chapters focus on high surface area mesoporous carbon supports used as sacrificial scaffolds to form hybrid MnO_2/carbon nanocomposites for electrochemical capacitors. Chapter 4 centers on using an amorphous mesoporous carbon support with MnO_2. High loadings up to 30 wt% MnO_2 are formed and highly dispersed throughout the ~8 nm pores of the AMC with a MnO_2 thickness of ~1 nm. For the composites in 1 M Na_2SO_4 at 2 mV/s, a low loading of 2 wt% MnO_2 gives a gravimetric MnO_2 pseudocapacitance of 560 F/g_{MnO2}, whereas 30 wt% MnO_2 drops to 200 F/g_{MnO2}. For 30 wt% MnO_2 at a high rate of 100 mV/s, the gravimetric MnO_2 pseudocapacitance drops to 137 F/g_{MnO2}. Diffusion of sodium ions is shown to be sufficient throughout the nanocomposite, whereas electron transport is possibly limited due to the amorphous nature of the support.

In an effort to improve the MnO_2 pseudocapacitance at high scan rates, a graphitic carbon support is used to form MnO_2/carbon nanocomposites in Chapter 5. This support has a much higher electronic conductivity (~1000x) compared to the AMC (Chapter 4). The aqueous MnO_2 precursor does not wet the GMC surface; hence, pretreatment must be done via nitric acid oxidation to increase the oxygen functionalities on the GMC to facilitate MnO_2 deposition. High loadings of 35 wt % MnO_2 with ~1 nm thick domains were achieved with high dispersion throughout the ~8 nm pores of the GMC. In 1 M Na_2SO_4 at 2 mV/s, the gravimetric MnO_2 pseudocapacitance reached 500 F/g_{MnO2}. A capacitance fade of only ~20% over a 100-fold change in scan rate was observed over all MnO_2 loadings, and a MnO_2 pseudocapacitance of 310 F/g_{MnO2} at 200 mV/s is achieved for 35 wt% MnO_2. 35 wt% MnO_2 also gave a high volumetric capacitance of 400 F/cm^3. The relaxation time constants of <1 s were short for the composites, indicating a high power density. The high graphitic character and disordered mesopores of the GMC facilitates electron and ion transport to the MnO_2 domains giving high MnO_2 pseudocapacitances at fast rates of 200 mV/s.

Chapter 6 gives the overall conclusions and recommendations for future work. Supporting information for Chapter 3, 4, and 5 can be found in Appendix A, B, and C, respectively. Appendix D contains experimental details, characterization, and capacitance data on MnO_2/carbon composites synthesized using a small pore disordered amorphous mesoporous carbon and an ordered amorphous mesoporous carbon supports.

1.7 REFERENCES

1. Simon, P.; Gogotsi, Y., Materials for electrochemical capacitors. *Nature Materials* **2008,** 7, (11), 845-854.

2. Rolison, D. R.; Long, J. W.; Lytle, J. C.; Fischer, A. E.; Rhodes, C. P.; McEvoy, T. M.; Bourg, M. E.; Lubers, A. M., Multifunctional 3D nanoarchitectures for energy storage and conversion. *Chemical Society Reviews* **2009,** 38, (1), 226-252.

3. Arico, A. S.; Bruce, P.; Scrosati, B.; Tarascon, J.-M.; van Schalkwijk, W., Nanostructured materials for advanced energy conversion and storage devices. *Nature Materials* **2005,** 4, (5), 366-377.

4. Kotz, R.; Carlen, M., Principles and applications of electrochemical capacitors. *Electrochimica Acta* **2000,** 45, (15-16), 2483-2498.

5. Pandolfo, A. G.; Hollenkamp, A. F., Carbon properties and their role in supercapacitors. *Journal of Power Sources* **2006,** 157, (1), 11-27.

6. Miller, J. R.; Burke, A. F., Electrochemical capacitors: challenges and opportunities for real-world applications. *Electrochemical Society Interface* **2008,** 17, (1), 53-57.

7. Miller, J. R.; Simon, P., Electrochemical Capacitors for Energy Management. *Science (Washington, DC, United States)* **2008,** 321, (5889), 651-652.

8. Conway, B. E., *Electrochemical Supercapacitors: Scientific Fundamentals and Technological Applications*. Kluwer Academic/Plenum Publishers: New York, 1999.

9. Rolison, D. R., Catalytic nanoarchitectures - The importance of nothing and the unimportance of periodicity. *Science (Washington, DC, United States)* **2003,** 299, (5613), 1698-1702.

10. Zhang, Q.; Xu, T.; Butterfield, D.; Misner, M. J.; Ryu, D. Y.; Emrick, T.; Russell, T. P., Controlled Placement of CdSe Nanoparticles in Diblock Copolymer Templates by Electrophoretic Deposition. *Nano Letters* **2005,** 5, (2), 357-361.

11. Hornyak, G.; Kroll, M.; Pugin, R.; Sawitowski, T.; Schmid, G.; Bovin, J.-O.; Karsson, G.; Hofmeister, H.; Hopfe, S., Gold clusters and colloids in alumina nanotubes. *Chemistry--A European Journal* **1997,** 3, (12), 1951-1956.

12. Kamada, K.; Fukuda, H.; Maehara, K.; Yoshida, Y.; Nakai, M.; Hasuo, S.; Matsumoto, Y., Insertion of SiO2 nanoparticles into pores of anodized aluminum by electrophoretic deposition in aqueous system. *Electrochemical and Solid-State Letters* **2004,** 7, (8), B25-B28.

13. Limmer, S. J.; Seraji, S.; Forbess, M. J.; Wu, Y.; Chou, T. P.; Nguyen, C.; Cao, G., Electrophoretic growth of lead zirconate titanate nanorods. *Advanced Materials (Weinheim, Germany)* **2001,** 13, (16), 1269-1272.

14. Islam, M. A.; Herman, I. P., Electrodeposition of patterned CdSe nanocrystal films using thermally charged nanocrystals. *Applied Physics Letters* **2002,** 80, (20), 3823-3825.

15. Chandrasekharan, N.; Kamat, P. V., Assembling gold nanoparticles as nanostructured films using an electrophoretic approach. *Nano Letters* **2001,** 1, (2), 67-70.

16. Trau, M.; Saville, D. A.; Aksay, I. A., Field-induced layering of colloidal crystals. *Science (Washington, D. C.)* **1996,** 272, (5262), 706-9.

17. Bailey, R. C.; Stevenson, K. J.; Hupp, J. T., Assembly of micropatterned colloidal gold thin films via microtransfer molding and electrophoretic deposition. *Advanced Materials (Weinheim, Germany)* **2000,** 12, (24), 1930-1934.

18. Murray, C. B.; Kagan, C. R.; Bawendi, M. G., Synthesis and characterization of monodisperse nanocrystals and close-packed nanocrystal assemblies. *Annual Review of Materials Science* **2000,** 30, 545-610.

19. Shevchenko, E. V.; Talapin, D. V.; Kotov, N. A.; O'Brien, S.; Murray, C. B., Structural diversity in binary nanoparticle superlattices. *Nature (London, United Kingdom)* **2006,** 439, (7072), 55-59.

20. Zheng, N.; Fan, J.; Stucky, G. D., One-Step One-Phase Synthesis of Monodisperse Noble-Metallic Nanoparticles and Their Colloidal Crystals. *Journal of the American Chemical Society* **2006,** 128, (20), 6550-6551.

21. Van der Biest, O. O.; Vandeperre, L. J., Electrophoretic deposition of materials. *Annual Review of Materials Science* **1999,** 29, 327-352.

22. Besra, L.; Liu, M., A review on fundamentals and applications of electrophoretic deposition (EPD). *Progress in Materials Science* **2006,** 52, (1), 1-61.

23. Dahlquist, J. A.; Brodie, I., Electrophoretic development of electrostatic charge images from colloidal suspensions of carbon. *Journal of Applied Physics* **1969,** 40, (7), 3020-3027.

24. Mohn, E., Kinetics of electrophoretic particle deposition and measurement of zeta potentials. *Photographic Science and Engineering* **1971,** 15, (6), 451-455.

25. Novotny, V., Applications on nonaqueous colloids. *Colloids and Surfaces* **1987,** 24, (4), 361-375.

26. Comiskey, B.; Albert, J. D.; Yoshizawa, H.; Jacobson, J., An electrophoretic ink for all-printed reflective electronic displays. *Nature (London)* **1998,** 394, (6690), 253-255.

27. Crowley, J. M.; Till, H. R. In *Image development by electrostatic lithography*, Proceedings of the Third International Congress on Advances in Non-Impact Printing Technologies, San Francisco, CA, Aug. 24-28, 1986, 1986; Society for Imaging Science and Technology: Springfield, VA, 1986: San Francisco, CA, 1986; pp pp 100-112.

28. Tulagin, V., Imaging method based on photoelectrophoresis. *Journal of the Optical Society of America* **1969,** 59, (3), 328-331.

29. Block, H.; Kelly, J. P., Electro-rheology. *Journal of Physics D: Applied Physics* **1988,** 21, (12), 1661-1677.

30. Gast, A. P.; Zukoski, C. F., Electrorheological fluids as colloidal suspensions. *Advances in Colloid and Interface Science* **1989,** 30, (3-4), 153-202.

31. Morrison, I. D., Electrical charges in nonaqueous media. *Colloids and Surfaces, A: Physicochemical and Engineering Aspects* **1993,** 71, (1), 1-37.

32. Kitahara, A., Nonaqueous systems. In *Electrical Phenomena at Interfaces: Fundamentals, Measurements, and Applications*, 2nd ed.; Ohshima, H.; Furusawa, K., Eds. Marcel Dekker: New York, 1998; Vol. 76, pp 135-150.

33. Parfitt, G. D.; Peacock, J., Stability of colloidal dispersions in nonaqueous media. *Surface and Colloid Science* **1978,** 10, 163-226.

34. Royall, C. P.; Leunissen, M. E.; van Blaaderen, A., A new colloidal model system to study long-range interactions quantitatively in real space. *Journal of Physics: Condensed Matter* **2003,** 15, (48), S3581-S3596.

35. Yethiraj, A.; van Blaaderen, A., A colloidal model system with an interaction tunable from hard sphere to soft and dipolar. *Nature (London, United Kingdom)* **2003,** 421, (6922), 513-517.

36. Hsu, M. F.; Dufresne, E. R.; Weitz, D. A., Charge Stabilization in Nonpolar Solvents. *Langmuir* **2005,** 21, (11), 4881-4887.

37. Ryoo, W.; Dickson, J. L.; Dhanuka, V. V.; Webber, S. E.; Bonnecaze, R. T.; Johnston, K. P., Electrostatic Stabilization of Colloids in Carbon Dioxide: Electrophoresis and Dielectrophoresis. *Langmuir* **2005,** 21, (13), 5914-5923.

38. Smith, P. G., Jr.; Ryoo, W.; Johnston, K. P., Electrostatically Stabilized Metal Oxide Particle Dispersions in Carbon Dioxide. *Journal of Physical Chemistry B* **2005,** 109, (43), 20155-20165.

39. Smith, P. G. J. r.; Patel, M. N.; Kim, J.; Milner, T. E.; Johnston, K. P., Effect of Surface Hydrophilicity on Charging Mechanism of Colloids in Low-Permittivity Solvents. *Journal of Physical Chemistry C* **2007,** 111, (2), 840-848.

40. Kitahara, A.; Karasawa, S.; Yamada, H., The effect of water on the electrokinetic potential and stability of suspensions in nonpolar media. *Journal of Colloid and Interface Science* **1967,** 25, (4), 490-5.

41. Kitahara, A.; Tamura, T.; Konno, K., Effect of water on flocculation of carbon black in nonaqueous surfactant solutions. *Separation Science and Technology* **1980,** 15, (3), 249-61.

42. Green, J. H.; Parfitt, G. D., Stability of concentrated colloidal dispersions in apolar media. *Particulate Science and Technology* **1987,** 5, (3), 289-99.

43. Pugh, R. J.; Matsunaga, T.; Fowkes, F. M., The dispersibility and stability of carbon black in media of low dielectric constant. 1. Electrostatic and steric contributions to colloidal stability. *Colloids and Surfaces* **1983,** 7, (3), 183-207.

44. Eicke, H. F.; Borkovec, M.; Das-Gupta, B., Conductivity of water-in-oil microemulsions: a quantitative charge fluctuation model. *Journal of Physical Chemistry* **1989,** 93, (1), 314-17.

45. Kallay, N.; Tomic, M.; Chittofrati, A., Conductivity of water-in-oil microemulsions: comparison of the Boltzmann statistics and the charge fluctuation model. *Colloid and Polymer Science* **1992,** 270, (2), 194-196.

46. Tscharnuter, W. W., Mobility measurements by phase analysis. *Applied Optics* **2001,** 40, (24), 3995-4003.

47. Ware, B. R., Electrophoretic Light scattering. *Advances in Colloid and Interface Science* **1974,** 4, (1), 1-44.

48. Miller, J. F.; Schaetzel, K.; Vincent, B., The determination of very small electrophoretic mobilities in polar and nonpolar colloidal dispersions using phase analysis light scattering. *Journal of Colloid and Interface Science* **1991,** 143, (2), 532-54.

49. Maranzano, B. J.; Wagner, N. J.; Fritz, G.; Glatter, O., Surface charge of 3-(trimethoxysilyl) propyl methacrylate (TPM) coated Stober silica colloids by zeta-phase analysis light scattering and small angle neutron scattering. *Langmuir* **2000,** 16, (26), 10556-10558.

50. Ito, T.; Sun, L.; Bevan, M. A.; Crooks, R. M., Comparison of Nanoparticle Size and Electrophoretic Mobility Measurements Using a Carbon-Nanotube-Based Coulter Counter, Dynamic Light Scattering, Transmission Electron Microscopy, and Phase Analysis Light Scattering. *Langmuir* **2004,** 20, (16), 6940-6945.

51. Smith, P. G., Jr.; Patel, M. N.; Kim, J.; Johnston, K. P.; Milner, T. E., Electrophoretic Mobility Measurement by Differential-Phase Optical Coherence Tomography. *Journal of Physical Chemistry C* **2007,** 111, (6), 2614-2622.

52. Jenkins, P.; Basu, S.; Keir, R. I.; Ralston, J.; Thomas, J. C.; Wolffenbuttel, B. M. A., The Electrochemistry of Nonaqueous Copper Phthalocyanine Dispersions in the Presence of a Metal Soap Surfactant: A Simple Equilibrium Site Binding Model. *Journal of Colloid and Interface Science* **1999,** 211, (2), 252-263.

53. Keir, R. I.; Suparno; Thomas, J. C., Charging Behavior in the Silica/Aerosol OT/Decane System. *Langmuir* **2002,** 18, (5), 1463-1465.

54. Thomas, J. C.; Crosby, B. J.; Keir, R. I.; Hanton, K. L., Observation of Field-Dependent Electrophoretic Mobility with Phase Analysis Light Scattering (PALS). *Langmuir* **2002,** 18, (11), 4243-4247.

55. Felici, N.; Lacroix, J. C., Electroconvection in insulating liquids with special reference to uni- and bi-polar injection. *Journal of Electrostatics* **1978,** 5, 135-144.

56. Davé, D. P.; Milner, T. E., Optical low-coherence reflectometer for differential phase measurement. *Optics letters* **2000,** 25, (4), 227-229.

57. Bartl, M. H.; Boettcher, S. W.; Frindell, K. L.; Stucky, G. D., 3-D Molecular Assembly of Function in Titania-Based Composite Material Systems. *Accounts of Chemical Research* **2005,** 38, (4), 263-271.

58. Diebold, U., The surface science of titanium dioxide. *Surface Science Reports* **2003,** 48, (5-8), 53-229.

59. Chen, X.; Mao, S. S., Titanium Dioxide Nanomaterials: Synthesis, Properties, Modifications, and Applications. *Chemical Reviews (Washington, DC, United States)* **2007,** 107, (7), 2891-2959.

60. Guliants, V. V.; Carreon, M. A.; Lin, Y. S., Ordered mesoporous and macroporous inorganic films and membranes. *Journal of Membrane Science* **2004,** 235, (1-2), 53-72.

61. Kamat, P. V., Meeting the Clean Energy Demand: Nanostructure Architectures for Solar Energy Conversion. *Journal of Physical Chemistry C* **2007,** 111, (7), 2834-2860.

62. Fischer, A. E.; Pettigrew, K. A.; Rolison, D. R.; Stroud, R. M.; Long, J. W., Incorporation of Homogeneous, Nanoscale MnO2 within Ultraporous Carbon Structures via Self-Limiting Electroless Deposition: Implications for Electrochemical Capacitors. *Nano Letters* **2007,** 7, (2), 281-286.

63. Fischer, A. E.; Saunders, M. P.; Pettigrew, K. A.; Rolison, D. R.; Long, J. W., Electroless deposition of nanoscale MnO2 on ultraporous carbon nanoarchitectures: correlation of evolving pore-solid structure and electrochemical performance. *Journal of the Electrochemical Society* **2008,** 155, (3), A246-A252.

64. Besson, S.; Gacoin, T.; Ricolleau, C.; Jacquiod, C.; Boilot, J.-P., 3D Quantum Dot Lattice Inside Mesoporous Silica Films. *Nano Letters* **2002,** 2, (4), 409-414.

65. Gu, J.; Xiong, L.; Shi, J.; Hua, Z.; Zhang, L.; Li, L., Thioether moiety functionalization of mesoporous silica films for the encapsulation of highly dispersed gold nanoparticles. *Journal of Solid State Chemistry* **2006,** 179, (4), 1060-1066.

66. Perez, M. D.; Otal, E.; Bilmes, S. A.; Soler-Illia, G. J. A. A.; Crepaldi, E. L.; Grosso, D.; Sanchez, C., Growth of Gold Nanoparticle Arrays in TiO2 Mesoporous Matrixes. *Langmuir* **2004,** 20, (16), 6879-6886.

67. Kumai, Y.; Tsukada, H.; Akimoto, Y.; Sugimoto, N.; Seno, Y.; Fukuoka, A.; Ichikawa, M.; Inagaki, S., Highly ordered platinum nanodot arrays with cubic symmetry in mesoporous thin films. *Advanced Materials (Weinheim, Germany)* **2006,** 18, (6), 760-762.

68. Gu, J.-L.; Shi, J.-L.; You, G.-J.; Xiong, L.-M.; Qian, S.-X.; Hua, Z.-L.; Chen, H.-R., Incorporation of highly dispersed gold nanoparticles into the pore channels of mesoporous silica thin films and their ultrafast nonlinear optical response. *Advanced Materials (Weinheim, Germany)* **2005,** 17, (5), 557-560.

69. Lee, U. H.; Lee, H.; Wen, S.; Mho, S.-i.; Kwon, Y.-U., Mesoporous titania thin films with pseudo-cubic structure: Synthetic studies and applications to nanomembranes and nanotemplates. *Microporous and Mesoporous Materials* **2006,** 88, (1-3), 48-55.

70. Stathatos, E.; Lianos, P.; Falaras, P.; Siokou, A., Photocatalytically deposited silver nanoparticles on mesoporous TiO2 films. *Langmuir* **2000,** 16, (5), 2398-2400.

71. Rioux, R. M.; Song, H.; Hoefelmeyer, J. D.; Yang, P.; Somorjai, G. A., High-Surface-Area Catalyst Design: Synthesis, Characterization, and Reaction Studies of Platinum Nanoparticles in Mesoporous SBA-15 Silica. *Journal of Physical Chemistry B* **2005,** 109, (6), 2192-2202.

72. Gupta, G.; Shah, P. S.; Zhang, X.; Saunders, A. E.; Korgel, B. A.; Johnston, K. P., Enhanced Infusion of Gold Nanocrystals into Mesoporous Silica with Supercritical Carbon Dioxide. *Chemistry of Materials* **2005,** 17, (26), 6728-6738.

73. Gupta, G.; Stowell, C. A.; Patel, M. N.; Gao, X.; Yacaman, M. J.; Korgel, B. A.; Johnston, K. P., Infusion of Presynthesized Iridium Nanocrystals into Mesoporous Silica for High Catalyst Activity. *Chemistry of Materials* **2006,** 18, (26), 6239-6249.

74. Gupta, G.; Patel, M. N.; Ferrer, D.; Heitsch, A. T.; Korgel, B. A.; Jose-Yacaman, M.; Johnston, K. P., Stable Ordered FePt Mesoporous Silica Catalysts with High Loadings. *Chemistry of Materials* **2008,** 20, (15), 5005-5015.

75. Liu, H.; Song, C.; Zhang, L.; Zhang, J.; Wang, H.; Wilkinson, D. P., A review of anode catalysis in the direct methanol fuel cell. *Journal of Power Sources* **2006,** 155, (2), 95-110.

76. Giersig, M.; Mulvaney, P., Formation of ordered two-dimensional gold colloid lattices by electrophoretic deposition. *Journal of Physical Chemistry* **1993,** 97, (24), 6334-6.

77. Giersig, M.; Mulvaney, P., Preparation of ordered colloid monolayers by electrophoretic deposition. *Langmuir* **1993,** 9, (12), 3408-13.

78. Subramanian, V.; Wolf, E.; Kamat, P. V., Semiconductor-Metal Composite Nanostructures. To What Extent Do Metal Nanoparticles Improve the Photocatalytic Activity of TiO2 Films? *Journal of Physical Chemistry B* **2001,** 105, (46), 11439-11446.

79. Islam, M. A.; Xia, Y.; Steigerwald, M. L.; Yin, M.; Liu, Z.; O'Brien, S.; Levicky, R.; Herman, I. P., Addition, suppression, and inhibition in the electrophoretic deposition of nanocrystal mixture films for CdSe nanocrystals with g-Fe2O3 and Au Nanocrystals. *Nano Letters* **2003,** 3, (11), 1603-1606.

80. Islam, M. A.; Xia, Y.; Telesca, D. A., Jr.; Steigerwald, M. L.; Herman, I. P., Controlled electrophoretic deposition of smooth and robust films of CdSe nanocrystals. *Chemistry of Materials* **2004,** 16, (1), 49-54.

81. Limmer, S. J.; Hubler, T. L.; Cao, G., Nanorods of Various Oxides and Hierarchically Structured Mesoporous Silica by Sol-Gel Electrophoresis. *Journal of Sol-Gel Science and Technology* **2003,** 26, (1/2/3), 577-581.

82. Limmer, S. J.; Cruz, S. V.; Cao, G. Z., Films and nanorods of transparent conducting oxide ITO by a citric acid sol route. *Applied Physics A: Materials Science & Processing* **2004,** 79, (3), 421-424.

83. Limmer, S. J.; Chou, T. P.; Cao, G. Z., A study on the influences of processing parameters on the growth of oxide nanorod arrays by sol electrophoretic deposition. *Journal of Sol-Gel Science and Technology* **2005,** 36, (2), 183-195.

84. Conway, B. E.; Birss, V.; Wojtowicz, J., The role and utilization of pseudocapacitance for energy storage by supercapacitors. *Journal of Power Sources* **1997,** 66, (1-2), 1-14.

85. Frackowiak, E.; Beguin, F., Carbon materials for the electrochemical storage of energy in capacitors. *Carbon* **2001,** 39, (6), 937-950.

86. Frackowiak, E., Carbon materials for supercapacitor application. *Physical Chemistry Chemical Physics* **2007,** 9, (15), 1774-1785.

87. Chmiola, J.; Yushin, G.; Gogotsi, Y.; Portet, C.; Simon, P.; Taberna, P. L., Anomalous Increase in Carbon Capacitance at Pore Sizes Less Than 1 Nanometer. *Science (Washington, DC, United States)* **2006,** 313, (5794), 1760-1763.

88. Fuertes, A. B.; Alvarez, S., Graphitic mesoporous carbons synthesised through mesostructured silica templates. *Carbon* **2004,** 42, (15), 3049-3055.

89. Fuertes, A. B.; Pico, F.; Rojo, J. M., Influence of pore structure on electric double-layer capacitance of template mesoporous carbons. *Journal of Power Sources* **2004,** 133, (2), 329-336.

90. Li, H.-Q.; Liu, R.-L.; Zhao, D.-Y.; Xia, Y.-Y., Electrochemical properties of an ordered mesoporous carbon prepared by direct tri-constituent co-assembly. *Carbon* **2007,** 45, (13), 2628-2635.

91. Liu, H.-Y.; Wang, K.-P.; Teng, H., A simplified preparation of mesoporous carbon and the examination of the carbon accessibility for electric double layer formation. *Carbon* **2005,** 43, (3), 559-566.

92. Vix-Guterl, C.; Frackowiak, E.; Jurewicz, K.; Friebe, M.; Parmentier, J.; Beguin, F., Electrochemical energy storage in ordered porous carbon materials. *Carbon* **2005,** 43, (6), 1293-1302.

93. Xing, W.; Qiao, S. Z.; Ding, R. G.; Li, F.; Lu, G. Q.; Yan, Z. F.; Cheng, H. M., Superior electric double layer capacitors using ordered mesoporous carbons. *Carbon* **2005,** 44, (2), 216-224.

94. Du, C.; Pan, N., High power density supercapacitor electrodes of carbon nanotube films by electrophoretic deposition. *Nanotechnology* **2006,** 17, (21), 5314-5318.

95. Obreja, V. V. N., On the performance of supercapacitors with electrodes based on carbon nanotubes and carbon activated material-A review. *Physica E: Low-Dimensional Systems & Nanostructures (Amsterdam, Netherlands)* **2008,** 40, (7), 2596-2605.

96. Ania, C. O.; Khomenko, V.; Raymundo-Pinero, E.; Parra, J. B.; Beguin, F., The large electrochemical capacitance of microporous doped carbon obtained by using a zeolite template. *Advanced Functional Materials* **2007,** 17, (11), 1828-1836.

97. Numao, S.; Judai, K.; Nishijo, J.; Mizuuchi, K.; Nishi, N., Synthesis and characterization of mesoporous carbon nano-dendrites with graphitic ultra-thin walls and their application to supercapacitor electrodes. *Carbon* **2009,** 47, (1), 306-312.

98. Wang, D.-W.; Li, F.; Liu, M.; Lu, G. Q.; Cheng, H.-M., 3D aperiodic hierarchical porous graphitic carbon material for high-rate electrochemical capacitive energy storage. *Angewandte Chemie, International Edition* **2008,** 47, (2), 373-376.

99. Dong, X.; Shen, W.; Gu, J.; Xiong, L.; Zhu, Y.; Li, H.; Shi, J., MnO2-Embedded-in-Mesoporous-Carbon-Wall Structure for Use as Electrochemical Capacitors. *Journal of Physical Chemistry B* **2006,** 110, (12), 6015-6019.

100. Kinoshita, K., *Carbon: Electrochemical and Physicochemical Properties*. Wiley-Interscience: New York, 1988.

101. Stoller, M. D.; Park, S.; Zhu, Y.; An, J.; Ruoff, R. S., Graphene-Based Ultracapacitors. *Nano Letters* **2008,** 8, (10), 3498-3502.

102. Zheng, J. P.; Jow, T. R., A new charge storage mechanism for electrochemical capacitors. *Journal of the Electrochemical Society* **1995,** 142, (1), L6-L8.

103. Zheng, J. P.; Cygan, P. J.; Jow, T. R., Hydrous ruthenium oxide as an electrode material for electrochemical capacitors. *Journal of the Electrochemical Society* **1995,** 142, (8), 2699-703.

104. Kim, I.-H.; Kim, K.-B., Ruthenium oxide thin film electrodes for supercapacitors. *Electrochemical and Solid-State Letters* **2001,** 4, (5), A62-A64.

105. Liang, Y.-Y.; Li, H. L.; Zhang, X.-G., Solid state synthesis of hydrous ruthenium oxide for supercapacitors. *Journal of Power Sources* **2007,** 173, (1), 599-605.

106. Subhramannia, M.; Balan, B. K.; Sathe, B. R.; Mulla, I. S.; Pillai, V. K., Template-Assisted Synthesis of Ruthenium Oxide Nanoneedles: Electrical and Electrochemical Properties. *Journal of Physical Chemistry C* **2007,** 111, (44), 16593-16600.

107. Hu, C.-C.; Chang, K.-H.; Lin, M.-C.; Wu, Y.-T., Design and Tailoring of the Nanotubular Arrayed Architecture of Hydrous RuO2 for Next Generation Supercapacitors. *Nano Letters* **2006,** 6, (12), 2690-2695.

108. Toupin, M.; Brousse, T.; Belanger, D., Charge Storage Mechanism of MnO2 Electrode Used in Aqueous Electrochemical Capacitor. *Chemistry of Materials* **2004,** 16, (16), 3184-3190.

109. Toupin, M.; Brousse, T.; Belanger, D., Influence of Microstructure on the Charge Storage Properties of Chemically Synthesized Manganese Dioxide. *Chemistry of Materials* **2002,** 14, (9), 3946-3952.

110. Long, J. W.; Swider-Lyons, K. E.; Stroud, R. M.; Rolison, D. R., Design of pore and matter architectures in manganese oxide charge-storage materials. *Electrochemical and Solid-State Letters* **2000,** 3, (10), 453-456.

111. Jeong, Y. U.; Manthiram, A., Nanocrystalline Manganese Oxides for Electrochemical Capacitors with Neutral Electrolytes. *Journal of the Electrochemical Society* **2002,** 149, (11), A1419-A1422.

112. Luo, J.-Y.; Xia, Y.-Y., Effect of pore structure on the electrochemical capacitive performance of MnO2. *Journal of the Electrochemical Society* **2007,** 154, (11), A987-A992.

113. Devaraj, S.; Munichandraiah, N., Effect of Crystallographic Structure of MnO2 on Its Electrochemical Capacitance Properties. *Journal of Physical Chemistry C* **2008,** 112, (11), 4406-4417.

114. Pang, S.-C.; Anderson, M. A.; Chapman, T. W., Novel electrode materials for thin-film ultracapacitors: comparison of electrochemical properties of sol-gel-derived and electrodeposited manganese dioxide. *Journal of the Electrochemical Society* **2000,** 147, (2), 444-450.

115. Pang, S.-C.; Anderson, M. A., Novel electrode materials for electrochemical capacitors: part II. Material characterization of sol-gel-derived and electrodeposited manganese dioxide thin films. *Journal of Materials Research* **2000,** 15, (10), 2096-2106.

116. Shinomiya, T.; Gupta, V.; Miura, N., Effects of electrochemical-deposition method and microstructure on the capacitive characteristics of nano-sized manganese oxide. *Electrochimica Acta* **2006,** 51, (21), 4412-4419.

117. Belanger, D.; Brousse, T.; Long, J. W., Manganese oxides: battery materials make the leap to electrochemical capacitors. *Electrochemical Society Interface* **2008,** 17, (1), 49-52.

118. Brock, S. L.; Sanabria, M.; Suib, S. L.; Urban, V.; Thiyagarajan, P.; Potter, D. I., Particle Size Control and Self-Assembly Processes in Novel Colloids of Nanocrystalline Manganese Oxide. *Journal of Physical Chemistry B* **1999,** 103, (35), 7416-7428.

119. Park, J.; Kang, E.; Bae, C. J.; Park, J.-G.; Noh, H.-J.; Kim, J.-Y.; Park, J.-H.; Park, H. M.; Hyeon, T., Synthesis, Characterization, and Magnetic Properties of Uniform-sized MnO Nanospheres and Nanorods. *Journal of Physical Chemistry B* **2004,** 108, (36), 13594-13598.

120. Ragupathy, P.; Vasan, H. N.; Munichandraiah, N., Synthesis and characterization of nano-MnO2 for electrochemical supercapacitor studies. *Journal of the Electrochemical Society* **2007,** 155, (1), A34-A40.

121. Seo, W. S.; Jo, H. H.; Lee, K.; Kim, B.; Oh, S. J.; Park, J. T., Size-dependent magnetic properties of colloidal Mn3O4 and MnO nanoparticles. *Angewandte Chemie, International Edition* **2004,** 43, (9), 1115-1117.

122. Chen, H.; Dong, X.; Shi, J.; Zhao, J.; Hua, Z.; Gao, J.; Ruan, M.; Yan, D., Templated synthesis of hierarchically porous manganese oxide with a crystalline nanorod framework and its high electrochemical performance. *Journal of Materials Chemistry* **2007,** 17, (9), 855-860.

123. Xu, C.-L.; Bao, S.-J.; Kong, L.-B.; Li, H.; Li, H.-L., Highly ordered MnO2 nanowire array thin films on Ti/Si substrate as an electrode for electrochemical capacitor. *Journal of Solid State Chemistry* **2006,** 179, (5), 1351-1355.

124. Doescher, M. S.; Pietron, J. J.; Dening, B. M.; Long, J. W.; Rhodes, C. P.; Edmondson, C. A.; Rolison, D. R., Using an Oxide Nanoarchitecture To Make or Break a Proton Wire. *Analytical Chemistry* **2005,** 77, (24), 7924-7932.

125. Chen, H.; He, J.; Zhang, C.; He, H., Self-Assembly of Novel Mesoporous Manganese Oxide Nanostructures and Their Application in Oxidative Decomposition of Formaldehyde. *Journal of Physical Chemistry C* **2007,** 111, (49), 18033-18038.

126. Broughton, J. N.; Brett, M. J., Investigation of thin sputtered Mn films for electrochemical capacitors. *Electrochimica Acta* **2004,** 49, (25), 4439-4446.

127. Jin, X.; Zhou, W.; Zhang, S.; Chen, G. Z., Nanoscale microelectrochemical cells on carbon nanotubes. *Small* **2007,** 3, (9), 1513-1517.

128. Raymundo-Pinero, E.; Khomenko, V.; Frackowiak, E.; Beguin, F., Performance of Manganese Oxide/CNTs Composites as Electrode Materials for Electrochemical Capacitors. *Journal of the Electrochemical Society* **2005,** 152, (1), A229-A235.

129. Fischer, A. E.; Long, J. W., Redox deposition of nanoscale MnO2 on ultraporous carbon nanoarchitectures: correlation of MnO2 deposition time and electrochemical performance. *ECS Transactions* **2007,** 3, (37, Electrochemical Capacitors 2006), 61-66.

130. Lei, Y.; Fournier, C.; Pascal, J.-L.; Favier, F., Mesoporous carbon-manganese oxide composite as negative electrode material for supercapacitors. *Microporous and Mesoporous Materials* **2008,** 110, (1), 167-176.

131. Lee, C. Y.; Tsai, H. M.; Chuang, H. J.; Li, S. Y.; Lin, P.; Tseng, T. Y., Characteristics and electrochemical performance of supercapacitors with manganese oxide-carbon nanotube nanocomposite electrodes. *Journal of the Electrochemical Society* **2005,** 152, (4), A716-A720.

132. Sharma, R. K.; Oh, H.-S.; Shul, Y.-G.; Kim, H., Carbon-supported, nano-structured, manganese oxide composite electrode for electrochemical supercapacitor. *Journal of Power Sources* **2007,** 173, (2), 1024-1028.

133. Xie, X.; Gao, L., Characterization of a manganese dioxide/carbon nanotube composite fabricated using an in situ coating method. *Carbon* **2007,** 45, (12), 2365-2373.

134. Zhang, L. L.; Wei, T.; Wang, W.; Zhao, X. S., Manganese oxide-carbon composite as supercapacitor electrode materials. *Microporous and Mesoporous Materials* **2009,** 123, (1-3), 260-267.

Chapter 2

Electrophoretic Mobility of Concentrated Carbon Black Dispersions in Low-Permittivity Solvents by Optical Coherence Tomography

Electrophoretic mobilities of concentrated dispersions of carbon black particles in a low-permittivity solvent were measured using differential-phase optical coherence tomography (DP-OCT). An electrode spacing of only 0.18 mm enables measurement of highly concentrated dispersions up to 1 wt% of highly absorbing carbon black. It also enables high electric fields, at low electric potentials, to measure low electrophoretic mobilities encountered in low-permittivity solvents. The zeta potential ranged from -24 mV to -12 mV as the concentration of surfactant sodium bis(2-ethyl-1-hexyl)sulfosuccinate (AOT) concentration was increased from 1 mM to 100 mM. A mechanism is presented to explain the electrostatic charging of the carbon black particles in terms of the partitioning of the ions between the reverse micelles in the double-layer and the surfactant adsorbed on the particle surface, as the AOT concentration is varied.

The contents of this chapter are being prepared for a manuscript.

2.1 INTRODUCTION

Carbon black particles are of great importance in applications such as ink-jet printing, electrophoretic displays,[1, 2] paints, and petroleum processing.[3, 4] In these systems, the particles are typically dispersed in a nonaqueous solvent where the electrostatic charge mechanism is not clearly understood. In aqueous systems, colloidal charging and stabilization are more clearly understood in terms of dissociation of surface groups or electrolyte adsorption playing a dominant role.[4] A fundamental understanding of the charging behavior of colloidal particles in low-permittivity media would be beneficial for advancing practical applications.

Electrostatic stabilization of colloids in low-permittivity solvents with a dielectric constant <5 generally requires additives such as polymers or surfactants to separate the ions in the bulk from the surface, that is to prevent ion pairing.[5-16] The thermodynamics of ion separation for a 1:1 electrolyte are given by the Bjerrum length, the ratio between electrostatic interaction energy and thermal energy, as

$$l_B = \frac{e^2}{4\pi\varepsilon_r\varepsilon_0 k_B T} \qquad (2.1)$$

where e is the elementary charge, ε_r is the dielectric constant (static permittivity), ε_0 is the vacuum permittivity, k_B is the Boltzmann constant, and T is the temperature. For water, the dielectric constant is high ($\varepsilon_r = 80$), and l_B is quite small at 0.7 nm. However, for nonaqueous low-permittivity solvents, such as toluene where $\varepsilon_r = 2.4$, it reaches 24 nm. Here, additives such as polymers, crown ethers, or micelles are needed to prevent ion pairing (Fig. 2.1). The colloid surface is balanced by charge carriers in the double layer in dynamic equilibrium. These micelles can be both positively and negatively charged in their own dynamic equilibrium with uncharged micelles as given by the charge fluctuation model.[17, 18] The charges are easily separated in the double-layer from the surface as the micelles (or charge carrying entities) can be ~5 nm in size, which is large enough to solubilize small ions (<1 nm).

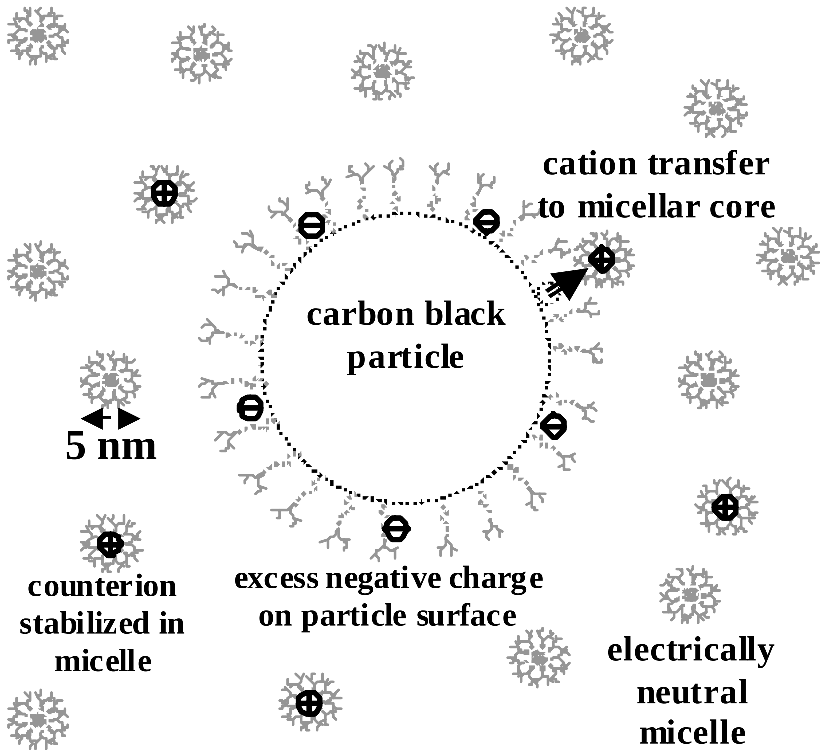

Figure 2.1: Schematic of carbon black particle surrounded by reverse micelles showing charge transfer between the particle surface and reverse micelles. (Adapted from Ryoo et al.[9])

The electrophoretic mobility, μ, of particles is much smaller in low-permittivity media compared to aqueous systems, and can thus be difficult to measure. The electrophoretic mobility is given by

$$\mu = (\zeta\varepsilon_r\varepsilon_0 f(\kappa a))/\eta \qquad (2.2)$$

where ζ is the zeta potential, κa is the reduced inverse Debye length, and η is the viscosity of the solvent.[19] The value of $f(\kappa a)$ is determined by the medium, electrolyte concentration, and size of the colloids. In aqueous systems where $\kappa a >> 1$, $f(\kappa a) = 1$ (Smoluchowski limit), while for nonaqueous systems $f(\kappa a) << 1$ and $f(\kappa a) = {}^2/_3$ (Hückel limit). Hence mobilities in nonaqueous systems are lower compared to their aqueous counterparts. More importantly, the mobility is greatly reduced by the low dielectric constant of the media which is ~33x lower for toluene compared to water. Only a limited number of techniques exist to adequately measure the mobility of particles in nonaqueous media.

Laser Doppler electrophoresis (LDE) can be used to measured mobilities using the frequency shift of light for particles that are sub-microscopic; however, the mobility of the particles must be $>1\times10^{-9}$ m^2/Vs.[20, 21] An extension of LDE is phase analysis light scattering (PALS), which provides for greater sensitivity to particle motion in an electric field.[22, 23] In PALS changes in the phase angle are used to determine the velocity of the particle in an electric field, making it 1000x more sensitive compared to LDE. However, given the large electrode spacings (1-4 mm),[24] the small mobilities in nonpolar media require large potentials,[25-27] which can produce undesired chemical reactions[23] and electrohydrodynamic instabilities.[28] Much smaller potentials may be used in differential-phase optical coherence tomography (DP-OCT) given the very narrow electrode spacing of 0.18 mm.[24, 29] Compared to techniques such as LDE and PALS, more turbid, concentrated dispersions can be analyzed with DP-OCT since only a small coherence detection volume is sampled. Previously, it was shown that concentrated dispersions (up to 0.12 wt%) of highly scattering TiO_2 particles dispersed in AOT-toluene could be easily measured using DP-OCT.[24] Mobilities as low as $\sim3\times10^{-10}$ m^2/Vs were measured for the ~200 nm diameter particles.

Carbon black dispersions with AOT in nonaqueous solvent have been studied with visual microelectrophoresis or LDE.[3, 12-14] In media such as cyclohexane, heptane, benzene, and dodecane, zeta potentials up to -120 mV have been reported. These studies employed large micron-size particles in dilute dispersions. With DP-OCT, smaller particles in concentrated dispersions can be analyzed.

The objectives of this study were to extend the domain of electrophoretic mobility measurement with DP-OCT to concentrated dispersions of highly absorbing particles in a solution of AOT in toluene and to describe the mechanisms that govern the particle electrostatic charging in the low-permittivity solvent. The particle size of carbon black was determined by dynamic light scattering, and the zeta potentials of the negatively charged particles were examined as a function of particle and AOT concentrations. Spectrograms from DP-OCT show the effects of particle concentration on the measurement intensity. The electrostatic charging of the carbon black particles is described in terms of the surfactant adsorption and structure on the particle surface and the preferential partitioning of ions between the adsorbed surfactant layers on the particle surface and the reverse micelles in the large double-layer.

2.2 MATERIALS SECTION

2.2.1 Materials

Carbon black sterling NSX76 was supplied from Cabot Corporation. Surfactant Aerosol-OT (sodium bis(2-ethyl-1-hexyl)sulfosuccinate) and toluene were supplied from Sigma and E-M Science, respectively, and used as received.

2.2.2 Dispersion Formation

The particle dispersions were prepared by mixing surfactant stock solutions with surfactant-free particle stock solutions. The dispersions were shaken vigorously before and after mixing to ensure homogeneity. The particle polarity was determined by using visual microelectrophoresis.

2.2.3 Dynamic Light Scattering

The size of carbon black particles in toluene was measured using a Brookhaven Instruments ZetaPlus dynamic light scattering (DLS) apparatus at a scattering angle of 90° and temperature of 25 °C. A dilute particle dispersion (<0.01 wt%) was used to acquire the particle size to avoid multiple scattering. The DLS data was analyzed using a non-negative least-squares (NNLS) method, which is based on the Stokes-Einstein equation for the diffusion coefficient of a sphere, $D_0=k_BT/3\pi\eta d_H$, where η is the solvent viscosity, and d_H is the distribution of hydrodynamic diameters.

2.2.4 Electrophoresis using Differential-Phase Optical Coherence Tomography

The Doppler shift of light scattered from moving particles was measured using DP-OCT velocimetry.[24] The electrophoresis chamber was a cylindrical void (10 mm diameter and 180 μm thick) in the electrophoresis chamber body, which was cut from a microscope cover slip. The electrodes were ITO-coated glass (Delta Technologies, CG-61IN-S115, 25 mm by 75 mm, 1.1 mm thick, 60-100 nm ITO layer). A 1 Hz frequency of the applied symmetric square wave electric field (10 V amplitude) was high enough to avoid significant accumulation of particles at the electrodes but low enough to provide a substantial duration (0.5 s) of electrophoresis between field reversals. The electric field was low enough also such that stripping of counterions from the particle did not occur to increase the electrophoretic mobility.[4] For TiO_2 particles in AOT-toluene, a linear increase in electrophoretic mobility was seen with electric field strength (28-56 kV/m), resulting in a constant zeta potential.[11, 24] The electrode separation d was measured as 180 μm using OCT giving an electric field strength of 56 kV/m for this study.

To perform a measurement, a micropipette was used to dispense at least 20 μL of sample into the electrophoresis chamber. The top electrode was placed and fastened, the electric field was applied, and scans were begun within typically 5 s. For each sample, at least 10 scans were collected, each of duration 2 s. The time between scans was typically 0.5-4 s. Carbon black dispersions that were completely opaque in vials with a 2 cm path length could be studied by DP-OCT in a 180 μm chamber.

For the data analysis, a spectrogram, a three-dimensional plot of intensity of frequencies as a function of time, was generated by short-time discrete Fourier transform.[24] The spectrogram was calculated for rapid preliminary evaluation of each 2-s scan, as it indicated signal strength and approximate Doppler shift as a function of electric field application time. The average Doppler shift with higher frequency resolution was calculated by a separate discrete Fourier transform.

2.3 RESULTS AND DISCUSSION

Dynamic light scattering gives the carbon black particle size distribution (Fig. 2.2). A dilute dispersion in 60 mM AOT-toluene showed a tight particle size distribution centered at ~216 nm with a range of 214-218 nm. The almost uniform size of the particles allows for easier measurements using DP-OCT as diffusional broadening from polydispersity is minimized.[24]

Spectrogram profiles for different concentrations of carbon black dispersions in 60 mM AOT-toluene are shown in Fig. 2.3. With higher particle concentrations, the number of scatters in the coherence detection volume increases, which can result in an increase in the intensity of the spectrogram. While a yellow intensity is satisfactory for identifying particles, a stronger red intensity is more favorable for analyzing the Doppler shift of the particles. At the lowest particle concentration of 0.01 wt% carbon black, the particles produce a yellow intensity in the spectrogram. At 0.1 wt% and 1 wt% carbon black, both yellow and red colors are visible signifying the particles. The DP-OCT technique is highly versatile for analyzing such a wide range in concentration. In our previous study, the highest concentration tested was only 0.12 wt% TiO_2,[24] nearly an order of magnitude lower. With DP-OCT, the coherence detection volume is small at ~2000 μm^3 since the objective diameter is 10 μm and the coherence length is 25 μm for the broadband light source. Other detection volumes are much larger e.g. for LDE it is 10^7 μm^3, which requires dilute dispersions to avoid multiple scattering.[24] Hence with the smaller detection volume, concentrated dispersions can be easily analyzed with DP-OCT when combined with close electrode spacings. The number of carbon black particles

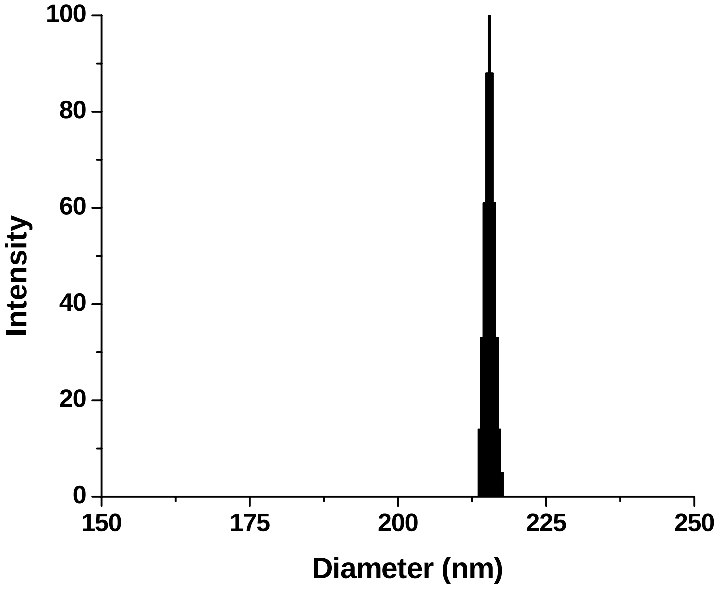

Figure 2.2: Dynamic light scattering size distribution data for dilute dispersion of carbon black in 60 mM AOT-toluene.

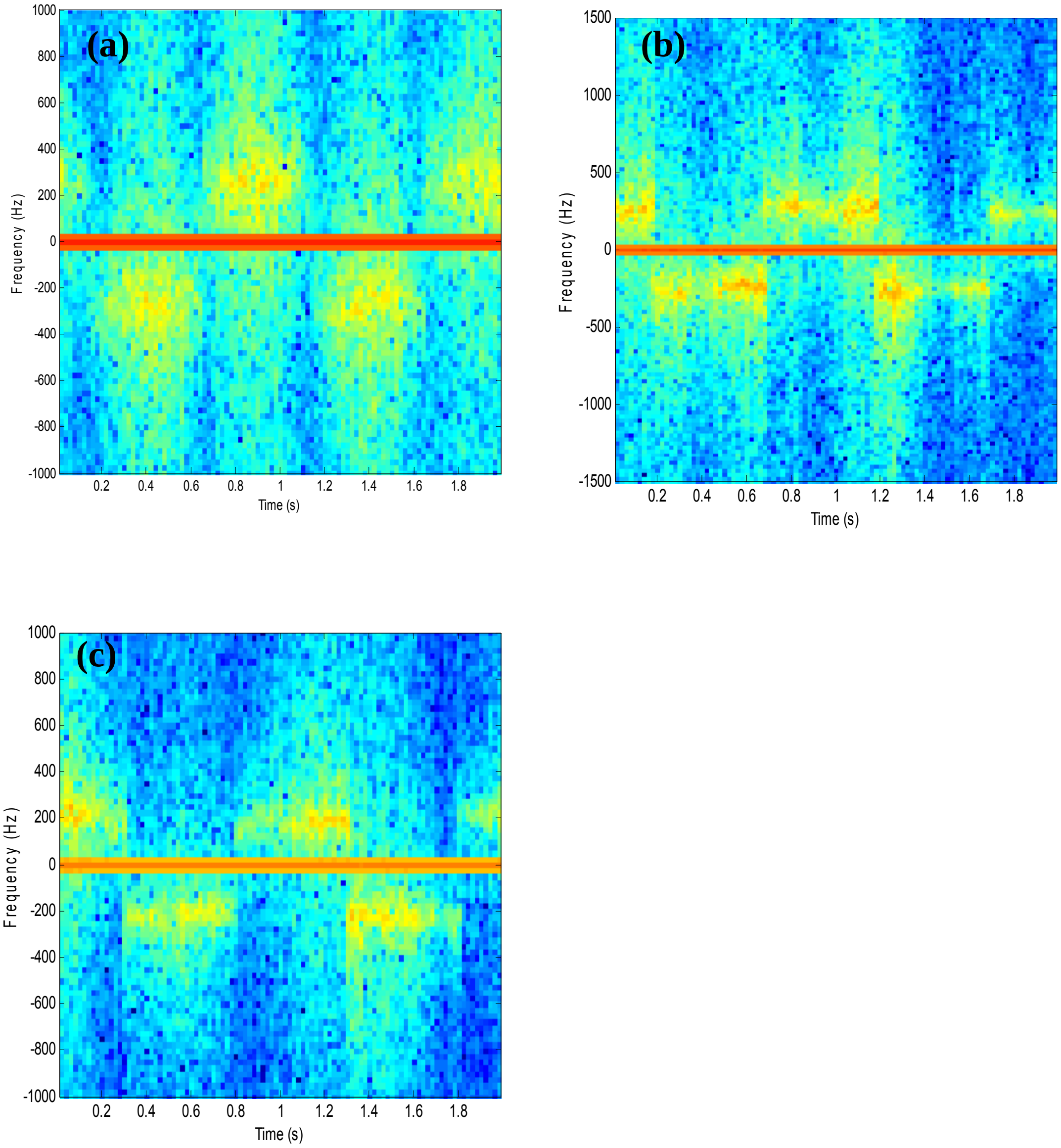

Figure 2.3: Spectrogram profiles showing carbon black concentration effect on intensity at 60 mM AOT-toluene: (a) 0.01 wt% , (b) 0.1 wt%, and (c) 1 wt%.

within the volume can be as few as 15 particles at 0.01 wt% or as high as 1500 particles at 1 wt%.

To confirm the particle concentrations had minimal effect on the charging of the particles, the zeta potentials for different carbon black weight fractions in a 60 mM AOT-toluene solution are given in Figure 2.4. The particle polarity was confirmed with visual microelectrophoresis. Although the small particles were not visible, a dark cloud can be seen to move towards the positive electrode between field reversals. The zeta potential was calculated from the electrophoretic mobility (eqn. 2.2) of the carbon black particles measured using DP-OCT, which was measured using the velocity of the particle computed from the beat frequency shift of light under an applied electric field (56 kV/m).[24] For particle concentrations from 0.01 wt% to 1.0 wt% carbon black, the zeta potential was between -13 mV and -12 mV. Therefore, the particle concentrations were low enough compared to the surfactant concentrations such that charging was caused by ion adsorption and not dissociation of ionizable groups on the particle surface.[11, 30] Conversely, high particle concentration dispersions can result in overlap of double-layers, leading to lower zeta potentials.[4, 11] With the relatively constant zeta potential over this particle concentration range, neither ionizable groups nor double layer overlap occurred. For the following experiments, the particle concentration was chosen to be 0.1 wt% since it gave high contrast in spectrograms and fell within the limits tested for particle concentration effects.

Surfactant concentrations were varied from 1 mM to 100 mM AOT in toluene as shown in Fig. 2.5 and Table 2.1 at a particle concentration of 0.1 wt% carbon black. Without AOT surfactant present, neither visual microelectrophoresis nor DP-OCT showed movement of the particles in an electric field. The particles settled after ~1 hr without AOT, but remained dispersed for >24 hrs with AOT. In contrast, a high zeta potential of -24 mV or electrophoretic mobility of -5.8×10^{-10} m^2/Vs was measured at the lowest surfactant concentration of 1 mM AOT. At the highest concentration of 100 mM AOT, the zeta potential decreased to -12 mV (-2.9×10^{-10} m^2/Vs). A similar type of trend of decreasing particle charge has been observed for TiO_2 particles dispersed in AOT-toluene.[11]

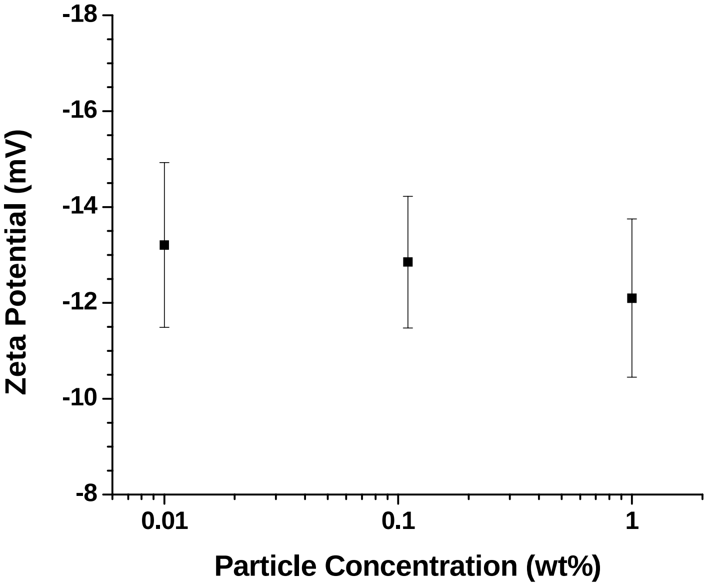

Figure 2.4. Minimal change in zeta potential with carbon black concentration at 60 mM AOT-toluene.

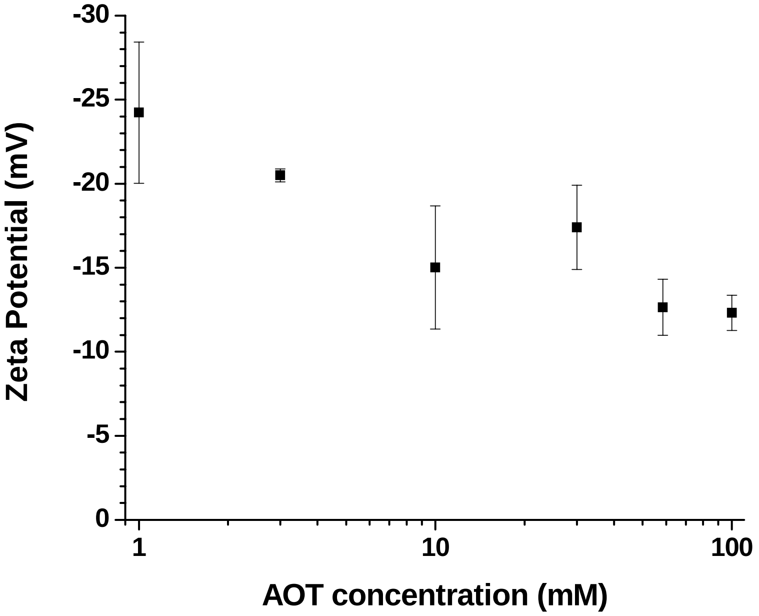

Figure 2.5: AOT surfactant concentration effect on zeta potential at 0.1 wt% carbon black in toluene.

Table 2.1. AOT surfactant concentration effect on 0.1 wt% carbon black particle charge in toluene.

AOT conc. (mM)	Electrophoretic mobility (10^{-10}) (m^2/Vs)	Elementary charges/particle	Zeta potential (mV)
1	-5.8	4.3	-24
3	-4.9	3.7	-21
10	-3.6	2.7	-15
30	-4.2	3.1	-17
60	-3.0	2.2	-13
100	-2.9	2.2	-12

Zeta potentials in the current study were much lower compared to previous reports (-25 to -115 mV) for carbon black dispersions in AOT-organic solvent systems.[12-14] For a carbon black dispersion in AOT-benzene, the zeta potential decreased from -115 mV to -70 mV for a range of 5-80 mM AOT.[12] The amount of water present in the system also plays a role in the absolute value of the particle zeta potential. For carbon black particles dispersed in 20 mM AOT-cyclohexane, the zeta potential decreased from -60 mV to -20 mV with increasing water content from 5-200 mM H_2O.[13] For the samples in the current study, no excess drying steps were taken. The amount of water is expected to be similar to the amounts in our previous study with 10-30 mM H_2O for 0-90 mM AOT.[11] Slightly more water is possibly introduced from the carbon black particles. Since the carbon black particles are amorphous and contain oxygen functional groups on the surface,[31] some amount of pre-adsorbed water is perhaps present. The lower zeta potentials of the carbon black particles with AOT herein also were too low to provide for complete electrostatic stabilization. An absolute zeta potential of ~30 mV[32] is needed to electrostatically stabilize the particles; hence, the AOT also provides steric stabilization to contribute in keeping the carbon particles well dispersed.

The adsorption of the bulky sulfosuccinate hydrocarbon chains takes place with a decreasing areal footprint with increasing AOT concentration. For graphite particles dispersed in cyclohexane with AOT, the AOT adsorption density increased from 0.5 μmol/m^2 at 1 mM AOT to 4.8 μmol/m^2 at 30 mM AOT.[33] Herein, at 0.1 wt% carbon black particles of 216 nm diameter, these adsorption densities would correlate to AOT concentrations of 0.005 mM and 0.05 mM AOT adsorbed onto the particle surface, which is much less compared to the bulk AOT concentrations of 1 mM and 30 mM AOT. Hence, the particle surface is already covered with AOT molecules at low surfactant concentrations as given in Fig. 2.6a, but with a large areal footprint (~330 Å^2). At high AOT concentrations (Fig. 2.6b), the areal footprint is small (~35 Å^2) with AOT molecules more closely packed on the particle surface.

A proposed mechanism for electrostatic charging of the carbon black particles is given in Figure 2.6 based on our previous study.[11] The soft sulfosuccinate hydrocarbon chains of AOT preferentially adsorb on the particle surface relative to the hard cations.

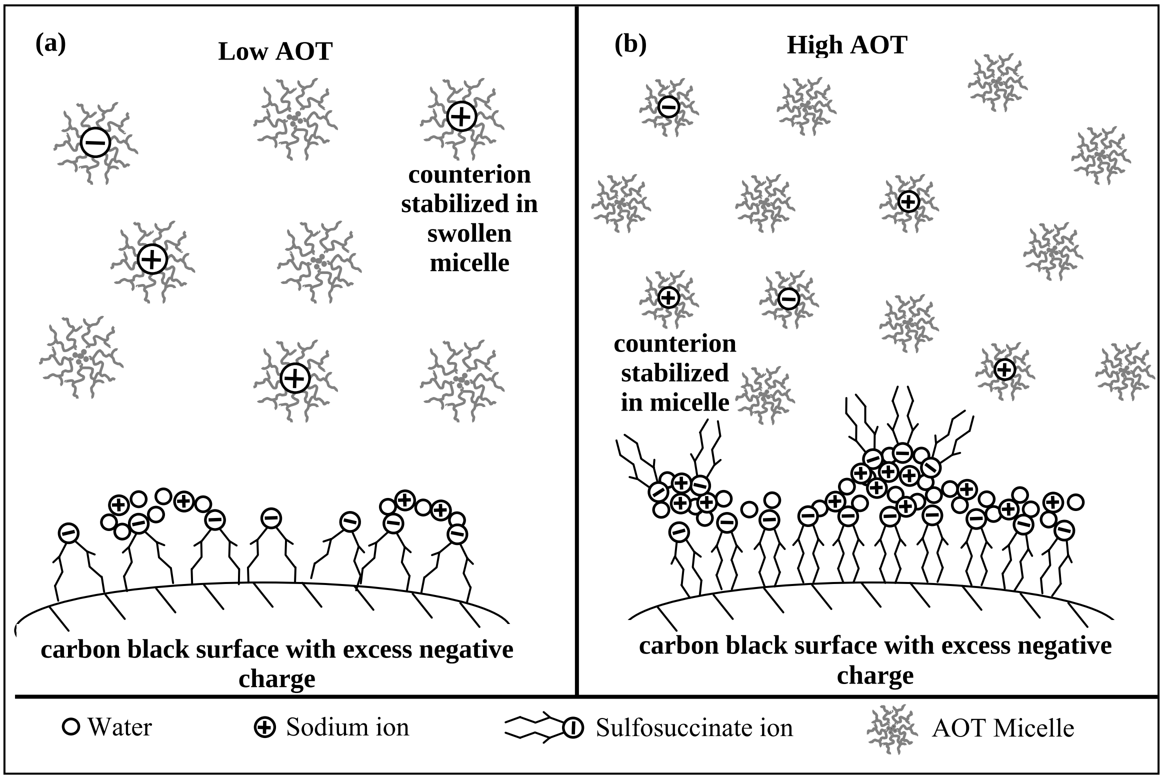

Figure 2.6: Electrostatic charging mechanism for negative carbon black particles dispersed in toluene with AOT at (a) low concentration where the W_o is high and AOT is loosely packed on particle surface and (b) high concentration where the W_o is low and surface is densely covered with AOT. (Adapted from Smith et al.[11])

At low concentrations, the particle surface is loosely covered with AOT molecules[11, 33] along with reverse micelles formed in the bulk (Fig. 2.6a). Water (>10 mM) is present in the system at low AOT concentrations and gives rise to a high W_o (water to surfactant ratio) and swollen micelles in the double-layer.[11] The carbon black has a negative charge formed from the sulfosuccinate anion with the hard sodium cation favoring the hydrated swollen reverse micelle cores in the thick double-layer. The net negative charge of the carbon particle, which has only ~4 elementary charges per particle, is balanced in the double layer by positive charges from the sodium cations in the hydrated reverse micelles. The double-layer is also in dynamic equilibrium with both positive and negative charges as given by the charge fluctuation model.[17, 18] With increasing surfactant concentration, the carbon black particle surface becomes covered by closely-packed sulfosuccinate ions and reverse micelle type entities form on the particle surface (Fig. 2.6b).[11, 16, 33] The number of reverse micelles in the double-layer increases much more than the water amount (>30 mM)[11] causing the W_o to decrease, and the water cores shrink in the reverse micelles. With the increase in the reverse micelles on the particle surface, and thus the hydrophilic domains, sodium ions migrate towards the particle and reduce the charge to ~2 elementary charges per particle. This change in sodium ion partitioning results in a decrease in the zeta potential as seen in Fig. 2.5. Hydrophobic TiO_2 particles dispersed in AOT-toluene followed a similar charging mechanism as described by Smith et al.[11]

2.4 CONCLUSIONS

The spectrogram intensities are sufficient in DP-OCT to determine electrophoretic mobilities even with highly absorbing carbon black particles in concentrated dispersions at 1 wt%. An advantage of the narrow electrode spacings (0.18 mm) in DP-OCT is that higher strength electric fields, needed to measure small mobilities accurately, may be realized at lower absolute potentials to reduce electrohydrodynamic instabilities and electrode reactions.[24] Zeta potentials in the range of -24 mV to -12 mV were measured for surfactant concentrations from 1 mM to 100 mM AOT-toluene. The electrostatic charge on the particles depends on the preferential partitioning of ions between the reverse micelles in the double-layer and the particle surface. At low concentrations the cations prefer the reverse micelles more strongly resulting in more negative zeta potentials, whereas at high concentrations the cations partition towards the particle surface and lower the magnitude of the charge. The ability to measure electrophoretic mobilities with DP-OCT with low electrical potentials and over a wide range of particle concentrations will be beneficial for further understanding the complex charging mechanisms for particles in low-permittivity solvents.

2.5 REFERENCES

1. Novotny, V., Applications on nonaqueous colloids. *Colloids and Surfaces* **1987,** 24, (4), 361-375.

2. Comiskey, B.; Albert, J. D.; Yoshizawa, H.; Jacobson, J., An electrophoretic ink for all-printed reflective electronic displays. *Nature (London)* **1998,** 394, (6690), 253-255.

3. Morrison, I. D., Electrical charges in nonaqueous media. *Colloids and Surfaces, A: Physicochemical and Engineering Aspects* **1993,** 71, (1), 1-37.

4. Kitahara, A., Nonaqueous systems. In *Electrical Phenomena at Interfaces: Fundamentals, Measurements, and Applications*, 2nd ed.; Ohshima, H.; Furusawa, K., Eds. Marcel Dekker: New York, 1998; Vol. 76, pp 135-150.

5. Parfitt, G. D.; Peacock, J., Stability of colloidal dispersions in nonaqueous media. *Surface and Colloid Science* **1978,** 10, 163-226.

6. Royall, C. P.; Leunissen, M. E.; van Blaaderen, A., A new colloidal model system to study long-range interactions quantitatively in real space. *Journal of Physics: Condensed Matter* **2003,** 15, (48), S3581-S3596.

7. Yethiraj, A.; van Blaaderen, A., A colloidal model system with an interaction tunable from hard sphere to soft and dipolar. *Nature (London, United Kingdom)* **2003,** 421, (6922), 513-517.

8. Hsu, M. F.; Dufresne, E. R.; Weitz, D. A., Charge Stabilization in Nonpolar Solvents. *Langmuir* **2005,** 21, (11), 4881-4887.

9. Ryoo, W.; Dickson, J. L.; Dhanuka, V. V.; Webber, S. E.; Bonnecaze, R. T.; Johnston, K. P., Electrostatic Stabilization of Colloids in Carbon Dioxide: Electrophoresis and Dielectrophoresis. *Langmuir* **2005,** 21, (13), 5914-5923.

10. Smith, P. G., Jr.; Ryoo, W.; Johnston, K. P., Electrostatically Stabilized Metal Oxide Particle Dispersions in Carbon Dioxide. *Journal of Physical Chemistry B* **2005,** 109, (43), 20155-20165.

11. Smith, P. G. J. r.; Patel, M. N.; Kim, J.; Milner, T. E.; Johnston, K. P., Effect of Surface Hydrophilicity on Charging Mechanism of Colloids in Low-Permittivity Solvents. *Journal of Physical Chemistry C* **2007,** 111, (2), 840-848.

12. Kitahara, A.; Karasawa, S.; Yamada, H., The effect of water on the electrokinetic potential and stability of suspensions in nonpolar media. *Journal of Colloid and Interface Science* **1967,** 25, (4), 490-5.

13. Kitahara, A.; Tamura, T.; Konno, K., Effect of water on flocculation of carbon black in nonaqueous surfactant solutions. *Separation Science and Technology* **1980,** 15, (3), 249-61.

14. Green, J. H.; Parfitt, G. D., Stability of concentrated colloidal dispersions in apolar media. *Particulate Science and Technology* **1987,** 5, (3), 289-99.

15. Pugh, R. J.; Matsunaga, T.; Fowkes, F. M., The dispersibility and stability of carbon black in media of low dielectric constant. 1. Electrostatic and steric contributions to colloidal stability. *Colloids and Surfaces* **1983,** 7, (3), 183-207.

16. Roberts, G. S.; Sanchez, R.; Kemp, R.; Wood, T.; Bartlett, P., Electrostatic charging of nonpolar colloids by reverse micelles. *Langmuir* **2008,** 24, (13), 6530-6541.

17. Eicke, H. F.; Borkovec, M.; Das-Gupta, B., Conductivity of water-in-oil microemulsions: a quantitative charge fluctuation model. *Journal of Physical Chemistry* **1989,** 93, (1), 314-17.

18. Kallay, N.; Tomic, M.; Chittofrati, A., Conductivity of water-in-oil microemulsions: comparison of the Boltzmann statistics and the charge fluctuation model. *Colloid and Polymer Science* **1992,** 270, (2), 194-196.

19. Tscharnuter, W. W., Mobility measurements by phase analysis. *Applied Optics* **2001,** 40, (24), 3995-4003.

20. Ware, B. R., Electrophoretic Light scattering. *Advances in Colloid and Interface Science* **1974,** 4, (1), 1-44.

21. Miller, J. F.; Schaetzel, K.; Vincent, B., The determination of very small electrophoretic mobilities in polar and nonpolar colloidal dispersions using phase analysis light scattering. *Journal of Colloid and Interface Science* **1991,** 143, (2), 532-54.

22. Maranzano, B. J.; Wagner, N. J.; Fritz, G.; Glatter, O., Surface charge of 3-(trimethoxysilyl) propyl methacrylate (TPM) coated Stober silica colloids by zeta-phase analysis light scattering and small angle neutron scattering. *Langmuir* **2000,** 16, (26), 10556-10558.

23. Ito, T.; Sun, L.; Bevan, M. A.; Crooks, R. M., Comparison of Nanoparticle Size and Electrophoretic Mobility Measurements Using a Carbon-Nanotube-Based

Coulter Counter, Dynamic Light Scattering, Transmission Electron Microscopy, and Phase Analysis Light Scattering. *Langmuir* **2004,** 20, (16), 6940-6945.

24. Smith, P. G., Jr.; Patel, M. N.; Kim, J.; Johnston, K. P.; Milner, T. E., Electrophoretic Mobility Measurement by Differential-Phase Optical Coherence Tomography. *Journal of Physical Chemistry C* **2007,** 111, (6), 2614-2622.

25. Jenkins, P.; Basu, S.; Keir, R. I.; Ralston, J.; Thomas, J. C.; Wolffenbuttel, B. M. A., The Electrochemistry of Nonaqueous Copper Phthalocyanine Dispersions in the Presence of a Metal Soap Surfactant: A Simple Equilibrium Site Binding Model. *Journal of Colloid and Interface Science* **1999,** 211, (2), 252-263.

26. Keir, R. I.; Suparno; Thomas, J. C., Charging Behavior in the Silica/Aerosol OT/Decane System. *Langmuir* **2002,** 18, (5), 1463-1465.

27. Thomas, J. C.; Crosby, B. J.; Keir, R. I.; Hanton, K. L., Observation of Field-Dependent Electrophoretic Mobility with Phase Analysis Light Scattering (PALS). *Langmuir* **2002,** 18, (11), 4243-4247.

28. Felici, N.; Lacroix, J. C., Electroconvection in insulating liquids with special reference to uni- and bi-polar injection. *Journal of Electrostatics* **1978,** 5, 135-144.

29. Davé, D. P.; Milner, T. E., Optical low-coherence reflectometer for differential phase measurement. *Optics letters* **2000,** 25, (4), 227-229.

30. Medrzycka, K. B., The effect of particle concentration on zeta potential in extremely dilute solutions. *Colloid and Polymer Science* **1991,** 269, (1), 85-90.

31. Kinoshita, K., *Carbon: Electrochemical and Physicochemical Properties*. Wiley-Interscience: New York, 1988.

32. Tabor, R. F.; Eastoe, J.; Dowding, P. J.; Grillo, I.; Heenan, R. K.; Hollamby, M., Formation of Surfactant-Stabilized Silica Organosols. *Langmuir* **2008,** 24, (22), 12793-12797.

33. Krishnakumar, S.; Somasundaran, P., Adsorption of Aerosol-OT on graphite from aqueous and non-aqueous media. *Colloids and Surfaces, A: Physicochemical and Engineering Aspects* **1996,** 117, (3), 227-233.

Chapter 3

Electrophoretic Deposition of Au Nanocrystals inside Perpendicular Mesochannels of TiO_2

Au nanocrystals stabilized by dodecanethiol were deposited into 100 to 150 nm thick TiO_2 films with evenly spaced perpendicular nanopillars and mesochannels on the order of 10 nm supported on conducting ITO/glass electrodes. Electrophoretic deposition was used to enhance nanocrystal deposition within the mesoporous TiO_2 film. X-ray photoelectron spectroscopy (XPS), scanning electron microscopy (SEM) with energy dispersive X-ray (EDX), UV–vis spectroscopy, variable angle spectroscopic ellipsometry (VASE), and scanning surface potential microscopy (SSPM) were used to characterize the resulting Au nanocrystal/TiO_2 composites. Au nanocrystal loadings reached 21 wt% and were not kinetically limited at 10 min, relative to depositions performed for 20 hours. Both VASE measurements of the anisotropy of the imaginary refractive index, k, and XPS depth profiling studies indicate that Au nanocrystals are dispersed within the vertically aligned mesopores and distributed throughout the film. The mean penetration depth of a single nanocrystal penetrating inside the film is described with a model in terms of the electric field and a local deposition rate constant, which is influenced by ligand binding and architecture on the nanocrystal surface.

Large portions of this chapter have been previously published in Patel, M. N.; Williams, R. D.; May, R. A.; Uchida, H.; Stevenson, K. J.; Johnston, K. P., *Chemistry of Materials*, 20, 6029-6040 (2008)

3.1 INTRODUCTION

Titanium dioxide has been widely used in solar cells,[1] sensors,[2] batteries,[3] and photocatalysis.[4] Tuning of the mesoporous structure and composition of TiO_2 has been explored as a means to tailor optical, magnetic, photonic, electronic, and catalytic properties.[5] For instance, mesoporous TiO_2 has been shown to be a more effective catalyst because of its large surface area and pore structure that result in increased surface reactivity and improved mass transport. The facile preparation of ordered mesoporous electrodes with uniformly-sized pores that are oriented perpendicular to the substrate are desirable for facilitating charge-transfer and mass transport.[6] Unfortunately, most synthetic strategies that use structure directing templates for preparing mesoporous TiO_2 films produce pore architectures with large pore size distributions with pores that are either tortuous in nature or that run parallel to the substrate.[7-12] In sol-gel synthesis of TiO_2 films using structure-directing block copolymers, the ratio of surfactant, metal oxide precursor, and solvent may be adjusted to control the morphology, pore size, and pore orientation.[13-16] This route involves evaporation-induced self-assembly (EISA),[17-20] where the film geometry begins to form as the growth substrate is withdrawn from a solution containing both surfactant and metal oxide precursor. As the solvent evaporates, the local surfactant concentration increases to form micelles which guide the metal oxide precursor into hydrophilic regions to form phase segregated regions. Our group and others have demonstrated that anatase mesoporous TiO_2 thin films with perpendicular pores can be prepared on polymer modified glass,[21] silicon wafers,[22] and conducting ITO/glass substrates.[23] Similarly, Watkins and coworkers have prepared mesoporous silica films on silicon, by facilitating diffusion and condensation reactions with supercritical CO_2.[24]

The incorporation of nanocrystals such as Au, Pt, and Ag into mesoporous TiO_2 is known to enhance optoelectronic and catalytic properties.[25-30] Metal/semiconductor films have typically been prepared by reduction of metal ion precursors inside a mesoporous thin film by heat, electrochemical deposition, or UV radiation.[28, 29, 31-36] However, with these methods it is difficult to control the nanocrystal morphology, size, and dispersion;

furthermore, the nanocrystals may grow until they block the pores.[37] To better control the nanocrystal composition, size, and dispersion within mesoporous powders, a novel approach has been developed in which pre-synthesized nanocrystals are infused into the mesoporous support.[38-40] Several methods have been used to drive nanocrystal infusion including sonication[38] and the addition of a nonsolvent, supercritical CO_2, to an organic solvent such as toluene.[39, 40] The $scCO_2$ strengthens the nanocrystal–mesoporous silica interaction leading to higher loadings. The stabilizing ligand may be designed to be removed at low temperatures after infusion.[40] This technique provides excellent control over the morphology of the mesoporous support as well as the nanocrystal size, shape, and composition for the purpose of achieving high catalytic activities and stabilities.[38, 40]

An alternative approach to designing nanocomposite thin films is electrophoretic deposition of presynthesized nanocrystals on flat substrates such as carbon coated copper grids[41, 42] and ITO/glass.[43, 44] Kamat et al. have used this technique in organic solvents to deposit charged Au, Pt, and Ir nanocrystals onto films composed of disordered 10–40 nm TiO_2 nanocrystals.[26, 27] The film thickness depends upon both the concentration and deposition time. Metal nanocrystal layers formed by electrophoretic deposition are generally thicker than those formed by Langmuir Blodgett, self-assembled monolayer, or adsorption techniques. The aggregated nanocrystals form nanoporous films.[45] Thick films of CdSe nanocrystals deposited from an organic solvent, hexane, have been deposited electrophoretically onto conducting planar substrates composed of a 150 nm Au/10 nm Ti/Si wafer.[46-48] CdSe nanocrystals were also electrophoretically deposited selectively onto patterned Au films.[46, 48] Electrophoretic deposition produced more uniform films than dry casting or spin casting.[46]

Very few studies report electrophoretic deposition of nanocrystals into mesoporous thin films. Preferably, the pores of the film should be perpendicular to the substrate and aligned with the electric field.[49, 50] Limmer et al. have infused small nanoclusters inside porous membranes such as track-etched polycarbonate or anodic alumina with pore sizes of 100–200 nm and thicknesses to 10 μm.[51-54] The nanoclusters completely filled the pores of the membranes and were heated to form nanowires. Zhang et al. used electrophoretic deposition to infuse 3 nm CdSe nanocrystals into thin polymer films with 15 nm pores and a thickness of 30–40 nm.[55] In both of these studies, the pore to nanocrystal diameter ratio, while a tunable feature, was over 5.

The objective of this study was to achieve high loadings and deep penetration of 3.1 nm Au nanocrystals into 10 nm perpendicular pores in ~150 nm thick mesoporous TiO_2 thin films supported on conducting ITO/glass electrodes. The effect of electrophoresis on the kinetics and thermodynamics of deposition is analyzed by comparison with control experiments without an applied electric field for deposition times of 10 min and 20 hours. The electric field was varied as well as the nanocrystal concentration in the bulk phase. The electrical and structural properties of the prepared mesoporous TiO_2 thin films were characterized by scanning surface potential microscopy, atomic force microscopy, and scanning electron microscopy. UV–vis spectroscopy of the nanocomposite films was used to provide a relative measure of the nanocrystal loading. These loadings will be shown to be consistent with the absolute loadings determined by EDX and elemental analysis. Spectroscopic ellipsometry and X-ray photoelectron spectroscopy indicate that the Au nanocrystals penetrated deeply into the pores of the TiO_2 film with a maximum loading of 21% by weight and 12% by volume. The influence of the various properties including the nanocrystal size, pore diameter, electrophoretic mobility, electric field strength, and local deposition rate constant on the mean penetration depth of a single nanocrystal was analyzed based on an electrophoretic deposition model, which is based on the Fokker-Planck equation.[56, 57] From the experimental mean deposition distance in the pores, a rate constant was estimated from the model. The penetration depth of the nanocrystals depends upon the strength of the nanocrystal-wall interactions, which are influenced by the coverage of the metal surface by the dodecanethiol ligands. The presynthesis of both the nanocrystals and the mesoporous thin films is shown to be a useful approach to control the nanocrystal shape, size, composition, and dispersion within the pores, as well as the mesoporous structure of the thin film.

3.2 EXPERIMENTAL SECTION

3.2.1 Materials

All chemicals were used as received. Titanium (IV) isopropoxide ($Ti(O\cdot i\text{-}C_3H_7)_4$) (97 %), hydrogen tetrachloroaurate(III) trihydrate ($HAuCl_4\cdot 3H_2O$) (99.9%), tetraoctylammonium bromide ($(C_8H_{17})_4\text{-}NBr$) (98%), sodium borohydride ($NaBH_4$) (99%), and 1-dodecanethiol ($C_{12}H_{25}SH$) (98%) were purchased from Sigma-Aldrich Cooperation, and toluene (99.9%), chloroform (99.9%), hydrocholoric acid (HCl) (35.5 %), ethanol (C_2H_5OH) (Absolute 200 proof), and 2-propanol ($(CH_3)_2CHOH$) (99.9 %) from Fisher Scientific. Non-ionic triblock copolymer surfactant Pluronic P123 (poly-(ethylene oxide) poly-(propylene oxide) poly-(ethylene oxide) $EO_{20}\text{-}PO_{70}\text{-}EO_{20}$) was supplied by BASF. Water (H_2O) was double-distilled and deionized. ITO/glass substrates were purchased from Delta Technologies, Limited.

3.2.2 Preparation of Substrates

The substrates for the mesoporous thin films were prepared as described elsewhere.[23] ITO/glass slides were cut into 1 x 1 cm^2 sections, rinsed using 2-propanol, and blown dry in air flow. A TiO_2-buffer layer was coated on the ITO/glass substrate by chemical solution deposition. The purpose of the buffer layer is to increase the surface energy of the substrate to facilitate self-assembly of the polymer micelles to template the mesoporous structure. Ti solution was prepared by mixing 0.03 g of $Ti(O\cdot i\text{-}C_3H_7)_4$ and 10 cm^3 of 2-propanol. ITO/glass substrates were dip-coated with a speed of ~ 6.0 cm/min, followed by heat-treatment at 200^{o}C for 5 min in air for drying and polymerization. The film thickness of the TiO_2 buffer layer was estimated to be approximately 2 nm by spectroscopic ellipsometry.[23]

3.2.3 Preparation of Mesoporous Titania Films

Mesoporous titania films were prepared by self-assembly of block copolymer surfactants in sol-gel solution as described elsewhere.[22, 23] 1.05 g of $Ti(O\cdot i\text{-}C_3H_7)_4$ was hydrolyzed using 0.74 g of concentrated aqueous HCl under stirring for 10 min at room temperature. The hydrolyzed sol was mixed with 0.2 g of P123 surfactant dissolved in

3.0 g of ethanol while stirring for 15 min at room temperature. The resulting solution was spin-coated on the substrates at a rate of ~7500 rpm for 60 seconds, followed by aging at –10 °C for 2 days under a controlled humidity of ~45–55%. The samples were subsequently calcined using a tube furnace at 400°C for 4 hours in air with a heating rate of 1.0 °C/min to remove the block copolymer template and fix the mesoporous structure of the film.

3.2.4 Au Nanocrystal Synthesis

Au nanocrystals were synthesized by a two-phase arrested precipitation technique.[58, 59] 15 mL of aqueous (0.064 M) hydrogen tetrachloroaurate(III) trihydrate ($HAuCl_4 \cdot 3H_2O$) was combined with 25 mL of toluene solution containing 2.7 g of phase transfer catalyst, tetraoctylammonium bromide. After stirring for 1 h, the organic phase, with the transferred Au, was collected. The Au salt was then reduced using 15 mL of an aqueous sodium borohydride ($NaBH_4$) solution (0.44 M), resulting in Au nanocrystals dispersed in toluene, protected by the phase transfer catalyst. To this solution, 0.240 mL of dodecanethiol was added 1 hr later and stirred for 1 more hr. The Au nanocrystals were washed and size selected using ethanol as an antisolvent. Finally, the Au nanocrystals were dispersed in chloroform. The Au nanocrystals were 3.1 ± 0.7 nm as measured by transmission electron microscopy with 1.9 nm length dodecanethiol[60] capping ligands.

3.2.5 Au/TiO_2 Composite Formation

In the electrophoretic deposition process, the mesoporous TiO_2 on ITO/glass was the negative electrode. Electrical contact was made on the naked edge of the ITO substrate to ensure good electrical contact. The positive counter electrode was bare ITO/glass with the same dimensions. The electrodes were spaced 3 mm apart and completely immersed in a 2.5 mL Au nanocrystal dispersion (~0.1–0.2 mg/mL) in chloroform. A potential of 25 or 50 V was applied for 10 min to infuse the Au nanocrystals inside the mesoporous TiO_2 film. A control experiment was done by dipping the mesoporous TiO_2 film in the Au nanocrystal dispersion (~0.1 mg/mL) for 10 min and 20 hours without an applied electric field. The Au nanocrystal dispersion showed no visual change in concentration (color) after nanocomposite formation, consistent with the very large number of nanocrystals in the bulk solution versus the small amount adsorbed.

3.2.6 Characterization

The microstructure of the mesoporous film was observed using a Zeiss Supra 40VP field emission scanning electron microscope. The SEM observation was performed at an accelerating voltage of 5–10 kV. UV–vis spectra were measured using a Varian Cary 5000 spectrophotometer. Scanning surface potential microscopy measurements of the mesoporous TiO_2 were performed on a Veeco Bioscope Atomic Force Microscope (AFM) with a Nanoscope IV controller. Scan sizes were 1 x 1 μm, and the scan rate was 1 Hz. The interleave scan used for surface potential measurements was fixed at 10 nm.[61] Potentials were applied to the mesoporous film by connecting the ITO support to the sample stage with conductive Cu tape. The SSPM probes used for data collection were custom fabricated from NSC15/Ti-Pt (Mikromasch) Pt coated AFM probes. Previous experiments have shown these probes have insufficient resolution for nanoscale SSPM studies,[62, 63] so they were modified in a dual-beam focused ion beam (FEI DB235) with a 30 keV beam and beam current of 20 nA. Cone angles of the probes were reduced from 30° to 10°, and tip radii were unchanged.

X-ray photoelectron spectroscopy was done with a PHI 5700 XPS system using a monochromatic Al X-ray source. The system was calibrated using Au4f, Ag3d, and Cu2p peaks. Ar ions at 3 kV and a 45° angle were used to sputter the sample for a known length of time. The sample was measured with XPS for Au and Ti after each sputtering time. The bottom of the film was defined as the point where a large increase in the amount of In was detected. Energy dispersive X-ray analysis was performed using a LEO 1530 SEM equipped with an IXRF EDX system, the latter operated with a 20 kV electron beam and 60 μm aperture (average counts ~2000 s^{-1}). Elemental analysis was done with a Varian GTA120 AA240-Z graphite tube atomizer. Nanocomposites were dissolved in aqua regia overnight. The solution containing Au ions was then analyzed to determine the Au content.

A J.A. Woolam M-2000 variable angle spectroscopic ellipsometer was used to determine the ellipsometry parameters Ψ and Δ from 200 to 800 nm at three different angles, 60°, 65°, and 70°. The same instrument was also used to record p-polarized transmission measurements from 300 to 800 nm. In order to extract the films thickness as well as the real (n) and imaginary (k) portion of the complex refractive index, the data was fit using a three layer model consisting of a glass substrate, indium tin oxide,[64] and the film layer. As described previously[23] mesoporous TiO_2 was modeled assuming isotropic optical constants with a Tauc-Lorentz (T-L) oscillator for the band gap and two additional Gaussian oscillators. Upon Au infusion this isotropic approximation did not adequately describe the ellipsometry and transmission data. As a result an anisotropic uniaxial model was used to model the TiO_2 films following Au infusion. The ordinary (x-y plane) portion of the uniaxial model used a T-L oscillator[65] for the band gap, a large Gaussian above the band gap whose tail also accounted for small Urbach absorption below the band gap, a Gaussian in the visible describing the Au plasmon band, and finally a Drude oscillator[66] accounting for broad free carrier type adsorption. The extreme (z plane) refractive index used the same T-L oscillator with a Gaussian above the band gap but absorption in the visible was modeled with only a Drude oscillator. A more complex description of the extreme absorption was not necessary, and the simple two variable Drude model is desirable because of the large number of fit parameters already present in the model.

3.3 RESULTS

Figure 3.1 shows an SEM image of the mesoporous TiO_2 films with a hexagonal close-packed geometry. The top down view in Figure 3.1a shows ~10 nm pores spaced apart by ~10 nm nanopillars on a TiO_2 buffered ITO/glass substrate. The inverse mesospace (pores) and nanopillars run perpendicular to the ITO conducting substrate as seen in the cross-section view of Figure 3.1b and the schematic of Figure 3.1c. Evenly spaced pillars are present with a continuous void space. The film thickness ranges from

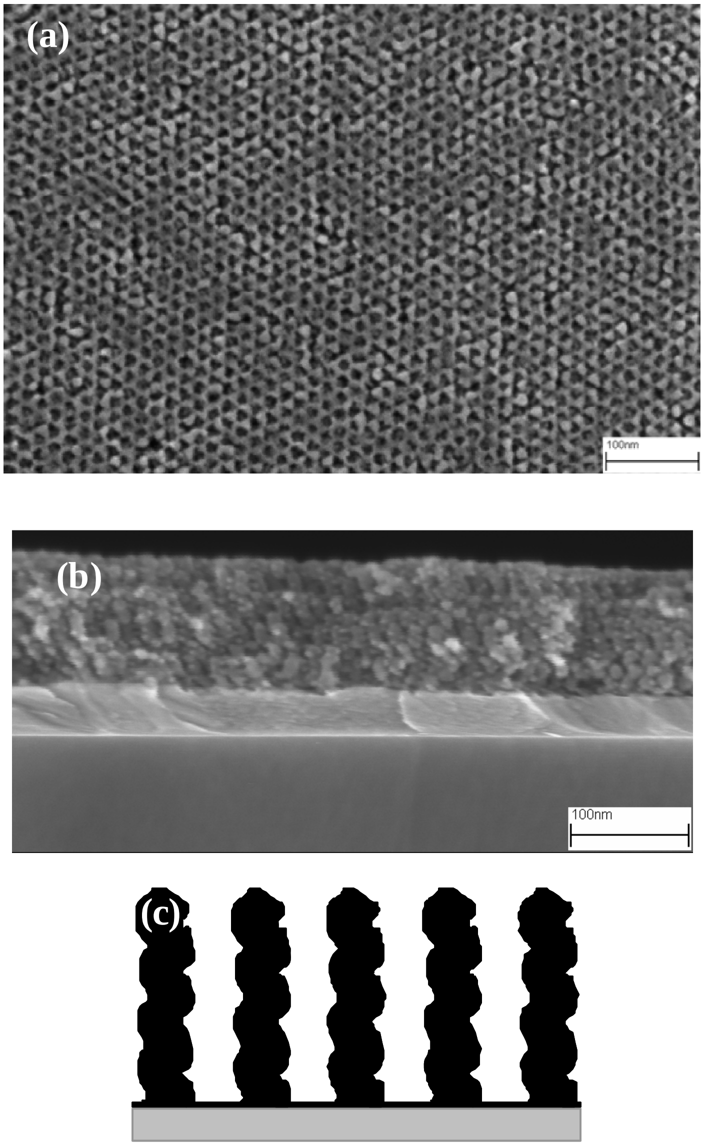

Figure 3.1: SEM image of ~110 nm mesoporous TiO_2 thin film on ITO/glass with 10 ± 2 nm pores and 10 ± 2 nm pillars. (a) top down view, (b) cross-section view, and (c) schematic of perpendicular nanopillars on ITO/glass.

~100–150 nm. The layer underneath the TiO_2 film is the conducting ITO which is approximately 60–100 nm thick as indicated by the manufacturers.

To gain insight into the electrical properties of the TiO_2 film without any Au, scanning surface potential microscopy was performed to determine the potential drop across the TiO_2 film. The AFM topography scan in Figure 3.2a resembles the structure seen in the SEM image (Figure 3.1a). The underlying ITO substrate was connected to an external voltage source and potentials of 0.0, 5.0, and 10.0 V were applied. Measured surface potentials were within 1% of the applied potential, thus the TiO_2 did not appreciably reduce the applied bias as shown in crossectional surface potential line scans (Figure 3.2b). This suggests that there is no large ohmic drop that would signify a highly resistive TiO_2 film. These small potential drops indicate that there is very little difference between the applied potential applied to the ITO electrode and the measured potential at the top of the TiO_2 film.

While the measured surface potentials were similar to the applied potential on large scales, nanoscale potential differences due to the porous symmetry of the film could not be resolved with conventional AFM probes. These potential differences, while very small in magnitude in comparison to the large potentials applied to the sample, are important to understand as they may influence Au nanocrystal transport within the mesoporous TiO_2 film. The determination of potential differences on such small size scales is not possible with conventional probe geometries,[67, 68] because they have a large tip diameter (~30 nm) and a cone angle of approximately 30°. This large tip diameter and cone angle leads to a large averaging effect in surface potential imaging and greatly reduces the resolution of the measurement.[62, 63] Successful imaging of the minute differences in surface potential along the surface of the TiO_2 required an AFM probe with a much smaller cone angle. To obtain the desired geometry, the probes were milled in a focused ion beam (FIB) to a resulting cone angle of 10° with a tip radius $\leq$ 20 nm. While the topographical resolution was very similar to that obtained with conventional Pt coated probes (Figure 3.3a), surface potential sensitivity was improved significantly. The mesoporous symmetry of the TiO_2 was clearly visible in the surface potential images, where potential differences between the mesopores and pore walls were typically 50 mV

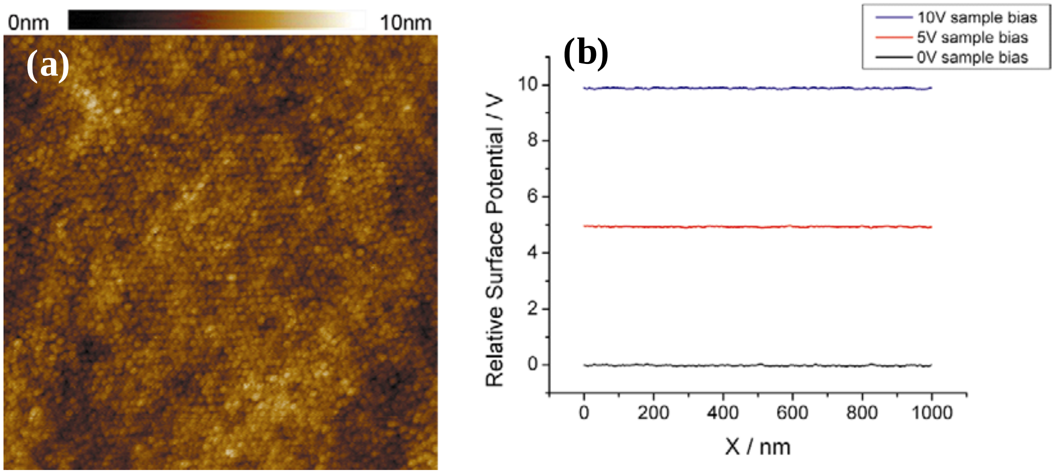

Figure 3.2: (a) 1 x 1 micron AFM topography image of the TiO_2 surface structure. (b) Crossectional line plots of surface potential measured across TiO_2 surface. Only a 1% error between the potential measured at the TiO_2 surface and that applied to the underlying ITO substrate indicates that the TiO_2 film had very little effect on the electrophoretic fields used for the Au nanocrystal insertion.

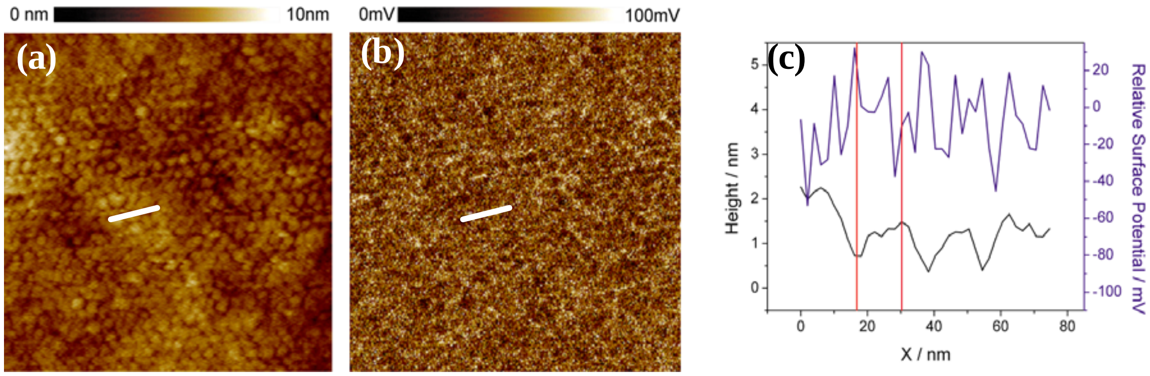

Figure 3.3: (a) 500 x 500 nm AFM topography image of Au/TiO_2 nanocomposite. (b) 500 x 500 nm surface potential image of (a) shows clear resolution of the porous structure. (c) Data from the line indicated in (a) and (b) shows typical potential differences (blue line) between the pore and the pillars (black line) of the Au/TiO_2 nanocomposite.

(Figure 3.3b). SSPM imaging of the Au/TiO_2 nanocomposite with no applied potential bias (0 V) showed surface potentials that were 50–90 mV higher in the mesopores relative to the pore walls (Fig. 3.3c). Presumably, this potential difference was found to be influenced by the addition of the Au nanocrystals in the pores since TiO_2 films without Au exhibit a potential difference between pores and pillars of the film below the noise floor of 12 mV (Appendix A, Figure A.1).

UV–vis spectroscopy of the Au/TiO_2 films is shown in Figure 3.4. The spectra have been normalized to an absorbance of 0 at 720 nm to aid visual comparison. A peak at ~515 nm is clearly present associated with the surface plasmon resonance (SPR) of Au. As shown in Figure 3.4a and Table 3.1, control experiments without an applied field at 10 min. and 20 hours gave the lowest absorbances of 0.987 and 1.05, respectively. The similar absorbance values indicated that the nanocrystal incorporation was not kinetically limited over 10 min, but thermodynamically limited. Figure 3.4a shows a control experiment in which the absorbance spectrum for Au/TiO_2 composite assembled by immersion for 20 hours without an applied voltage exhibits a peak of diminished absorbance at 502 nm corresponding to roughly a 33% decrease in absorbance relative to Au/TiO_2 composites assembled with an applied electric field (Figure 3.4b). Very similar results were obtained in 10 min. without an applied voltage. Brownian motion led to significant deposition, but less than in the electrophoretic deposition experiments with an applied field. Figure 3.4b shows the spectra for Au nanocrystals deposited electrophoretically at two different electric field strengths, 83 and 167 V/cm, corresponding to 25 and 50 V, respectively. There was a slight increase in the maximum absorbance on doubling the electric field, as shown in Table 3.1. Increasing the nanocrystal dispersion concentration by approximately a factor of two nearly doubled the maximum absorbance in the nanocomposite as shown in Figure 3.4c and Table 3.1 at a given field of 83 V/cm. Also the amount of nanocrystals loaded in each case was less than 2% of the total number of nanocrystals in bulk, so that the concentration of nanocrystals in the solution can be assumed to be constant.

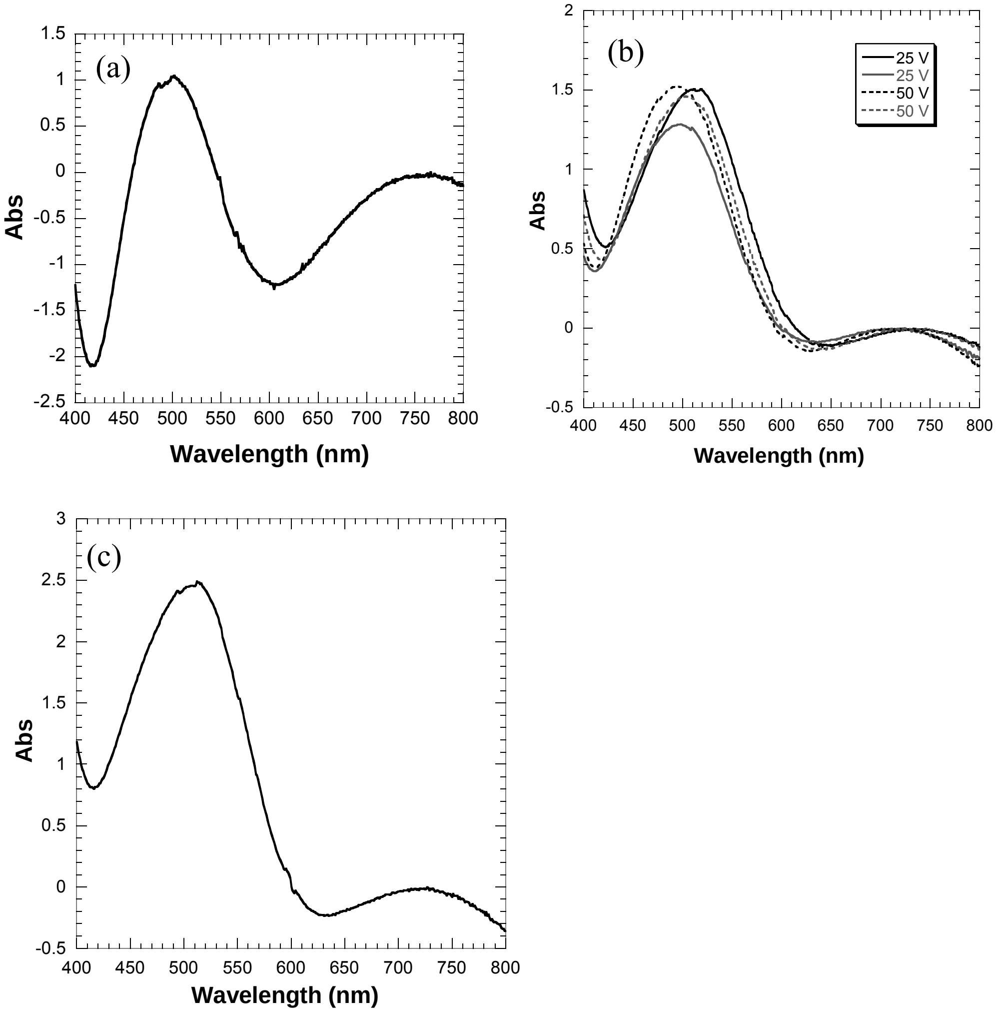

Figure 3.4: UV–vis spectroscopy of Au/TiO_2 nanocomposites. Experimental conditions: (a) ~0.1 mg/mL, 20 hrs, 0 V, (b) ~0.1 mg/mL, 10 min, 25 or 50 V, and (c) ~0.2 mg/mL, 10 min, 25 V.

Table 3.1: Maximum absorbance for surface plasmon resonance of Au for initial Au concentration of 0.1 mg/mL and 10 min. deposition time.

	Max Abs
Control (0 V)	0.987
Control (0 V)[a]	1.05
25 V	1.4 ± 0.2
50 V	1.50 ± 0.04
25 V[b]	2.49

[a]Deposition time was 20 hours. [b]Initial Au nanocrystal concentration = 0.2 mg/mL.

The complicated oscillating absorbance spectrum, which is most prevalent in Figure 3.4a with the lowest Au deposition, is attributed to interference effects occurring from the multiple interfaces comprising the ordered mesoporous film. The interfaces between the TiO_2, ITO, and glass produce interference fringes leading to the oscillations in the absorbance even with no Au present (Appendix A, Figure A.2). Small shifts of the SPR can also be seen in the spectra and can be attributed either to the slight changes in the relative dielectric constant in the immediate vicinity of the nanocrystal or to the interference effects from the films.

SEM EDX and elemental analysis of the Au/TiO_2 nanocomposite films were utilized to further quantify the nanocrystal loadings for a constant nanocrystal concentration of 0.1 mg/mL. As shown in Table 3.2, the values from SEM EDX are slightly higher than those obtained from elemental analysis, but are within experimental error for two of the three conditions. The control experiment without an applied potential gave the lowest amount of Au incorporation with a loading of ~4 wt% by SEM EDX for 10 min and ~4.6 wt% by SEM EDX and ~4.7 wt% by elemental analysis for 20 hours, where wt% reflects the amount of Au relative to the total weight of Au and TiO_2. In comparison pore filling for the control experiments led to Au loadings of 1.9 and 2.3 vol%, respectively, where vol% is volume of Au over the film pore volume. The SEM EDX data for the control experiment further corroborate that the loadings are thermodynamically limited and not kinetically limited as nanocrystal adsorption reaches equilibrium in 10 min. The loadings were comparable for the nanocomposites made by electrophoretic deposition at the two electric field strengths of 83 and 167 V/cm, on the order of 8 wt% (~4.0 vol%). The small effect of doubling the electric field confirmed the results from UV-vis spectroscopy (Figure 3.4 and Table 3.1). For the more concentrated Au dispersion (0.2 mg/mL), the loading reached ~21 wt% Au according to SEM EDX at 83 V/cm. With this highest loading, the amount of pore volume occupied is 12 vol%. The ratio of loadings at 0.2 versus 0.1 mg/mL dispersion was comparable with a ratio of ~1.7 from SEM EDX and ~1.8 from the absorbance maxima from UV–vis spectroscopy.

Table 3.2: Au loading as determined by SEM EDX and elemental analysis for initial Au concentration of 0.1 mg/mL and 10 min deposition time.

	SEM EDX (wt%)	Elemental Analysis (wt%)	Volume %
Control (0 V)	4 ± 1	-	1.9
Control (0 V)[a]	4.6 ± 0.5	4.7	2.3
25 V	12 ± 2	7.9	4.0
50 V	9 ± 3	8.2	4.1
25 V[b]	21 ± 5	-	12

[a] Deposition time was 20 hours. [b] Initial Au nanocrystal concentration = 0.2 mg/mL.

A top down view SEM image of the Au/TiO_2 nanocomposite film is given in Figure 3.5b. The empty porous TiO_2 film is provided in Figure 3.5a for easier comparison with the synthesized Au/TiO_2 nanocomposite. The Au nanocrystals are evenly dispersed across the TiO_2 film. The depth of field is limited by the short working distance of the microscope making it difficult to image deep within the pores. Thus, this orientation does not provide depth resolution for these nanocrystals with respect to the mesopores. In Figure 3.5a the mesopores of the film are seen as dark spots. In Figure 3.5b, the pores of the film are not as dark, possibly indicating the presence of Au nanocrystals within the pores. The nanocrystals in the image retain their size and shape after electrophoretic deposition without aggregation. The SEM images were very similar for nanocomposites produced by electrophoretic deposition and adsorption without an electric field. The nanocrystal diameter in Figure 3.5b is 3.7 ± 0.8 nm. This size is only slightly larger than the as-synthesized nanocrystal size of 3.1 ± 0.7 nm and is attributed to the difficulty in sizing the nanocrystals from the image due to the blurred edges.

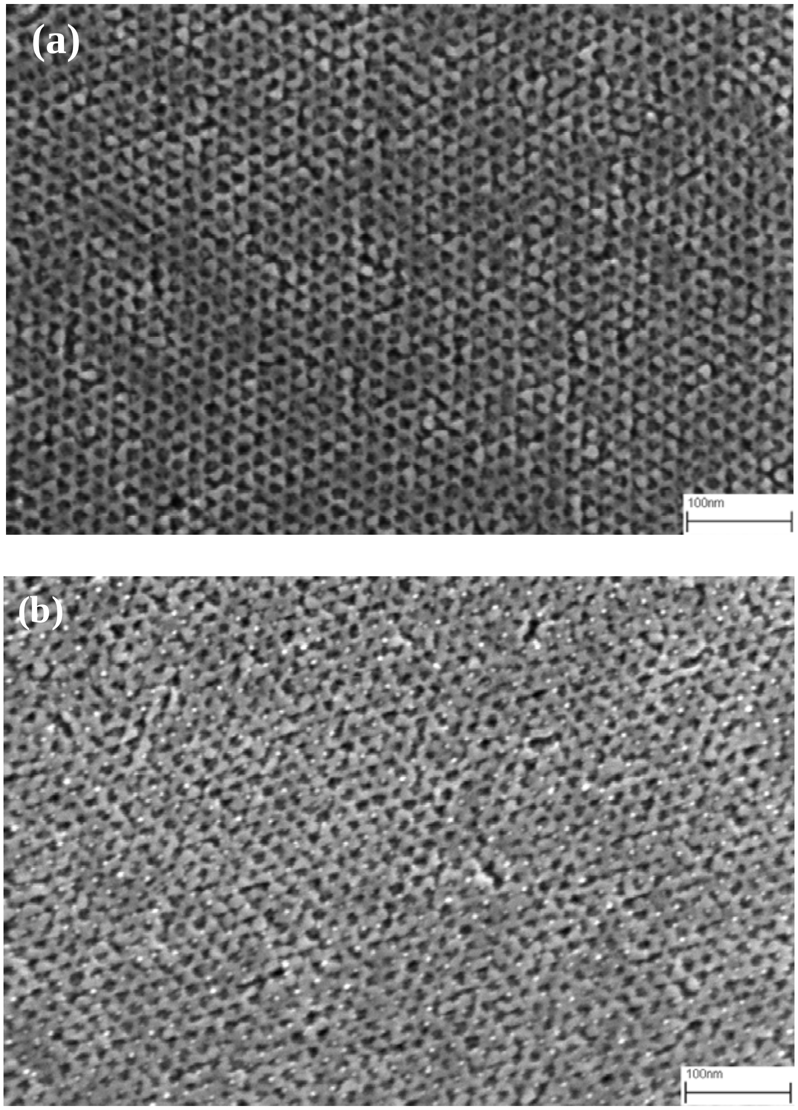

Figure 3.5: SEM top down view of (a) mesoporous TiO_2 and (b) Au/TiO_2 nanocomposite.

The films were further characterized by variable angle spectroscopic ellipsometry. Despite the anisotropic geometry of the columnar mesoporous TiO_2, good model fits of ellipsometric and transmission data have been obtained by assuming isotropic films, that is, the same optical constants regardless of orientation.[23] However, for Au infused films, the best fit isotropic model is unsatisfactory and overestimates Ψ from ~450 to 650 nm and Δ from ~570 to 800 nm (Figure 3.6). A uniaxial anisotropic model, in which the film's z axis has different optical constants than the x and y axis, remedies this problem resulting in good fits across the spectral range. The extracted optical constants (Figure 3.7) provide insight into how Au is loaded into the film. Mesoporous TiO_2 behaves like a classic semiconductor with no absorption and normal dispersion before the band gap and a sharp increase in absorbance in the UV corresponding to a band gap transition. Following infusion of ~21 wt% Au the ordinary, x-y plane, optical constants (n_o and k_o) of the film are similar to those found before infusion with the addition of a plasmon absorbance at ~550 nm and a small broad absorbance extending out into the near IR (Figure 3.7b). This extra absorbance shifts n_o upward due to the Kramers-Kronig relationship (Figure 3.7a). A similar attenuation of absorbance in the visible to near IR was observed by Granqvist and Hunderi[69] for individually isolated 3 to 4 nm Au nanocrystals.

The extreme (z plane) imaginary refractive index, k_e, is significantly enhanced compared to the weak absorbance, small k_o, of the x-y plane (Figure 3.7b). This large absorbance in the visible to near IR arises from free electron absorbance due to the formation of a conduction band by overlapping orbitals, indicating that the Au nanocrystals are in close contact.[69] From these observations two important conclusions are reached. First, the lack of absorbance in the x-y plane means that any residual Au nanocrystals on the TiO_2 surface are so dispersed that they are not in contact with each other. This corroborates SEM data which indicates that very few nanocrystals are located on the surface, and implies that most of the Au detected by elemental analysis and EDX is packed into the TiO_2 mesopores. Inside the mesopores the small pore diameter limits lateral contact between the nanocrystals in the x-y plane. Second, the large absorbance in the z direction means that light oriented in this direction 'sees' more of the free electron

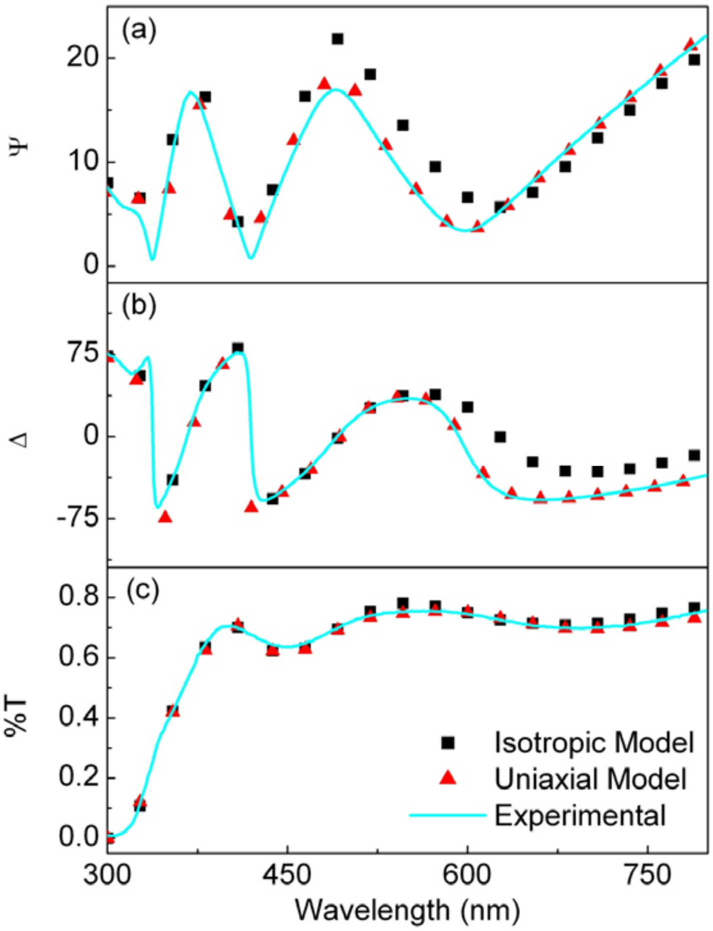

Figure 3.6: Ψ (a), Δ (b), and %T (c) experimental (line) and model fits (symbols) for best fit isotropic (square) and uniaxial (triangle) models of mesoporous TiO_2 infused with 21 wt. % Au. The misfit of the isotropic model in the visible region justifies the inclusion of anisotropy using the more complex uniaxial model.

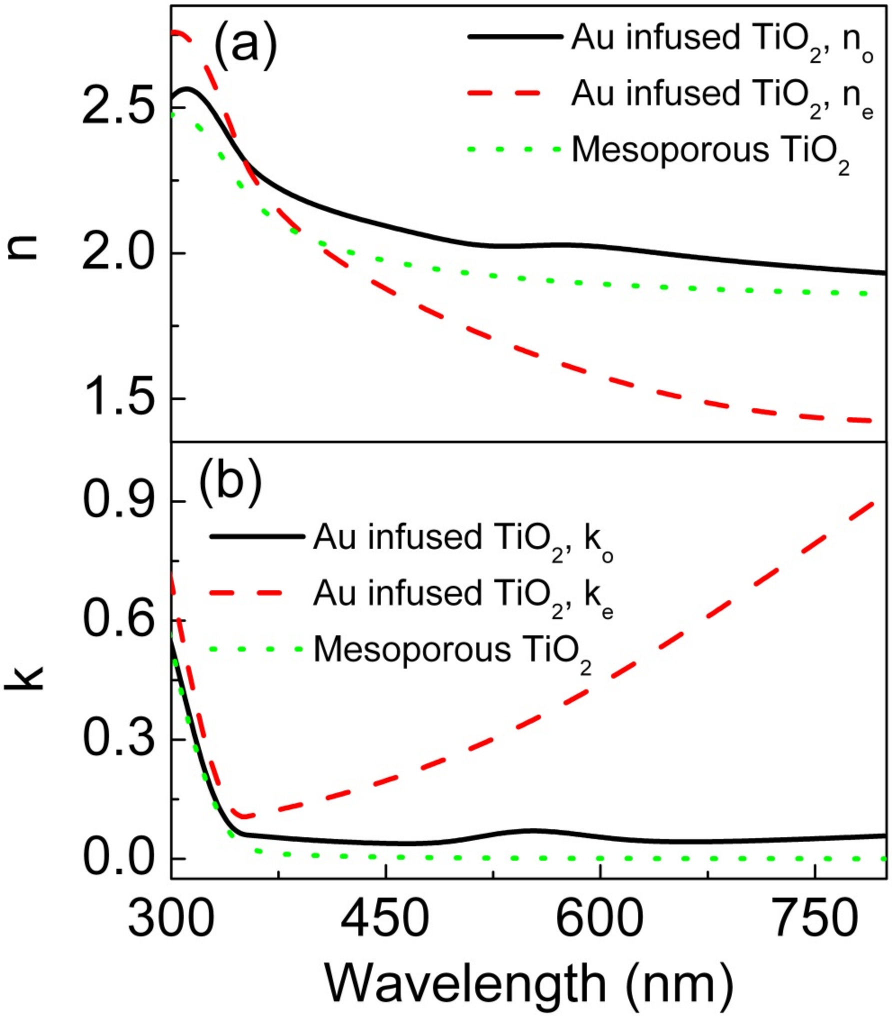

Figure 3.7: Real (a) and imaginary (b) components of the complex refractive index for mesoporous TiO_2 (green dots) as well as the normal (solid) and extreme (red dash) refractive index of mesoporous TiO_2 infused with 21 wt. % Au. The large k_e in the visible spectrum indicates alignment of the Au particles along the film's z axis.

absorption associated with nanocrystals in contact with one another. Since the z direction is oriented with the film's columnar mesopores, the obvious conclusion is that the Au nanocrystals are loaded vertically into the pores.

XPS was performed on the 21 wt% Au/TiO_2 nanocomposite film. Figure 3.8 shows the Au concentration as a function of sputtering time and film depth. The sample was sputtered for a certain length of time and the Au concentration was measured relative to the Ti concentration. A simple linear correlation between sputtering time and the film thickness was used to generate the depth profile. The time where a sharp increase in the indium concentration occurred was used as the time at which the film bottom was reached. Many of the Au nanocrystals reside near the top half of the mesoporous TiO_2 film. The Au concentration steadily decreases with film depth. Although there are a significant number of Au nanocrystals near the bottom of the film, this value could be inflated by small amounts of Au being forced downward into the film by the sputtering process. The average Au concentration throughout the film thickness was ~20 wt% in good agreement with the SEM EDX value of 21 wt%.

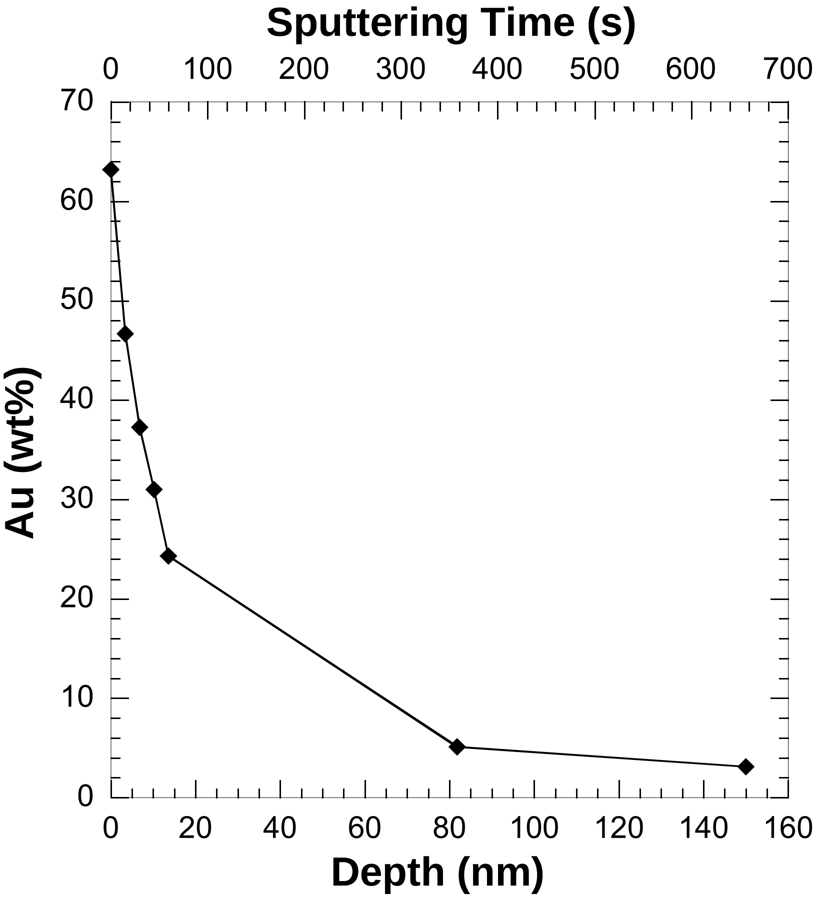

Figure 3.8: Au4f XPS depth profiling experiment. Plot of Au wt % versus sputtering time and depth for 21 wt% Au in mesoporous TiO_2 thin film.

3.4 DISCUSSION

A significant amount of nanocrystals were adsorbed onto the TiO_2 surface even in the absence of an applied potential. This loading was caused by the interaction between the nanocrystals and TiO_2 surface along with rapid diffusion through the pores due to the high ratio of the film's internal surface area to the top surface area (~26:1). This adsorption is over an order of magnitude larger than for similar dodecanethiol coated nanocrystals into mesoporous silica particles.[39] The greater adsorption is facilitated by the stronger interaction of the nanocrystals with TiO_2. Higher activities have also been reported for Au/TiO_2 relative to Au/SiO_2 for CO oxidation[70, 71] implying that the interaction of Au with TiO_2 is stronger than Au with SiO_2. The increase in nanocrystal loading with the application of an electric field may be caused by: (1) an increase in the local nanocrystal concentration at the pore entrance produced by electrophoresis, (2) a change in the nanocrystal-TiO_2 interaction based on the surface charge on the TiO_2, or (3) deeper penetration into the pores caused by an enhancement in the electrophoretic velocity in the pores. The SSPM measurements suggest that the pores of the TiO_2 film extend throughout the length of the film thickness, as the surface potential measured across the pores is slightly larger as compared to the pore walls. The electric field in the pores described by this gradient can produce electrophoresis within the pores.

Theoretical calculations of a close-packed surface coverage of a monolayer of nanocrystals on the top planar TiO_2 film surface will now be used to show that the majority of the nanocrystals are contained within the pores. From an analysis of Figure 3.1, the area fraction of voids on the top surface of the film is ~30%. Consequently, the top planar surface area for the pillars is 1.7 m^2/g TiO_2 for a film thickness of 150 nm. For 3.1 nm diameter Au nanocrystals, the area/g of a nanocrystal is 25 m^2/g Au. A close-packed monolayer with a packing density of 0.907 (2D hexagonal) of Au nanocrystals on the top planar surface of TiO_2 would correspond to a loading of 5.9 wt%, or equivalently, ~9 nanocrystals on top of each pillar. The highest experimental loading (~21 wt%) was more than three times greater than this close-packed value. Moreover, Figure 3.5b indicates the amount of Au on the top planar film surface of ~0.3 wt% Au is far below the close-packed value, and the VASE results also indicate that the nanocrystals are dispersed in the pores of the film. Hence, the vast majority of nanocrystals are within the pores and not on the top surface.

The experimental loading may be compared with the theoretical loading for a monolayer of Au nanocrystals on each pillar. For films with ~8 wt% (4.0 vol%, relative to the film pore volume) and ~21 wt% (12 vol%) Au loading, there would be ~30 and ~90 nanocrystals, respectively, around each pillar, if all of the nanocrystals were associated directly with a pillar. These values were estimated by dividing the total number of nanocrystals by the number of pillars. These 90 nanocrystals would cover ~15% of the pillar surface area, excluding the surface area on top of the pillar. The nanocrystals inside the film are closer together than this value of 15% in z-direction, but not along the nanopillar circumference. Assuming a maximum packing fraction of 74 vol% for spheres inside of the void volume of the film (porosity = 30% from Figure 3.1), the maximum loading would be 62 wt % Au, corresponding to ~560 nanocrystals per pillar. With the ~10 nm gap between pillars, not all of the nanocrystals would be required to be directly on a pillar. For example another 4 nm would be available between two pillars after attaching two 3.1 nm nanocrystals directly on the pillars. Of the estimated 560 nanocrystals around each pillar, ~470 would be directly attached to the pillar surface (62 vol% of the max. 74 vol% packing in the total void volume) and ~90 would be found in the annular region (12 vol%). Hence, even with the experimental number of nanocrystals adsorbed directly onto the pillars, there exists sufficient space for more nanocrystals to access the pores of the film. The tortuosity of the pores may be expected to inhibit nanocrystals from reaching the film bottom, although diffusion in the circumferential direction for the interconnected annuli is favorable. Thus, the apparent thermodynamic limit after 10 minutes is likely not the true thermodynamic limit for perfect nanopillar geometry. XPS shows that the distribution of nanocrystals favors the upper regions of the film.

The motivation for using a low dielectric constant (ε) nonpolar organic solvent in this study was several-fold. In a polar solvent such as water or ethanol, the charge on the surface of a Au nanocrystal may be achieved more readily, and the higher ε favors a higher electrophoretic mobility. However, the nanocrystal size of Au may be controlled more precisely for synthesis in nonpolar solvents.[58] Furthermore, both positive and negatively charged nanocrystals may be present simultaneously in low ε organic solvents. Also, electrochemical reactions at the electrode surface such as hydrogen and oxygen evolution in the case of water are avoided with an inert organic solvent. With organic solvents, higher potentials (>5 V) can be used without the problems of electrolysis and joule heating.[72, 73] Using conservative estimates, the temperature increase during an electrophoretic deposition experiment would be only ~0.2 K at 50 V applied.[74] However, the potentials in this study were kept low enough to avoid electrohydrodynamic instabilities and other nonlinearities. Potentials were kept below the critical voltage as given by the laminar-to-turbulent transition voltage equation[75]

$$V_{inst} = \frac{30\eta}{\sqrt{\rho\varepsilon_r\varepsilon_o}} \tag{3.1}$$

where η is the solvent viscosity, ρ is the solvent density, ε_r is the relative dielectric constant, and ε_o is the permittivity of free space. For chloroform, V_{inst} = 64.5 V (η = 0.539 cP, ρ = 1.48 g/mL, and ε_r = 4.8). Hence, the potentials applied in this study, 50 V maximum, were well below the threshold value.

The Au nanocrystals dispersed in chloroform possess an excess positive charge as the darkly colored nanocrystals were observed to accumulate near the negative electrode, while the region near the positive electrode became transparent, when an electrophoretic potential of 25 V was applied for an electrode spacing of 3 mm. While the surface charge on the Au nanocrystals was not determined quantitatively, Zheng et al. have previously reported a distribution of electrophoretic mobilities for 3.5 nm Au nanocrystals capped with dodecanethiol ligands dispersed in chloroform.[76] Roughly 85% of the nanocrystals had mobilities ranging between 0.1 to 0.5 (μm/s)/(V/cm) while a smaller percentage exhibited values from -0.2 to 0.1 (μm/s)/(V/cm). Hence, a large majority of the nanocrystals exhibit a positive charge. Since the Au nanocrystals in the present study were synthesized by similar means, a comparable distribution of mobilities and charges may be expected. Although the origin of the surface charge was not given by Zheng et al., it is possible that loss of dodecanethiol capping ligands can result in an excess positive charge on the nanocrystal.[77] The electrophoretic mobility (μ) is related to the surface charge (Q) by

$$Q = 6\pi\mu\eta a \qquad (3.2)$$

where a is the nanocrystal radius. The reported average mobility of 0.30 (μm/s)/(V/cm)[76] translates to a surface charge of $5.4\text{x}10^{-20}$ C per nanocrystal or a charge of +0.34 per nanocrystal.

In general, the mechanism of electrophoretic deposition involves electrophoresis of particles, along with deposition on the surface.[72, 78] The velocity of the nanocrystals (v) can be estimated from the measured μ of Zheng et al[76] from the relationship

$$v = \mu E. \qquad (3.3)$$

The calculated velocities were 25 μm/s and 50 μm/s for electric fields of 83 V/cm and 170 V/cm, respectively, assuming an electrophoretic mobility of 0.30 (μm/s)/(V/cm).[76] With the electrode spacing maintained at 3 mm, the charged nanocrystals at the positive electrode would require ~120 s and ~60 s, respectively, to reach the TiO_2 surface at the negative electrode. With the nanocrystals congregated at the TiO_2 film surface, the effective concentration at the film surface is greatly increased compared to the initial concentration as with the control experiment with no electric field. A kinematic shock layer[79] may form with a sharp increase in the local concentration next to the film compared to the bulk. The higher local nanocrystal concentration at the pore entrance will raise the chemical potential of the nanocrystals and thus drive adsorption.[72, 78] Additionally, fluid flow around the pore opening can accelerate particle insertion into the pores[55, 80, 81] although this behavior is not well understood in organic media with large double layers. The potential drop which occurs across the pore length measured by SSPM is capable of producing electrophoresis and electro-osmosis.[56, 57, 82]

Haber et al. have developed a model to describe the average depth of penetration of a single particle inside a long cylindrical pore using the Fokker-Planck equation for the probability distribution.[56, 57] The model takes into account the stochastic and electric field induced motion of the particle and the fluid. The electric field is aligned in the axial direction. The effects of electrophoresis, diffusion, and deposition onto the substrate may be characterized by two key numbers, the Peclet number (Pe–ratio of convection to diffusion) and the Damkohler number (Da–ratio of deposition to diffusion),[56, 57] defined as

$$\mathrm{Pe} = v_t b/D \tag{3.4}$$

$$\mathrm{Da} = \kappa b/D \tag{3.5}$$

where v_t is the sum of the electrophoretic and electro-osmotic velocities, b is the mean pore radius, κ is the local deposition rate, and D is the diffusion coefficient. From the SSPM data, the potential drop across the film, and by assumption the pore channel, was measured to be ~1%. For a 25 V bias, the potential drop would be ~0.25 V across a pore length of 150 nm, corresponding to an electric field of ~17 kV/cm in the pore. From eq. 3.3, the nanocrystal electrophoretic velocity is 5.0 mm/s using an electrophoretic mobility of 0.30 (μm/s)/(V/cm)[76], and Pe = 0.096. With the pores closed at one end at the ITO substrate, no net volume flow exits the pore channel. Microscopic flows are possible with nonlinear velocity profiles to account for conservation of volume, but with the small pore size of only 10 nm and the low concentration of ions in the system, the electroosmotic flow is assumed to be negligible. Thus, the total velocity is given by the electrophoretic velocity, v, through the pore, and Pe remains 0.096.

The local deposition rate is unknown and depends upon many factors including the particle shape and size, electrostatic, van der Waals and hydrodynamic forces, as well as specific chemical interactions between Au and the substrate.[57] However, κ may be approximated from an electrophoretic model[57] given the experimental average depth of nanocrystal penetration inside the pore channel from XPS data. Assuming an average depth of the nanocrystal in the pore, z, as ~50 nm, the dimensionless mean penetration depth (χ)

$$\chi = z/(b \times \mathrm{Pe}) \tag{3.6}$$

is 105. Since the electro-osmotic velocity is assumed to be very small, we chose the lowest ratio of the electro-osmotic to electrophoretic velocity, ζ, considered in the model, $\zeta = 0.1$.[57]

Haber et al developed a correlation to fit the results from the Fokker-Planck equation[57]

$$\chi = -\frac{1}{15} + \frac{1}{\zeta}\left(\frac{1}{3} + \frac{1}{Da}\right) \tag{3.7}$$

From equation 3.7, Da is approximately 0.099 given our values of χ and ζ. Thus the local deposition rate, κ, is 0.52 cm/s. This unusually small Da results from the extremely small pore radius, b. The relatively weak Au-wall specific interactions, given the high surface coverage and strong binding of the dodecanethiol ligands, and small nanocrystal radius may lower κ. For example, similar Ag nanocrystals were shown to have a dodecanethiol surface coverage of ~75%.[83] However, the Au-TiO_2 interactions were strong enough to produce reasonably high loadings even with no applied electric field (E = 0). The low Da, favors relatively deep penetration of a nanocrystal inside the pore (high χ), despite the low Pe. The low Pe results from the small pore radius, b, and low dielectric constant, ε, which leads to a small mobility and small velocity, v. Upon deposition of the nanocrystal onto the negatively charged TiO_2 pore wall, charge neutralization most likely occurs.[46, 47] Thus, the neutral deposited nanocrystal will not repel incoming charged nanocrystals electrostatically.

Figure 3.9 shows the relationship between the average depth of the nanocrystal in the pore z vs. Pe for various Da values according to eq. 3.6 and 3.7 where the pore radius b = 5 nm and $\zeta = 0.1$. Hence for a given Da, z is linearly proportional to Pe and decreases with Da. It is assumed that the pore length exceeds z and the nanocrystals do not reach the bottom. Even without an applied field, Brownian motion produced a significant degree of adsorption given the concentration of nanocrystals in solution. This process is not described by the Haber model; however, the addition of an electric field did increase the baseline adsorption level.

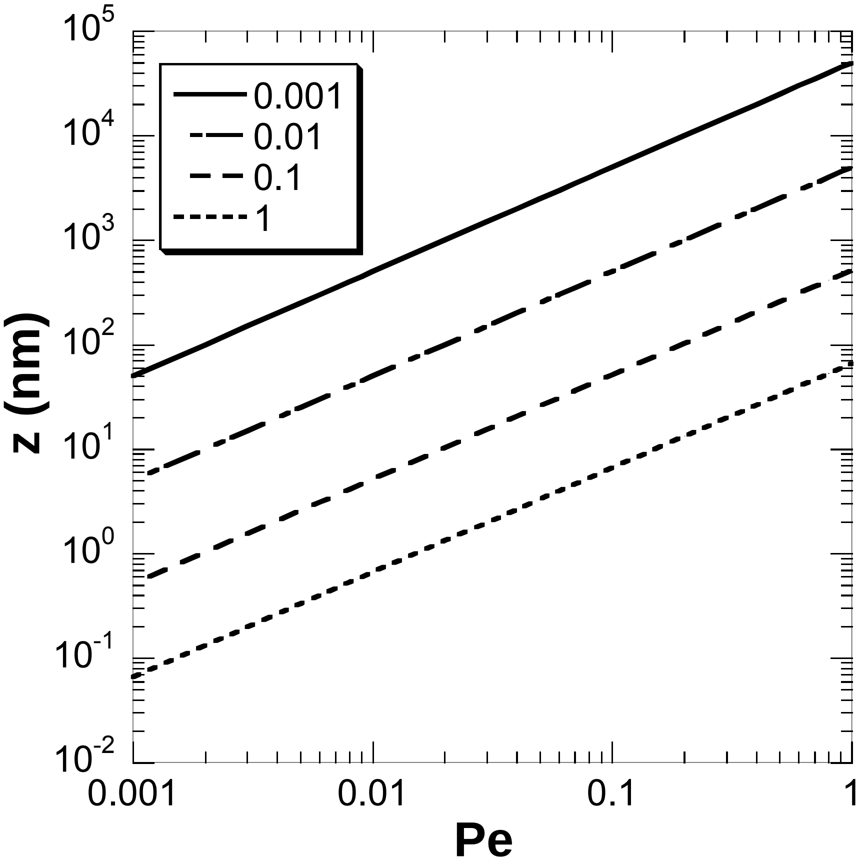

Figure 3.9: Average depth of penetration of a nanocrystal into a pore vs. Peclet number for various Damkohler numbers assuming a pore radius b = 5 nm and ζ = 0.1 (low electro-osmosis relative to electrophoresis).

To gain more general insight into how the various factors influence the depth of penetration of a single nanocrystal into the pore, we examine the model further using eq. 3.7 (Table 3.3). The base case corresponds to the parameters in this study as described above. An increase in the pore size by a factor of 3 and 10 raises the average depth, z, from 50 nm to 160 nm and 640 nm, respectively. Thus, the increase in *z* linearly correlates with the increase in b. Both Pe and Da increase linearly with the pore size. The average depth to pore size ratio remains constant. Small changes in the nanocrystal size have little effect on pore penetration as doubling the nanocrystal size increases Pe and Da by a factor of two, resulting in opposing effects. The model becomes unreliable as the nanocrystal size begins to approach the pore size, and an overestimation in the average depth into the pore is likely. An increase in either μ or *E* raises v, increasing Pe and resulting in a linear increase in z. Even for chloroform with $\varepsilon = 4.8$ and thus a relatively small μ, the electrophoretic velocity is sufficient to give deep deposition of the nanocrystals, likely because of the small κ and Da. Higher local deposition rates can be achieved by choosing different ligands during the synthesis of the nanocrystals. With weakly binding ligands and low nanocrystal surface coverage, the nanocrystal–TiO_2 surface interaction would increase. This leads to a higher local deposition rate, an increase in Da, and a decrease in the nanocrystal penetration depth.

Table 3.3: Kinetic model of average depth of penetration of a single nanocrystal into a cylindrical pore, Peclet number, and Damkohler number as a function of various parameters. (Base case: pore diameter b = 10 nm, particle diameter 2a = 3.1 nm, electrophoretic mobility μ = 0.30 (μm/s)/(V/cm), electric field E = 17 kV/cm, local deposition rate κ = 0.52 cm/s)

Variable	Peclet (Pe) ($\times 10^2$)	Damkohler (Da) ($\times 10^2$)	Average depth into pore (z) (nm)
Base case			
	9.6	9.9	50
Pore size			
$b = 30$	29	30	160
$b = 100$	96	99	640
Particle size			
$2a = 2$	6.2	6.4	50
$2a = 6$	18	19	52
Electrophoretic mobility			
$\mu = 0.15$	4.8	9.9	32
$\mu = 0.60$	19	9.9	100
Electric field			
$E = 8.3$	4.8	9.9	25
$E = 33$	19	9.9	100
Local deposition rate const.			
$\kappa = 0.052$	9.6	0.99	490
$\kappa = 5.2$	9.6	99	6.4

For deposition of a large number of nanocrystals from solution into a pore, the single particle model only describes part of the deposition mechanism. If the first particle occupies a site near the top of a nanopillar, the second particle may deposit onto a lower unoccupied site. The nanocrystals adsorbed on the nanopillars are less likely to block the pores than in the case of cylindrical pores. The SE results suggest that the nanocrystals did not tend to contact each other in the lateral direction. Thus the annular region about a layer of nanocrystals on each nanopillar may remain open for further particle diffusion into the pores. In addition, part of the nanocrystal's penetration into the pores may be produced by surface diffusion. The significant adsorption of nanocrystals even without an applied electric field (E=0) and the large increase in loading upon doubling the bulk nanocrystal concentration (Table 3.2), to 12 vol% with the field present, are not addressed with the single particle model of Haber. Future work is needed to determine how changes in the binding of the ligand would influence particle-wall interactions and the adsorption and electrophoretic deposition of large numbers of particles versus pore depth.

3.5 CONCLUSIONS

Herein, we have demonstrated that 3.1 nm diameter nanocrystals can be deposited electrophoretically into ordered mesoporous TiO_2 films on ITO/glass electrodes, to reach loadings up to 21 wt.%. The loadings were not limited kinetically in 10 min. relative to 20 hours indicating that the open geometry of the mesochannels is beneficial for diffusion. The nanocrystals are located throughout the mesopores with only a small portion occupying the top planar surface of the film. The relatively small potential drop across the film is beneficial for electrophoretic loading of Au nanocrystals. Both VASE measurements of the anisotropy of the imaginary refractive index, k, and XPS depth profiling studies indicate that Au nanocrystals are dispersed within the vertically aligned mesopores and distributed throughout the film. Presumably, the high coverage of the strongly-bound thiol ligands on the Au nanocrystals weakens the Au/TiO_2 interactions.

Therefore, electrophoresis is beneficial for increasing the concentration of nanocrystals near the film, enhancing the thermodynamic driving force for adsorption of Au nanocrystals upon mesoporous TiO_2 with high loadings.

3.6 REFERENCES

1. Gratzel, M., Photoelectrochemical cells. *Nature (London, United Kingdom)* **2001,** 414, (6861), 338-344.

2. Iwanaga, T.; Hyodo, T.; Shimizu, Y.; Egashira, M., H2 sensing properties and mechanism of anodically oxidized TiO2 film contacted with Pd electrode. *Sensors and Actuators, B: Chemical* **2003,** B93, (1-3), 519-525.

3. Long, J. W.; Dunn, B.; Rolison, D. R.; White, H. S., Three-Dimensional Battery Architectures. *Chemical Reviews (Washington, DC, United States)* **2004,** 104, (10), 4463-4492.

4. Huang, S. Y.; Kavan, L.; Exnar, I.; Graetzel, M., Rocking chair lithium battery based on nanocrystalline TiO2 (anatase). *Journal of the Electrochemical Society* **1995,** 142, (9), L142-L144.

5. Guliants, V. V.; Carreon, M. A.; Lin, Y. S., Ordered mesoporous and macroporous inorganic films and membranes. *Journal of Membrane Science* **2004,** 235, (1-2), 53-72.

6. Etienne, M.; Grosso, D.; Boissiere, C.; Sanchez, C.; Walcarius, A., Electrochemical evidences of morphological transformation in ordered mesoporous titanium oxide thin films. *Chemical Communications (Cambridge, United Kingdom)* **2005**, (36), 4566-4568.

7. Alberius, P. C. A.; Frindell, K. L.; Hayward, R. C.; Kramer, E. J.; Stucky, G. D.; Chmelka, B. F., General Predictive Syntheses of Cubic, Hexagonal, and Lamellar Silica and Titania Mesostructured Thin Films. *Chemistry of Materials* **2002,** 14, (8), 3284-3294.

8. Wang, K.; Yao, B.; Morris, M. A.; Holmes, J. D., Supercritical Fluid Processing of Thermally Stable Mesoporous Titania Thin Films with Enhanced Photocatalytic Activity. *Chemistry of Materials* **2005,** 17, (19), 4825-4831.

9. Crepaldi, E. L.; de Soler-Illia, G. J.; Grosso, D.; Cagnol, F.; Ribot, F.; Sanchez, C., Controlled Formation of Highly Organized Mesoporous Titania Thin Films: From Mesostructured Hybrids to Mesoporous Nanoanatase TiO2. *Journal of the American Chemical Society* **2003,** 125, (32), 9770-9786.

10. Carreon, M. A.; Choi, S. Y.; Mamak, M.; Chopra, N.; Ozin, G. A., Pore architecture affects photocatalytic activity of periodic mesoporous nanocrystalline anatase thin films. *Journal of Materials Chemistry* **2007,** 17, (1), 82-89.

11. Choi, S. Y.; Mamak, M.; Coombs, N.; Chopra, N.; Ozin, G. A., Thermally stable two-dimensional hexagonal mesoporous nanocrystalline anatase, meso-nc-TiO2: Bulk and crack-free thin film morphologies. *Advanced Functional Materials* **2004,** 14, (4), 335-344.

12. Grosso, D.; Soler-Illia, G. J. d. A. A.; Babonneau, F.; Sanchez, C.; Albouy, P.-A.; Brunet-Bruneau, A.; Balkenende, A. R., Highly organized mesoporous titania thin films showing mono-oriented 2D hexagonal channels. *Advanced Materials (Weinheim, Germany)* **2001,** 13, (14), 1085-1090.

13. Boettcher, S. W.; Fan, J.; Tsung, C.-K.; Shi, Q.; Stucky, G. D., Harnessing the Sol-Gel Process for the Assembly of Non-Silicate Mesostructured Oxide Materials. *Accounts of Chemical Research* **2007,** 40, (9), 784-792.

14. Grosso, D.; Soler-Illia, G. J. d. A. A.; Crepaldi, E. L.; Cagnol, F.; Sinturel, C.; Bourgeois, A.; Brunet-Bruneau, A.; Amenitsch, H.; Albouy, P. A.; Sanchez, C., Highly Porous TiO2 Anatase Optical Thin Films with Cubic Mesostructure Stabilized at 700 DegC. *Chemistry of Materials* **2003,** 15, (24), 4562-4570.

15. Sanchez, C.; Boissiere, C.; Grosso, D.; Laberty, C.; Nicole, L., Design, Synthesis, and Properties of Inorganic and Hybrid Thin Films Having Periodically Organized Nanoporosity. *Chemistry of Materials* **2008,** 20, (3), 682-737.

16. Lancelle-Beltran, E.; Prene, P.; Boscher, C.; Belleville, P.; Buvat, P.; Lambert, S.; Guillet, F.; Boissiere, C.; Grosso, D.; Sanchez, C., Nanostructured Hybrid Solar Cells Based on Self-Assembled Mesoporous Titania Thin Films. *Chemistry of Materials* **2006,** 18, (26), 6152-6156.

17. Lu, Y.; Ganguli, R.; Drewien, C. A.; Anderson, M. T.; Brinker, C. J.; Gong, W.; Guo, Y.; Soyez, H.; Dunn, B.; Huang, M. H.; Zink, J. I., Continuous formation of supported cubic and hexagonal mesoporous films by sol-gel dip-coating. *Nature (London)* **1997,** 389, (6649), 364-368.

18. Brinker, C. J.; Lu, Y.; Sellinger, A.; Fan, H., Evaporation-induced self-assembly. Nanostructures made easy. *Advanced Materials (Weinheim, Germany)* **1999,** 11, (7), 579-585.

19. Cagnol, F.; Grosso, D.; Soler-Illia, G. J. d. A. A.; Crepaldi, E. L.; Babonneau, F.; Amenitsch, H.; Sanchez, C., Humidity-controlled mesostructuration in CTAB-templated silica thin film processing. The existence of a modulable steady state. *Journal of Materials Chemistry* **2003,** 13, (1), 61-66.

20. Grosso, D.; Cagnol, F.; Soler-Illia, G. J. D. A. A.; Crepaldi, E. L.; Amenitsch, H.; Brunet-Bruneau, A.; Bourgeois, A.; Sanchez, C., Fundamentals of mesostructuring through evaporation-induced self-assembly. *Advanced Functional Materials* **2004,** 14, (4), 309-322.

21. Koganti, V. R.; Dunphy, D.; Gowrishankar, V.; McGehee, M. D.; Li, X.; Wang, J.; Rankin, S. E., Generalized Coating Route to Silica and Titania Films with Orthogonally Tilted Cylindrical Nanopore Arrays. *Nano Letters* **2006,** 6, (11), 2567-2570.

22. Wu, C.-W.; Ohsuna, T.; Kuwabara, M.; Kuroda, K., Formation of Highly Ordered Mesoporous Titania Films Consisting of Crystalline Nanopillars with Inverse Mesospace by Structural Transformation. *Journal of the American Chemical Society* **2006,** 128, (14), 4544-4545.

23. Uchida, H.; Patel, M. N.; May, R. A.; Gupta, G.; Stevenson, K. J.; Johnston, K. P., Perpendicularly-Oriented Mesoporous Titania Thin Films Prepared via Surfactant Assembly on Conductive Indium-Tin-Oxide / Glass Substrate. **In prep.**

24. Pai, R. A.; Humayun, R.; Schulberg, M. T.; Sengupta, A.; Sun, J.-N.; Watkins, J. J., Mesoporous Silicates Prepared Using Preorganized Templates in Supercritical Fluids. *Science (Washington, DC, United States)* **2004,** 303, (5657), 507-511.

25. Kamat, P. V., Meeting the Clean Energy Demand: Nanostructure Architectures for Solar Energy Conversion. *Journal of Physical Chemistry C* **2007,** 111, (7), 2834-2860.

26. Chandrasekharan, N.; Kamat, P. V., Assembling gold nanoparticles as nanostructured films using an electrophoretic approach. *Nano Letters* **2001,** 1, (2), 67-70.

27. Subramanian, V.; Wolf, E.; Kamat, P. V., Semiconductor-Metal Composite Nanostructures. To What Extent Do Metal Nanoparticles Improve the Photocatalytic Activity of TiO2 Films? *Journal of Physical Chemistry B* **2001,** 105, (46), 11439-11446.

28. Kumai, Y.; Tsukada, H.; Akimoto, Y.; Sugimoto, N.; Seno, Y.; Fukuoka, A.; Ichikawa, M.; Inagaki, S., Highly ordered platinum nanodot arrays with cubic symmetry in mesoporous thin films. *Advanced Materials (Weinheim, Germany)* **2006,** 18, (6), 760-762.

29. Perez, M. D.; Otal, E.; Bilmes, S. A.; Soler-Illia, G. J. A. A.; Crepaldi, E. L.; Grosso, D.; Sanchez, C., Growth of Gold Nanoparticle Arrays in TiO2 Mesoporous Matrixes. *Langmuir* **2004,** 20, (16), 6879-6886.

30. Cortial, G.; Siutkowski, M.; Goettmann, F.; Moores, A.; Boissiere, C.; Grosso, D.; Le Floch, P.; Sanchez, C., Metallic nanoparticles hosted in mesoporous oxide thin films for catalytic applications. *Small* **2006,** 2, (8-9), 1042-1045.

31. Besson, S.; Gacoin, T.; Ricolleau, C.; Jacquiod, C.; Boilot, J.-P., 3D Quantum Dot Lattice Inside Mesoporous Silica Films. *Nano Letters* **2002,** 2, (4), 409-414.

32. Gu, J.-L.; Shi, J.-L.; You, G.-J.; Xiong, L.-M.; Qian, S.-X.; Hua, Z.-L.; Chen, H.-R., Incorporation of highly dispersed gold nanoparticles into the pore channels of mesoporous silica thin films and their ultrafast nonlinear optical response. *Advanced Materials (Weinheim, Germany)* **2005,** 17, (5), 557-560.

33. Gu, J.; Xiong, L.; Shi, J.; Hua, Z.; Zhang, L.; Li, L., Thioether moiety functionalization of mesoporous silica films for the encapsulation of highly dispersed gold nanoparticles. *Journal of Solid State Chemistry* **2006,** 179, (4), 1060-1066.

34. Bartl, M. H.; Boettcher, S. W.; Frindell, K. L.; Stucky, G. D., 3-D Molecular Assembly of Function in Titania-Based Composite Material Systems. *Accounts of Chemical Research* **2005,** 38, (4), 263-271.

35. Lee, U. H.; Lee, H.; Wen, S.; Mho, S.-i.; Kwon, Y.-U., Mesoporous titania thin films with pseudo-cubic structure: Synthetic studies and applications to nanomembranes and nanotemplates. *Microporous and Mesoporous Materials* **2006,** 88, (1-3), 48-55.

36. Stathatos, E.; Lianos, P.; Falaras, P.; Siokou, A., Photocatalytically deposited silver nanoparticles on mesoporous TiO2 films. *Langmuir* **2000,** 16, (5), 2398-2400.

37. Rolison, D. R., Catalytic nanoarchitectures - The importance of nothing and the unimportance of periodicity. *Science (Washington, DC, United States)* **2003,** 299, (5613), 1698-1702.

38. Rioux, R. M.; Song, H.; Hoefelmeyer, J. D.; Yang, P.; Somorjai, G. A., High-Surface-Area Catalyst Design: Synthesis, Characterization, and Reaction Studies of Platinum Nanoparticles in Mesoporous SBA-15 Silica. *Journal of Physical Chemistry B* **2005,** 109, (6), 2192-2202.

39. Gupta, G.; Shah, P. S.; Zhang, X.; Saunders, A. E.; Korgel, B. A.; Johnston, K. P., Enhanced Infusion of Gold Nanocrystals into Mesoporous Silica with Supercritical Carbon Dioxide. *Chemistry of Materials* **2005,** 17, (26), 6728-6738.

40. Gupta, G.; Stowell, C. A.; Patel, M. N.; Gao, X.; Yacaman, M. J.; Korgel, B. A.; Johnston, K. P., Infusion of Presynthesized Iridium Nanocrystals into Mesoporous Silica for High Catalyst Activity. *Chemistry of Materials* **2006,** 18, (26), 6239-6249.

41. Giersig, M.; Mulvaney, P., Preparation of ordered colloid monolayers by electrophoretic deposition. *Langmuir* **1993,** 9, (12), 3408-13.

42. Giersig, M.; Mulvaney, P., Formation of ordered two-dimensional gold colloid lattices by electrophoretic deposition. *Journal of Physical Chemistry* **1993,** 97, (24), 6334-6.

43. Trau, M.; Saville, D. A.; Aksay, I. A., Field-induced layering of colloidal crystals. *Science (Washington, D. C.)* **1996,** 272, (5262), 706-9.

44. Bailey, R. C.; Stevenson, K. J.; Hupp, J. T., Assembly of micropatterned colloidal gold thin films via microtransfer molding and electrophoretic deposition. *Advanced Materials (Weinheim, Germany)* **2000,** 12, (24), 1930-1934.

45. Chandrasekharan, N.; Kamat, P. V., Improving the Photoelectrochemical Performance of Nanostructured TiO2 Films by Adsorption of Gold Nanoparticles. *Journal of Physical Chemistry B* **2000,** 104, (46), 10851-10857.

46. Islam, M. A.; Herman, I. P., Electrodeposition of patterned CdSe nanocrystal films using thermally charged nanocrystals. *Applied Physics Letters* **2002,** 80, (20), 3823-3825.

47. Islam, M. A.; Xia, Y.; Steigerwald, M. L.; Yin, M.; Liu, Z.; O'Brien, S.; Levicky, R.; Herman, I. P., Addition, suppression, and inhibition in the electrophoretic deposition of nanocrystal mixture films for CdSe nanocrystals with g-Fe2O3 and Au Nanocrystals. *Nano Letters* **2003,** 3, (11), 1603-1606.

48. Islam, M. A.; Xia, Y.; Telesca, D. A., Jr.; Steigerwald, M. L.; Herman, I. P., Controlled electrophoretic deposition of smooth and robust films of CdSe nanocrystals. *Chemistry of Materials* **2004,** 16, (1), 49-54.

49. Hornyak, G.; Kroll, M.; Pugin, R.; Sawitowski, T.; Schmid, G.; Bovin, J.-O.; Karsson, G.; Hofmeister, H.; Hopfe, S., Gold clusters and colloids in alumina nanotubes. *Chemistry--A European Journal* **1997,** 3, (12), 1951-1956.

50. Kamada, K.; Fukuda, H.; Maehara, K.; Yoshida, Y.; Nakai, M.; Hasuo, S.; Matsumoto, Y., Insertion of SiO2 nanoparticles into pores of anodized aluminum by electrophoretic deposition in aqueous system. *Electrochemical and Solid-State Letters* **2004,** 7, (8), B25-B28.

51. Limmer, S. J.; Seraji, S.; Forbess, M. J.; Wu, Y.; Chou, T. P.; Nguyen, C.; Cao, G., Electrophoretic growth of lead zirconate titanate nanorods. *Advanced Materials (Weinheim, Germany)* **2001,** 13, (16), 1269-1272.

52. Limmer, S. J.; Hubler, T. L.; Cao, G., Nanorods of Various Oxides and Hierarchically Structured Mesoporous Silica by Sol-Gel Electrophoresis. *Journal of Sol-Gel Science and Technology* **2003,** 26, (1/2/3), 577-581.

53. Limmer, S. J.; Cruz, S. V.; Cao, G. Z., Films and nanorods of transparent conducting oxide ITO by a citric acid sol route. *Applied Physics A: Materials Science & Processing* **2004,** 79, (3), 421-424.

54. Limmer, S. J.; Chou, T. P.; Cao, G. Z., A study on the influences of processing parameters on the growth of oxide nanorod arrays by sol electrophoretic deposition. *Journal of Sol-Gel Science and Technology* **2005,** 36, (2), 183-195.

55. Zhang, Q.; Xu, T.; Butterfield, D.; Misner, M. J.; Ryu, D. Y.; Emrick, T.; Russell, T. P., Controlled Placement of CdSe Nanoparticles in Diblock Copolymer Templates by Electrophoretic Deposition. *Nano Letters* **2005,** 5, (2), 357-361.

56. Haber, S.; Gal-Or, L., Deep electrophoretic penetration and deposition of ceramic particles inside porous substrates. I. Analytical model. *Journal of the Electrochemical Society* **1992,** 139, (4), 1071-8.

57. Haber, S., Deep electrophoretic penetration and deposition of ceramic particles inside impermeable porous substrates. *Journal of Colloid and Interface Science* **1996,** 179, (2), 380-390.

58. Brust, M.; Walker, M.; Bethell, D.; Schiffrin, D. J.; Whyman, R., Synthesis of thiol-derivatized gold nanoparticles in a two-phase liquid-liquid system. *Journal of the Chemical Society, Chemical Communications* **1994**, (7), 801-2.

59. Brust, M.; Fink, J.; Bethell, D.; Schiffrin, D. J.; Kiely, C., Synthesis and reactions of functionalized gold nanoparticles. *Journal of the Chemical Society, Chemical Communications* **1995**, (16), 1655-6.

60. Aslam, M.; Mulla, I. S.; Vijayamohanan, K., Insulator-metal transition in Coulomb blockade nanostructures. *Applied Physics Letters* **2001,** 79, (5), 689-691.

61. McMurray, H. N.; Williams, G., Probe diameter and probe-specimen distance dependence in the lateral resolution of a scanning Kelvin probe. *Journal of Applied Physics* **2002,** 91, (3), 1673-1679.

62. Jacobs, H. O.; Leuchtmann, P.; Homan, O. J.; Stemmer, A., Resolution and contrast in Kelvin probe force microscopy. *Journal of Applied Physics* **1998,** 84, (3), 1168-1173.

63. Williams, R. D.; Stevenson, K. J., unpublished results.

64. May, R. A.; Kondrachova, L.; Hahn, B. P.; Stevenson, K. J., Optical Constants of Electrodeposited Mixed Molybdenum-Tungsten Oxide Films Determined by Variable-Angle Spectroscopic Ellipsometry. *Journal of Physical Chemistry C* **2007,** 111, (49), 18251-18257.

65. Jellison, G. E., Jr.; Modine, F. A., Parameterization of the optical functions of amorphous materials in the interband region. *Applied Physics Letters* **1996,** 69, (3), 371-373.

66. Tompkins, H. G.; McGahan, W. A., *Spectroscopic Ellipsometry and Reflectometry*. Wiley-Interscience: 1999.

67. Zerweck, U.; Loppacher, C.; Otto, T.; Grafstroem, S.; Eng, L. M., Accuracy and resolution limits of Kelvin probe force microscopy. *Physical Review B: Condensed Matter and Materials Physics* **2005,** 71, (12), 125424/1-125424/9.

68. Jacobs, H. O.; Knapp, H. F.; Mueller, S.; Stemmer, A., Surface potential mapping: A qualitative material contrast in SPM. *Ultramicroscopy* **1997,** 69, (1), 39-49.

69. Granqvist, C. G.; Hunderi, O., Optical properties of ultrafine gold particles. *Physical Review B: Solid State* **1977,** 16, (8), 3513-34.

70. Overbury, S. H.; Ortiz-Soto, L.; Zhu, H.; Lee, B.; Amiridis, M. D.; Dai, S., Comparison of Au catalysts supported on mesoporous titania and silica: Investigation of Au particle size effects and metal-support interactions. *Catalysis Letters* **2004,** 95, (3-4), 99-106.

71. Wang, X.; Na, N.; Zhang, S.; Wu, Y.; Zhang, X., Rapid Screening of Gold Catalysts by Chemiluminescence-Based Array Imaging. *Journal of the American Chemical Society* **2007,** 129, (19), 6062-6063.

72. Van der Biest, O. O.; Vandeperre, L. J., Electrophoretic deposition of materials. *Annual Review of Materials Science* **1999,** 29, 327-352.

73. Besra, L.; Liu, M., A review on fundamentals and applications of electrophoretic deposition (EPD). *Progress in Materials Science* **2006,** 52, (1), 1-61.

74. Smith, P. G., Jr.; Patel, M. N.; Kim, J.; Johnston, K. P.; Milner, T. E., Electrophoretic Mobility Measurement by Differential-Phase Optical Coherence Tomography. *Journal of Physical Chemistry C* **2007,** 111, (6), 2614-2622.

75. Novotny, V. J., Physics of nonaqueous colloids. In *Colloids Surf. Reprogr. Technol.*, American Chemical Society: 1982; Vol. 200, pp 281-306.

76. Zheng, N.; Stucky, G. D., A General Synthetic Strategy for Oxide-Supported Metal Nanoparticle Catalysts. *Journal of the American Chemical Society* **2006,** 128, (44), 14278-14280.

77. Evans, D. F.; Wennerstrom, H., *The colloidal domain : where physics, chemistry, biology, and technology meet*. 2nd ed.; Wiley-VCH: New York, 1999; p 632.

78. Fukada, Y.; Nagarajan, N.; Mekky, W.; Bao, Y.; Kim, H. S.; Nicholson, P. S., Electrophoretic deposition - mechanisms, myths and materials. *Journal of Materials Science* **2004,** 39, (3), 787-801.

79. Biesheuvel, P. M.; Verweij, H., Theory of cast formation in electrophoretic deposition. *Journal of the American Ceramic Society* **1999,** 82, (6), 1451-1455.

80. Nadal, F.; Argoul, F.; Hanusse, P.; Pouligny, B.; Ajdari, A., Electrically induced interactions between colloidal particles in the vicinity of a conducting plane. *Physical Review E: Statistical, Nonlinear, and Soft Matter Physics* **2002,** 65, (6-1), 061409/1-061409/8.

81. Nadal, F.; Argoul, F.; Kestener, P.; Pouligny, B.; Ybert, C.; Ajdari, A., Electrically induced flows in the vicinity of a dielectric stripe on a conducting plate. *European Physical Journal E: Soft Matter* **2002,** 9, (4), 387-399.

82. Gal-Or, L.; Liubovich, S.; Haber, S., Deep electrophoretic penetration and deposition of ceramic particles inside porous substrates. II. Experimental model. *Journal of the Electrochemical Society* **1992,** 139, (4), 1078-81.

83. Korgel, B. A.; Fullam, S.; Connolly, S.; Fitzmaurice, D., Assembly and Self-Organization of Silver Nanocrystal Superlattices: Ordered \"Soft Spheres\". *Journal of Physical Chemistry B* **1998,** 102, (43), 8379-8388.

Chapter 4

Hybrid MnO_2/Disordered Amorphous Mesoporous Carbon Nanocomposites for Electrochemical Pseudocapacitors

MnO_2/mesoporous carbon hybrid nanocomposites were synthesized to achieve high values of redox pseudocapacitance at scan rates of 100 mV/s. High resolution transmission electron microscopy (HRTEM) along with energy dispersive X-ray spectroscopy (EDX) demonstrated that ~1 nm thick MnO_2 was conformally distributed throughout the mesoporous carbon structure. HRTEM and X-ray diffraction (XRD) showed formation of MnO_2 nanocrystals with lattice planes corresponding to birnessite. The electrochemical redox pseudocapacitance of these composite materials in aqueous 1 M Na_2SO_4 electrolyte containing as little as 2 wt % MnO_2 exhibited a high gravimetric MnO_2 pseudocapacitance (C_{MnO2}) of ~560 F/g_{MnO2}. Even for 30 wt% MnO_2, a high C_{MnO2} of 137 F/g_{MnO2} was observed at 100 mV/s. Sodium ion diffusion coefficients on the order of 10^{-9}–10^{-10} cm^2/s were measured using chronoamperometry. The controlled growth and conformal coating of redox-active MnO_2/mesoporous carbon composites offers the potential for achieving high power energy storage with low cost materials.

The contents of this chapter are being prepared for a manuscript.

4.1 INTRODUCTION

Electrochemical capacitors (ECs) are of interest in transportation for starting, acceleration and regenerative braking, in load leveling for smart grids, e.g. those which contain variable energy sources such as windmills and solar cells, and for high clock speed switching in microelectronics.[1-5] ECs offer a very high gravimetric capacitance C_g, up to 1000 F/g of active material, and power densities 10^3-fold that of batteries; however, the energy densities are typically about 10- to 100-fold smaller. The gravimetric capacitance and consequently, the energy and power densities of ECs may be improved by designing high surface area nanostructured electrodes to enhance charge transfer and ion diffusion.[3, 6]

Electrochemical capacitors may store energy in the electric double layer and by surface redox (Faradaic) reactions.[3, 7] The gravimetric capacitance of a material is directly proportional to the surface area and indirectly proportional to the double layer thickness.[8] The separation of static charges is small, on the order of ~1 nm in the electric double layer.[4, 7, 8] For carbon-based electric double layer capacitors (EDLCs), the various allotropes, pore structure, surface area, and graphitic content have been manipulated to tailor the conductivity and C_g.[9-20] Activated carbons with surface areas between 500 to 2500 m^2/g typically have a capacitance between 10 to 35 F/g.[8] The electric double layer capacitance may be further increased by either surface functionalization or surface modification with redox-active sites that promote a surface redox pseudocapacitance.[3, 4, 7] Electrode materials for redox pseudocapacitors are typically conductive polymers or transition metal oxides such as ruthenium or manganese oxide. Ruthenium oxide has a high gravimetric pseudocapacitance (as high as 720 F/g_{RuO2}) and high electronic conductivity but is too costly.[21-26] Manganese oxide, a low cost alternative with low toxicity and a high theoretical pseudocapacitance of ~1370 F/g_{MnO2},[27] has been studied extensively for ECs.[27-43] However, to overcome the low electronic conductivity of MnO_2,[44] it is often mixed with conductive agents such as activated carbon to facilitate electron transfer.

Novel nanocomposite redox pseudocapacitors may be designed by combining conductive carbon materials with a redox-active transition metal oxide to increase the gravimetric capacitance. These metal oxides store electrochemical charge by reversible surface redox reactions and are generally known as pseudocapacitors. In this regard, manganese oxide has been deposited by electrodeposition and electroless deposition on various carbon supports.[44-52] One emerging design strategy is to use mesoporous carbons as scaffolds for MnO_2 where the porous channels in the carbon support provide high surface area, and the conductive carbon scaffold facilitates electronic conductivity. A conformal coating of MnO_2, no thicker than a few nm, may be grown within the mesopores of the highly conductive carbon to improve the utilization of the pseudocapacitive material.[3, 28] For an MnO_2 loading on the order of 30 wt.%, a uniform coating in ~10 nm mesopores would correspond to a film thickness of ~1 nm. Thin MnO_2 films in mesoporous (2-50 nm) supports with pore sizes of 5-10 nm would be favorable for rapid ion and electron transport to achieve high capacitance. Dong et al. have recently reported MnO_2 embedded in mesoporous carbon pore walls displaying a large C_g.[45] High C_g values were also achieved with carbon nanofoam structures that possessed a large pore size distribution and >30 nm MnO_2 particles deposited throughout the support.[44, 48] However, few studies have evaluated charge storage capacities at high rates (≥100mV/s). At higher scan rates, sloping profiles in the current-potential curves are often observed which suggests kinetic limitations due to sluggish ion and electron transport. Furthermore, typical MnO_2 modified carbons display substantial capacity fade and low faradaic efficiencies at high scan rates.

Herein we report the synthesis and characterization of MnO_2 modified disordered mesoporous carbons (MnO_2/C). The morphology of the MnO_2 on the mesoporous carbon was characterized by scanning electron microscopy (SEM) along with EDX, as well as thermogravimetric analysis (TGA) to determine the MnO_2 content of the nanocomposites. Nitrogen porosimetry was used to characterize the surface area, pore volume, and pore diameter as a function of the MnO_2 content. X-ray diffraction and high resolution transmission electron microscopy were used to determine the crystal structure and size of the MnO_2. HRTEM EDX was used to establish the dispersibility of the MnO_2

coating throughout the carbon support. For loadings up to 30 wt% MnO_2, a ~1 nm thick MnO_2 conformal coating on high surface area disordered mesoporous carbon support with ~8 nm pore size was shown to produce high C_{MnO2} up to 137 F/g_{MnO2} at a high scan rate of 100 mV/s using cyclic voltammetry. Chronoamperometry measurements were used to estimate an apparent diffusion coefficient of Na^+ of 10^{-9}–10^{-10} cm^2 s^{-1} demonstrating facile ion transport in the nanocomposites. The mechanism for the high pseudocapacitance, especially at high scan rates, is discussed in terms of the morphology of the MnO_2 coating and electrochemical properties of the nanocomposites.

4.2 EXPERIMENTAL SECTION

4.2.1 Materials

All chemicals were used as received. Sodium sulfate (>99%) and tetrabutylammonium perchlorate (>98%) were acquired from Sigma-Aldrich Cooperation, and potassium permanganate, propylene carbonate (99%), and ethanol (Absolute 200 proof) from Fisher Scientific. High purity deionized water (resistance ~18 MΩ-cm) was used. Argon (research grade, 99.999% purity) was purchased from Praxair.

4.2.2 Disordered Amorphous Mesoporous Carbon Synthesis

Disordered mesoporous carbon was prepared via self-assembly of block copolymer and phenolic resin under acidic conditions as described in previous reports.[53, 54] Typically, 16.5 g of resorcinol and 16.5 g of F127 ($EO_{106}PO_{70}EO_{106}$) were dissolved in 67.5 mL of ethanol and 67.5 mL of HCl aqueous solution (3.0 M). To this solution, 19.5 g of formaldehyde (37 wt % in H_2O) was added with stirring at room temperature. As the polymerization reaction of resorcinol and formaldehyde proceeded, self-assembly of *in situ* formed phenolic resin and F127 induced a phase separation. The polymer-rich gel phase was collected in the bottom of centrifuge tubes by centrifugation at 9500 rpm for 4 min after the mixture was stirred for 30 min. The gel was re-dissolved in a mixed solvent of 18 g of THF and 12 g of ethanol and the mixture was loaded on a substrate, dried at room temperature overnight, and cured at 80 °C for 24 h. Carbonization was carried out under N_2 atmosphere at 400 °C for 2 h with a heating rate of 1 °C/min, which was followed by further heat treatment at 850 °C for 3 h with a heating rate of 5 °C/min.

4.2.3 Preparation of MnO_2/C Composites

30 mg of disordered mesoporous carbon was mixed with 10 mL of aqueous $KMnO_4$ solution of known concentration ranging from 0.001 M to 0.1 M and mixed for 5 min. The solution was filtered and washed with DI water to remove un-reacted $KMnO_4$. The MnO_2/C nanocomposite was subsequently calcined in air at 200 °C for 6 hours.

4.2.4 Characterization

High resolution transmission electron microscopy was performed on a TECNAI G2 F20 X-TWIN microscope in both bright field and scanning transmission electron microscopy (STEM) mode at an accelerating voltage of 200 kV. Drift corrected spectrum mappings were obtained by choosing a reference region in a STEM image to prevent the EDX probe scanning direction from deviating from the area of interest to give enhanced sensitivity and spatial resolution. The EDX mapping was acquired with a dwell time of 3000 ms at any given position, and the map size was 400 positions per nanostructure. The spatial resolution of this technique is ~1 nm. HRTEM images were obtained at the optimum Scherzer defocus. Nanocomposites were deposited from a dilute ethanol solution onto 200 mesh carbon-coated copper TEM grids.

Wide angle X-ray diffraction was performed with samples prepared on a quartz slide using a Bruker-Nonius D8 Advance diffractometer. Samples were scanned for 4 h at a scan rate of 0.3 deg/min with 0.05 deg increments. The average nanocrystal size was estimated from the Scherrer equation using JADE software (by Molecular Diffraction Inc).

Scanning electron microscopy was carried out using a Zeiss Supra 40VP field emission scanning electron microscope. The SEM observation was performed at an accelerating voltage of 10 kV. Energy dispersive X-ray analysis was performed using a LEO 1530 SEM equipped with an IXRF EDX system, the latter operated with a 20 kV electron beam and 60 μm aperture (average counts ~2000 s^{-1}). Thermogravimetric analysis was done with a Perkin Elmer TGA 7 instrument. The carbon from the nanocomposites was burned off by heating the sample to 800 °C and holding the temperature for 30 min.

Nitrogen sorption analysis was performed on a Micromeritics Tristar 3000 analyzer at -196 °C. Prior to measurements, the samples were heated at 150 °C with flowing N_2 at a Micromeritics FlowPrep 060 sample degas system for 4 h. The specific surface area was calculated using the BET method from the nitrogen adsorption data in the relative pressure range (P/P_0) of 0.04-0.30. The total pore volume was determined from the amount of N_2 uptake at $P/P_0 = 0.98$. Micropore and mesopore areas were calculated using the t-plot method.[55]

Electrochemical measurements were carried out using a CHI 832 electrochemical analyzer (CH instruments Inc.). A three-electrode cell with a Au wire counter electrode and a Hg/Hg_2SO_4 reference electrode were used. A glassy carbon electrode (0.196 cm^2, from Pine Instruments) was used as a substrate for the nanocomposite. The glassy carbon electrode was polished with a 0.3 μm followed by a 0.05 μm alumina suspension to give a mirror finish. The MnO_2/C nanocomposites were mixed with polytetrafluoroethylene (PTFE) in an agate mortar in a 90:10 weight ratio. 1.0 mg of MnO_2/C was suspended by sonication in 500 μL of ethanol. A total of 15 μL of MnO_2/C suspension was deposited onto the glassy carbon substrate and dried at room temperature. Electrochemical tests were done in 1 M Na_2SO_4 at room temperature. Aqueous potentials are referenced vs. Hg/Hg_2SO_4. Experiments were also performed in 0.5 M tetrabutylammonium perchlorate ($TBAClO_4$) in propylene carbonate (PC) using a custom designed Ag/AgO_x reference electrode (1.02 V vs. NHE) at a scan rate of 2 mV/s.

4.3 RESULTS

Figure 4.1 shows high resolution SEM images of the mesoporous carbon and the MnO_2/C nanocomposites at various loadings. For the pure carbon (Fig. 4.1a) and 2 wt% MnO_2 (Fig. 4.1b) samples, the mesopores of the carbon are clearly visible. At intermediate loadings of 16 wt% (Fig. 4.1c), the porous structure is more difficult to

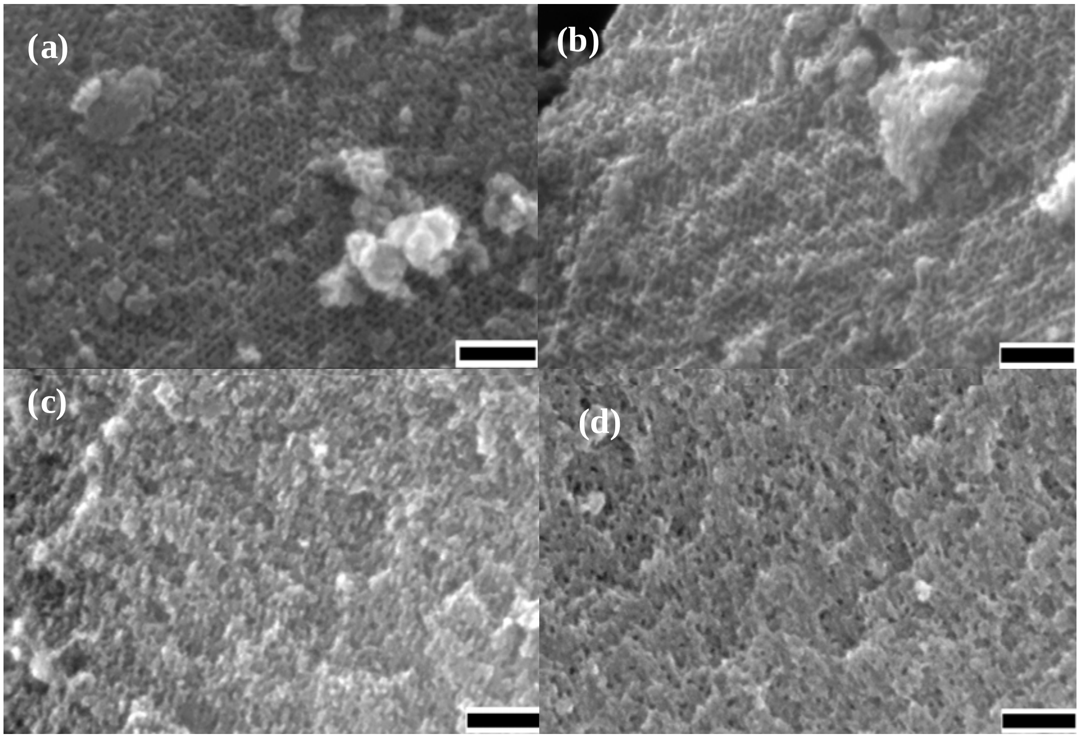

Figure 4.1: SEM images of (a) mesoporous carbon and that modified with (b) 2 wt% MnO_2, (c) 16 wt% MnO_2, and (d) 30 wt% MnO_2. Black scale bar is 100 nm.

visualize; however, the formation of short MnO_2 ribbon structures is noticeable. At the highest loading of 30 wt% (Fig. 4.1d), the ribbon-like structures are considerably more pronounced and are dispersed throughout the porous carbon structure. From XRD analysis, the MnO_2 is birnessite, which is commonly formed during the reaction between potassium permanganate and carbon.[44, 45, 56]

MnO_2/C nanocomposites from 2 wt% to 30 wt% were synthesized, and the amount in the compositions was evaluated by SEM EDX and TGA (Appendix B, Table B.1). The TGA values are slightly higher compared to the SEM EDX results for all samples due to residual amounts of potassium deposited onto the mesoporous carbon substrate during the synthesis. Although the nanocomposites were cleaned by washing with DI water, all of the potassium ions could not be removed. Thus, the MnO_2 compositions determined by SEM EDX were used to determine the gravimetric capacitance with respect to MnO_2 content (C_{MnO2}).

Nitrogen sorption of the nanocomposites provided the BET surface area, pore volume, and the pore size distribution (Table 4.1, Figure 4.2). The nitrogen sorption isotherms are available in Appendix B (Fig. B.1). The mesoporous carbon has a high surface area of 617 m^2/g, a pore volume of 0.72 cm^3/g, and a mean pore diameter centered at 8.4 nm. The micropore (<2 nm) and mesopore (2-50 nm) area of the carbon are 297 m^2/g and 320 m^2/g, respectively. The micropore and mesopore area were calculated using the t-plot method.[55] For the MnO_2/C nanocomposites, the surface area and pore volume decrease with increasing MnO_2 content as expected. With 8.4 wt% MnO_2, there is a marked drop in both surface area and pore volume to 291 m^2/g and 0.49 cm^3/g. These values decrease with MnO_2 loading up to 30% indicating most of the MnO_2 coats the mesopores rather than the outermost surface. The decrease in surface area can be attributed to the addition of MnO_2 throughout the carbon mesopores, the blockage of the micropores, and the higher molecular weight of MnO_2. For the MnO_2/C nanocomposites, there is almost no micropore area, according to t-plot method calculations on the sorption isotherms. The introduction of MnO_2 causes a decrease in the mean pore size and selectively removes the larger pores (Fig. 4.2). The mean pore

Table 4.1: Nitrogen sorption data for mesoporous carbon and MnO_2/C nanocomposites along with capacitance at 2 mV/s in 1 M Na_2SO_4.

	Nitrogen sorption			Capacitance		
MnO_2 content (wt%)	BET surface area (m^2/g)	Pore volume (cm^3/g)	Mean pore diameter (nm)	Gravimetric (F/g)	Areal (μF/cm^2)	Volumetric (F/cm^3)
0	617	0.72	8.4	28	4.5	24
8.4	291	0.49	7.5	68	23	74
21	238	0.37	7.1	77	32	98
30	186	0.34	7.0	79	42	108

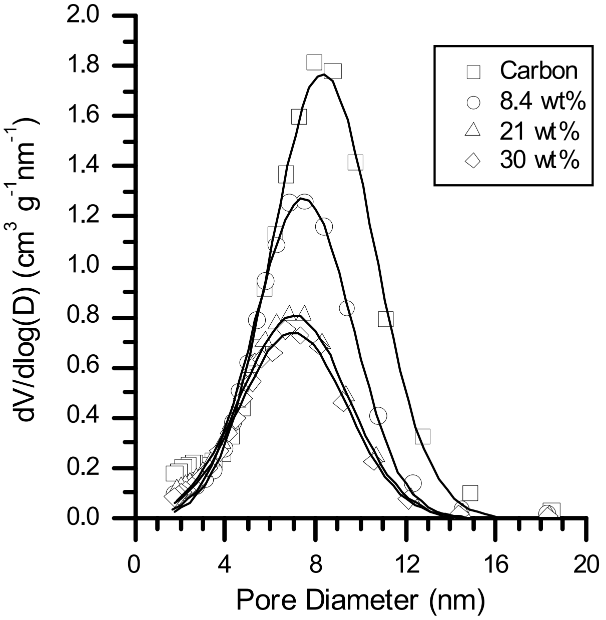

Figure 4.2: Pore size distribution for mesoporous carbon and MnO_2/C nanocomposites for various compositions. The lines represent best fit Gaussians through the displayed data points.

diameter decreases from 8.4 nm to 7.5 nm with 8.4 wt% MnO_2. At the 30 wt% loading, the mean pore diameter decreases to 7.0 nm, and a coating thickness of ~0.7 nm is derived using nitrogen porosimetry. A uniform coating thickness through the carbon mesopores can also be estimated on a mass basis from the MnO_2. Assuming a cylindrical geometry, the coating thickness in an annular region within a pore is

$$t = r_2 - \sqrt{r_2^2 - \left(\frac{wt\%_{MnO_2}}{100 - wt\%_{MnO_2}}\right)\frac{2r_2}{\rho_{MnO_2} A_{Mesopore}}} \tag{4.1}$$

where t is the thickness, r_2 is carbon pore radius (4.35 nm), ρ_{MnO2} is the MnO_2 density (3.4 g/cc), and $A_{mesopore}$ is the carbon mesopore surface area (320 m^2/g). For 30 wt% MnO_2, the coating thickness would be 0.4 nm. Given the large uncertainty from subtracting the mean pore sizes from nitrogen porosimetry before and after MnO_2 addition, the agreement between the two techniques is reasonable. However, this small thickness would indicate the MnO_2 is only an atomic layer thick, which is not conceivable given the deposition method. Most likely the MnO_2 forms domains which are at least a few atomic layers thick, which would give thicknesses of >1 nm.

In Figure 4.3 the XRD patterns for the mesoporous carbon and 21 wt% and 30 wt% MnO_2/C nanocomposites are shown relative to pure carbon. The large peaks at 23° and 43° indicate the degree of graphitization of the carbon. The broad peaks suggest that the material has some degree of graphitic character from the aromatic carbon precursor, but less than that found for similar mesoporous carbons calcined at higher temperatures.[57, 58] With MnO_2 loaded into the carbon, these peaks diminish and additional small peaks appear at 36.8° and 65.7°. These peaks correspond to the (006) and (119) planes of birnessite (JCPDF #18-0802), respectively.[49, 59] The nanocrystal size of the MnO_2 domains was estimated using the peak at 36.8°. For the 21 wt% and 30 wt% nanocomposites, the nanocrystal sizes were calculated by the Scherrer equation to be 3.8 and 3.5 nm, respectively. From the small size of the peaks, it can be construed that both crystalline and amorphous MnO_2 domains exist within the nanocomposite.

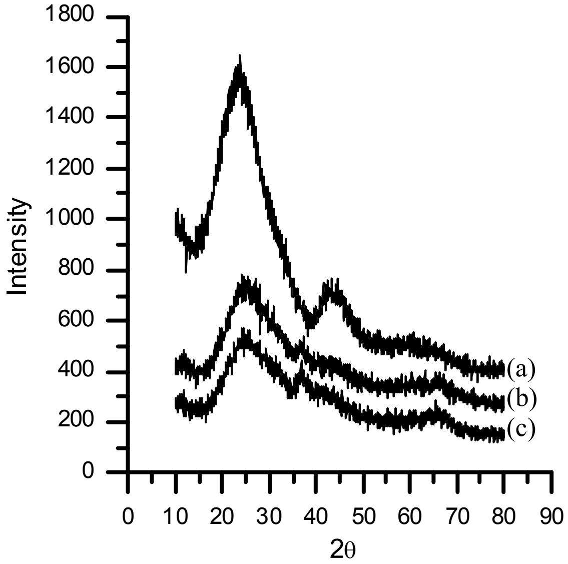

Figure 4.3: XRD of (a) mesoporous carbon, and that modified with (b) 21 wt% MnO_2, and (c) 30 wt% MnO_2 showing birnessite peak present (spectra offset for clarity).

HRTEM was used to characterize the nanostructure of the 30 wt% MnO_2/C nanocomposite. From the low magnification image in Fig. 4.4a, MnO_2 nanocrystals appear as small dark spots. At higher magnification (Fig. 4.4b), the lattice planes are evident for the MnO_2 nanocrystals, in accord to that seen from XRD. The lattice fringes have a lattice spacing of 2.33 Å, close to the value of 2.44 Å for the (006) planes of birnessite, which were present in the XRD pattern (Fig. 4.2) at 36.8°. This lattice spacing is large enough to accommodate transport of Na^+ ions with a crystal radius of 0.95 Å,[32] The nanocrystal size from the HRTEM image was measured to be 3.6 ± 0.7 nm, in good agreement with the XRD value of 3.5 nm. The dispersion of MnO_2 crystallites in Fig. 4.4a,b is also shown to be consistent with the amount of MnO_2 estimated from TGA and SEM as no large MnO_2 domains are present. The image in Figure 4.4b with a feature size of 3.6 nm is a top down image and does not show the particle thickness. The TEM images also show gaps between the discrete nanodomains. Thus, the thickness of each discrete crystallite would be larger than the thickness of 0.4-0.7 nm from mass based calculations and nitrogen porosimetry. This idea is further supported by an effective spherical particle diameter obtained from XRD measurements of 3.5 nm, which would not be consistent with a thickness of only 0.7 nm. For simplicity, we will refer to the thickness of the MnO_2 domains as ~1 nm.

To supplement the HRTEM images, EDX in STEM mode was performed to show the degree of MnO_2 dispersion throughout the nanocomposite (Fig. 4.4c). STEM-EDX mapping enables imaging the elemental distribution in a fine area with its high-resolution, and the specimen-drift auto-compensation system gives enhanced sensitivity and spatial resolution. In STEM mode, the image contrast is proportional to the mass density times the atomic number squared. Therefore Mn will give a much higher intensity than C since the ratio of the atomic numbers squared is 20. From Fig. 4.4c, the small bright white dots correspond to the MnO_2 nanocrystals. In Fig. 4.4d-f, the K-line energies of the Mn, O, and C intensities are given in red, green, and blue, respectively. The red intensity is visible across the entire nanocomposite and indicates the Mn is uniformly distributed throughout the carbon support. Comparison of the STEM image in Fig. 4.4c with the EDX shows a strong correspondence between the MnO_2 nanocrystals

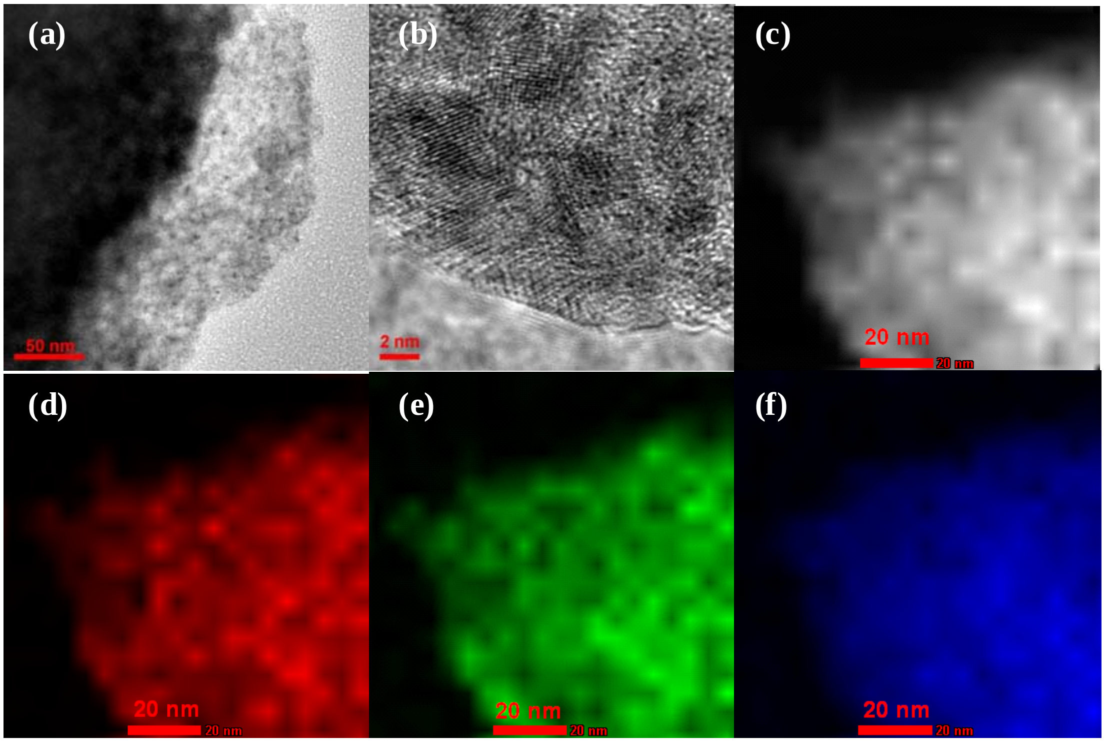

Figure 4.4: HRTEM images and EDX of 30 wt% MnO_2/C nanocomposite: (a) Low mag, (b) high mag, (c) STEM, and STEM-EDX intensities for (d) Mn, (e) O, (f) C.

and the strong red intensities from Mn and green intensities from O. Hence, the EDX mapping of the MnO_2/C nanocomposite shows deposition of MnO_2 crystallites throughout the support.

Cyclic voltammetry (CV) was utilized to estimate the pseudocapacitive properties of the MnO_2/C nanocomposites as shown in Figure 4.5 between 0.4 to -0.4 V at a both 2 and 100 mV/s in 1 M Na_2SO_4. The profiles are relatively flat and rectangular which is typical for electrochemical double-layer capacitors as well as for some redox pseudocapacitors composed of MnO_2.[3, 5] At 2 mV/s with a loading of 2 wt% MnO_2, the capacitance increases ~40% compared to the mesoporous carbon. With higher loadings of 16 wt% and 30 wt%, the flat profile is still evident, which indicates the conductivity remains sufficient at this low scan rate even with a large amount of MnO_2 material. At the higher scan rate (100 mV/s), the flat profiles are still present indicating both good ion transport and conductivity for the nanocomposites. Figure 4.6 shows the gravimetric capacitance values at both 2 and 100 mV/s with respect to MnO_2 mass (Fig. 4.6a) and total composite mass (MnO_2 + carbon) (Fig. 4.6b). The total gravimetric capacitance C_g values were calculated with the following equation

$$C_g = (\Delta I/2)/(\nu m) \tag{4.2}$$

where ΔI is the current difference at 0 V in the two different scanning directions, ν is the scan rate, and m is the mass of active material. A maximum C_{MnO2} of 560 F/g_{MnO2} was measured for the 2 wt% MnO_2/C nanocomposite and decreases with higher loadings of MnO_2 for both scan rates. At 2 mV/s, the C_{MnO2} decreased almost linearly up to 21 wt% MnO_2; however, it remained at ~200 F/g_{MnO2} for 30 wt%. At 100 mV/s, the behavior changed as the C_{MnO2} appeared to level off at 16 wt% with a final C_{MnO2} of 137 F/g_{MnO2} at 30 wt%. At 2 mV/s, the C_g (Fig. 4.6b) increased sharply at lower mass loadings and then leveled off. The maximum C_g was 79 F/g at 30 wt%, an increase of almost threefold compared to the unmodified mesoporous carbon. At 100 mV/s this increase was similar. At the high scan rate, the C_g is nearly linear in the loading of MnO_2 over the entire range (Fig. 4.6b). For the 30 wt% MnO_2/C nanocomposite, there is a 32% drop in C_g with over a 50-fold change in the scan rate.

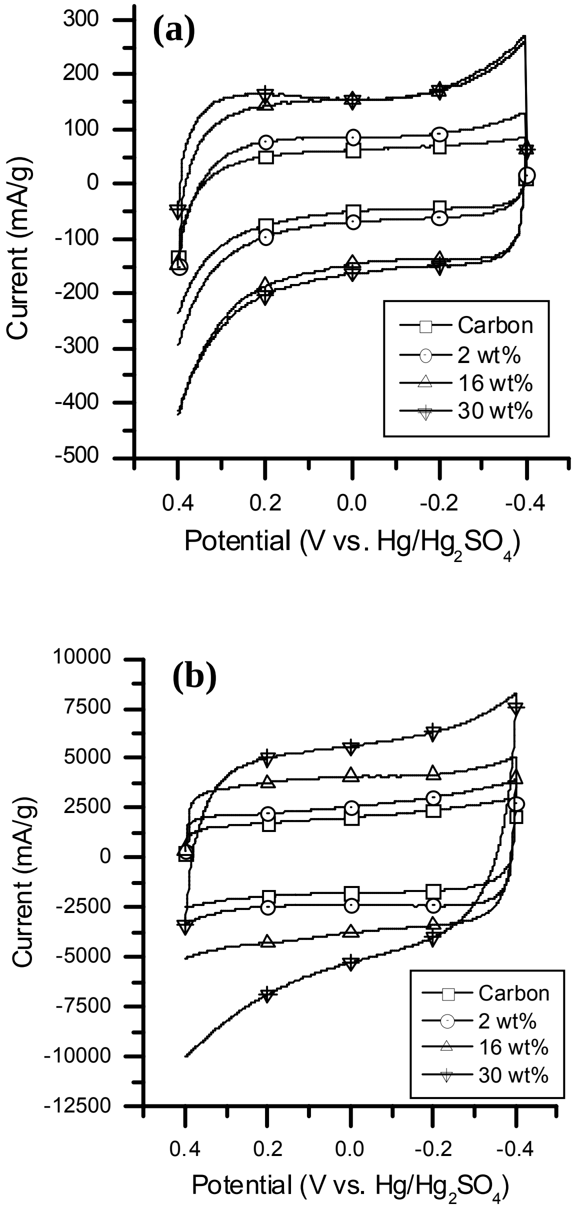

Figure 4.5: Cyclic voltammetry of the mesoporous carbon and MnO_2/C nanocomposite for various compositions at (a) 2 mV/s and (b) 100 mV/s in 1 M Na_2SO_4.

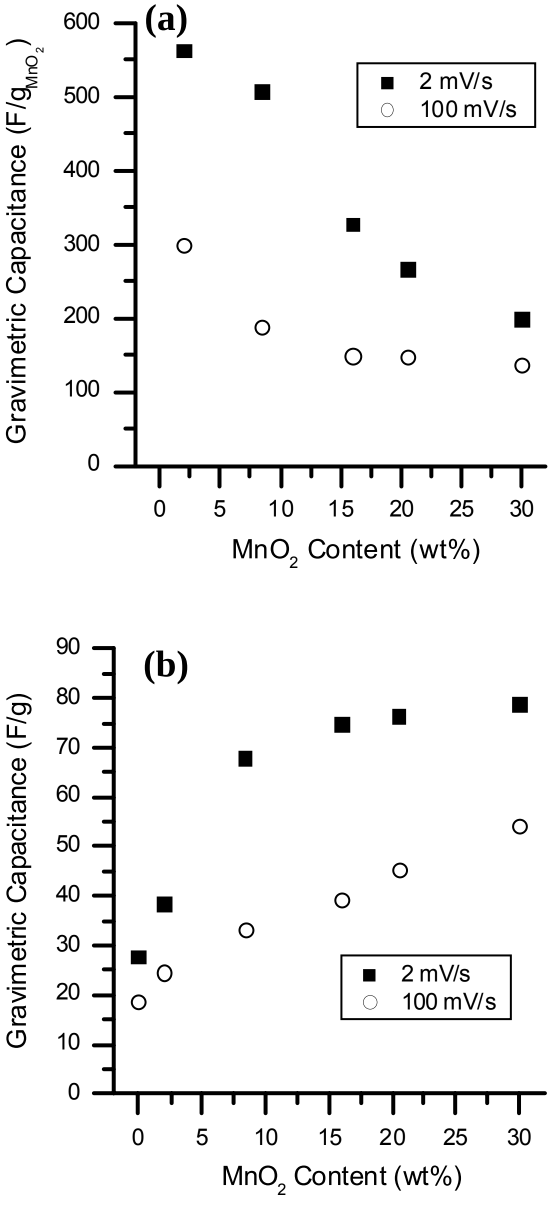

Figure 4.6: Gravimetric capacitance values for MnO_2/C nanocomposites at 2 mV/s and 100 mV/s in 1 M Na_2SO_4 based on (a) MnO_2 mass (b) total mass.

The maximum energy density (E_{max}) can be calculated from the C_g,

$$E_{max} = \frac{1}{2}C_{cell}V^2 \qquad (4.3)$$

where V is the potential window and taken to be a maximum of 1.2 V, the breakdown of water, and C_{cell} is the device capacitance ($C_g/2$). The highest energy density is for the 30 wt% MnO_2/C sample, which exhibits the highest C_g. At 2 and 100 mV/s, the maximum energy densities were 7.9 and 5.4 Wh/kg, respectively. These values fall within typical pseudoapacitor energy densities (1-10 Wh/kg).[8]

Using the nitrogen sorption data for the MnO_2/C nanocomposites, the areal and volumetric capacitances are calculated at 2 mV/s (Table 4.1). With a higher MnO_2 content, the BET surface area decreases; accordingly, the areal capacitance increases by almost an order of magnitude from 4.5 μF/cm^2 for the mesoporous carbon to 42 μF/cm^2 for the 30 wt% MnO_2/C nanocomposite. This increase reflects the greater storage capacity of the redox pseudocapacitance of MnO_2 reaction relative to EDLC of carbon. From the pore volume, the volumetric capacitance can also be calculated and increases similarly to the C_g. For the mesoporous carbon the volumetric capacitance is 24 F/cm^3, and with 30 wt% MnO_2/C, it increases by 450% to 108 F/cm^3.

Chronoamperometry was used to measure the apparent diffusion coefficient (or ambipolar diffusion coefficient) D, which is composed of both the ionic and electronic diffusion. Estimation of D includes an intrinsic thermodynamic enhancement factor, which can be expressed as the product of the transference number of the electron and the ratio of the change in ion activity to change in ion concentration.[60] With increasing MnO_2 content, D decreases for both insertion and deinsertion (Fig. 4.7). The bare carbon support has a high insertion value of 7.4×10^{-9} cm^2/s and a slightly lower deinsertion value of 5.0×10^{-9} cm^2/s. These values are several orders of magnitude slower than for Na^+ diffusion through bulk solution (~10^{-5} cm^2/s). With the addition of MnO_2 into the pores, D begins to decrease. At 30 wt% MnO_2, D drops by an order of magnitude to 8.0×10^{-10} and 4.7×10^{-10} cm^2/s for insertion and deinsertion, respectively. The lower D at high MnO_2 content results predominately from ionic diffusion into the MnO_2 layer.

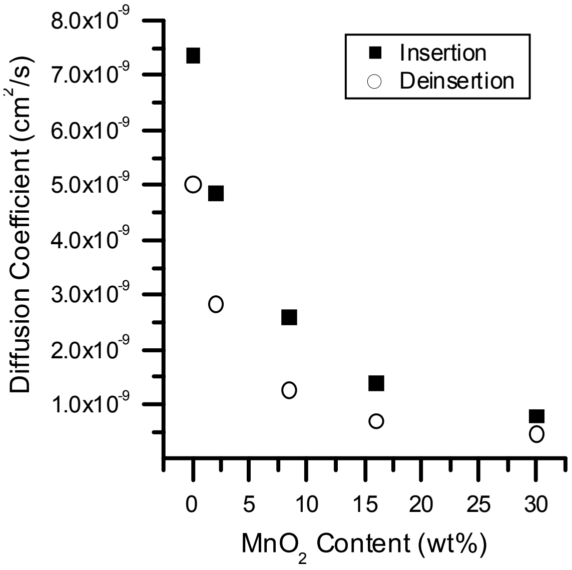

Figure 4.7: Apparent diffusion coefficient values for insertion and deinsertion of Na^+ in MnO_2/C nanocomposites in 1 M Na_2SO_4.

The nanocomposite materials were also tested in propylene carbonate (PC) with tetrabutylammonium perchlorate, $TBAClO_4$, as the electrolyte (Appendix B, Fig. B.2, Table B.3). The large cation size of ~9 Å[61] prevents entrance into the MnO_2 lattice. Consequently, contributions to the capacitance due faradaic pseudocapacitance are insignificant in nonaqueous solvents. Therefore, these experiments provide a means for estimating contributions due to double-layer charging processes.[49] The C_g is similar for all of the nanocomposites tested (~26 F/g) and about the same as for mesoporous carbon (28 F/g) in the aqueous electrolyte, as expected. The current-potential curves at 2 mV/s were also flat rectangular profiles indicating satisfactory electronic conductivity (Appendix B, Fig. B.2) similar to Fig. 4.5 with 1 M Na_2SO_4. Together, these results confirm that no pseudocapacitive contribution was present, and the electric double-layer capacitance was constant with MnO_2 content. These measurements indicate that there is very little change in the electrochemically active surface area of the carbon after modification with MnO_2.[49] Hence, the additional capacitance found in Na_2SO_4 was due to the faradaic contribution involving MnO_2.

4.4 DISCUSSION

The redox charge storage mechanism in MnO_2 occurs via insertion/deinsertion of sodium ions

$$Mn^{IV}O_2 + Na^+ + e^- \leftrightarrow Mn^{III}OONa \tag{4.4}$$

or by surface adsorption via

$$(Mn^{IV}O_2)_{surface} + Na^+ + e^- \leftrightarrow (Mn^{III}O_2^-Na^+)_{surface} \tag{4.5}$$.

Both mechanisms are sufficiently fast to yield reasonable power densities.[3] With the inclusion of MnO_2 inside of the mesopores, the surface area per mass of MnO_2 decreases due to the decrease in pore diameter, micropore blockage, and the heavier MnO_2. However, even with this slight decrease in surface area, the contribution from the double-layer capacitance remains constant as measured with the large tetrabutylammonium cation, TBA^+, which does not penetrate MnO_2 and contribute to pseudocapacitance. For all the samples, the gravimetric capacitance decreased with scan rate indicating limits in electron and/or ion transport.

The decrease in C_{MnO2} with higher MnO_2 content (Fig. 4.6a) can be explained in terms of the EDLC and the pseudocapacitance contributions. At low MnO_2 content, most of the MnO_2 is present as a "surface oxide", and the surface Faradaic contribution (rxn. 4.5) dominates. With more MnO_2 incorporated into the composite, the thickness of the film increases, and the classical diffusion based insertion/deinsertion mechanism becomes more important. Here the C_{MnO2} decreases, indicating a smaller fraction of MnO_2 is fully utilized. Perhaps most of the surface sites (rxn. 4.5) are utilized, but only a small fraction of the underlying more bulk-like sites (rxn. 4.4) are utilized at faster scan rates. Assuming the smallest diffusion coefficient D of 4.7×10^{-10} cm^2/s and a short time of 0.01 s, the diffusion length $L = (D\tau)^{1/2}$ would be 22 nm. Hence diffusion into the ~1 nm thick MnO_2 coating should be facile, yet the capacitance fades at high scan rates. Thus, this loss is likely influenced significantly by limitations in electronic conductivity of the carbon support, which is not surprising given the less graphitic character of this mesoporous carbon relative to other forms of carbon. For MnO_2/C nanocomposites utilizing more graphitic carbons, presumably ~1 nm MnO_2 coatings would be more fully utilized and display higher faradaic efficiencies at high scan rates.

The choice of pore size for the carbon support is an important factor for influencing electrolyte transport and MnO_2 utilization. For a given MnO_2 loading, the MnO_2 thickness can be estimated for infinitely long cylindrical pores from the equation

$$\frac{r_2}{r_1} = \sqrt{\frac{1-\phi}{1-\frac{1}{\varepsilon}\phi}} \tag{4.6}$$

where r_2 is the carbon pore radius, r_1 is the pore radius after coating with MnO_2, ε is the carbon porosity, and φ is the volume fraction MnO_2 inside the pore. Assuming a carbon porosity of 50% and MnO_2 loading of 30 wt. %, the MnO_2 thickness would be 0.16, 0.8, and 4.0 nm for pore sizes of 2, 10, and 50 nm. Micropores (<2 nm) would be unfavorable because of high solution resistance and possible pore blockage.[9] For macropores (>50 nm), the film thickness becomes too large leading to poor conductivity in MnO_2, especially for larger values of ϕ. Hence, mesopores (2-50 nm) are a desirable geometry for supporting MnO_2 domains, as shown in the current study for a pore size of ~10 nm and a MnO_2 thickness of ~1 nm, to facilitate rapid ion and electron transport.

Table 4.2 provides a comparison between this study and two other recent reports of carbon-based nanocomposites with similar MnO_2 loadings. For ordered mesoporous carbon modified using $KMnO_4$, amorphous MnO_2 particles were embedded inside of the carbon walls.[45] The CV curves had sloping profiles, which increased with MnO_2 content, indicating a larger electrolyte and ohmic resistance from the non-conducting MnO_2 even at a low scan rate. The authors measured the gravimetric capacitance at the maximum possible current difference between anodic and cathodic scans, rather than in the middle of the potential range in the CV profiles as is the common benchmark.[45] Re-analysis of the data in Dong et al. yields a specific capacitance in 2 M KCl of 95 F/g (149 F/g_{MnO2}, 11 $\mu F/cm^2$) at 9.4 wt% MnO_2 and 110 F/g (167 F/g_{MnO2}, 16 $\mu F/cm^2$) at 26 wt% MnO_2. Although the C_g is higher compared to the present study, the C_{MnO2} is much lower. At 8.4 wt%, the C_{MnO2} of 507 F/g_{MnO2} is threefold higher in the present study. At 30 wt%, the C_{MnO2} is still slightly higher at 199 F/g_{MnO2} than for composites with 26 wt% MnO_2 reported by Dong et al. The ordered carbon pores in Dong et al. may limit the ion diffusion and increase the electrolyte resistance, as suggested by the sloping CV curves. The areal capacitance is also two times higher in the present study. Perhaps a composite displaying a more disordered porous system with many transport pathways facilitates far more facile ion transport[63] and leads to flatter CV profiles, as acquired in the present study (Fig. 4.5).

Carbon nanofoams with a 3D disordered pore structure (pore size distribution from 1 to 100 nm) have also been used as supports.[44, 48, 62] The foams contained MnO_2 particles from 10 to 30 nm. A C_g in 1 M Na_2SO_4 of 74 F/g (187 F/g_{MnO2}, 20 $\mu F/cm^2$, 49 F/cm^3) was obtained at 28 wt% MnO_2 (Table 4.2) at low scan rates, comparable to those in the present study. However, the estimated volumetric and areal capacitances at low scan rates in the present study were twice as large presumably due to a more optimal pore size and uniform pore size distribution.

Table 4.2. Comparison of different carbon supports and MnO_2/carbon nanocomposites.

Carbon type	MnO_2 content (wt%)	BET surface area (m^2/g)	Pore volume (cm^3/g)	Pore size (nm)	F/g	F/g$_{MnO2}$	µF/cm^2	F/cm^3	ref
Ordered mesoporous	0	968	0.96	3.6	90[a] (*105*[b])	-	9.3[a] (*11*[b])	64[a] (*74*[b])	Dong et al.[45]
Ordered mesoporous	9.4	900	0.94	3.6	95[a] (*152*[b])	149[a] (*605*[b])	11[a] (*17*[b])	69[a] (*111*[b])	Dong et al.[45]
Ordered mesoporous	26	708	0.57	3.5	110[a] (*220*[b])	167[a] (*547*[b])	16[a] (*31*[b])	114[a] (*227*[b])	Dong et al.[45]
Nanofoam	0	437	0.61	1 to 100	30	-	6.9	16	Fischer et al.[48,c]
Nanofoam	28	379	0.65	1 to 100	74	187[d]	20	49	Fischer et al.[48,c]
Disordered mesoporous	0	577	0.72	8.4	28	-	4.8	24	This study[e]
Disordered mesoporous	8.4	291	0.49	7.5	68	507	23	74	This study[e]
Disordered mesoporous	30	186	0.34	7.0	79	199	42	108	This study[e]

[a] Values recalculated based on CV data of Dong et al.[45] and at same potential as this study.
[b] Data taken at 5 mV/s in 2 M KCl.[45]
[c] Data taken at 2 mV/s in 1 M Na_2SO_4.[48]
[d] Value calculated using aerogel capacitance and gravimetric MnO_2 content.
[e] Data taken at 2 mV/s in 1 M Na_2SO_4.

MnO_2 on highly conductive multi-walled carbon nanotube (CNT) composites have been investigated.[52] A loading of ~55 wt% MnO_2 produced ~6 nm coating with an ε-MnO_2 crystallinity. At 2 mV/s with 0.5 M Na_2SO_4, the C_g and C_{MnO2} were high at 205 F/g and 350 F/g_{MnO2}. However, at 100 mV/s, they dropped to 25 F/g and 37 F/g_{MnO2}. The C_g and C_{MnO2} of 54 F/g and 137 F/g_{MnO2} in the present study were more than twofold larger, indicating a much smaller decrease as the scan rate increased. The CVs for the CNT composites have large sloping profiles suggesting ohmic resistance from the thick 6 nm MnO_2 coatings on the CNTs. The ~1 nm thick MnO_2 nanodomains in the current study result in flatter profiles for the CVs and higher capacitances at high scan rates.

In the present study, soft-templated disordered mesoporous carbon was synthesized and coated with both amorphous and crystalline MnO_2 domains. The soft-template synthesis strategy for carbon is advantageous in that a sacrificial template is not required and excess synthesis and activation steps can be avoided. The narrow pore size distribution used in this study centered at 8.4 nm allows for enough space for MnO_2 domains to form with a thickness ~1 nm throughout the carbon structure. As seen in the pore size distribution data for 30 wt% MnO_2/C nanocomposites (Fig. 4.2), the pore size is ~7.0 nm, a decrease of only ~17%, which still provides enough open porosity to facilitate facile ion transport. The 3D pore interconnectivity also aids in decreasing the solution resistance by providing multiple pathways for ion transport.[63] The degree of crystallinity of the MnO_2 domains can also be influential factors as amorphous areas are still present. With large interlayer spacings possible from various MnO_2 polymorphs, an improved crystal structure can possibly lead to higher pseudocapacitance.[32] The graphitic nature of the mesoporous carbon can influence the electronic conductivity and the MnO_2 coating process. For our materials the disordered mesoporous carbon is fairly amorphous as evidenced by broad XRD peaks, suggesting small graphitic domains (Fig. 4.3). It is well known that more graphitic carbons are more electronically conductive.[54, 58] In addition, graphitic carbon supports can be functionalized in a controlled matter, e.g. by oxidation, to promote wetting and deposition of MnO_2 at edge plane sites,[64] which is more difficult to achieve with amorphous carbons. Both graphitization of the carbon substrate and use of thin MnO_2 layers may be expected to lead to decreased ohmic resistance and higher energy densities for high rate applications. Further modification in the design of the nanocomposites can lead to improvements in the energy density approaching those of batteries.

4.5 CONCLUSIONS

Herein, we have demonstrated an enhancement in C_g of almost threefold for MnO_2/C nanocomposites with 30 wt% MnO_2 compared to the bare mesoporous carbon support. The deposition of redox-active MnO_2 coatings upon a nanostructured mesoporous carbon support augments the double-layer capacitance with substantial redox pseudocapacitance. The thin nanodomains with a thickness of ~1 nm within the support allow for a high pseudocapacitance, while preserving open and available disordered pores that facilitate ion transport. At high scan rates, the total gravimetric capacitance exhibited a linear increase with MnO_2 content, whereas the C_{MnO2} decreased and leveled off. Even for 30 wt% MnO_2, a high C_{MnO2} of 137 F/g_{MnO2} was observed at 100 mV/s, consistent with a relatively small change in the diffusion coefficient with loading according to chronoamperometry. The leveling off in C_{MnO2} with scan rate indicates that the Na^+ continues to diffuse throughout a significant fraction of the MnO_2 domains. The high C_{MnO2} of these nanodomains at high scan rates is a significant advancement towards the ultimate goal of high energy and power densities for electrochemical capacitors with thin conformal coatings of MnO_2.

4.6 REFERENCES

1. Miller, J. R.; Burke, A. F., Electrochemical capacitors: challenges and opportunities for real-world applications. *Electrochemical Society Interface* 2008, 17, (1), 53-57.

2. Miller, J. R.; Simon, P., Electrochemical Capacitors for Energy Management. *Science (Washington, DC, United States)* 2008, 321, (5889), 651-652.

3. Simon, P.; Gogotsi, Y., Materials for electrochemical capacitors. *Nature Materials* 2008, 7, (11), 845-854.

4. Conway, B. E., *Electrochemical Supercapacitors: Scientific Fundamentals and Technological Applications*. Kluwer Academic/Plenum Publishers: New York, 1999.

5. Kotz, R.; Carlen, M., Principles and applications of electrochemical capacitors. *Electrochimica Acta* 2000, 45, (15-16), 2483-2498.

6. Arico, A. S.; Bruce, P.; Scrosati, B.; Tarascon, J.-M.; van Schalkwijk, W., Nanostructured materials for advanced energy conversion and storage devices. *Nature Materials* 2005, 4, (5), 366-377.

7. Conway, B. E.; Birss, V.; Wojtowicz, J., The role and utilization of pseudocapacitance for energy storage by supercapacitors. *Journal of Power Sources* 1997, 66, (1-2), 1-14.

8. Pandolfo, A. G.; Hollenkamp, A. F., Carbon properties and their role in supercapacitors. *Journal of Power Sources* 2006, 157, (1), 11-27.

9. Frackowiak, E.; Beguin, F., Carbon materials for the electrochemical storage of energy in capacitors. *Carbon* 2001, 39, (6), 937-950.

10. Frackowiak, E., Carbon materials for supercapacitor application. *Physical Chemistry Chemical Physics* 2007, 9, (15), 1774-1785.

11. Chmiola, J.; Yushin, G.; Gogotsi, Y.; Portet, C.; Simon, P.; Taberna, P. L., Anomalous Increase in Carbon Capacitance at Pore Sizes Less Than 1 Nanometer. *Science (Washington, DC, United States)* 2006, 313, (5794), 1760-1763.

12. Fuertes, A. B.; Alvarez, S., Graphitic mesoporous carbons synthesised through mesostructured silica templates. *Carbon* 2004, 42, (15), 3049-3055.

13. Fuertes, A. B.; Pico, F.; Rojo, J. M., Influence of pore structure on electric double-layer capacitance of template mesoporous carbons. *Journal of Power Sources* 2004, 133, (2), 329-336.

14. Li, H.-Q.; Liu, R.-L.; Zhao, D.-Y.; Xia, Y.-Y., Electrochemical properties of an ordered mesoporous carbon prepared by direct tri-constituent co-assembly. *Carbon* 2007, 45, (13), 2628-2635.

15. Liu, H.-Y.; Wang, K.-P.; Teng, H., A simplified preparation of mesoporous carbon and the examination of the carbon accessibility for electric double layer formation. *Carbon* 2005, 43, (3), 559-566.

16. Vix-Guterl, C.; Frackowiak, E.; Jurewicz, K.; Friebe, M.; Parmentier, J.; Beguin, F., Electrochemical energy storage in ordered porous carbon materials. *Carbon* 2005, 43, (6), 1293-1302.

17. Xing, W.; Qiao, S. Z.; Ding, R. G.; Li, F.; Lu, G. Q.; Yan, Z. F.; Cheng, H. M., Superior electric double layer capacitors using ordered mesoporous carbons. *Carbon* 2005, 44, (2), 216-224.

18. Du, C.; Pan, N., High power density supercapacitor electrodes of carbon nanotube films by electrophoretic deposition. *Nanotechnology* 2006, 17, (21), 5314-5318.

19. Obreja, V. V. N., On the performance of supercapacitors with electrodes based on carbon nanotubes and carbon activated material-A review. *Physica E: Low-Dimensional Systems & Nanostructures (Amsterdam, Netherlands)* 2008, 40, (7), 2596-2605.

20. Ania, C. O.; Khomenko, V.; Raymundo-Pinero, E.; Parra, J. B.; Beguin, F., The large electrochemical capacitance of microporous doped carbon obtained by using a zeolite template. *Advanced Functional Materials* 2007, 17, (11), 1828-1836.

21. Zheng, J. P.; Cygan, P. J.; Jow, T. R., Hydrous ruthenium oxide as an electrode material for electrochemical capacitors. *Journal of the Electrochemical Society* 1995, 142, (8), 2699-703.

22. Zheng, J. P.; Jow, T. R., A new charge storage mechanism for electrochemical capacitors. *Journal of the Electrochemical Society* 1995, 142, (1), L6-L8.

23. Kim, I.-H.; Kim, K.-B., Ruthenium oxide thin film electrodes for supercapacitors. *Electrochemical and Solid-State Letters* 2001, 4, (5), A62-A64.

24. Liang, Y.-Y.; Li, H. L.; Zhang, X.-G., Solid state synthesis of hydrous ruthenium oxide for supercapacitors. *Journal of Power Sources* 2007, 173, (1), 599-605.

25. Subhramannia, M.; Balan, B. K.; Sathe, B. R.; Mulla, I. S.; Pillai, V. K., Template-Assisted Synthesis of Ruthenium Oxide Nanoneedles: Electrical and Electrochemical Properties. *Journal of Physical Chemistry C* 2007, 111, (44), 16593-16600.

26. Hu, C.-C.; Chang, K.-H.; Lin, M.-C.; Wu, Y.-T., Design and Tailoring of the Nanotubular Arrayed Architecture of Hydrous RuO2 for Next Generation Supercapacitors. *Nano Letters* 2006, 6, (12), 2690-2695.

27. Toupin, M.; Brousse, T.; Belanger, D., Influence of Microstructure on the Charge Storage Properties of Chemically Synthesized Manganese Dioxide. *Chemistry of Materials* 2002, 14, (9), 3946-3952.

28. Toupin, M.; Brousse, T.; Belanger, D., Charge Storage Mechanism of MnO2 Electrode Used in Aqueous Electrochemical Capacitor. *Chemistry of Materials* 2004, 16, (16), 3184-3190.

29. Long, J. W.; Swider-Lyons, K. E.; Stroud, R. M.; Rolison, D. R., Design of pore and matter architectures in manganese oxide charge-storage materials. *Electrochemical and Solid-State Letters* 2000, 3, (10), 453-456.

30. Jeong, Y. U.; Manthiram, A., Nanocrystalline Manganese Oxides for Electrochemical Capacitors with Neutral Electrolytes. *Journal of the Electrochemical Society* 2002, 149, (11), A1419-A1422.

31. Luo, J.-Y.; Xia, Y.-Y., Effect of pore structure on the electrochemical capacitive performance of MnO2. *Journal of the Electrochemical Society* 2007, 154, (11), A987-A992.

32. Devaraj, S.; Munichandraiah, N., Effect of Crystallographic Structure of MnO2 on Its Electrochemical Capacitance Properties. *Journal of Physical Chemistry C* 2008, 112, (11), 4406-4417.

33. Pang, S.-C.; Anderson, M. A.; Chapman, T. W., Novel electrode materials for thin-film ultracapacitors: comparison of electrochemical properties of sol-gel-derived and electrodeposited manganese dioxide. *Journal of the Electrochemical Society* 2000, 147, (2), 444-450.

34. Shinomiya, T.; Gupta, V.; Miura, N., Effects of electrochemical-deposition method and microstructure on the capacitive characteristics of nano-sized manganese oxide. *Electrochimica Acta* 2006, 51, (21), 4412-4419.

35. Belanger, D.; Brousse, T.; Long, J. W., Manganese oxides: battery materials make the leap to electrochemical capacitors. *Electrochemical Society Interface* 2008, 17, (1), 49-52.

36. Brock, S. L.; Sanabria, M.; Suib, S. L.; Urban, V.; Thiyagarajan, P.; Potter, D. I., Particle Size Control and Self-Assembly Processes in Novel Colloids of Nanocrystalline Manganese Oxide. *Journal of Physical Chemistry B* 1999, 103, (35), 7416-7428.

37. Park, J.; Kang, E.; Bae, C. J.; Park, J.-G.; Noh, H.-J.; Kim, J.-Y.; Park, J.-H.; Park, H. M.; Hyeon, T., Synthesis, Characterization, and Magnetic Properties of Uniform-sized MnO Nanospheres and Nanorods. *Journal of Physical Chemistry B* 2004, 108, (36), 13594-13598.

38. Ragupathy, P.; Vasan, H. N.; Munichandraiah, N., Synthesis and characterization of nano-MnO2 for electrochemical supercapacitor studies. *Journal of the Electrochemical Society* 2007, 155, (1), A34-A40.

39. Seo, W. S.; Jo, H. H.; Lee, K.; Kim, B.; Oh, S. J.; Park, J. T., Size-dependent magnetic properties of colloidal Mn3O4 and MnO nanoparticles. *Angewandte Chemie, International Edition* 2004, 43, (9), 1115-1117.

40. Chen, H.; Dong, X.; Shi, J.; Zhao, J.; Hua, Z.; Gao, J.; Ruan, M.; Yan, D., Templated synthesis of hierarchically porous manganese oxide with a crystalline nanorod framework and its high electrochemical performance. *Journal of Materials Chemistry* 2007, 17, (9), 855-860.

41. Xu, C.-L.; Bao, S.-J.; Kong, L.-B.; Li, H.; Li, H.-L., Highly ordered MnO2 nanowire array thin films on Ti/Si substrate as an electrode for electrochemical capacitor. *Journal of Solid State Chemistry* 2006, 179, (5), 1351-1355.

42. Doescher, M. S.; Pietron, J. J.; Dening, B. M.; Long, J. W.; Rhodes, C. P.; Edmondson, C. A.; Rolison, D. R., Using an Oxide Nanoarchitecture To Make or Break a Proton Wire. *Analytical Chemistry* 2005, 77, (24), 7924-7932.

43. Chen, H.; He, J.; Zhang, C.; He, H., Self-Assembly of Novel Mesoporous Manganese Oxide Nanostructures and Their Application in Oxidative Decomposition of Formaldehyde. *Journal of Physical Chemistry C* 2007, 111, (49), 18033-18038.

44. Fischer, A. E.; Pettigrew, K. A.; Rolison, D. R.; Stroud, R. M.; Long, J. W., Incorporation of Homogeneous, Nanoscale MnO2 within Ultraporous Carbon Structures via Self-Limiting Electroless Deposition: Implications for Electrochemical Capacitors. *Nano Letters* 2007, 7, (2), 281-286.

45. Dong, X.; Shen, W.; Gu, J.; Xiong, L.; Zhu, Y.; Li, H.; Shi, J., MnO2-Embedded-in-Mesoporous-Carbon-Wall Structure for Use as Electrochemical Capacitors. *Journal of Physical Chemistry B* 2006, 110, (12), 6015-6019.

46. Jin, X.; Zhou, W.; Zhang, S.; Chen, G. Z., Nanoscale microelectrochemical cells on carbon nanotubes. *Small* 2007, 3, (9), 1513-1517.

47. Raymundo-Pinero, E.; Khomenko, V.; Frackowiak, E.; Beguin, F., Performance of Manganese Oxide/CNTs Composites as Electrode Materials for Electrochemical Capacitors. *Journal of the Electrochemical Society* 2005, 152, (1), A229-A235.

48. Fischer, A. E.; Saunders, M. P.; Pettigrew, K. A.; Rolison, D. R.; Long, J. W., Electroless deposition of nanoscale MnO2 on ultraporous carbon nanoarchitectures: correlation of evolving pore-solid structure and electrochemical performance. *Journal of the Electrochemical Society* 2008, 155, (3), A246-A252.

49. Lei, Y.; Fournier, C.; Pascal, J.-L.; Favier, F., Mesoporous carbon-manganese oxide composite as negative electrode material for supercapacitors. *Microporous and Mesoporous Materials* 2008, 110, (1), 167-176.

50. Lee, C. Y.; Tsai, H. M.; Chuang, H. J.; Li, S. Y.; Lin, P.; Tseng, T. Y., Characteristics and electrochemical performance of supercapacitors with manganese oxide-carbon nanotube nanocomposite electrodes. *Journal of the Electrochemical Society* 2005, 152, (4), A716-A720.

51. Sharma, R. K.; Oh, H.-S.; Shul, Y.-G.; Kim, H., Carbon-supported, nano-structured, manganese oxide composite electrode for electrochemical supercapacitor. *Journal of Power Sources* 2007, 173, (2), 1024-1028.

52. Xie, X.; Gao, L., Characterization of a manganese dioxide/carbon nanotube composite fabricated using an in situ coating method. *Carbon* 2007, 45, (12), 2365-2373.

53. Liang, C.; Dai, S., Synthesis of Mesoporous Carbon Materials via Enhanced Hydrogen-Bonding Interaction. *Journal of the American Chemical Society* 2006, 128, (16), 5316-5317.

54. Wang, X.; Liang, C.; Dai, S., Facile Synthesis of Ordered Mesoporous Carbons with High Thermal Stability by Self-Assembly of Resorcinol-Formaldehyde and Block Copolymers under Highly Acidic Conditions. *Langmuir* 2008, 24, (14), 7500-7505.

55. Gregg, S. J.; Sing, K. S. W., *Adsorption, surface area and porosity*. 2nd ed.; Academic Press: London; New York, 1982.

56. Ma, S.-B.; Lee, Y.-H.; Ahn, K.-Y.; Kim, C.-M.; Oh, K.-H.; Kim, K.-B., Spontaneously Deposited Manganese Oxide on Acetylene Black in an Aqueous

Potassium Permanganate Solution. *Journal of the Electrochemical Society* 2006, 153, (1), C27-C32.

57. Liang, C.; Li, Z.; Dai, S., Mesoporous carbon materials: synthesis and modification. *Angewandte Chemie, International Edition* 2008, 47, (20), 3696-3717.

58. Shanahan, P. V.; Xu, L.; Liang, C.; Waje, M.; Dai, S.; Yan, Y. S., Graphitic mesoporous carbon as a durable fuel cell catalyst support. *Journal of Power Sources* 2008, 185, (1), 423-427.

59. Gaillot, A.-C.; Flot, D.; Drits, V. A.; Manceau, A.; Burghammer, M.; Lanson, B., Structure of Synthetic K-rich Birnessite Obtained by High-Temperature Decomposition of KMnO4. I. Two-Layer Polytype from 800 DegC Experiment. *Chemistry of Materials* 2003, 15, (24), 4666-4678.

60. McEvoy, T. M.; Stevenson, K. J., Spatially Resolved Imaging of Inhomogeneous Charge Transfer Behavior in Polymorphous Molybdenum Oxide. II. Correlation of Localized Coloration/Insertion Properties Using Spectroelectrochemical Microscopy. *Langmuir* 2005, 21, (8), 3529-3538.

61. Lytle, J. C.; Rhodes, C. P.; Long, J. W.; Pettigrew, K. A.; Stroud, R. M.; Rolison, D. R., The importance of combining disorder with order for Li-ion insertion into cryogenically prepared nanoscopic ruthenia. *Journal of Materials Chemistry* 2007, 17, (13), 1292-1299.

62. Fischer, A. E.; Long, J. W., Redox deposition of nanoscale MnO2 on ultraporous carbon nanoarchitectures: correlation of MnO2 deposition time and electrochemical performance. *ECS Transactions* 2007, 3, (37, Electrochemical Capacitors 2006), 61-66.

63. Rolison, D. R., Catalytic nanoarchitectures - The importance of nothing and the unimportance of periodicity. *Science (Washington, DC, United States)* 2003, 299, (5613), 1698-1702.

64. Jia, N.; Martin, R. B.; Qi, Z.; Lefebvre, M. C.; Pickup, P. G., Modification of carbon supported catalysts to improve performance in gas diffusion electrodes. *Electrochimica Acta* 2001, 46, (18), 2863-2869.

Chapter 5

High Specific Capacity and High Rate MnO_2/Graphitic Mesoporous Carbon Electrochemical Capacitors

Nanocomposites composed of MnO_2 and graphitic disordered mesoporous carbon (MnO_2/C) were synthesized for high specific capacitance or redox pseudocapacitance (C_{MnO2}) at high rates of 200 mV/s. High resolution transmission electron microscopy (HRTEM) with energy dispersive X-ray spectroscopy (EDX) demonstrated that MnO_2 nanodomains were highly dispersed throughout the mesoporous carbon structure. According to HRTEM and X-ray diffraction (XRD), the MnO_2 domains are shown to be primarily amorphous, with a thickness of ~1 nm from nitrogen porosimetry. For these composites in aqueous 1 M Na_2SO_4 electrolyte, C_{MnO2} reached 500 F/g_{MnO2} at 2 mV/s for 8.8 wt% MnO_2. A capacitance fade of only 20% over a 100-fold change in scan rate was observed for a high loading of 35 wt% MnO_2 with a C_{MnO2} of 310 F/g_{MnO2} at the highest scan rate of 200 mV/s. The 35 wt% MnO_2/C exhibited a high volumetric capacitance of 400 F/cm^3. The relaxation time constants of <1 s were unusually short because of the nanocomposite architecture and high conductivity. The high electronic conductivity of the graphitic 3D disordered mesoporous carbon support in conjunction with the ~1 nm thick MnO_2 nanodomains facilitate rapid electron and ion transport offering the potential of improved high power density energy storage pseudocapacitors.

The contents of this chapter are being prepared for a manuscript.

5.1 INTRODUCTION

Electrochemical double-layer capacitors (EDLCs), pseudocapacitors, and supercapacitors are commonly used monikers for a class of electrochemical energy-storage devices already used in digital cameras, cell phones, circuit boards, industrial equipment, and transportation vehicles.[1, 2] Electrochemical capacitors can be grouped into two categories: an electrochemical double-layer capacitor and a redox pseudocapacitor (otherwise known as a supercapacitor). EDLCs store electrical energy from double-layer capacitance generated by charge separation at the interface between a solid electrode and a liquid electrolyte. High surface area carbon materials such as activated carbon, carbon nanotubes (CNTs), and carbon aerogels/foams are commonly used as electrode materials for EDLCs. In contrast, redox pseudocapacitors store electrical energy from fast and electrochemically reversible faradaic redox reactions occurring at or near a solid electrode. In this class, electrode materials for pseudocapacitors are typically conducting polymers such as polyaniline and transition metal oxides such as RuO_2 and MnO_2. The higher specific power of electrochemical capacitors is ideally suited for the rapid storage and release of energy relative to most batteries, whereas their specific energy is somewhat lower. Through appropriate materials and cell design, both the specific energy and specific power ranges can span several orders of magnitude. Thus pseudocapacitors are attractive for energy storage and supply either alone or in combination with batteries in hybrid systems.[3] The characteristic combination of high power capability and good specific energy allows pseudocapacitors to occupy a functional position between batteries and conventional capacitors, especially with regard to the advanced development of hybrid electric vehicles and load leveling smart grids.[4, 5] With improved design of material architectures, the gap between pseudocapacitors and batteries can be narrowed resulting in cheaper, longer-lasting materials[3, 6, 7]

For MnO_2, a redox-active material, high gravimetric pseudocapacitances around 700 F/g_{MnO2} on nickel foil at a scan rate of 50 mV/s[8] or a low current density of 160 $\mu A/cm^2$[9] were reported for thin films on conductive planar substrates. An atypically large

C_{MnO2} of ~1380 F/g_{MnO2} at a low scan rate was reported for 420 nm agglomerated MnO_2 porous particles deposited on highly conductive platinum foil.[10] This value is essentially the theoretical limit of 1370 F/g_{MnO2} for a redox reaction with a single electron per manganese atom.[10] However, the C_{MnO2} is known to drop off markedly when sub-10 nm MnO_2 domains are supported on high surface area porous carbon, that has much lower conductivity, relative to Pt.[11] The properties of a carbon support can be tailored to increase the capacitance by changing the surface area, pore structure, and electronic conductivity.[3, 12-19] The gravimetric capacitance in an EDLC is directly proportional to the accessible surface area. For carbon EDLCs, the gravimetric capacitance reaches values of 250 F/g for high surface areas on the order of 2000 m^2/g.[12] The high surface area results mainly from micropores (<2 nm) with little contribution from mesopores (2-50 nm) and macropores (>50 nm). However, limited ion transport through micropores[13, 15] lowers the capacitance at high rates.

The energy density of a pseudocapacitor may be enhanced with mesoporous materials with pore sizes of 5-10 nm that favor rapid ion transport and also offer relatively high surface areas on the order of 300 m^2/g.[6, 13] Furthermore, the pore size is sufficiently large for deposition of a thin conformal coating of a pseudocapacitive material[20-23] with a thickness on the order of 1 nm. High C_{MnO2} were achieved at 50 mV/s but were much lower than the values at 5 mV/s.[22] In the previous chapter, disordered mesoporous carbon composites with highly dispersed MnO_2 at loadings of 30 wt% were formed and achieved a high C_{MnO2} of 137 F/g_{MnO2} at a high scan rate of 100 mV/s. A high volumetric capacitance of 110 F/cm^3 was also attained as a consequence of the high loading and high surface area to volume support. Despite the relatively high utilization of the MnO_2, the C_{MnO2} was limited by the low electronic conductivity of the carbon support, given the low graphitic content produced by heat treatment at only at 850 °C. A higher electronic conductivity would accelerate electron transfer throughout the carbon support to the MnO_2 domains to compliment rapid ion diffusion in the pores and raise the C_{MnO2}.

For mesoporous carbons graphitized at only ~850 °C, the electronic conductivity is low ~0.3 S/cm.[16, 24] In contrast, electronic conductivities can reach 4.2 S/cm[16] to 330

S/cm[24] for higher levels of graphitization with heat treatments ≥2300 °C. These materials are composed of carbon atoms sp^2 hybridized in stacked, highly ordered hexagonal rings.[25] EDLCs composed of 3D aperiodic hierarchical porous (1-100 nm) graphitic carbon materials give a capacitance fade of only ~10% going from 5 to 100 mV/s.[18] However, upon deposition of a redox-active metal oxide into this type of architecture, the smaller pores in the broad pore size distribution support ranging from 1-100 nm may become blocked, and the surface area may be limited for conformal coating for the larger pores. Alternatively, CNT electrodes have received a lot of attention as they possess uniform diameters of tens of nanometers, are highly electronically conductive, and have mesoporous character.[14, 15] Carbons of this type with 3D interpenetrating void and solid structures comprising ionic and electronic conductive networks are more optimal for use as pseudocapacitor electrodes. Therefore, graphitic carbon supports with a high surface area, mesopores, and high electronic conductivity would be more beneficial for improving the electrochemical utilization of the redox-active metal oxide or polymer as a pseudocapacitive material. Using a soft-template strategy, this architecture can be designed readily to give high surface area mesoporous carbon supports with uniform pore size distributions and high electronic conductivities.[26]

Herein we report high MnO_2 pseudocapacitance at high rates by depositing MnO_2 nanodomains into highly graphitic mesoporous carbon with high electronic conductivity. The synthesis of the 3D disordered pores with a soft-template leads to thicker walls than with typical hard templates. The thicker walls enable a higher electronic conductivity, for example, ~330 S/cm for heat treatment at 2600 °C.[24] High loadings of MnO_2 to 35 wt% with excellent dispersion are achieved by electroless deposition inside the mesoporous carbon support with ~8 nm pores. The as-synthesized graphitic carbon surface is hydrophobic and impedes wetting of the aqueous precursor, limiting loadings to <1 wt%. The carbon was oxidized to increase the hydrophilicity to promote wetting and deposition of MnO_2 at edge plane sites. The high support electronic conductivity in conjunction with the 3D high surface area disordered mesopores, which favor high MnO_2 loading and rapid ion transport, are shown to enable high C_{MnO2}, even at very high scan rates of 200 mV/s. A high C_{MnO2} of 310 F/g_{MnO2} is achieved even for 35 wt% MnO_2 at

200 mV/s. The structure and composition of the nanocomposites is characterized using scanning electron microscopy, X-ray diffraction, nitrogen porosimetry, and high resolution transmission electron microscopy with energy dispersive spectroscopy. XRD and HRTEM are used to probe the degree of crystallinity of the MnO_2. HRTEM EDX shows the MnO_2 is well dispersed throughout the carbon support. Electrochemical impedance spectroscopy is utilized to evaluate the charge transfer resistance, diffusional resistance of the ions through the pores of the composite, and the dielectric relaxation time constant, which provides a relative indication of the power density.[21]

5.2 EXPERIMENTAL SECTION

5.2.1 Materials

All chemicals were used as received. Sodium sulfate (>99%) was acquired from Sigma-Aldrich Cooperation, and potassium permanganate, and ethanol (Absolute 200 proof) from Fisher Scientific. High purity deionized water (resistance ~18 MΩ-cm) was used. Argon (research grade, 99.999% purity) was purchased from Praxair.

5.2.2 Graphitic Mesoporous Carbon Synthesis

Disordered mesoporous carbon was prepared via self-assembly of block copolymer and phenolic resin under acidic conditions as described in previous reports.[27, 28] Typically, 16.5 g of resorcinol and 16.5 g of F127 ($EO_{106}PO_{70}EO_{106}$) were dissolved in 67.5 mL of ethanol and 67.5 mL of HCl aqueous solution (3.0 M). To this solution, 19.5 g of formaldehyde (37 wt % in H_2O) was added with stirring at room temperature. As the polymerization reaction of resorcinol and formaldehyde proceeded, self-assembly of *in situ* formed phenolic resin and F127 induced a phase separation. The polymer-rich gel phase was collected in the bottom of centrifuge tubes by centrifugation at 9500 rpm for 4 min after the mixture was stirred for 30 min. The gel was re-dissolved in a mixed solvent of 18 g of THF and 12 g of ethanol and the mixture was loaded on a substrate, dried at room temperature overnight, and cured at 80 °C for 24 h. Carbonization was carried out under N_2 atmosphere at 400 °C for 2 h with a heating rate of 1 °C/min, which was followed by further heat treatment at 2600 °C for 3 h with a heating rate of 5 °C/min.

5.2.3 Preparation of Oxidized Graphitic Mesoporous Carbon

100 mg of graphitic mesoporous carbon was mixed with 20 mL of 5 M HNO_3. The solution was stirred and refluxed overnight. The oxidized graphitic mesoporous carbon was filtered, washed with copious amounts of DI H_2O, and dried at 100 °C.

5.2.4 Preparation of MnO_2/C Composites

20 mg of oxidized graphitic mesoporous carbon (OGMC) was mixed with 10 mL of aqueous 0.1 M $KMnO_4$ solution in neutral pH for various times from 10 min to 24 hrs. The solution was filtered and washed with DI water to removed un-reacted $KMnO_4$. The MnO_2/C nanocomposite was subsequently calcined at 100 °C in air overnight.

5.2.5 Characterization

High Resolution Transmission Electron Microscopy was performed on a TECNAI G2 F20 X-TWIN microscope in both bright field and scanning transmission electron microscopy (STEM) mode at an accelerating voltage of 200 kV. Drift corrected spectrum mappings were obtained by choosing a reference region in a STEM image to prevent the EDX probe scanning direction from deviating from the area of interest. The EDX mapping was acquired with a dwell time of 3000 ms at any given position, and the map size was 400 positions per nanostructure. The spatial resolution of this technique was close to 1 nm. HRTEM images were obtained at the optimum Scherzer defocus. Nanocomposites were deposited from a dilute ethanol solution onto 200 mesh carbon-coated copper TEM grids.

Wide angle X-ray diffraction was performed with samples prepared on a quartz slide using a Bruker-Nonius D8 Advance diffractometer. Samples were analyzed in 0.05 deg increments with a dwell time of 10 s. The average nanocrystal size was estimated from the Scherrer equation using JADE software (by Molecular Diffraction Inc).

Scanning electron microscopy (SEM) was carried out using a Zeiss Supra 40VP field emission scanning electron microscope. The SEM observation was performed at an accelerating voltage of 10 kV. The MnO_2 content of the nanocomposites was determined using energy dispersive X-ray analysis on a LEO 1530 SEM equipped with an IXRF EDX system, the latter operated with a 20 kV electron beam and 60 μm aperture (average counts ~2000 s^{-1}).

Nitrogen sorption analysis was performed on a high-speed surface area BET analyzer (NOVA 2000, Quantachrome Instruments, Boynton Beach, FL) at a temperature of 77 K. Prior to measurements, the samples were degassed overnight. The specific surface area was calculated using the BET method from the nitrogen adsorption data in the relative pressure range (P/P_0) of 0.05-0.30. The total pore volume was determined from the amount of N_2 uptake at $P/P_0 = 0.95$. Pore size distributions were analyzed using the adsorption branch of the isotherm.

Cyclic voltammetry was carried out using a CHI 832A electrochemical analyzer (CH Instruments Inc.). A three-electrode cell with a Au wire counter electrode and a Hg/Hg_2SO_4 reference electrode was used. A glassy carbon electrode (0.196 cm^2, from Pine Instruments) was used as a substrate for the MnO_2/C nanocomposite. The glassy carbon electrode was polished with a 0.3 μm followed by a 0.05 μm alumina suspension to give a mirror finish. The MnO_2/C nanocomposites were ground in an agate mortar prior to testing. 2.0 mg of MnO_2/C was suspended by sonication in 1 mL of ethanol. 15 μL of MnO_2/C suspension was deposited onto the glassy carbon substrate and dried at room temperature. Electrochemical tests were performed in 1 M Na_2SO_4 at room temperature and neutral pH between 0.4 to -0.4 V vs. Hg/Hg_2SO_4. Aqueous potentials cited in this article are vs. Hg/Hg_2SO_4. Electrochemical impedance spectroscopy measurements were made using an Autolab PGSTAT30 potentiostat. The potential was fixed at 0 V vs. Hg/Hg_2SO_4, and frequencies from 10 kHz to 10 mHz were analyzed.

5.3 RESULTS

Figure 5.1 shows the structure of the mesoporous carbon and MnO_2/C nanocomposites from high resolution SEM. Small disordered mesopores are visible for all of the samples. Oxidation shows little visible change from the GMC (Fig. 5.1a) to the OGMC (Fig. 5.1b). At the lowest loading of 5.4 wt% MnO_2 (Fig. 5.1c), small platelet-like deposits of MnO_2 appear on the exterior of the carbon structure. At an intermediate loading of 16 wt% (Fig. 5.1d), these platelet-like deposits are more pronounced limiting the visibility of the pore openings. At the highest loading of 35 wt% (Fig. 5.1e), larger MnO_2 deposits occupy the exterior, some of which may potentially block the pores of the OGMC. Although these deposits are visible on the exterior of the particle, the majority of the MnO_2 may be expected reside in the interior of the OGMC since the ratio of internal surface area to external surface area is very large (10^4:1).

Nitrogen porosimetry was used to characterize the BET surface area, pore volume, and pore size for the MnO_2/C nanocomposites (Table 5.1, Figure 5.2). The sorption isotherms are offered in Appendix C (Fig. C.1). GMC had a surface area of 262 m^2/g and a pore volume of 0.4 cm^3/g. Upon oxidation, these values increase significantly to 434 m^2/g and 0.54 cm^3/g as the surface roughness increased.[25] These increases may be attributed primarily to micropores, since the GMC has almost no micropores (based on t-plot method).[29] At the highest loading of 35 wt% MnO_2, the surface area and porosity dropped substantially to 67 m^2/g and 0.09 cm^3/g. The higher molecular weight of MnO_2 versus carbon further contributes to the decrease in specific surface area. The MnO_2 occupies the majority of the micropores as well as coating the mesopores of the OGMC. The average pore size changes little with the oxidation of the carbon going from 7.6 nm for the GMC to 7.5 nm for the OGMC (Fig. 5.2). At 35 wt% MnO_2, the average pore size decreases to 6.7 nm with a reduction in pore volume over a wide range of pore sizes. The thickness of a uniform MnO_2 film inside the mesopores is estimated to be ~0.4 nm thick from the change in the mean pore diameter. From mass basis calculations assuming straight cylindrical pores, the coating thickness in an annulus would be ~0.4 nm, which

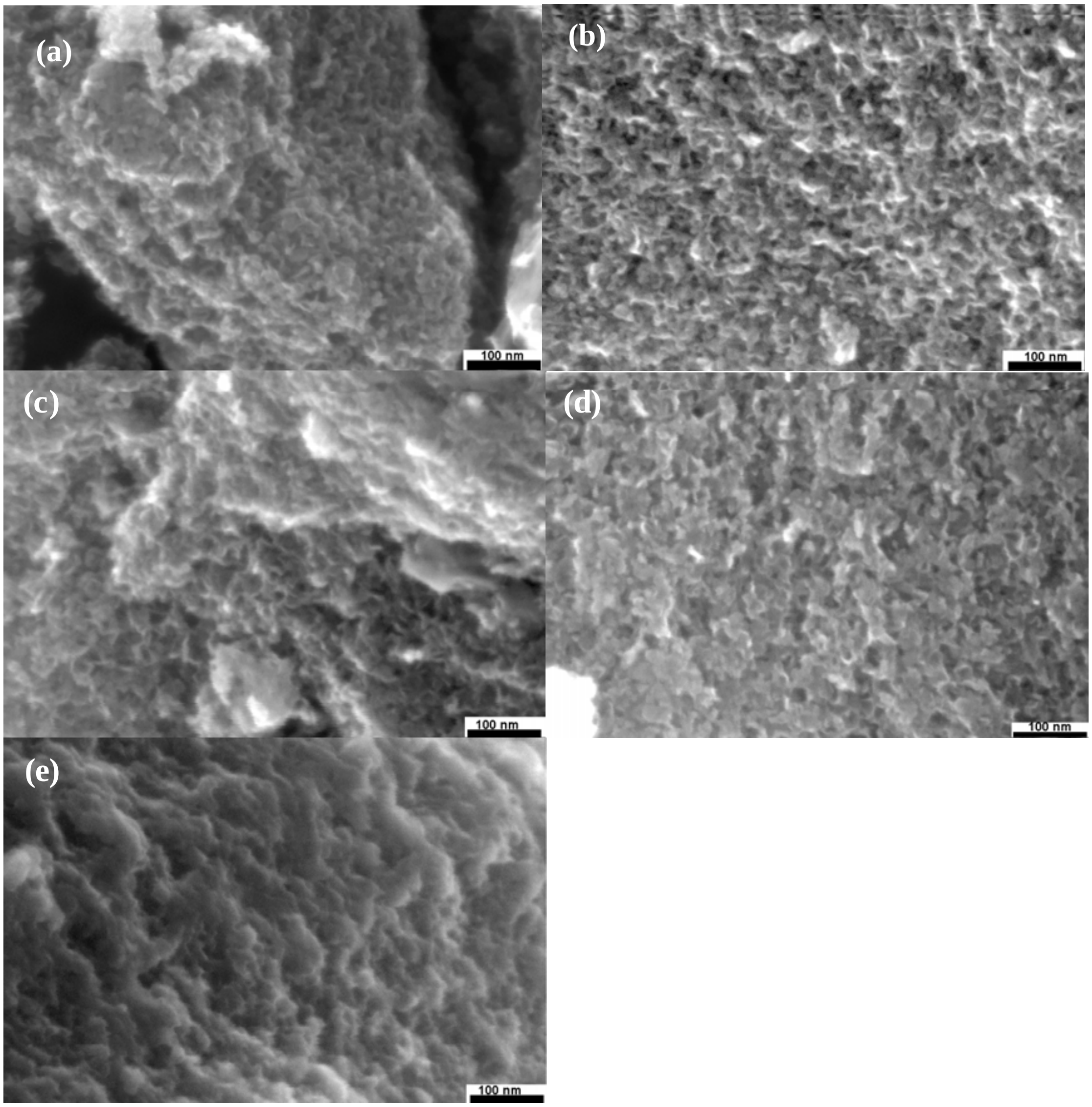

Figure 5.1: SEM images of (a) GMC, (b) OGMC, (c) 5.4 wt% MnO_2/C, (d) 15 wt% MnO_2/C, (e) 35 wt% MnO_2/C.

Table 5.1: Capacitance (2 mV/s) and morphology of graphitic mesoporous carbon (GMC), oxidized GMC (OGMC) and composites of OGMC and MnO_2

	Nitrogen sorption data			Capacitance		
	BET surface area (m^2/g)	Pore volume (cm^3/g)	Mean pore diameter (nm)	Gravimetric (F/g)	Areal ($\mu F/cm^2$)	Volumetric (F/cm^3)
GMC	262	0.40	7.6	21	7.9	24
OGMC	434	0.54	7.5	33	7.7	34
15 wt% MnO_2/C	280	0.34	7.2	86	31	120
35 wt% MnO_2/C	67	0.09	6.7	160	240	400

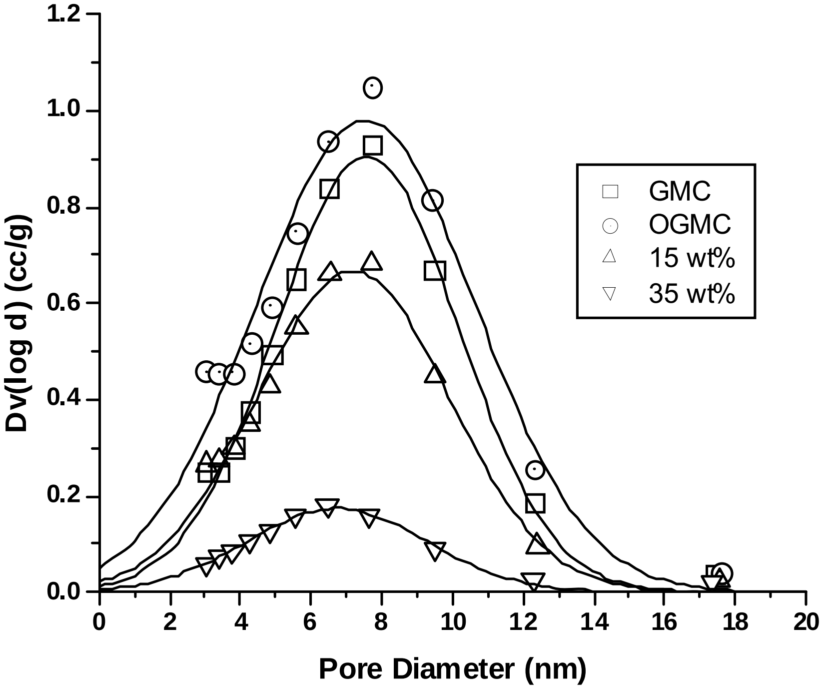

Figure 5.2: Pore size distribution of GMC, OGMC, 15 wt% and 35 wt% MnO_2/C nanocomposites. The lines represent best fit Gaussians through the displayed data points.

agrees remarkable well with the nitrogen sorption data. This small dimension would correspond to ~one atomic layer of MnO_2. However, from XRD and HRTEM, individual nanodomains are present with a size of ~4 nm, which is at least a few atomic layers thick, with uncoated regions between the domains.

X-ray diffraction of the nanocomposites and carbon support are shown in Figure 5.3. For the GMC, a sharp peak at 26° and small peak at 42.2°, corresponding to the (002) and (100) planes, indicate a high degree of graphitization resulting from the heat treatment at 2600 °C. After oxidation with nitric acid, these peaks are still present. Although the 42.2° peak disappears at loadings greater than 20 wt% MnO_2, the sharp peak at 26° remains for all of the MnO_2/C nanocomposites, indicating high graphitization, and consequently high electronic conductivity. For all the samples except for 35 wt%, no peaks for MnO_2 are evident indicating an amorphous layer is deposited inside of the carbon. The MnO_2 is amorphous because of the small domain sizes and since the annealing temperature for the nanocomposites is only 100 °C and not high enough to promote crystallization. However, for the highest loaded sample at 35 wt%, MnO_2 peaks begin to form at 36.8° and 65.7° indicating some crystallization. These peaks correspond to the (006) and (119) crystal planes of birnessite (JCPDF#18-0802), a polymorph of MnO_2.[30, 31] The crystallite size is estimated to be 4.2 nm from Scherrer's equation. The crystallization at 35 wt% occurs presumably from the longer reaction time during the synthesis of the nanocomposite and the larger nanodomains. The small size of the peaks for birnessite at 35 wt% suggests that amorphous domains of MnO_2 are prevalent.

From HRTEM, the graphitic structure of the GMC and OGMC are characterized by bent layered ribbon like planes representing graphene sheets (Fig. 5.4a and 5.4b). These results support the XRD observation of minimal loss in graphitization upon nitric acid treatment. At 15 wt% MnO_2, the graphene layers are visible; however, no discernable structure is evident for MnO_2 (Fig. 5.4c). Here MnO_2 is amorphous as given by XRD and HRTEM. At 35 wt% MnO_2, large dark spots are observable indicating MnO_2 domains dispersed throughout the carbon support (Fig. 5.4d). At higher

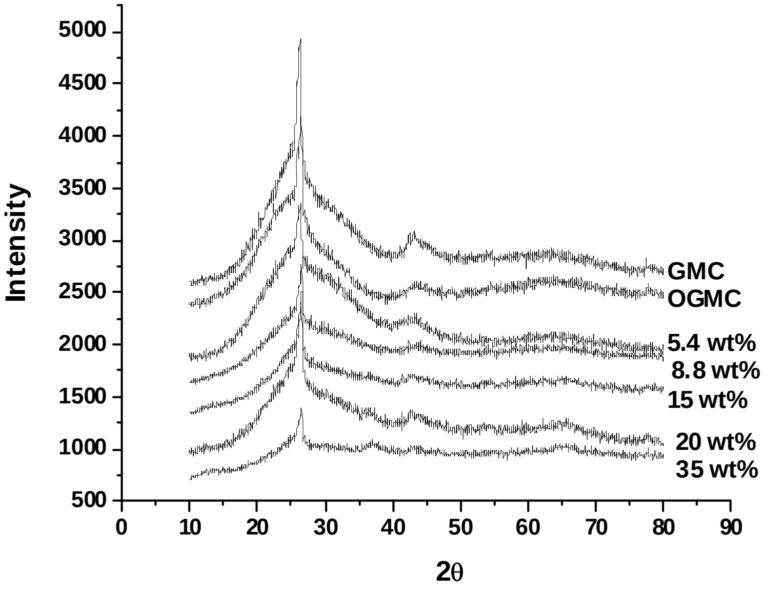

Figure 5.3: XRD patterns for GMC, OGMC, and MnO_2/C nanocomposites (spectra offset for clarity).

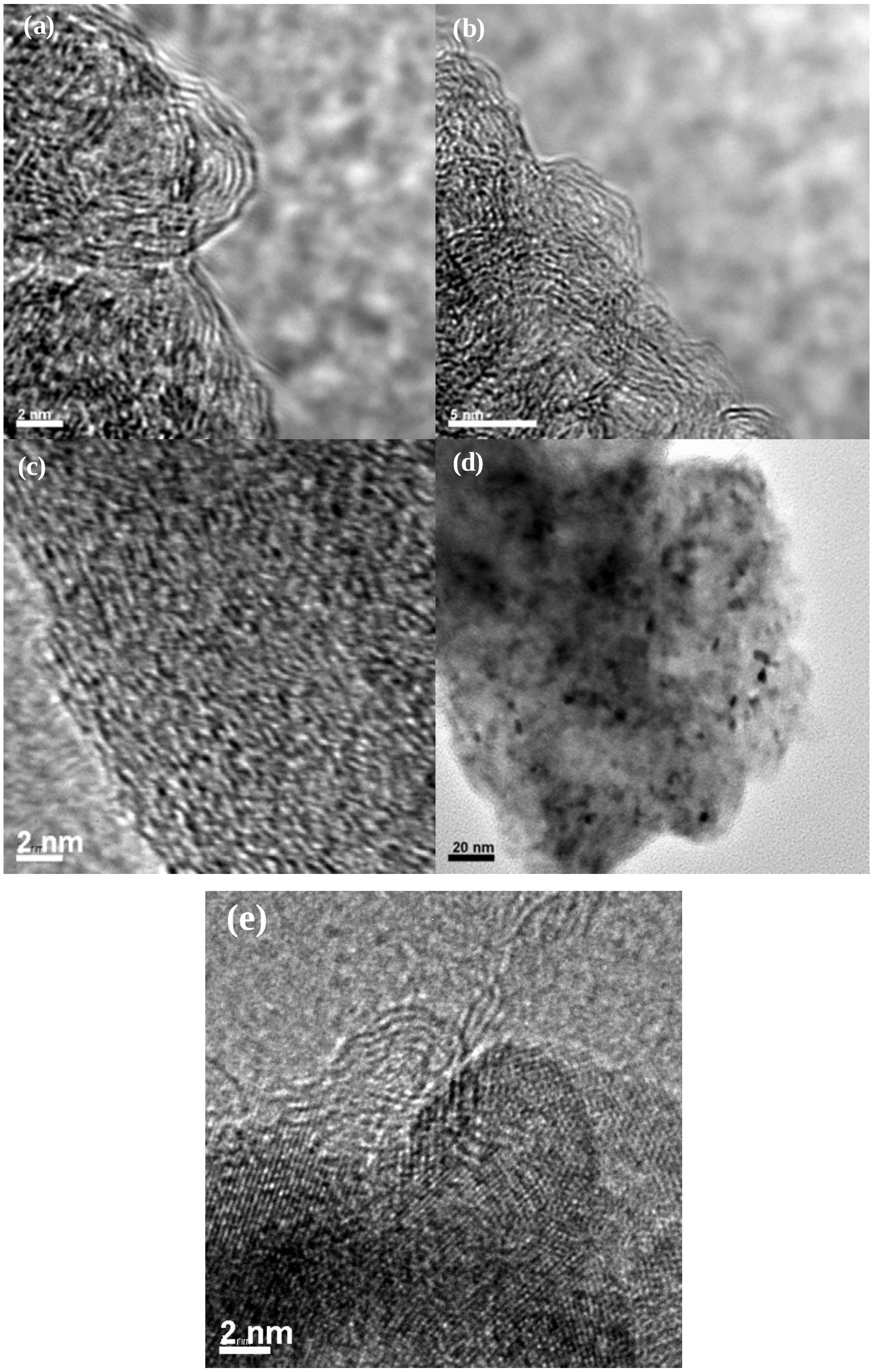

Figure 5.4: HRTEM images of (a) GMC, (b) OGMC, (c) 15 wt% MnO_2/C, and (d), (e) 35 wt% MnO_2/C.

magnification overlapping crystalline lattice planes of the MnO_2 polymorph birnessite are visible along with the graphene layers underneath (Fig. 5.4e). The MnO_2 lattice spacing is measured to be ~2.5 Å in the (006) plane, corresponding well with the XRD (006) plane dimension of 2.44 Å for birnessite (JCPDF#18-0802). This spacing is sufficient for facile transport of Na^+ (0.95 Å)[32] throughout the birnessite lattice. The average crystallite size is estimated to be 3.8 nm, which matches well with the XRD size of 4.2 nm. Thus, HRTEM confirms the XRD result that the graphitic structure in GMC remains in the nanocomposites and the MnO_2 domains are on the order of ~1 nm thickness, presumably a few atomic layers thick.

In addition to HRTEM, the nanocomposites were viewed using STEM and analyzed with EDX (Fig. 5.5). In the STEM mode, Mn with a higher atomic number than C produces a higher intensity. Fig. 5.5a and 5.5b shows the STEM images for the 15 wt% and 35 wt% MnO_2 samples, respectively. The images are both uniformly bright denoting the MnO_2 is dispersed throughout the carbon support. The 35 wt% MnO_2 composite appears brighter in the center where the particle is the thickest than at the edges. To further characterize the dispersion of the MnO_2 within the carbon, EDX analysis was performed on 15 wt% (Fig. 5.5c-e) and 35 wt% (Fig. 5.5f-h) samples. In Fig. 5.5c-h, the K-line energies for Mn, O, and C are represented in red, green, and blue, respectively. The Mn and O intensities correspond well with each other and denote MnO_2. In these areas of high Mn and O intensity, the C intensity is less. For both the 15 wt% and 35 wt% EDX data, the MnO_2 is shown to be uniformly dispersed throughout the carbon support.

Cyclic voltammetry was carried out in 1 M Na_2SO_4 to determine the gravimetric capacitance of the nanocomposites. The shape of the cyclic voltammograms in Fig. 5.6 is characteristic of electric double layer capacitors and MnO_2 redox pseudocapacitors. Relatively flat rectangular-shaped profiles are evident in the scans at 2, 20 and 200 mV/s at all MnO_2 contents even up to 35 wt%. At higher scan rates, the slope of the profiles can increase significantly presumably due to hindered ion and electron transport;[23] however, all of the composites in Fig. 5.6 exhibit high double layer charging profiles with minimal sloping character. The higher scan rates lead accordingly to higher currents as

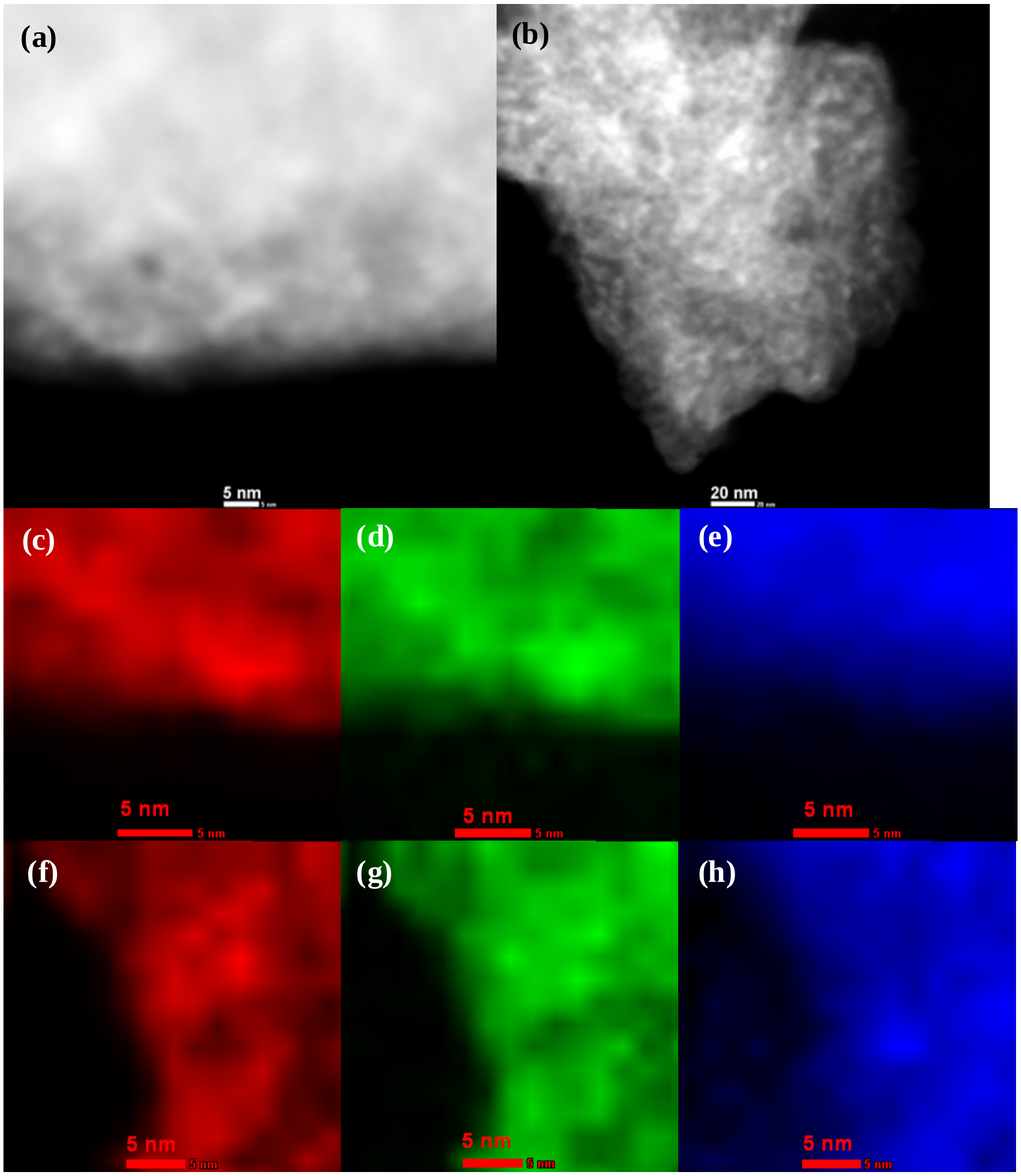

Figure 5.5: STEM images and EDX of (a), (c) Mn, (d) O, (e) C for 15 wt% MnO_2/C and (b), (f) Mn, (g) O, (h) C for 35 wt% MnO_2/C.

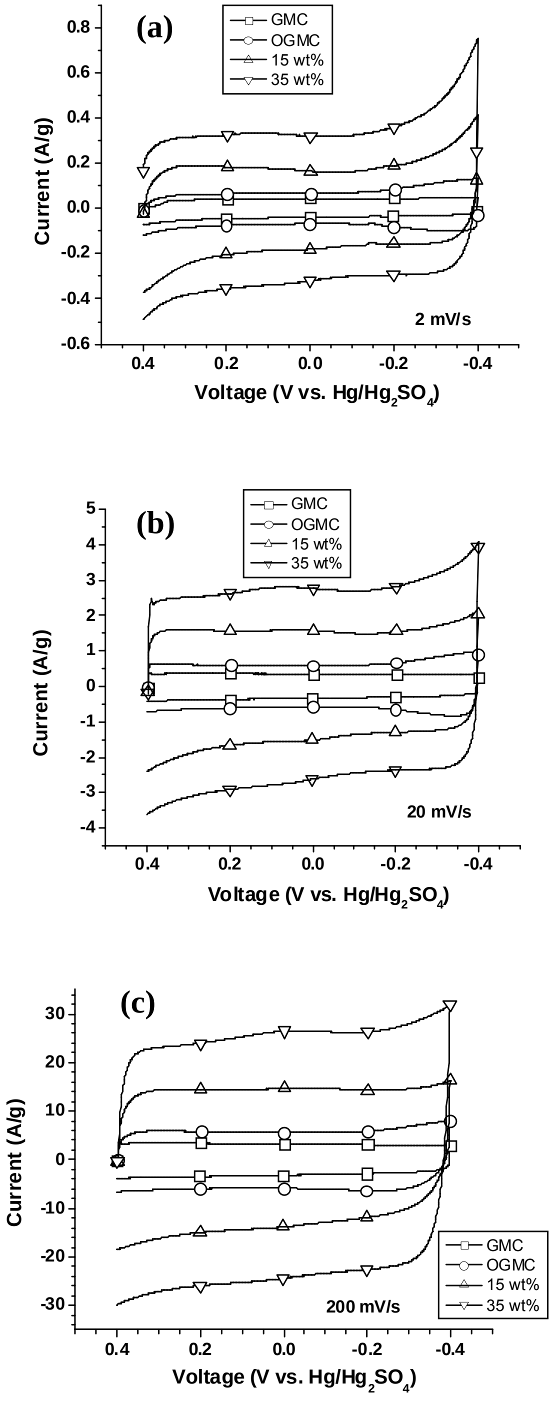

Figure 5.6: Cyclic voltammetry curves in 1 M Na_2SO_4 at scan rates of (a) 2 mV/s, (b) 20 mV/s, and (c) 200 mV/s

the current should scale linearly with scan rate.

Total gravimetric capacitance C_g values were calculated with the following equation

$$C_g = (\Delta I/2)/(\nu m) \tag{5.1}$$

where ΔI is the current difference at 0 V in the two different scanning directions, ν is the scan rate, and m is the mass of active material. The C_g as a function of scan rate is shown in Fig. 5.7a. The C_g of GMC was 21 F/g at 2 mV/s and dropped only a small amount at 200 mV/s. After oxidation of the carbon, the C_g for OGMC increased to 33 F/g at 2 mV/s as the surface area increased. The C_g fade for the OGMC was ~14% at 200 mV/s, indicating any loss in electronic conductivity from oxidation had a minor effect. As MnO_2 was deposited into the carbon, the C_g increased reaching 160 F/g at 2 mV/s at 35 wt%, and 127 F/g at 200 mV/s, an eightfold improvement in C_g compared to the GMC. For the various MnO_2/C nanocomposites and pure carbon supports, the C_g drops by ~10% as the scan rate goes from 2 to 10 mV/s and then only drops by an additional ~10% from 10 to 200 mV/s.

The gravimetric MnO_2 pseudocapacitance contribution is shown in Fig. 5.7b as a function of scan rate. A maximum C_{MnO2} of 500 F/g_{MnO2} is achieved at 2 mV/s for 8.8 wt% MnO_2. At 200 mV/s for 8.8 wt% MnO_2, the C_{MnO2} drops to only 400 F/g_{MnO2}. For all the other MnO_2/C nanocomposites, the C_{MnO2} is 400-450 F/g_{MnO2} at 2 mV/s and drops to 310-340 F/g_{MnO2} at 200 mV/s. These C_{MnO2} values are exceptionally large for the high scan rate of 200 mV/s. Similar to the C_g, the C_{MnO2} drops by ~10% from 2 to 10 mV/s and by ~10% from 10 to 200 mV/s for each composite.

The maximum energy density (E_{max}) of the MnO_2/C nanocomposites can be computed from the C_g values using the equation

$$E_{max} = \tfrac{1}{2} C_{cell} V^2 \tag{5.2}$$

where V is the potential window and taken to be a maximum of 1.2 V, the breakdown of water, and C_{cell} is the device capacitance ($C_g/2$). The GMC has a low energy density of only 2.1 Wh/kg. With the 35 wt% sample, the energy density increases eight-fold to 16 Wh/kg at 2 mV/s. At the highest scan rate of 200 mV/s, the energy density is still 12.7

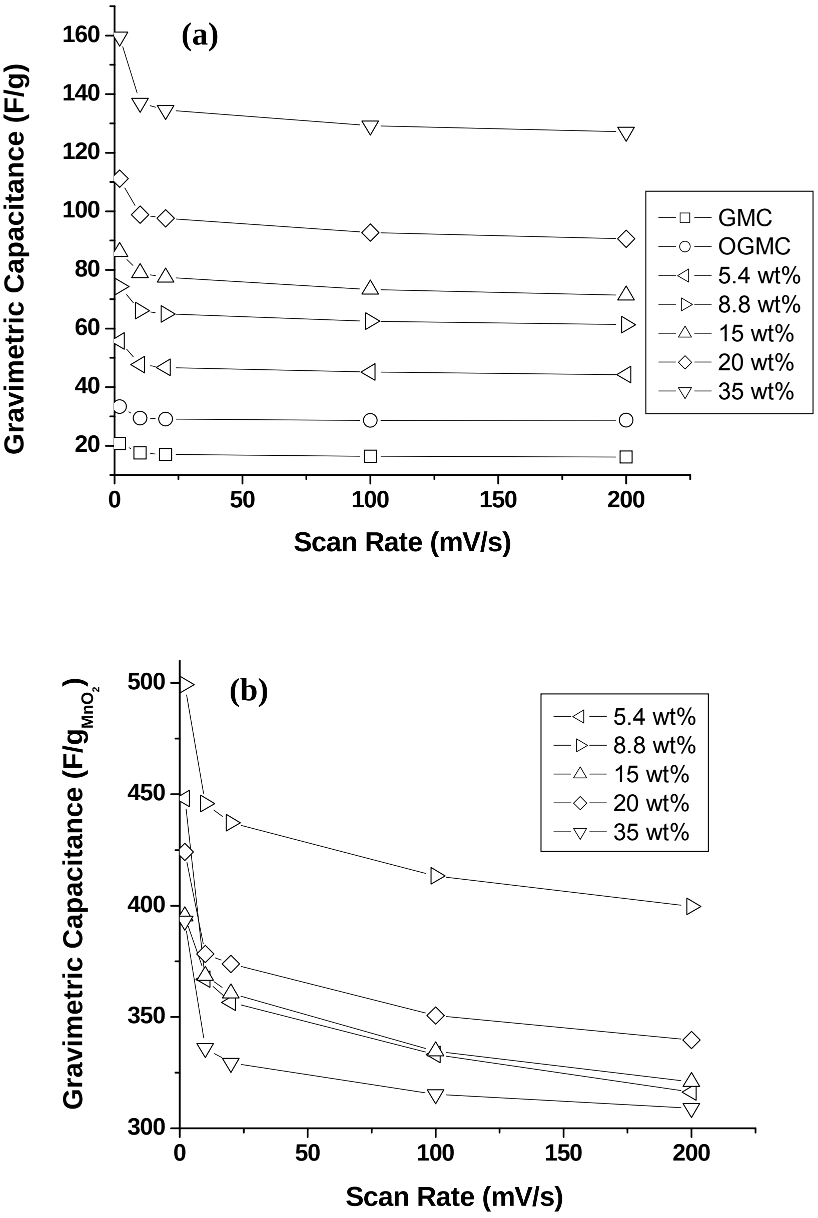

Figure 5.7: Gravimetric capacitance in 1 M Na_2SO_4 based on (a) total mass and (b) MnO_2 mass as a function of scan rate.

Wh/kg. This high energy density begins to approach the values observed for batteries (>10 Wh/kg).[7, 12]

The areal and volumetric capacitances of the samples at 2 mV/s were calculated given the nitrogen sorption data (Table 5.1). For the GMC the areal and volumetric capacitance are 7.9 μF/cm^2 and 24 F/cm^3. Upon oxidation the areal capacity drops marginally to 7.7 μF/cm^2, but the volumetric capacitance increases to 34 F/cm^3, which can be related to the increase in pore volume. Incorporation of MnO_2 at 15 wt% increases the areal capacity by fourfold to 31 μF/cm^2 and the volumetric capacitance by five-fold to 120 F/cm^3. With the 35 wt% MnO_2, the areal and volumetric capacitances increase dramatically to 240 μF/cm^2 and 400 F/cm^3, respectively. These high values result from the low BET surface area and pore volume for the composite at the high loading.

Electrochemical impedance spectroscopy was used to characterize the resistance, response time, and diffusion coefficient of the MnO_2/C nanocomposites. Nyquist plots are shown in Fig. 5.8, which are multiplied by 0.196 cm^2 to normalize with respect to geometric area. The linear slopes indicate that the carbon supports and MnO_2/C nanocomposites exhibit almost purely capacitive behavior at low frequencies (high Z') with a phase angle of ~88°. The Warburg impedance, in the mid-range frequency region is influenced by ion diffusion through the pores of the carbon support.[33] At high frequencies, capacitance is negligible, and resistance is dominant. The resistance can be manifested as a semi-circle or arc; however, these shapes were not present (Fig. 5.8). Thus, the contact resistance between MnO_2/C particles, and the particle-electrode surface were minimal.[1, 34, 35]

The bulk solution resistance (R_Ω), charge transfer resistance (R_{ct}), and diffusional resistance in the pores (R_d) can be extracted from the EIS data. The bulk solution resistance can be found from the real impedance x-intercept of the Nyquist plot at high frequencies.[33, 36] For all of the samples, the bulk solution resistance is ~2 Ω cm^2. This bulk solution resistance is large with the beaker cell configuration used and would be lower for a two electrode setup with a thin electrolyte layer.[19] The charge transfer resistance can be found from a plot of Z' vs. $1/\omega^{1/2}$ where ω is the angular frequency and

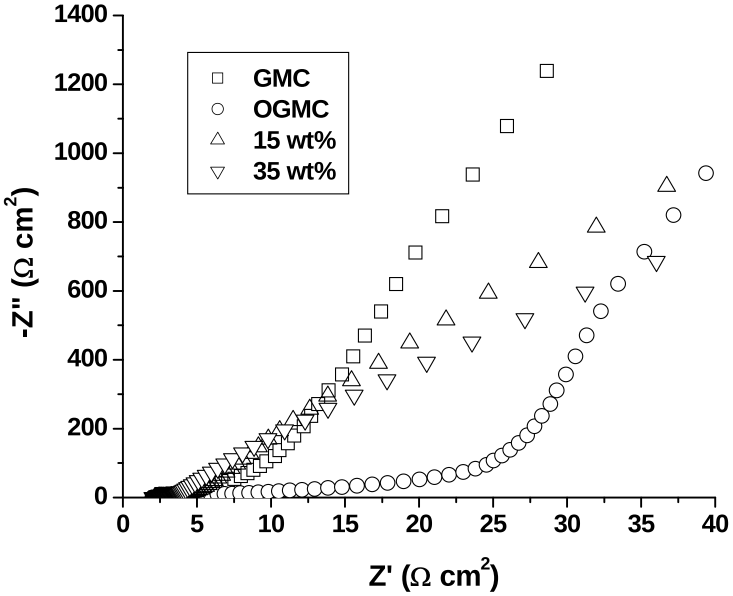

Figure 5.8: Nyquist plots for GMC, OGMC, 15 wt%, and 35 wt% MnO_2/C nanocomposites given with respect to geometric area.

the y-intercept gives $R_{ct} + R_{\Omega}$.[33] For all the samples, the R_{ct} is $<0.2\ \Omega\ cm^2$ indicating charge transfer in the thin MnO_2 domains adds little to the resistance. The R_d, which describes the diffusion of ions in the porous structure, is found from extrapolating the Warburg impedance ($R_d + R_{\Omega}$) at the knee frequency, which is intersection of the Warburg and capacitive branch in the Nyquist plot, to the real impedance axis.[21, 36] Upon subtracting R_{Ω} from the Warburg impedance, the R_d is given in Table 5.2. For the GMC, R_d is very small at $0.20\ \Omega\ cm^2$. For the OGMC, R_d increases by almost 2 orders of magnitude to $23\ \Omega\ cm^2$. With 15 wt% and 35 wt% MnO_2, R_d drops back down to $0.80\ \Omega\ cm^2$ and $1.2\ \Omega\ cm^2$, respectively. The large increase in R_d for the OGMC possibly results from the nitric acid treatment introducing surface functionalities and from poor ion transport through the micropores.[13] The larger R_d for the MnO_2/C nanocomposites compared to GMC results from the narrowing pore size distribution.

The real part of the capacitance can be calculated from the Nyquist plots using the imaginary part of the impedance, Z". The real part of the total gravimetric capacitance, C_g', is given by the equation[37-39]

$$C_g' = 1/(\omega(-Z''(\omega))m) \quad (5.3).$$

The Bode plot is shown in Fig. 5.9. For GMC, C_g' fade with frequency is minimal. With oxidation of the carbon, the higher surface area results in an increased capacitance at low frequencies. However at higher frequencies, the C_g' for OGMC drops below that of the GMC, as a result of the much higher diffusional resistance. With MnO_2 incorporated into carbon support, the increase in the C_g' at low frequencies is similar to that seen from cyclic voltammetry. The C_g' decreases for the MnO_2/C nanocomposites at >1 Hz and converges with the GMC and OGMC C_g' at the highest frequencies. At the highest frequencies, the Faradaic redox process from MnO_2 becomes too slow to contribute to the C_g'.

The dielectric relaxation time constant, τ, of the carbon support and MnO_2/C nanocomposites was computed from the Bode plot of the imaginary capacitance, C_g" (Fig. 5.10). The C_g" is given by[21, 37, 38]

$$C_g'' = Z'(\omega)/(\omega|Z(\omega)|^2 m) \quad (5.4).$$

Table 5.2: Parameters extracted from electrochemical impedance spectroscopy.

Sample	Diffusional resistance (Ω cm^2)	Time constant (s)	Diffusion coefficient (cm^2/s)
GMC	0.20	0.02	2.1×10^{-7}
OGMC	23	1.0	2.1×10^{-8}
15 wt% MnO_2/C	0.80	0.25	2.9×10^{-8}
35 wt% MnO_2/C	1.2	0.40	4.3×10^{-9}

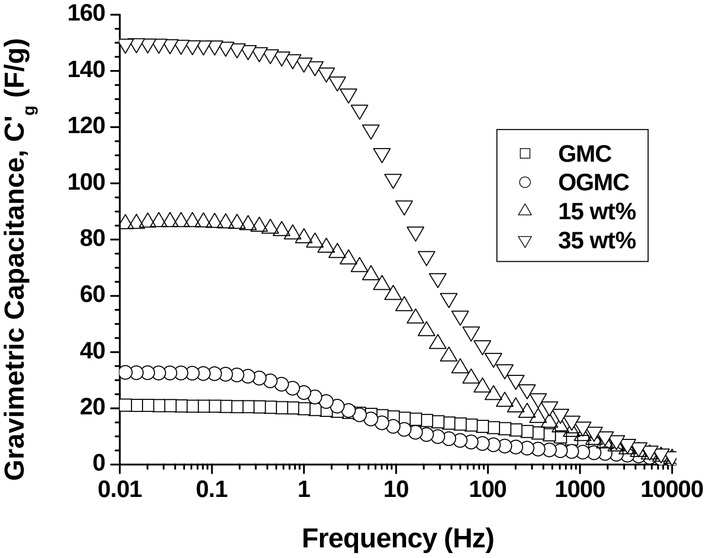

Figure 5.9: Bode plot from the real part of capacitance using EIS data for GMC, OGMC, 15 wt% MnO_2/C and 35 wt% MnO_2/C nanocomposites.

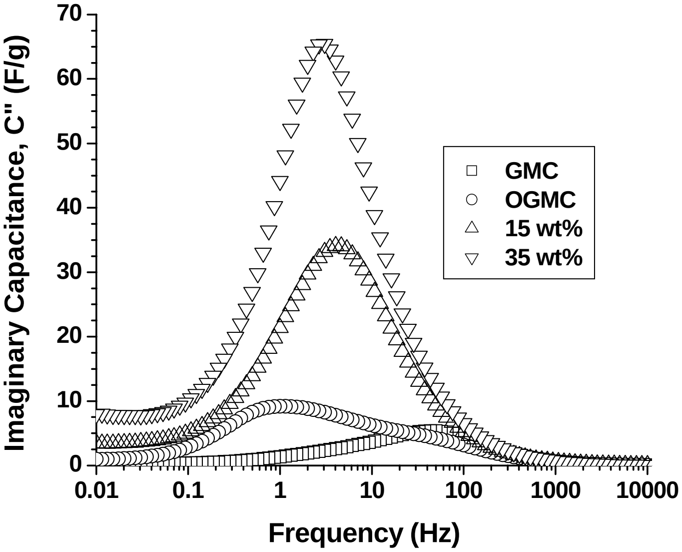

Figure 5.10: Bode plot for the imaginary part of the capacitance to determine dielectric relaxation time constants for GMC, OGMC, 15 wt% MnO_2/C, and 35 wt% MnO_2/C.

The frequency at the maxima of the Bode plot is the inverse of τ (Table 5.2). This τ provides a measure for the speed at which the electrode can discharge (i.e. power density).[21] For GMC, τ is only 0.02 s. With oxidation, it increases to 1.0 s for OGMC, but is only 0.4 s at 35 wt% MnO_2. The τ follow the same trend as for the diffusional resistances with a large τ for OGMC possibly resulting from micropores.[13] Using τ and estimating the diffusion length, L, as the thickness of the electrode film, the diffusion coefficient D of Na^+ (Table 5.2) can be calculated from $D = L^2/\tau$. The D is high at 2.1×10^{-7} cm^2/s for GMC, and decreases about an order of magnitude for OGMC. At 35% MnO_2, the D of 4.3×10^{-8} cm^2/s is still quite high. With MnO_2 added to the porous carbon support, the D decreases slightly since ions must diffuse through the solid MnO_2 layer for redox.

5.4 DISCUSSION

A key advancement of this study over the previous chapter with a 3D mesoporous nanocomposite was the large improvement in the electronic conductivity of the carbon support as a result of the soft-template technique and high heat treatment temperature. Previous studies with MnO_x/carbon composites have utilized primarily hard-templated mesoporous carbon (HMC) supports synthesized using mesoporous silica SBA-15.[22, 23] Fuertes et al. have reported the electronic conductivity for HMC increases by tenfold with an increase of heat treatment temperature from 900 °C (0.30 S/cm) to 2300 °C (4.2 S/cm).[16] Because of the thin carbon filaments of the pore-walls of hard-templated carbons, pore collapse upon graphitization at high temperatures can increase the electronic conductivity only moderately.[24] For HMC supports used for MnO_x/carbon composites that were heat treated at ~900 °C, a low degree of graphitic character was observed via broad XRD peaks for carbon,[22, 23] resulting in an estimated electronic conductivity of ~0.3 S/cm.[16] The GMC support in the current study was synthesized via a soft-template strategy.[26-28] At a low heat treatment temperature (~900 °C), carbons produced by hard- and soft-templates have similar electronic conductivities. However, at high heat treatment temperatures (>2300 °C), the electronic conductivity of 330 S/cm[24] for soft-templated carbons is ~100-fold higher than for hard-templated carbons. The soft-template route leads to stronger pore-wall structures through covalently/hydrogen bonded frameworks and thick pore-walls.[24, 27] The soft-template technique allows for more facile graphitization of the carbon to give higher electronic conductivities at high heat treatment temperatures.

The MnO_2/C nanocomposites were synthesized via a self-limiting redox reaction between the OGMC and potassium permanganate. The carbon support serves as a sacrificial reducing agent for heterogeneous nucleation of MnO_2 on the carbon surface.[40] By varying the reaction time and permanganate to carbon ratio, the MnO_2 loading can be controlled. In neutral pH, the permanganate ions diffuse readily throughout the porous carbon support to form a relatively uniform dispersion of MnO_2 nanodomains.[20, 21] For the as-synthesized GMC, the loadings were <1 wt% MnO_2 as the surface hydrophobicity impeded the aqueous precursor from fully penetrating the pores and wetting the carbon surface. In contrast, loadings of 30 wt% MnO_2 were achieved readily for more wettable hydrophilic amorphous carbons with less graphitic content and more polar oxygenated sites (Chapter 4). In order to facilitate the deposition of MnO_2 onto the hydrophobic GMC carbon, it was first oxidized in nitric acid.[41] The nitric acid dissolved very little of the graphitic carbon while only slightly increasing the surface area, as shown in Table 5.1, consistent with previous studies.[25, 41] Oxidation of the carbon increases the oxygen content (e.g. polar acidic groups) at edge plane sites[2] which aids wetting by the aqueous MnO_2 precursor, resulting in high loadings. Loadings as high as 35 wt% in 0.1 M $KMnO_4$ were achieved on OGMC upon deposition for 24 hours.

The MnO_2 charge storage mechanism occurs via insertion/extraction sodium ions and/or possibly protons via

$$Mn^{IV}O_2 + X^+ + e^- \leftrightarrow Mn^{III}O_2X \tag{5.5}$$

where $X^+ = Na^+$ or H^+. The reaction is sufficiently fast to give a high power density.[3] The relative pseudocapacitive contributions from surface and intercalation capacitance can be estimated from the scan rate dependence with plots of C_{MnO2} vs. $\nu^{-1/2}$ and $(C_{MnO2})^{-1}$ vs. $\nu^{1/2}$, which both show linear behavior (Appendix C, Fig. C.2).[42, 43] At high scan rates, ion diffusion is limited and only surface capacitance contributes, whereas at low scan rates, both surface and intercalation capacitance are present. The surface capacitance can be found from extrapolation of C_{MnO2} to $\nu=\infty$ (i.e. $\nu^{-1/2}=0$), and the total pseudocapacitance can be extrapolated from $\nu=0$ (i.e. $\nu^{1/2}=0$). The ratio of the surface contribution to the total pseudocapacitance is found to be high at 81-88% for all of the composites, which is consistent with the linear dependence between current and ν (Appendix C, Fig. C.3a). The high surface contribution describes the more rapid surface pseudocapacitance, relative to the slower intercalation based charge storage mechanism which is diffusional in nature and would exhibit a linear dependence between current and $\nu^{1/2}$, which is not the case for the composites (Appendix C, Fig. C.3b).[44] The high contribution of surface capacitance is consistent with a recent study of 2-3 nm thick RuO_2 nanoskins.[45] Hence, the high surface pseudocapacitance is given by the high fraction of the Mn atoms on the surface for the extremely small nanodomains (~1 nm) based on nitrogen porosimetry, XRD, and HRTEM characterization.

The effect of the electronic conductivity of the carbon support on C_{MnO2} may be examined by comparing the results for OGMC with the previous chapter on amorphous mesoporous carbon (AMC), with essentially the same disordered pore structure and MnO_2 loading. The C_{MnO2} was similar (~500 F/g_{MnO2}) for AMC and OGMC loaded samples at low loadings and low scan rates (Table 5.3) where the MnO_2 nanodomains are very small. However, with higher loadings and at higher scan rates, the C_{MnO2} is over twofold greater for OGMC supported MnO_2. In the previous chapter, the AMC was graphitized at 850 °C giving a conductivity of only 0.25 S/cm,[24] and the C_{MnO2} fade was >30% going from 2 to 100 mV/s. The Na^+ diffusion coefficient was 4.7×10^{-10} cm^2/s for 30 wt% MnO_2/AMC, as determined from chronoamperometry. Considering the limit or boundary condition where all of the resistance is in the diffusion through MnO_2, for a short time of 0.01 s, the diffusion length would be 22 nm, well above the ~4 nm MnO_2 domains observed in the AMC support. Thus, other resistances were present, in particular, the low electronic conductivity of the carbon support. With GMC, a much more conductive carbon support, the C_{MnO2} fade is only ~20% going from 2 to 100 mV/s (Table 5.3). With a Na^+ diffusion coefficient of 4.3×10^{-9} cm^2/s for 35 wt% MnO_2, the

Table 5.3: Comparison of MnO_2 gravimetric capacitance for MnO_2 modified disordered mesoporous carbon supports in 1 M Na_2SO_4. Amorphous carbon data taken from Chapter 4.

MnO_2/Carbon Composite	C_g, MnO_2 mass (F/g_{MnO2})	
	2 mV/s	100 mV/s
8.4 wt% / Amorphous	507	188
30 wt% / Amorphous	199	137
8.8 wt% / Graphitic	500	413
35 wt% / Graphitic	393	315

diffusion length in MnO_2 would be 66 nm (τ = 0.01 s), far above the ~4 nm MnO_2 domains. Here, the diffusion coefficient is an order of magnitude larger than for the MnO_2/AMC composite. For both the previous AMC and current OGMC nanocomposites, the diffusion coefficient decreases with increased MnO_2 loading, falling by an order of magnitude at the highest MnO_2 loading relative to the pure carbon support. This decrease is caused by a small decrease in pore size upon coating with MnO_2, and more significantly, by slower diffusion through the thicker MnO_2 domains. Given the sufficiently high diffusion lengths in both amorphous and graphitized carbon supported MnO_2 composites, the much higher C_{MnO2} at high scan rates (315-413 F/g_{MnO2}) and lower C_{MnO2} fade with OGMC composites is influenced markedly by the higher electronic conductivity. The high performance results from the fast ion transport in the 3D disordered mesopores and thin, primarily amorphous, MnO_2 nanodomains combined with the high electronic conductivity.

The values of C_{MnO2} on highly conductive GMC are also larger than for manganese oxide nanodomains formed on an ordered amorphous mesoporous carbon support reported recently.[23] Ordered mesoporous carbon supports synthesized via a hard template technique with amorphous MnO_2 nanoparticles embedded in the pore walls were prepared via electroless deposition with $KMnO_4$. Dong et al achieved a highest loading of 26 wt% MnO_2 inside the 3.6 nm pores of the carbon support.[23] At 26 wt% MnO_2, analysis of their CV curve in 2 M KCl in the middle of the current-potential profile gives a C_{MnO2} of 167 F/g_{MnO2} at 5 mV/s, which would drop substantially at higher rates. In the study by Dong et al.[23] and the previous chapter, the lower conductivity of the mesoporous carbons, graphitized at relatively low temperatures (~900 °C), led to lower values of C_{MnO2} at high scan rates and greater C_{MnO2} fade with scan rate, relative to the current study with highly conductive GMC. The current-potential curves for Dong et al. also do not exhibit flat rectangular profiles at 5 mV/s[23] which are seen in the current study for a high scan rate of 200 mV/s, where the C support is more conductive. Furthermore, the larger pore size (~8 nm) of the GMC support allows for high loadings up to 35 wt% MnO_2. The large pore size and disordered pore structure of the GMC provides for more facile electrolyte mass transport throughout the porous support than for mesoporous carbons containing small pore sizes[13] and ordered structure.[7, 46]

3D disordered carbon nanofoams (pore size distribution 1-100 nm) have been used as carbon supports for electroless deposition of MnO_2 particles of size 10-30 nm.[20, 21, 47] A high C_g in 1 M Na_2SO_4 of 130 F/g at 2 mV/s was achieved at 37 wt% MnO_2 with a C_{MnO2} of ~300 F/g_{MnO2}. The dielectric relaxation time constant, τ, for the bare carbon nanofoam was 7.1 s and increased to 80 s with 37 wt% MnO_2. In the current study, τ was much lower at 0.02 s for the GMC and 0.40 s with 35 wt% MnO_2/C. The larger τ for the carbon nanofoam results in part from the lower heat treatment temperature (1000 °C)[21], and consequently, moderately lower electronic conductivity (25-100 S/cm, Marketech, Inc.) compared to the GMC (330 S/cm).[24] From the Bode plots, the drop-off in C_g for the 37 wt% MnO_2/nanofoam is at ~0.02 Hz[21] compared to the higher frequency of ~1 Hz for 35 wt% MnO_2/C in the current study. The higher drop-off frequency is due in part to the higher electronic conductivity. The diffusional resistance for the 37 wt% MnO_2/nanofoam (0.46 Ω cm^2)[21] is lower than for the 35 wt% MnO_2/C (1.2 Ω cm^2) in the current study. The slightly lower diffusional resistance for the nanofoam composite possibly results from the larger macropores present which would aid electrolyte mass transport. The carbon nanofoam supported MnO_2 is a good alternative; however, the higher electronic conductivity and small MnO_2 domain sizes in the present study with GMC supported MnO_2 lead to higher C_{MnO2} at high rates.

Carbonaceous materials such as carbon nanotubes possess high electronic conductivities which are desirable for EDLCs. For instance, CNTs can have conductivities as high as 1000 S/cm, depending on their preparation.[14] Mesoporous carbons have reported electronic conductivities upwards of 330 S/cm[24] as with the GMC support in the current study. As such, designer mesoporous supports offer the benefit of pore walls composed of sp^2 hybridized graphite for high electronic conductivity, as well as tailored pore size, and 3D pore structure. Possibly with further optimization in electronic conductivity and porosity of the carbon support the specific capacitance of MnO_2 can approach the theoretical value of 1370 F/g_{MnO2}.[10]

5.5 CONCLUSIONS

Herein, we have demonstrated high gravimetric pseudocapacitance of ~1 nm thick MnO_2 domains well dispersed in a highly graphitic 3D disordered mesoporous carbon support with high electronic conductivity. Despite the high loading of 35 wt% MnO_2, the C_{MnO2} of 310 F/g_{MnO2} was over twofold larger than amorphous carbon supported MnO_2 at a high scan rate of 200 mV/s. Oxidation of the carbon surface at edge plane sites enabled wetting to achieve deposition of the MnO_2 at high loadings. The soft-template synthesis technique and high heat treatment temperature of 2600 ^{o}C promoted a high degree of graphitization for the carbon support to yield a high electronic conductivity (330 S/cm).[24] Mesoporous supports offer the benefit of highly conductive pore walls composed of sp^2 hybridized graphite domains with high surface area interconnected 3D mesopores. The ~8 nm disordered pores provide sufficient space for thin MnO_2 domains at high loadings along with ion diffusion via multiple flow pathways.[46] The thin MnO_2 nanodomains produce a high C_{MnO2} primarily via a surface redox reaction mechanism at high rates. With rapid electron and ion transfer to the small MnO_2 domains, high C_{MnO2} values are achieved at high rates of 200 mV/s.

5.6 REFERENCES

1. Kotz, R.; Carlen, M., Principles and applications of electrochemical capacitors. *Electrochimica Acta* **2000,** 45, (15-16), 2483-2498.

2. Conway, B. E., *Electrochemical Supercapacitors: Scientific Fundamentals and Technological Applications*. Kluwer Academic/Plenum Publishers: New York, 1999.

3. Simon, P.; Gogotsi, Y., Materials for electrochemical capacitors. *Nature Materials* **2008,** 7, (11), 845-854.

4. Miller, J. R.; Burke, A. F., Electrochemical capacitors: challenges and opportunities for real-world applications. *Electrochemical Society Interface* **2008,** 17, (1), 53-57.

5. Miller, J. R.; Simon, P., Electrochemical Capacitors for Energy Management. *Science (Washington, DC, United States)* **2008,** 321, (5889), 651-652.

6. Arico, A. S.; Bruce, P.; Scrosati, B.; Tarascon, J.-M.; van Schalkwijk, W., Nanostructured materials for advanced energy conversion and storage devices. *Nature Materials* **2005,** 4, (5), 366-377.

7. Rolison, D. R.; Long, J. W.; Lytle, J. C.; Fischer, A. E.; Rhodes, C. P.; McEvoy, T. M.; Bourg, M. E.; Lubers, A. M., Multifunctional 3D nanoarchitectures for energy storage and conversion. *Chemical Society Reviews* **2009,** 38, (1), 226-252.

8. Pang, S.-C.; Anderson, M. A.; Chapman, T. W., Novel electrode materials for thin-film ultracapacitors: comparison of electrochemical properties of sol-gel-derived and electrodeposited manganese dioxide. *Journal of the Electrochemical Society* **2000,** 147, (2), 444-450.

9. Broughton, J. N.; Brett, M. J., Investigation of thin sputtered Mn films for electrochemical capacitors. *Electrochimica Acta* **2004,** 49, (25), 4439-4446.

10. Toupin, M.; Brousse, T.; Belanger, D., Charge Storage Mechanism of MnO2 Electrode Used in Aqueous Electrochemical Capacitor. *Chemistry of Materials* **2004,** 16, (16), 3184-3190.

11. Luo, J.-Y.; Xia, Y.-Y., Effect of pore structure on the electrochemical capacitive performance of MnO2. *Journal of the Electrochemical Society* **2007,** 154, (11), A987-A992.

12. Pandolfo, A. G.; Hollenkamp, A. F., Carbon properties and their role in supercapacitors. *Journal of Power Sources* **2006,** 157, (1), 11-27.

13. Frackowiak, E.; Beguin, F., Carbon materials for the electrochemical storage of energy in capacitors. *Carbon* **2001,** 39, (6), 937-950.

14. Frackowiak, E., Carbon materials for supercapacitor application. *Physical Chemistry Chemical Physics* **2007,** 9, (15), 1774-1785.

15. Obreja, V. V. N., On the performance of supercapacitors with electrodes based on carbon nanotubes and carbon activated material-A review. *Physica E: Low-Dimensional Systems & Nanostructures (Amsterdam, Netherlands)* **2008,** 40, (7), 2596-2605.

16. Fuertes, A. B.; Alvarez, S., Graphitic mesoporous carbons synthesised through mesostructured silica templates. *Carbon* **2004,** 42, (15), 3049-3055.

17. Numao, S.; Judai, K.; Nishijo, J.; Mizuuchi, K.; Nishi, N., Synthesis and characterization of mesoporous carbon nano-dendrites with graphitic ultra-thin walls and their application to supercapacitor electrodes. *Carbon* **2009,** 47, (1), 306-312.

18. Wang, D.-W.; Li, F.; Liu, M.; Lu, G. Q.; Cheng, H.-M., 3D aperiodic hierarchical porous graphitic carbon material for high-rate electrochemical capacitive energy storage. *Angewandte Chemie, International Edition* **2008,** 47, (2), 373-376.

19. Park, S.; Liang, C.; Sheng, D.; Dudney, N.; DePaoli, D., Mesoporous Carbon Materials as Electrodes for Electrochemical Double-Layer Capacitor. *Materials Research Society Symposium Proceedings* **2007,** 973E, (Mobile Energy), No pp given, Paper #: 0973-BB07-04.

20. Fischer, A. E.; Pettigrew, K. A.; Rolison, D. R.; Stroud, R. M.; Long, J. W., Incorporation of Homogeneous, Nanoscale MnO2 within Ultraporous Carbon Structures via Self-Limiting Electroless Deposition: Implications for Electrochemical Capacitors. *Nano Letters* **2007,** 7, (2), 281-286.

21. Fischer, A. E.; Saunders, M. P.; Pettigrew, K. A.; Rolison, D. R.; Long, J. W., Electroless deposition of nanoscale MnO2 on ultraporous carbon nanoarchitectures: correlation of evolving pore-solid structure and electrochemical performance. *Journal of the Electrochemical Society* **2008,** 155, (3), A246-A252.

22. Zhang, L. L.; Wei, T.; Wang, W.; Zhao, X. S., Manganese oxide-carbon composite as supercapacitor electrode materials. *Microporous and Mesoporous Materials* **2009,** 123, (1-3), 260-267.

23. Dong, X.; Shen, W.; Gu, J.; Xiong, L.; Zhu, Y.; Li, H.; Shi, J., MnO2-Embedded-in-Mesoporous-Carbon-Wall Structure for Use as Electrochemical Capacitors. *Journal of Physical Chemistry B* **2006,** 110, (12), 6015-6019.

24. Shanahan, P. V.; Xu, L.; Liang, C.; Waje, M.; Dai, S.; Yan, Y. S., Graphitic mesoporous carbon as a durable fuel cell catalyst support. *Journal of Power Sources* **2008,** 185, (1), 423-427.

25. Kinoshita, K., *Carbon: Electrochemical and Physicochemical Properties*. Wiley-Interscience: New York, 1988.

26. Liang, C.; Li, Z.; Dai, S., Mesoporous carbon materials: synthesis and modification. *Angewandte Chemie, International Edition* **2008,** 47, (20), 3696-3717.

27. Liang, C.; Dai, S., Synthesis of Mesoporous Carbon Materials via Enhanced Hydrogen-Bonding Interaction. *Journal of the American Chemical Society* **2006,** 128, (16), 5316-5317.

28. Wang, X.; Liang, C.; Dai, S., Facile Synthesis of Ordered Mesoporous Carbons with High Thermal Stability by Self-Assembly of Resorcinol-Formaldehyde and Block Copolymers under Highly Acidic Conditions. *Langmuir* **2008,** 24, (14), 7500-7505.

29. Gregg, S. J.; Sing, K. S. W., *Adsorption, Surface Area and Porosity*. 2nd ed.; 1982; p 303 pp.

30. Lei, Y.; Fournier, C.; Pascal, J.-L.; Favier, F., Mesoporous carbon-manganese oxide composite as negative electrode material for supercapacitors. *Microporous and Mesoporous Materials* **2008,** 110, (1), 167-176.

31. Gaillot, A.-C.; Flot, D.; Drits, V. A.; Manceau, A.; Burghammer, M.; Lanson, B., Structure of Synthetic K-rich Birnessite Obtained by High-Temperature Decomposition of KMnO4. I. Two-Layer Polytype from 800 DegC Experiment. *Chemistry of Materials* **2003,** 15, (24), 4666-4678.

32. Devaraj, S.; Munichandraiah, N., Effect of Crystallographic Structure of MnO2 on Its Electrochemical Capacitance Properties. *Journal of Physical Chemistry C* **2008,** 112, (11), 4406-4417.

33. Brett, C. M. A.; Brett, A. M. O., *Electrochemistry: Principles, Methods, and Applications*. Oxford University Press: Oxford, 1993.

34. Bordjiba, T.; Belanger, D., Direct Redox Deposition of Manganese Oxide on Multiscaled Carbon Nanotube/Microfiber Carbon Electrode for Electrochemical Capacitor. *Journal of the Electrochemical Society* **2009,** 156, (5), A378-A384.

35. Ruiz, V.; Blanco, C.; Santamaria, R.; Ramos-Fernandez, J. M.; Martinez-Escandell, M.; Sepulveda-Escribano, A.; Rodriguez-Reinoso, F., An activated carbon monolith as an electrode material for supercapacitors. *Carbon* **2009,** 47, (1), 195-200.

36. Bard, A. J.; Faulkner, L. R., *Electrochemical Methods: Fundamentals and Applications*. 2nd ed.; John Wiley & Sons, Inc.: 2001.

37. Taberna, P. L.; Simon, P.; Fauvarque, J. F., Electrochemical characteristics and impedance spectroscopy studies of carbon-carbon supercapacitors. *Journal of the Electrochemical Society* **2003,** 150, (3), A292-A300.

38. Portet, C.; Taberna, P. L.; Simon, P.; Flahaut, E.; Laberty-Robert, C., High power density electrodes for Carbon supercapacitor applications. *Electrochimica Acta* **2005,** 50, (20), 4174-4181.

39. Portet, C.; Yushin, G.; Gogotsi, Y., Electrochemical performance of carbon onions, nanodiamonds, carbon black and multiwalled nanotubes in electrical double layer capacitors. *Carbon* **2007,** 45, (13), 2511-2518.

40. Ma, S.-B.; Lee, Y.-H.; Ahn, K.-Y.; Kim, C.-M.; Oh, K.-H.; Kim, K.-B., Spontaneously Deposited Manganese Oxide on Acetylene Black in an Aqueous Potassium Permanganate Solution. *Journal of the Electrochemical Society* **2006,** 153, (1), C27-C32.

41. Jia, N.; Martin, R. B.; Qi, Z.; Lefebvre, M. C.; Pickup, P. G., Modification of carbon supported catalysts to improve performance in gas diffusion electrodes. *Electrochimica Acta* **2001,** 46, (18), 2863-2869.

42. Ardizzone, S.; Fregonara, G.; Trasatti, S., "Inner" and "outer" active surface of ruthenium dioxide electrodes. *Electrochimica Acta* **1990,** 35, (1), 263-7.

43. Zolfaghari, A.; Ataherian, F.; Ghaemi, M.; Gholami, A., Capacitive behavior of nanostructured MnO2 prepared by sonochemistry method. *Electrochimica Acta* **2007,** 52, (8), 2806-2814.

44. Liu, T. C.; Pell, W. G.; Conway, B. E.; Roberson, S. L., Behavior of molybdenum nitrides as materials for electrochemical capacitors. *Journal of the Electrochemical Society* **1998,** 145, (6), 1882-1888.

45. Chervin, C. N.; Lubers, A. M.; Pettigrew, K. A.; Long, J. W.; Westgate, M. A.; Fontanella, J. J.; Rolison, D. R., Making the Most of a Scarce Platinum-Group Metal: Conductive Ruthenia Nanoskins on Insulating Silica Paper. *Nano Letters* **2009,** 9, (6), 2316-2321.

46. Rolison, D. R., Catalytic nanoarchitectures - The importance of nothing and the unimportance of periodicity. *Science (Washington, DC, United States)* **2003,** 299, (5613), 1698-1702.

47. Fischer, A. E.; Long, J. W., Redox deposition of nanoscale MnO2 on ultraporous carbon nanoarchitectures: correlation of MnO2 deposition time and electrochemical performance. *ECS Transactions* **2007,** 3, (37, Electrochemical Capacitors 2006), 61-66.

Chapter 6

Conclusions and Recommendations

6.1 CONCLUSIONS

6.1.1 Charging Mechanism of Carbon Black Particles in Low-Permittivity Media

Electrophoretic mobilities of highly absorbing carbon black particles in concentrated dispersions at 1 wt% were measured using differential-phase optical coherence tomography (DP-OCT) with sufficient spectrogram intensities for facile analysis. An advantage of the narrow electrode spacing (0.18 mm) in DP-OCT is that higher strength electric fields, needed to measure the small mobilities in the low-permittivity solvent accurately, may be realized at lower absolute potentials. Zeta potentials in the range of -24 mV to -12 mV were measured for surfactant concentrations from 1 mM to 100 mM AOT-toluene. The electrostatic charging mechanism of the carbon black particles depends on the preferential partitioning of sodium cations between the hydrated reverse micelles in the double-layer and the adsorbed surfactant on the particle surface. At low concentrations the cations prefer the larger, more hydrated reverse micelles resulting in more negative zeta potentials, whereas at high concentrations the cations partition towards the increasingly hydrated surfactant-laden particle surface and lower the magnitude of the particle charge.

6.1.2 Electrophoretic Deposition of Au Nanocrystals inside a Mesoporous TiO_2 Film

Small charged Au nanocrystals of ~3.1 nm in a low-permittivity solvent were electrophoretically deposited into ordered mesoporous TiO_2 films on ITO/glass electrodes, with loadings up to 21 wt%. The loadings were not limited kinetically in 10 min relative to 20 h, indicating that the open geometry of the mesochannels is beneficial for diffusion of the nanocrystals. The Au nanocrystals are highly dispersed throughout the mesopores with only a small fraction (~0.3 wt%) occupying the top planar surface of the film. The relatively small potential drop (~0.05 V) across the non-conducting film is beneficial for electrophoretic deposition of Au nanocrystals. Both variable angle spectroscopic ellipsometry measurements of the anisotropy of the imaginary refractive index, k, and XPS depth profiling studies indicated that Au nanocrystals were dispersed within the vertically aligned mesopores and distributed throughout the film. Presumably, the high coverage of the strongly-bound thiol ligands on the Au nanocrystals weakens the Au/TiO_2 interactions, leading to low loadings of <5 wt% Au. Therefore, electrophoresis is beneficial for increasing the concentration of nanocrystals near the pore openings of the film, enhancing the thermodynamic driving force for adsorption of Au nanocrystals upon mesoporous TiO_2 with high loadings.

6.1.3 Hybrid MnO_2/Mesoporous Carbon Composites for Redox Pseudocapacitors

Composites formed by electroless deposition of redox-active MnO_2 nanoparticles in disordered mesoporous carbon were tested as electrochemical capacitors. The MnO_2 pseudocapacitance augmented the electric double-layer capacitance of the carbon support to give a high gravimetric capacitance composite. Enhancements of threefold and eightfold in gravimetric capacitance were achieved with amorphous (AMC) and graphitic (GMC) carbon supports, respectively, at high loadings of MnO_2. A high loading of 30 wt% MnO_2 was achieved in the AMC, whereas oxidation of the GMC was required to achieve a loading of 35 wt% MnO_2. Hence, the wettability of the aqueous MnO_2 precursor on the carbon support is crucial in attaining high loadings of MnO_2. AMC, which contains more oxygen functional groups, is easily wet inside the pores, whereas GMC must be oxidized to introduce these oxygen functionalities for deposition of MnO_2. The ~8 nm pores of the carbon supports allow for enough space for ~1 nm thick MnO_2 domains to be formed throughout the support while still preserving open mesopores to facilitate ion transport. High MnO_2 pseudocapacitances of >500 F/g_{MnO2} were measured at low loadings (<10 wt%) and low scan rate of 2 mV/s for both supports. At these conditions, both electrons and ions have sufficient time to move through the carbon support and pores for redox of the MnO_2 domains. However, at high loadings of ≥30 wt% MnO_2 and high scan rate of ≥100 mV/s, the effects of the higher electronic conductivity of the GMC are more evident with MnO_2/GMC giving more than twofold higher MnO_2 pseudocapacitance, relative to MnO_2/AMC. Heat treatment at 2600 °C for the GMC resulted in a ~1000x increase in electronic conductivity, compared to heat treatment at 850 °C for the AMC.[1] Since sodium ion diffusion was facile through both supports, the higher MnO_2 pseudocapacitance for MnO_2/GMC is attributed to its much higher electronic conductivity. Mesoporous supports with highly conductive pore walls composed of graphene and high surface area interconnected 3D mesopores offer the potential for synthesizing novel nanocomposites for high MnO_2 pseudocapacitance. The high MnO_2 pseudocapacitance of these nanodomains at high scan rates is a significant advancement towards the ultimate goal of high energy and power densities for electrochemical capacitors with thin conformal coatings of MnO_2.

6.2 RECOMMENDATIONS

6.2.1 Electrophoretic Mobilities of Metal Nanocrystals

Differential phase optical coherence tomography (DP-OCT) has been successfully used to measure electrophoretic mobilities of highly scattering TiO_2(Smith, 2007) and highly absorbing carbon black colloids in this dissertation. These colloids were relatively large with ~200 nm diameters. It would be of interest to extend the domain of DP-OCT to measure 3 to 100 nm diameter nanoparticles. Many nanoparticles are synthesized in nonaqueous solvents,[2] which makes DP-OCT ideal for measuring the low expected mobilities. Mobilities of Au and PbSe nanocrystals dispersed in chloroform with various surfactants have been measured showing charges of one or two electronic charges per nanocrystal.[3, 4] Further study of charged nanocrystal dispersions would beneficial for nanoparticle assemblies and nanocomposite formation.

6.2.2 Conductive Carbon Supports and Crystalline MnO_2 for Redox Pseudocapacitors

Further research can be done on hybrid MnO_2/carbon composites to understand the MnO_2 pseudocapacitance behavior to reach the theoretical value of 1370 F/g_{MnO2}.[5] As shown herein the electronic conductivity of the carbon support can have a large effect on the pseudocapacitance at high scan rates. Hence one route would be to find ways to further increase the electronic conductivity of the carbon support to facilitate electron transport to the MnO_2 domains to enhance the redox reactions. An alternative would be to change the crystallinity of the MnO_2 domains. Herein, the MnO_2 domains were primarily amorphous given the low annealing temperature of the composite. Increasing the temperature would induce crystallization of the MnO_2 possibly leading to more facile ion and electron diffusion through the MnO_2. Presynthesis of MnO_2 nanocrystals followed by infusion into mesoporous carbon can also be done to control the MnO_2 crystallinity, morphology, and size. The electrolyte in the current study is also known to give a lower capacitance compared to other, more basic electrolytes.[6] Hence, switching to more a more basic electrolyte such as KOH would lead to improved ion penetration through the pores and MnO_2 to give higher pseudocapacitance. Varying the MnO_2 deposition method also would lead to different crystalline formations and the possibility to precisely form a ~1 nm thin conformal coating throughout the porous carbon support.

6.2.3 Mixed Metal Oxides on Mesoporous Carbon Supports for Redox Pseudocapacitors

Other transition metal oxides show redox-active pseudocapacitive behavior similar to MnO_2. These include oxides of Ru, Mo, Fe, V, Cr, W, Ir, Ni, and Co to name a few.[7-10] Relatively few studies have looked at combinations of these metal oxides to see the effects of cascading redox reactions for pseudocapacitors. By using mixed metal oxides, multiple oxidation states can exist, increasing the charge storage capacity. Combining these mixed metal oxides, which intrinsically could possess high electronic conductivity, with a 3D high surface area pore architecture would further enhance the energy density of these pseudocapacitive materials.

6.3 REFERENCES

1. Shanahan, P. V.; Xu, L.; Liang, C.; Waje, M.; Dai, S.; Yan, Y. S., Graphitic mesoporous carbon as a durable fuel cell catalyst support. *Journal of Power Sources* **2008,** 185, (1), 423-427.

2. Murray, C. B.; Kagan, C. R.; Bawendi, M. G., Synthesis and characterization of monodisperse nanocrystals and close-packed nanocrystal assemblies. *Annual Review of Materials Science* **2000,** 30, 545-610.

3. Shevchenko, E. V.; Talapin, D. V.; Kotov, N. A.; O'Brien, S.; Murray, C. B., Structural diversity in binary nanoparticle superlattices. *Nature (London, United Kingdom)* **2006,** 439, (7072), 55-59.

4. Zheng, N.; Fan, J.; Stucky, G. D., One-Step One-Phase Synthesis of Monodisperse Noble-Metallic Nanoparticles and Their Colloidal Crystals. *Journal of the American Chemical Society* **2006,** 128, (20), 6550-6551.

5. Toupin, M.; Brousse, T.; Belanger, D., Charge Storage Mechanism of MnO2 Electrode Used in Aqueous Electrochemical Capacitor. *Chemistry of Materials* **2004,** 16, (16), 3184-3190.

6. Xie, X.; Gao, L., Characterization of a manganese dioxide/carbon nanotube composite fabricated using an in situ coating method. *Carbon* **2007,** 45, (12), 2365-2373.

7. Hu, C.-C.; Tsou, T.-W., The optimization of specific capacitance of amorphous manganese oxide for electrochemical supercapacitors using experimental strategies. *Journal of Power Sources* **2003,** 115, (1), 179-186.

8. Simon, P.; Gogotsi, Y., Materials for electrochemical capacitors. *Nature Materials* **2008,** 7, (11), 845-854.

9. Kotz, R.; Carlen, M., Principles and applications of electrochemical capacitors. *Electrochimica Acta* **2000,** 45, (15-16), 2483-2498.

10. Conway, B. E., *Electrochemical Supercapacitors: Scientific Fundamentals and Technological Applications*. Kluwer Academic/Plenum Publishers: New York, 1999.

Appendix A

Au Nanocrystals in Mesoporous TiO_2 Films

These figures and tables relate to Au nanocrystals electrophoretically deposited inside mesoporous TiO_2 films, as described in Chapter 3.

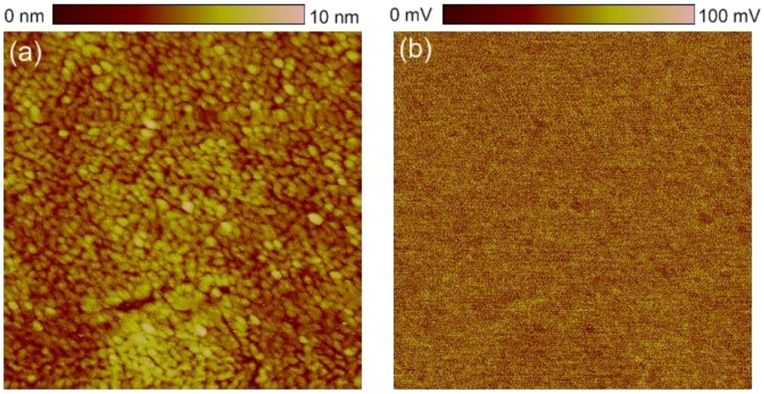

Figure A.1: (a) 500 x 500 nm AFM topography image of TiO_2 thin film. (b) 500 x 500 nm surface potential image of (a) shows no significant potential differences between pillars and pores.

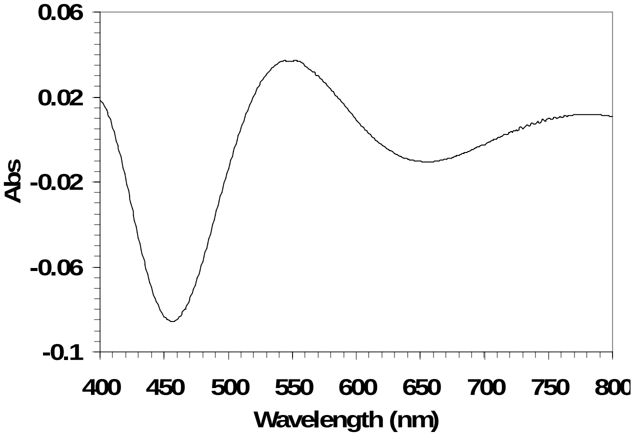

Figure A.2: UV–vis spectroscopy of mesoporous TiO_2 film on ITO/glass with “waves” resulting from the interference of multiple interfaces (TiO_2/ITO/glass).

Table A.1: Fit parameters for x/y axis of Au/TiO_2 nanocomposite, e_1= 1.95.

Oscillator	Amplitude	Center Energy	Broadening	Band Gap
T-L	142.68	3.98	1.27	3.52
Gauss. 1	1.91	7.90	5.16	N/A
Gauss. 2	0.14	2.24	0.37	N/A
Drude	1.56	N/A	0.76	N/A

Table A.2: Fit parameters for z axis of Au/TiO_2 nanocomposite, e_1=1.23.

Oscillator	Amplitude	Center Energy	Broadening	Band Gap
T-L	287.09	3.98	1.76	3.52
Gauss. 1	0.65	7.90	6.02	N/A
Drude	9.31	N/A	1.35	N/A

Appendix B

MnO_2/Amorphous Mesoporous Carbon Composites for Electrochemical Capacitors

These figures and tables relate to MnO_2/amorphous mesoporous carbon (AMC) composites for electrochemical capacitors, as described in Chapter 4.

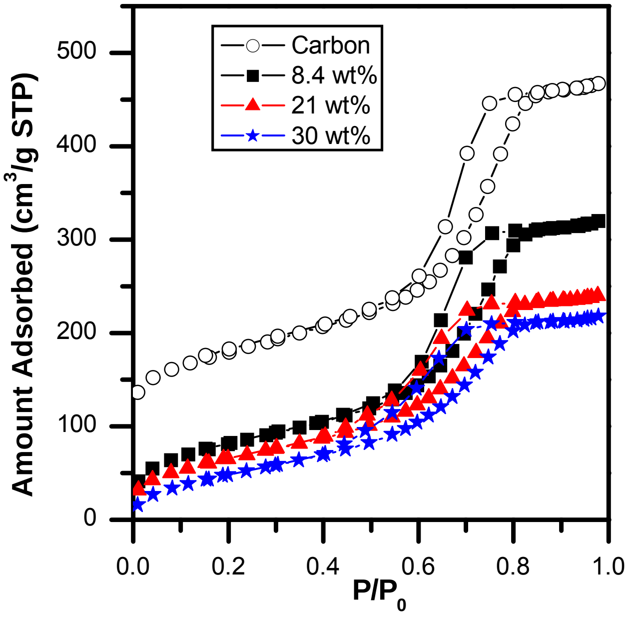

Figure B.1: Nitrogen sorption isotherms for amorphous mesoporous carbon and MnO_2/AMC nanocomposites for various compositions.

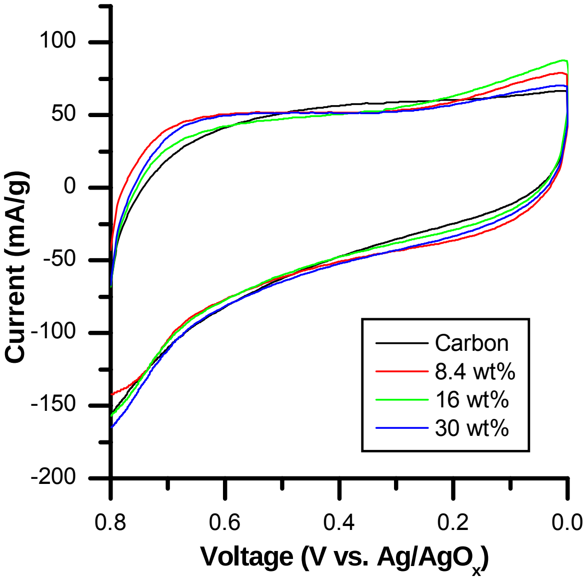

Figure B.2: Cyclic voltammetry of the mesoporous carbon and MnO_2/AMC nanocomposite for various compositions at 2 mV/s in 0.5 M $TBAClO_4$ in PC.

Table B.1: SEM EDX and TGA values for MnO_2 content (wt%) in nanocomposites.

SEM EDX	TGA
2	4.1
8.4	9.9
16	16
21	24
30	35

Table B.2: Gravimetric capacitance values at various scan rates for mesoporous carbon and MnO_2/C nanocomposites in 1 M Na_2SO_4.

MnO_2 Content (wt%)	Gravimetric Capacitance, total mass (F/g)					Gravimetric Capacitance, MnO_2 mass (F/g_{MnO2})			
	2 mV/s	10 mV/s	50 mV/s	100 mV/s		2 mV/s	10 mV/s	50 mV/s	100 mV/s
0	28	25	21	19					
2	38	33	27	25		563	405	361	299
8.4	68	50	39	33		507	319	238	188
16	75	55	45	39		327	215	177	148
21	77	64	54	45		266	214	181	148
30	79	73	63	54		199	185	164	137

Table B.3: Gravimetric capacitance values for mesoporous carbon and MnO_2/C nanocomposites for various compositions based on total mass at 2 mV/s in 0.5 M $TBAClO_4$ in PC.

MnO_2 content (wt%)	Gravimetric capacitance (F/g)
0	26
8.4	26
16	25
30	26

Appendix C

MnO_2/Graphitic Mesoporous Carbon Composites for Electrochemical Capacitors

These figures relate to MnO_2/graphitic mesoporous carbon (GMC) composites for electrochemical capacitors, as described in Chapter 5.

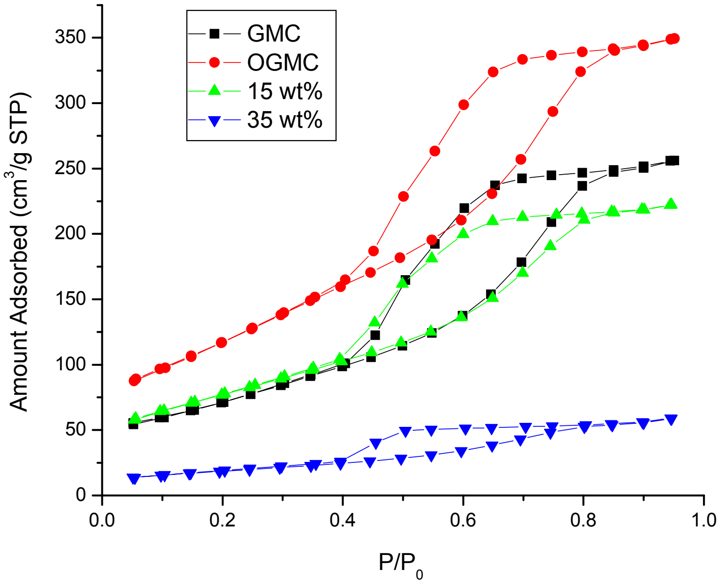

Figure C.1: Nitrogen sorption isotherms for GMC, OGMC, 15 wt% MnO_2/C, and 35% MnO_2/C.

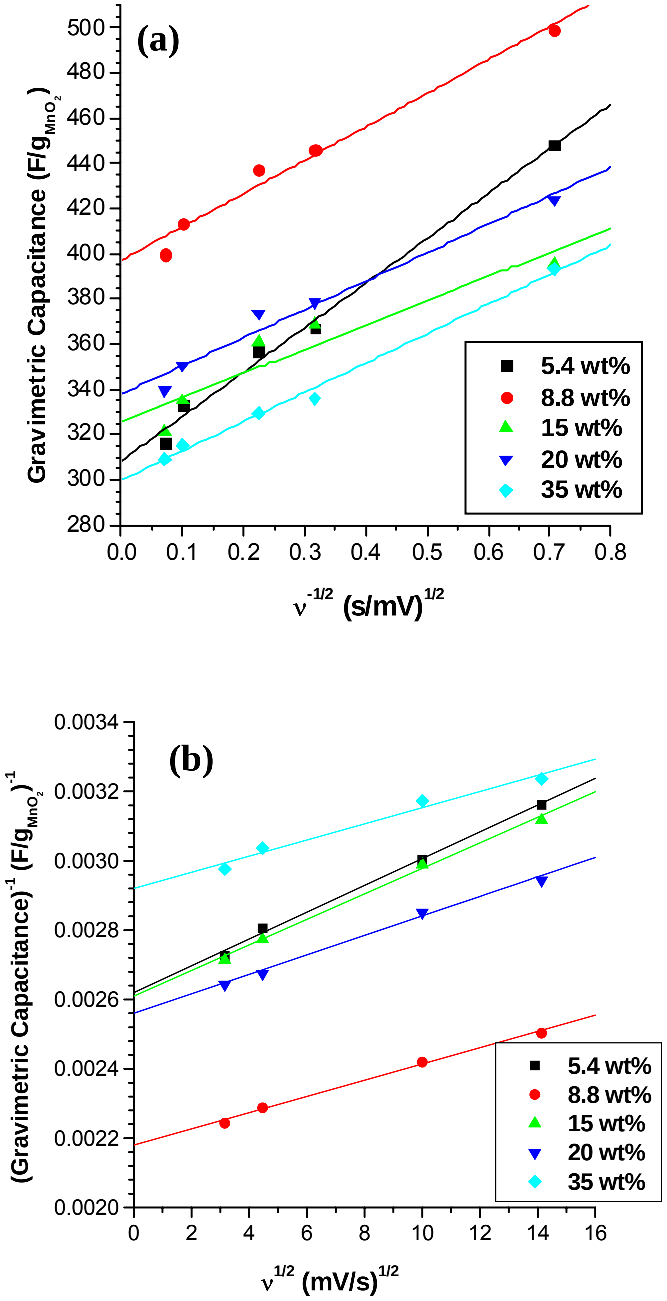

Figure C.2: Linear dependence of (a) C_{MnO2} with $\nu^{-1/2}$ and (b) $(C_{MnO2})^{-1}$ with $\nu^{1/2}$ to determine the surface contribution to pseudocapacitance compared to the total capacitance.

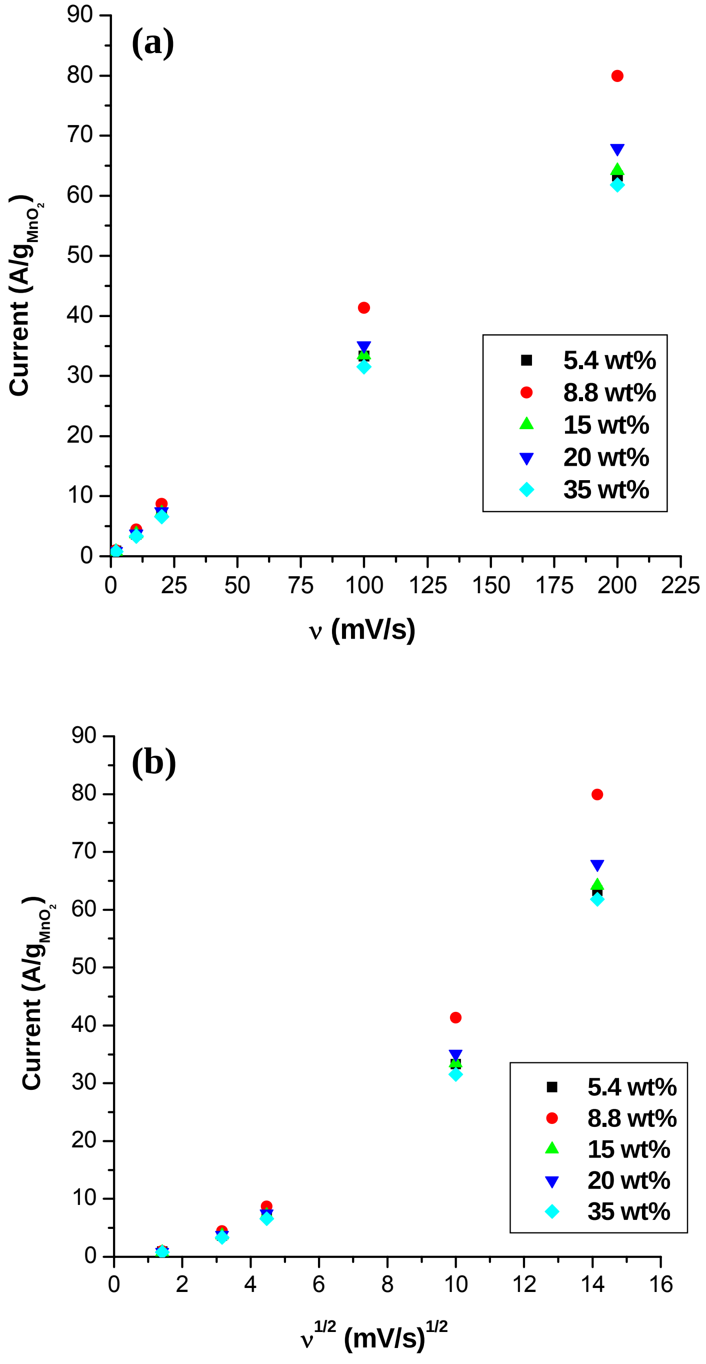

Figure C.3: (a) Linear dependence of current with ν and (b) nonlinear behavior of current with $\nu^{1/2}$ indicating that the capacitance is based on a surface mechanism and is not diffusion limited.

Appendix D

MnO_2/Carbon Nanocomposites using Various Carbon Supports for Electrochemical Capacitors

This appendix contains experimental details and results for two more carbon supports used in the formation of MnO_2/C composites tested for electrochemical capacitors. One support is a small pore disordered amorphous mesoporous carbon support (SMC) with a mean pore size of ~3.8 nm. The other support is an ordered amorphous mesoporous carbon support (OMC) with a mean pore size of ~7.4 nm.

D.1 EXPERIMENTAL SECTION

D.1.1 Materials

All chemicals were used as received. Sodium sulfate (>99%) was acquired from Sigma-Aldrich Cooperation, and potassium permanganate and ethanol (Absolute 200 proof) from Fisher Scientific. High purity deionized water (resistance ~18 MΩ-cm) was used. Argon (research grade, 99.999% purity) was purchased from Praxair.

D.1.2 Small Pore Disordered Amorphous Mesoporous Carbon (SMC) Synthesis

In a typical synthesis,[1] 1.1 g of resorcinol and 0.77 g of F87 were dissolved in 4.5 mL of EtOH and 4.5 mL of HCl aqueous solution (3.0 M). To this solution, 1.3 g of formaldehyde (37%) was then added. After stirring for about 11 min at room temperature, the clear mixture turned turbid, indicating the formation of RF-F87 nanocomposite and a phase separation. The polymer-rich gel phase was obtained by centrifugation at 9500 rpm for 4 min after the mixture was stirred for 40 min. The gel was then loaded on a large Petri dish, dried at room temperature overnight, and subsequently cured at 80 °C and 120 °C for 24 h each. Carbonization was carried out under N_2 atmosphere at 400 °C for 2 h with a heating rate of 1 °C/min, which was followed by further treatment at 850 °C for 3 h with a heating rate of 5 °C/min.

D.1.3 Ordered Mesoporous Carbon (OMC) Synthesis

In a typical synthesis,[2] 1.1 g of resorcinol and 1.1 g of F127 were dissolved in 4.5 mL of EtOH and 4.5 mL of HCl aqueous solution (3.0 M). To this solution, 1.3 g of formaldehyde (37%) was then added. After stirring for about 11 min at room temperature, the clear mixture turned turbid, indicating the formation of RF-F127 nanocomposite and a phase separation. The polymer-rich gel phase was obtained by centrifugation at 9500 rpm for 4 min after the mixture was stirred for 40 min. The gel was then loaded on a large Petri dish, dried at room temperature overnight, and subsequently cured at 80 °C and 120 °C for 24 h each. Carbonization was carried out under N_2 atmosphere at 400 °C for 2 h with a heating rate of 1 °C/min, which was followed by further treatment at 850 °C for 3 h with a heating rate of 5 °C/min.

D.1.4 Preparation of MnO_2/SMC Composites

30 mg of SMC was mixed with 10 mL of aqueous $KMnO_4$ solution of known concentration ranging from 0.001 M to 0.1 M and mixed for 10 min to 24 hrs. The solution was filtered and washed with DI water to remove un-reacted $KMnO_4$. The MnO_2/SMC nanocomposite was subsequently calcined in air at 100 °C overnight.

D.1.5 Preparation of MnO_2/OMC Composites

30 mg of OMC was mixed with 10 mL of aqueous $KMnO_4$ solution of known concentration ranging from 0.001 M to 0.1 M and mixed for 10 min. The solution was filtered and washed with DI water to remove un-reacted $KMnO_4$. The MnO_2/OMC nanocomposite was subsequently calcined in air at 100 °C overnight.

D.1.7 Characterization

Wide angle X-ray diffraction (XRD) was performed with samples prepared on a quartz slide using a Bruker-Nonius D8 Advance diffractometer. Samples were analyzed in 0.05 deg increments with a dwell time of 10 s. The average nanocrystal size was estimated from the Scherrer equation using JADE software (by Molecular Diffraction Inc).

The MnO_2 content was determined using energy dispersive X-ray analysis using a LEO 1530 SEM equipped with an IXRF EDX system, the latter operated with a 20 kV electron beam and 60 μm aperture (average counts ~2000 s^{-1}).

Nitrogen sorption analysis was performed on a Micromeritics Tristar 3000 analyzer at -196 °C. Prior to measurements, the samples were heated at 150 °C with flowing N_2 at a Micromeritics FlowPrep 060 sample degas system for 4 h. The specific surface area was calculated using the BET method from the nitrogen adsorption data in the relative pressure range (P/P_0) of 0.04-0.30.

Electrochemical measurements were carried out using a CHI 832A electrochemical analyzer (CH instruments Inc.). A three-electrode cell with a Au wire counter electrode and a Hg/Hg_2SO_4 reference electrode were used. A glassy carbon electrode (0.196 cm^2, from Pine Instruments) was used as a substrate for the nanocomposite. The glassy carbon electrode was polished with a 0.3 μm followed by a 0.05 μm alumina suspension to give a mirror finish. The MnO_2/C nanocomposites were ground in an agate mortar prior to testing. 2.0 mg of MnO_2/C was suspended by sonication in 1 mL of ethanol. 15 μL of MnO_2/C suspension was deposited onto the glassy carbon substrate and dried at room temperature. Electrochemical tests were done in 1 M Na_2SO_4 at room temperature.

D.2 RESULTS

D.2.1 MnO_2/SMC composites

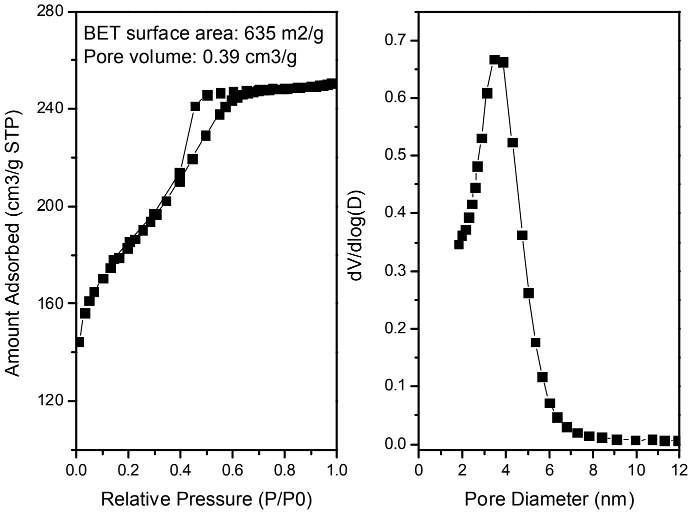

Figure D.1: Nitrogen sorption isotherm and pore size distribution data for SMC.

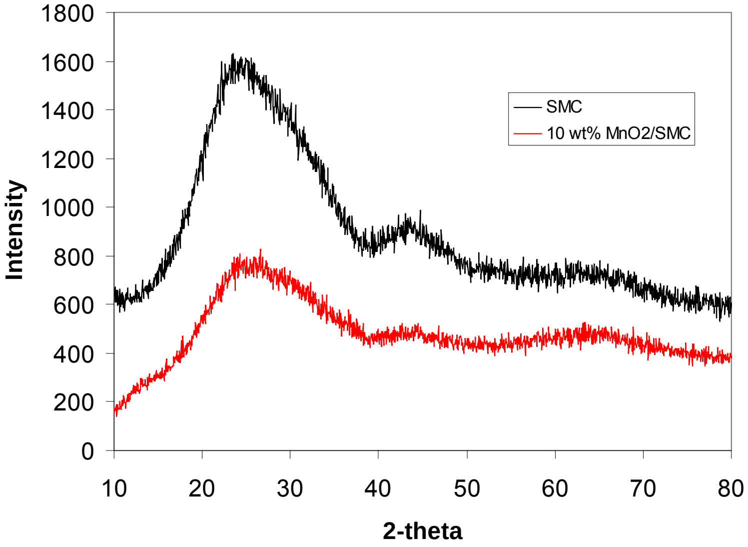

Figure D.2: XRD of SMC and 10 wt% MnO_2/SMC.

Table D.1: Total gravimetric capacitance values at scan rates for SMC and MnO_2/SMC nanocomposites in 1 M Na_2SO_4.

	Scan rate (mV/s) dependence of total gravimetric capacitance (F/g)				
MnO_2 content (wt%)	2	10	20	100	200
0%	51	38	33	26	24
2.2%	61	48	44	38	35
7.6%	81	67	63	55	50
10 %	87	71	64	49	42
18%	103	74	60	35	27
30%	110	74	55	28	20

Table D.2: Gravimetric MnO_2 pseudocapacitance values at scan rates for MnO_2/SMC nanocomposites in 1 M Na_2SO_4.

	Scan rate (mV/s) dependence of gravimetric MnO_2 pseudocapacitance (F/g_{MnO2})				
MnO_2 content (wt%)	2	10	20	100	200
2.2%	537	492	520	562	551
7.6%	453	417	420	402	372
10%	416	366	337	257	212
18%	345	242	184	74	44
30%	251	159	108	31	12

D.2.2 MnO$_2$/OMC composites

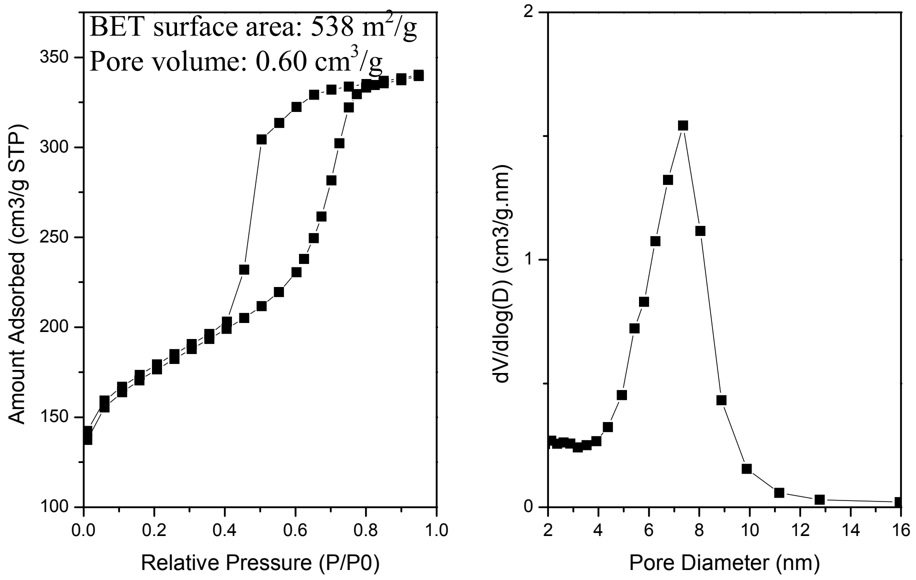

Figure D.3: Nitrogen sorption isotherm and pore size distribution data for OMC.

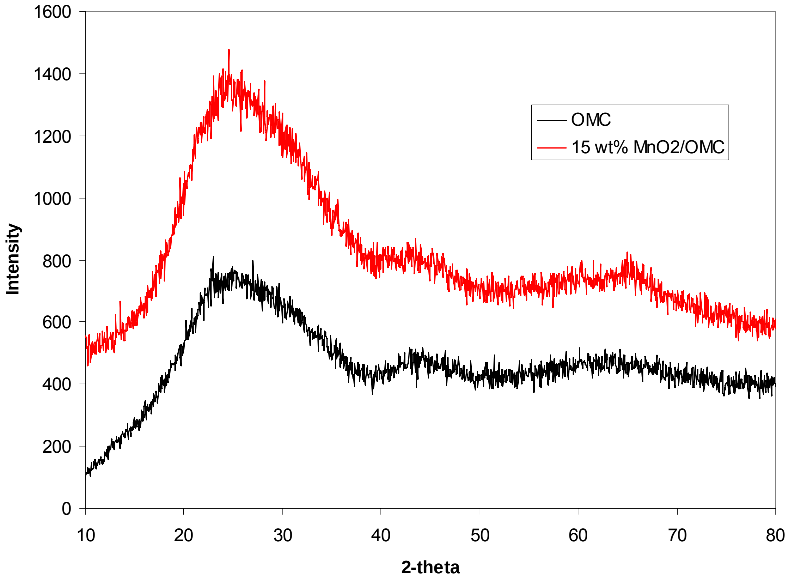

Figure D.4: XRD of OMC and 10 wt% MnO$_2$/OMC.

Table D.3: Total gravimetric capacitance values at scan rates for OMC and MnO_2/OMC nanocomposites in 1 M Na_2SO_4.

	Scan rate (mV/s) dependence of total gravimetric capacitance (F/g)				
MnO_2 content (wt%)	2	10	20	100	200
0%	52	37	32	24	21
2.8%	69	52	48	41	38
7.6%	73	58	53	42	37
15%	82	68	62	49	42

Table D.4: Gravimetric MnO_2 pseudocapacitance values at scan rates for MnO_2/OMC nanocomposites in 1 M Na_2SO_4.

	Scan rate (mV/s) dependence of gravimetric MnO_2 pseudocapacitance (F/g_{MnO2})				
MnO_2 content (wt%)	2	10	20	100	200
2.8%	684	605	609	634	636
7.6%	330	317	307	256	227
15%	260	249	240	189	164

D.3 REFERENCES

1. Liang, C.; Dai, S., Synthesis of Mesoporous Carbon Materials via Enhanced Hydrogen-Bonding Interaction. *Journal of the American Chemical Society* **2006,** 128, (16), 5316-5317.

2. Wang, X.; Liang, C.; Dai, S., Facile Synthesis of Ordered Mesoporous Carbons with High Thermal Stability by Self-Assembly of Resorcinol-Formaldehyde and Block Copolymers under Highly Acidic Conditions. *Langmuir* **2008,** 24, (14), 7500-7505.

References

Alberius, P. C. A.; Frindell, K. L.; Hayward, R. C.; Kramer, E. J.; Stucky, G. D.; Chmelka, B. F., General Predictive Syntheses of Cubic, Hexagonal, and Lamellar Silica and Titania Mesostructured Thin Films. Chemistry of Materials 2002, 14, (8), 3284-3294.

Ania, C. O.; Khomenko, V.; Raymundo-Pinero, E.; Parra, J. B.; Beguin, F., The large electrochemical capacitance of microporous doped carbon obtained by using a zeolite template. Advanced Functional Materials 2007, 17, (11), 1828-1836.

Ardizzone, S.; Fregonara, G.; Trasatti, S., "Inner" and "outer" active surface of ruthenium dioxide electrodes. Electrochimica Acta 1990, 35, (1), 263-7.

Arico, A. S.; Bruce, P.; Scrosati, B.; Tarascon, J.-M.; van Schalkwijk, W., Nanostructured materials for advanced energy conversion and storage devices. Nature Materials 2005, 4, (5), 366-377.

Aslam, M.; Mulla, I. S.; Vijayamohanan, K., Insulator-metal transition in Coulomb blockade nanostructures. Applied Physics Letters 2001, 79, (5), 689-691.

Bailey, R. C.; Stevenson, K. J.; Hupp, J. T., Assembly of micropatterned colloidal gold thin films via microtransfer molding and electrophoretic deposition. Advanced Materials (Weinheim, Germany) 2000, 12, (24), 1930-1934.

Bard, A. J.; Faulkner, L. R., Electrochemical Methods: Fundamentals and Applications. 2nd ed.; John Wiley & Sons, Inc.: 2001.

Bartl, M. H.; Boettcher, S. W.; Frindell, K. L.; Stucky, G. D., 3-D Molecular Assembly of Function in Titania-Based Composite Material Systems. Accounts of Chemical Research 2005, 38, (4), 263-271.

Belanger, D.; Brousse, T.; Long, J. W., Manganese oxides: battery materials make the leap to electrochemical capacitors. Electrochemical Society Interface 2008, 17, (1), 49-52.

Besra, L.; Liu, M., A review on fundamentals and applications of electrophoretic deposition (EPD). Progress in Materials Science 2006, 52, (1), 1-61.

Besson, S.; Gacoin, T.; Ricolleau, C.; Jacquiod, C.; Boilot, J.-P., 3D Quantum Dot Lattice Inside Mesoporous Silica Films. Nano Letters 2002, 2, (4), 409-414.

Biesheuvel, P. M.; Verweij, H., Theory of cast formation in electrophoretic deposition. Journal of the American Ceramic Society 1999, 82, (6), 1451-1455.

Biesheuvel, P. M.; Verweij, H., Comment on \"electrophoretic deposition-mechanisms, myths and materials\" by Y. Fukuda, N. Nagarajan, W. Mekky, Y. Bao, H.-S. Kim and P. S. Nicholson (J. Mater. Sci. 39 (2004) 787). Journal of Materials Science 2004, 39, (23), 7081-7083.

Block, H.; Kelly, J. P., Electro-rheology. Journal of Physics D: Applied Physics 1988, 21, (12), 1661-1677.

Boettcher, S. W.; Fan, J.; Tsung, C.-K.; Shi, Q.; Stucky, G. D., Harnessing the Sol-Gel Process for the Assembly of Non-Silicate Mesostructured Oxide Materials. Accounts of Chemical Research 2007, 40, (9), 784-792.

Bordjiba, T.; Belanger, D., Direct Redox Deposition of Manganese Oxide on Multiscaled Carbon Nanotube/Microfiber Carbon Electrode for Electrochemical Capacitor. Journal of the Electrochemical Society 2009, 156, (5), A378-A384.

Brett, C. M. A.; Brett, A. M. O., Electrochemistry: Principles, Methods, and Applications. Oxford University Press: Oxford, 1993.

Brinker, C. J.; Lu, Y.; Sellinger, A.; Fan, H., Evaporation-induced self-assembly. Nanostructures made easy. Advanced Materials (Weinheim, Germany) 1999, 11, (7), 579-585.

Brock, S. L.; Sanabria, M.; Suib, S. L.; Urban, V.; Thiyagarajan, P.; Potter, D. I., Particle Size Control and Self-Assembly Processes in Novel Colloids of Nanocrystalline Manganese Oxide. Journal of Physical Chemistry B 1999, 103, (35), 7416-7428.

Broughton, J. N.; Brett, M. J., Investigation of thin sputtered Mn films for electrochemical capacitors. Electrochimica Acta 2004, 49, (25), 4439-4446.

Brousse, T.; Toupin, M.; Belanger, D., A hybrid activated carbon-manganese dioxide capacitor using a mild aqueous electrolyte. Journal of the Electrochemical Society 2004, 151, (4), A614-A622.

Browning, G. J.; Donne, S. W., Proton diffusion in g-manganese dioxide. Journal of Applied Electrochemistry 2005, 35, (9), 871-878.

Brust, M.; Fink, J.; Bethell, D.; Schiffrin, D. J.; Kiely, C., Synthesis and reactions of functionalized gold nanoparticles. Journal of the Chemical Society, Chemical Communications 1995, (16), 1655-6.

Brust, M.; Walker, M.; Bethell, D.; Schiffrin, D. J.; Whyman, R., Synthesis of thiol-derivatized gold nanoparticles in a two-phase liquid-liquid system. Journal of the Chemical Society, Chemical Communications 1994, (7), 801-2.

Cagnol, F.; Grosso, D.; Soler-Illia, G. J. d. A. A.; Crepaldi, E. L.; Babonneau, F.; Amenitsch, H.; Sanchez, C., Humidity-controlled mesostructuration in CTAB-templated silica thin film processing. The existence of a modulable steady state. Journal of Materials Chemistry 2003, 13, (1), 61-66.

Carreon, M. A.; Choi, S. Y.; Mamak, M.; Chopra, N.; Ozin, G. A., Pore architecture affects photocatalytic activity of periodic mesoporous nanocrystalline anatase thin films. Journal of Materials Chemistry 2007, 17, (1), 82-89.

Chandrasekharan, N.; Kamat, P. V., Improving the Photoelectrochemical Performance of Nanostructured TiO2 Films by Adsorption of Gold Nanoparticles. Journal of Physical Chemistry B 2000, 104, (46), 10851-10857.

Chandrasekharan, N.; Kamat, P. V., Assembling gold nanoparticles as nanostructured films using an electrophoretic approach. Nano Letters 2001, 1, (2), 67-70.

Chen, H.; Dong, X.; Shi, J.; Zhao, J.; Hua, Z.; Gao, J.; Ruan, M.; Yan, D., Templated synthesis of hierarchically porous manganese oxide with a crystalline nanorod framework and its high electrochemical performance. Journal of Materials Chemistry 2007, 17, (9), 855-860.

Chen, H.; He, J.; Zhang, C.; He, H., Self-Assembly of Novel Mesoporous Manganese Oxide Nanostructures and Their Application in Oxidative Decomposition of Formaldehyde. Journal of Physical Chemistry C 2007, 111, (49), 18033-18038.

Chen, X.; Mao, S. S., Titanium Dioxide Nanomaterials: Synthesis, Properties, Modifications, and Applications. Chemical Reviews (Washington, DC, United States) 2007, 107, (7), 2891-2959.

Chervin, C. N.; Lubers, A. M.; Pettigrew, K. A.; Long, J. W.; Westgate, M. A.; Fontanella, J. J.; Rolison, D. R., Making the Most of a Scarce Platinum-Group Metal: Conductive Ruthenia Nanoskins on Insulating Silica Paper. Nano Letters 2009, 9, (6), 2316-2321.

Chmiola, J.; Yushin, G.; Gogotsi, Y.; Portet, C.; Simon, P.; Taberna, P. L., Anomalous Increase in Carbon Capacitance at Pore Sizes Less Than 1 Nanometer. Science (Washington, DC, United States) 2006, 313, (5794), 1760-1763.

Choi, S. Y.; Mamak, M.; Coombs, N.; Chopra, N.; Ozin, G. A., Thermally stable two-dimensional hexagonal mesoporous nanocrystalline anatase, meso-nc-TiO2: Bulk and crack-free thin film morphologies. Advanced Functional Materials 2004, 14, (4), 335-344.

Coakley, K. M.; Liu, Y.; McGehee, M. D.; Frindell, K. L.; Stucky, G. D., Infiltrating semiconducting polymers into self-assembled mesoporous titania films for photovoltaic applications. Advanced Functional Materials 2003, 13, (4), 301-306.

Comiskey, B.; Albert, J. D.; Yoshizawa, H.; Jacobson, J., An electrophoretic ink for all-printed reflective electronic displays. Nature (London) 1998, 394, (6690), 253-255.

Conway, B. E., Electrochemical Supercapacitors: Scientific Fundamentals and Technological Applications. Kluwer Academic/Plenum Publishers: New York, 1999.

Conway, B. E.; Birss, V.; Wojtowicz, J., The role and utilization of pseudocapacitance for energy storage by supercapacitors. Journal of Power Sources 1997, 66, (1-2), 1-14.

Cortial, G.; Siutkowski, M.; Goettmann, F.; Moores, A.; Boissiere, C.; Grosso, D.; Le Floch, P.; Sanchez, C., Metallic nanoparticles hosted in mesoporous oxide thin films for catalytic applications. Small 2006, 2, (8-9), 1042-1045.

Crepaldi, E. L.; de Soler-Illia, G. J.; Grosso, D.; Cagnol, F.; Ribot, F.; Sanchez, C., Controlled Formation of Highly Organized Mesoporous Titania Thin Films: From Mesostructured Hybrids to Mesoporous Nanoanatase TiO2. Journal of the American Chemical Society 2003, 125, (32), 9770-9786.

Crepaldi, E. L.; Grosso, D.; Soler-Illia, G. J. d. A. A.; Albouy, P.-A.; Amenitsch, H.; Sanchez, C., Formation and Stabilization of Mesostructured Vanadium-Oxo-Based Hybrid Thin Films. Chemistry of Materials 2002, 14, (8), 3316-3325.

Crowley, J. M.; Till, H. R. In Image development by electrostatic lithography, Proceedings of the Third International Congress on Advances in Non-Impact Printing Technologies, San Francisco, CA, Aug. 24-28, 1986, 1986; Society for Imaging Science and Technology: Springfield, VA, 1986: San Francisco, CA, 1986; pp pp 100-112.

Dahlquist, J. A.; Brodie, I., Electrophoretic development of electrostatic charge images from colloidal suspensions of carbon. Journal of Applied Physics 1969, 40, (7), 3020-3027.

Davé, D. P.; Milner, T. E., Optical low-coherence reflectometer for differential phase measurement. Optics letters 2000, 25, (4), 227-229.

Devaraj, S.; Munichandraiah, N., Effect of Crystallographic Structure of MnO2 on Its Electrochemical Capacitance Properties. Journal of Physical Chemistry C 2008, 112, (11), 4406-4417.

Diebold, U., The surface science of titanium dioxide. Surface Science Reports 2003, 48, (5-8), 53-229.

Doescher, M. S.; Pietron, J. J.; Dening, B. M.; Long, J. W.; Rhodes, C. P.; Edmondson, C. A.; Rolison, D. R., Using an Oxide Nanoarchitecture To Make or Break a Proton Wire. Analytical Chemistry 2005, 77, (24), 7924-7932.

Dong, X.; Shen, W.; Gu, J.; Xiong, L.; Zhu, Y.; Li, H.; Shi, J., MnO2-Embedded-in-Mesoporous-Carbon-Wall Structure for Use as Electrochemical Capacitors. Journal of Physical Chemistry B 2006, 110, (12), 6015-6019.

Du, C.; Pan, N., High power density supercapacitor electrodes of carbon nanotube films by electrophoretic deposition. Nanotechnology 2006, 17, (21), 5314-5318.

Eicke, H. F.; Borkovec, M.; Das-Gupta, B., Conductivity of water-in-oil microemulsions: a quantitative charge fluctuation model. Journal of Physical Chemistry 1989, 93, (1), 314-17.

Etienne, M.; Grosso, D.; Boissiere, C.; Sanchez, C.; Walcarius, A., Electrochemical evidences of morphological transformation in ordered mesoporous titanium oxide thin films. Chemical Communications (Cambridge, United Kingdom) 2005, (36), 4566-4568.

Evans, D. F.; Wennerstrom, H., The colloidal domain : where physics, chemistry, biology, and technology meet. 2nd ed.; Wiley-VCH: New York, 1999; p 632.

Felici, N.; Lacroix, J. C., Electroconvection in insulating liquids with special reference to uni- and bi-polar injection. Journal of Electrostatics 1978, 5, 135-144.

Fischer, A. E.; Long, J. W., Redox deposition of nanoscale MnO2 on ultraporous carbon nanoarchitectures: correlation of MnO2 deposition time and electrochemical performance. ECS Transactions 2007, 3, (37, Electrochemical Capacitors 2006), 61-66.

Fischer, A. E.; Pettigrew, K. A.; Rolison, D. R.; Stroud, R. M.; Long, J. W., Incorporation of Homogeneous, Nanoscale MnO2 within Ultraporous Carbon Structures via Self-Limiting Electroless Deposition: Implications for Electrochemical Capacitors. Nano Letters 2007, 7, (2), 281-286.

Fischer, A. E.; Saunders, M. P.; Pettigrew, K. A.; Rolison, D. R.; Long, J. W., Electroless deposition of nanoscale MnO2 on ultraporous carbon nanoarchitectures:

correlation of evolving pore-solid structure and electrochemical performance. Journal of the Electrochemical Society 2008, 155, (3), A246-A252.

Frackowiak, E., Carbon materials for supercapacitor application. Physical Chemistry Chemical Physics 2007, 9, (15), 1774-1785.

Frackowiak, E.; Beguin, F., Carbon materials for the electrochemical storage of energy in capacitors. Carbon 2001, 39, (6), 937-950.

Fuertes, A. B.; Alvarez, S., Graphitic mesoporous carbons synthesised through mesostructured silica templates. Carbon 2004, 42, (15), 3049-3055.

Fuertes, A. B.; Pico, F.; Rojo, J. M., Influence of pore structure on electric double-layer capacitance of template mesoporous carbons. Journal of Power Sources 2004, 133, (2), 329-336.

Fukada, Y.; Nagarajan, N.; Mekky, W.; Bao, Y.; Kim, H. S.; Nicholson, P. S., Electrophoretic deposition - mechanisms, myths and materials. Journal of Materials Science 2004, 39, (3), 787-801.

Gaillot, A.-C.; Flot, D.; Drits, V. A.; Manceau, A.; Burghammer, M.; Lanson, B., Structure of Synthetic K-rich Birnessite Obtained by High-Temperature Decomposition of KMnO4. I. Two-Layer Polytype from 800 DegC Experiment. Chemistry of Materials 2003, 15, (24), 4666-4678.

Galo, C. T.; Viviana, D. G.; Jose, A. E.; Lima, C. A. S., Synthesis of iron and iron-manganese colloids and nanoparticles using organic solvents. Journal of the Chilean Chemical Society 2005, 50, (2), 455-460.

Gal-Or, L.; Liubovich, S.; Haber, S., Deep electrophoretic penetration and deposition of ceramic particles inside porous substrates. II. Experimental model. Journal of the Electrochemical Society 1992, 139, (4), 1078-81.

Gast, A. P.; Zukoski, C. F., Electrorheological fluids as colloidal suspensions. Advances in Colloid and Interface Science 1989, 30, (3-4), 153-202.

Ghaemi, M.; Ataherian, F.; Zolfaghari, A.; Jafari, S. M., Charge storage mechanism of sonochemically prepared MnO2 as supercapacitor electrode: Effects of physisorbed water and proton conduction. Electrochimica Acta 2008, 53, (14), 4607-4614.

Giersig, M.; Mulvaney, P., Formation of ordered two-dimensional gold colloid lattices by electrophoretic deposition. Journal of Physical Chemistry 1993, 97, (24), 6334-6.

Giersig, M.; Mulvaney, P., Preparation of ordered colloid monolayers by electrophoretic deposition. Langmuir 1993, 9, (12), 3408-13.

Gierszal, K. P.; Kim, T.-W.; Ryoo, R.; Jaroniec, M., Adsorption and Structural Properties of Ordered Mesoporous Carbons Synthesized by Using Various Carbon Precursors and Ordered Siliceous P6mm and Ia.hivin.3d Mesostructures as Templates. Journal of Physical Chemistry B 2005, 109, (49), 23263-23268.

Granqvist, C. G.; Hunderi, O., Optical properties of ultrafine gold particles. Physical Review B: Solid State 1977, 16, (8), 3513-34.

Gratzel, M., Photoelectrochemical cells. Nature (London, United Kingdom) 2001, 414, (6861), 338-344.

Green, J. H.; Parfitt, G. D., Stability of concentrated colloidal dispersions in apolar media. Particulate Science and Technology 1987, 5, (3), 289-99.

Gregg, S. J.; Sing, K. S. W., Adsorption, Surface Area and Porosity. 2nd ed.; 1982; p 303 pp.

Grosso, D.; Cagnol, F.; Soler-Illia, G. J. D. A. A.; Crepaldi, E. L.; Amenitsch, H.; Brunet-Bruneau, A.; Bourgeois, A.; Sanchez, C., Fundamentals of mesostructuring through evaporation-induced self-assembly. Advanced Functional Materials 2004, 14, (4), 309-322.

Grosso, D.; Soler-Illia, G. J. d. A. A.; Babonneau, F.; Sanchez, C.; Albouy, P.-A.; Brunet-Bruneau, A.; Balkenende, A. R., Highly organized mesoporous titania thin films showing mono-oriented 2D hexagonal channels. Advanced Materials (Weinheim, Germany) 2001, 13, (14), 1085-1090.

Grosso, D.; Soler-Illia, G. J. d. A. A.; Crepaldi, E. L.; Cagnol, F.; Sinturel, C.; Bourgeois, A.; Brunet-Bruneau, A.; Amenitsch, H.; Albouy, P. A.; Sanchez, C., Highly Porous TiO2 Anatase Optical Thin Films with Cubic Mesostructure Stabilized at 700 DegC. Chemistry of Materials 2003, 15, (24), 4562-4570.

Gu, J.; Shi, J.; Xiong, L.; Chen, H.; Ruan, M., A new strategy to incorporate highly dispersed nanoparticles into the pore channels of mesoporous silica thin films. Microporous and Mesoporous Materials 2004, 74, (1-3), 199-204.

Gu, J.; Xiong, L.; Shi, J.; Hua, Z.; Zhang, L.; Li, L., Thioether moiety functionalization of mesoporous silica films for the encapsulation of highly dispersed gold nanoparticles. Journal of Solid State Chemistry 2006, 179, (4), 1060-1066.

Gu, J.-L.; Shi, J.-L.; You, G.-J.; Xiong, L.-M.; Qian, S.-X.; Hua, Z.-L.; Chen, H.-R., Incorporation of highly dispersed gold nanoparticles into the pore channels of mesoporous silica thin films and their ultrafast nonlinear optical response. Advanced Materials (Weinheim, Germany) 2005, 17, (5), 557-560.

Guliants, V. V.; Carreon, M. A.; Lin, Y. S., Ordered mesoporous and macroporous inorganic films and membranes. Journal of Membrane Science 2004, 235, (1-2), 53-72.

Gupta, G.; Patel, M. N.; Ferrer, D.; Heitsch, A. T.; Korgel, B. A.; Jose-Yacaman, M.; Johnston, K. P., Stable Ordered FePt Mesoporous Silica Catalysts with High Loadings. Chemistry of Materials 2008, 20, (15), 5005-5015.

Gupta, G.; Shah, P. S.; Zhang, X.; Saunders, A. E.; Korgel, B. A.; Johnston, K. P., Enhanced Infusion of Gold Nanocrystals into Mesoporous Silica with Supercritical Carbon Dioxide. Chemistry of Materials 2005, 17, (26), 6728-6738.

Gupta, G.; Stowell, C. A.; Patel, M. N.; Gao, X.; Yacaman, M. J.; Korgel, B. A.; Johnston, K. P., Infusion of Presynthesized Iridium Nanocrystals into Mesoporous Silica for High Catalyst Activity. Chemistry of Materials 2006, 18, (26), 6239-6249.

Haber, S., Deep electrophoretic penetration and deposition of ceramic particles inside impermeable porous substrates. Journal of Colloid and Interface Science 1996, 179, (2), 380-390.

Haber, S.; Gal-Or, L., Deep electrophoretic penetration and deposition of ceramic particles inside porous substrates. I. Analytical model. Journal of the Electrochemical Society 1992, 139, (4), 1071-8.

Hornyak, G.; Kroll, M.; Pugin, R.; Sawitowski, T.; Schmid, G.; Bovin, J.-O.; Karsson, G.; Hofmeister, H.; Hopfe, S., Gold clusters and colloids in alumina nanotubes. Chemistry--A European Journal 1997, 3, (12), 1951-1956.

Hsu, M. F.; Dufresne, E. R.; Weitz, D. A., Charge Stabilization in Nonpolar Solvents. Langmuir 2005, 21, (11), 4881-4887.

Hu, C.-C.; Chang, K.-H.; Lin, M.-C.; Wu, Y.-T., Design and Tailoring of the Nanotubular Arrayed Architecture of Hydrous RuO2 for Next Generation Supercapacitors. Nano Letters 2006, 6, (12), 2690-2695.

Hu, C.-C.; Tsou, T.-W., The optimization of specific capacitance of amorphous manganese oxide for electrochemical supercapacitors using experimental strategies. Journal of Power Sources 2003, 115, (1), 179-186.

Huang, C.-H.; Huang, C.-H.; Nguyen, T.-P.; Hsu, C.-S., Self-assembly monolayer of anatase titanium oxide from solution process on indium tin oxide glass substrate for polymer photovoltaic cells. Thin Solid Films 2007, 515, (16), 6493-6496.

Huang, S. Y.; Kavan, L.; Exnar, I.; Graetzel, M., Rocking chair lithium battery based on nanocrystalline TiO2 (anatase). Journal of the Electrochemical Society 1995, 142, (9), L142-L144.

Islam, M. A.; Herman, I. P., Electrodeposition of patterned CdSe nanocrystal films using thermally charged nanocrystals. Applied Physics Letters 2002, 80, (20), 3823-3825.

Islam, M. A.; Xia, Y.; Steigerwald, M. L.; Yin, M.; Liu, Z.; O'Brien, S.; Levicky, R.; Herman, I. P., Addition, suppression, and inhibition in the electrophoretic deposition of nanocrystal mixture films for CdSe nanocrystals with g-Fe2O3 and Au Nanocrystals. Nano Letters 2003, 3, (11), 1603-1606.

Islam, M. A.; Xia, Y.; Telesca, D. A., Jr.; Steigerwald, M. L.; Herman, I. P., Controlled electrophoretic deposition of smooth and robust films of CdSe nanocrystals. Chemistry of Materials 2004, 16, (1), 49-54.

Ito, T.; Sun, L.; Bevan, M. A.; Crooks, R. M., Comparison of Nanoparticle Size and Electrophoretic Mobility Measurements Using a Carbon-Nanotube-Based Coulter Counter, Dynamic Light Scattering, Transmission Electron Microscopy, and Phase Analysis Light Scattering. Langmuir 2004, 20, (16), 6940-6945.

Iwanaga, T.; Hyodo, T.; Shimizu, Y.; Egashira, M., H2 sensing properties and mechanism of anodically oxidized TiO2 film contacted with Pd electrode. Sensors and Actuators, B: Chemical 2003, B93, (1-3), 519-525.

Jacobs, H. O.; Knapp, H. F.; Mueller, S.; Stemmer, A., Surface potential mapping: A qualitative material contrast in SPM. Ultramicroscopy 1997, 69, (1), 39-49.

Jacobs, H. O.; Leuchtmann, P.; Homan, O. J.; Stemmer, A., Resolution and contrast in Kelvin probe force microscopy. Journal of Applied Physics 1998, 84, (3), 1168-1173.

Jellison, G. E., Jr.; Modine, F. A., Parameterization of the optical functions of amorphous materials in the interband region. Applied Physics Letters 1996, 69, (3), 371-373.

Jenkins, P.; Basu, S.; Keir, R. I.; Ralston, J.; Thomas, J. C.; Wolffenbuttel, B. M. A., The Electrochemistry of Nonaqueous Copper Phthalocyanine Dispersions in the Presence of a Metal Soap Surfactant: A Simple Equilibrium Site Binding Model. Journal of Colloid and Interface Science 1999, 211, (2), 252-263.

Jeong, Y. U.; Manthiram, A., Nanocrystalline Manganese Oxides for Electrochemical Capacitors with Neutral Electrolytes. Journal of the Electrochemical Society 2002, 149, (11), A1419-A1422.

Jia, N.; Martin, R. B.; Qi, Z.; Lefebvre, M. C.; Pickup, P. G., Modification of carbon supported catalysts to improve performance in gas diffusion electrodes. Electrochimica Acta 2001, 46, (18), 2863-2869.

Jin, X.; Zhou, W.; Zhang, S.; Chen, G. Z., Nanoscale microelectrochemical cells on carbon nanotubes. Small 2007, 3, (9), 1513-1517.

Kallay, N.; Tomic, M.; Chittofrati, A., Conductivity of water-in-oil microemulsions: comparison of the Boltzmann statistics and the charge fluctuation model. Colloid and Polymer Science 1992, 270, (2), 194-196.

Kamada, K.; Fukuda, H.; Maehara, K.; Yoshida, Y.; Nakai, M.; Hasuo, S.; Matsumoto, Y., Insertion of SiO2 nanoparticles into pores of anodized aluminum by electrophoretic deposition in aqueous system. Electrochemical and Solid-State Letters 2004, 7, (8), B25-B28.

Kamat, P. V., Meeting the Clean Energy Demand: Nanostructure Architectures for Solar Energy Conversion. Journal of Physical Chemistry C 2007, 111, (7), 2834-2860.

Keir, R. I.; Suparno; Thomas, J. C., Charging Behavior in the Silica/Aerosol OT/Decane System. Langmuir 2002, 18, (5), 1463-1465.

Kim, I.-H.; Kim, K.-B., Ruthenium oxide thin film electrodes for supercapacitors. Electrochemical and Solid-State Letters 2001, 4, (5), A62-A64.

Kinoshita, K., Carbon: Electrochemical and Physicochemical Properties. Wiley-Interscience: New York, 1988.

Kitahara, A., Nonaqueous systems. In Electrical Phenomena at Interfaces: Fundamentals, Measurements, and Applications, 2nd ed.; Ohshima, H.; Furusawa, K., Eds. Marcel Dekker: New York, 1998; Vol. 76, pp 135-150.

Kitahara, A.; Karasawa, S.; Yamada, H., The effect of water on the electrokinetic potential and stability of suspensions in nonpolar media. Journal of Colloid and Interface Science 1967, 25, (4), 490-5.

Kitahara, A.; Tamura, T.; Konno, K., Effect of water on flocculation of carbon black in nonaqueous surfactant solutions. Separation Science and Technology 1980, 15, (3), 249-61.

Koganti, V. R.; Dunphy, D.; Gowrishankar, V.; McGehee, M. D.; Li, X.; Wang, J.; Rankin, S. E., Generalized Coating Route to Silica and Titania Films with Orthogonally Tilted Cylindrical Nanopore Arrays. Nano Letters 2006, 6, (11), 2567-2570.

Korgel, B. A.; Fullam, S.; Connolly, S.; Fitzmaurice, D., Assembly and Self-Organization of Silver Nanocrystal Superlattices: Ordered \"Soft Spheres\". Journal of Physical Chemistry B 1998, 102, (43), 8379-8388.

Kotz, R.; Carlen, M., Principles and applications of electrochemical capacitors. Electrochimica Acta 2000, 45, (15-16), 2483-2498.

Krishnakumar, S.; Somasundaran, P., Adsorption of Aerosol-OT on graphite from aqueous and non-aqueous media. Colloids and Surfaces, A: Physicochemical and Engineering Aspects 1996, 117, (3), 227-233.

Kumai, Y.; Tsukada, H.; Akimoto, Y.; Sugimoto, N.; Seno, Y.; Fukuoka, A.; Ichikawa, M.; Inagaki, S., Highly ordered platinum nanodot arrays with cubic symmetry in mesoporous thin films. Advanced Materials (Weinheim, Germany) 2006, 18, (6), 760-762.

Lancelle-Beltran, E.; Prene, P.; Boscher, C.; Belleville, P.; Buvat, P.; Lambert, S.; Guillet, F.; Boissiere, C.; Grosso, D.; Sanchez, C., Nanostructured Hybrid Solar Cells Based on Self-Assembled Mesoporous Titania Thin Films. Chemistry of Materials 2006, 18, (26), 6152-6156.

Lee, C. Y.; Tsai, H. M.; Chuang, H. J.; Li, S. Y.; Lin, P.; Tseng, T. Y., Characteristics and electrochemical performance of supercapacitors with manganese oxide-carbon nanotube nanocomposite electrodes. Journal of the Electrochemical Society 2005, 152, (4), A716-A720.

Lee, U. H.; Lee, H.; Wen, S.; Mho, S.-i.; Kwon, Y.-U., Mesoporous titania thin films with pseudo-cubic structure: Synthetic studies and applications to nanomembranes and nanotemplates. Microporous and Mesoporous Materials 2006, 88, (1-3), 48-55.

Lei, Y.; Fournier, C.; Pascal, J.-L.; Favier, F., Mesoporous carbon-manganese oxide composite as negative electrode material for supercapacitors. Microporous and Mesoporous Materials 2008, 110, (1), 167-176.

Li, H.-Q.; Liu, R.-L.; Zhao, D.-Y.; Xia, Y.-Y., Electrochemical properties of an ordered mesoporous carbon prepared by direct tri-constituent co-assembly. Carbon 2007, 45, (13), 2628-2635.

Liang, C.; Dai, S., Synthesis of Mesoporous Carbon Materials via Enhanced Hydrogen-Bonding Interaction. Journal of the American Chemical Society 2006, 128, (16), 5316-5317.

Liang, C.; Li, Z.; Dai, S., Mesoporous carbon materials: synthesis and modification. Angewandte Chemie, International Edition 2008, 47, (20), 3696-3717.

Liang, Y.-Y.; Li, H. L.; Zhang, X.-G., Solid state synthesis of hydrous ruthenium oxide for supercapacitors. Journal of Power Sources 2007, 173, (1), 599-605.

Limmer, S. J.; Chou, T. P.; Cao, G. Z., A study on the influences of processing parameters on the growth of oxide nanorod arrays by sol electrophoretic deposition. Journal of Sol-Gel Science and Technology 2005, 36, (2), 183-195.

Limmer, S. J.; Cruz, S. V.; Cao, G. Z., Films and nanorods of transparent conducting oxide ITO by a citric acid sol route. Applied Physics A: Materials Science & Processing 2004, 79, (3), 421-424.

Limmer, S. J.; Hubler, T. L.; Cao, G., Nanorods of Various Oxides and Hierarchically Structured Mesoporous Silica by Sol-Gel Electrophoresis. Journal of Sol-Gel Science and Technology 2003, 26, (1/2/3), 577-581.

Limmer, S. J.; Seraji, S.; Forbess, M. J.; Wu, Y.; Chou, T. P.; Nguyen, C.; Cao, G., Electrophoretic growth of lead zirconate titanate nanorods. Advanced Materials (Weinheim, Germany) 2001, 13, (16), 1269-1272.

Liu, H.; Song, C.; Zhang, L.; Zhang, J.; Wang, H.; Wilkinson, D. P., A review of anode catalysis in the direct methanol fuel cell. Journal of Power Sources 2006, 155, (2), 95-110.

Liu, H.-Y.; Wang, K.-P.; Teng, H., A simplified preparation of mesoporous carbon and the examination of the carbon accessibility for electric double layer formation. Carbon 2005, 43, (3), 559-566.

Liu, K.; Zhang, M.; Zhou, W.; Li, L.; Wang, J.; Fu, H., Preparation, characterization, and photo-induced hydrophilicity of nanocrystalline anatase thin films synthesized through evaporation-induced assembly. Nanotechnology 2005, 16, (12), 3006-3011.

Liu, T. C.; Pell, W. G.; Conway, B. E.; Roberson, S. L., Behavior of molybdenum nitrides as materials for electrochemical capacitors. Journal of the Electrochemical Society 1998, 145, (6), 1882-1888.

Long Jeffrey, W., Architectural design, interior decoration, and three-dimensional plumbing en route to multifunctional nanoarchitectures. Accounts of chemical research 2007, 40, (9), 854-62.

Long, J. W.; Dunn, B.; Rolison, D. R.; White, H. S., Three-Dimensional Battery Architectures. Chemical Reviews (Washington, DC, United States) 2004, 104, (10), 4463-4492.

Long, J. W.; Rolison, D. R., Architectural Design, Interior Decoration, and Three-Dimensional Plumbing en Route to Multifunctional Nanoarchitectures. Accounts of Chemical Research 2007, 40, (9), 854-862.

Long, J. W.; Swider-Lyons, K. E.; Stroud, R. M.; Rolison, D. R., Design of pore and matter architectures in manganese oxide charge-storage materials. Electrochemical and Solid-State Letters 2000, 3, (10), 453-456.

Lu, Y.; Ganguli, R.; Drewien, C. A.; Anderson, M. T.; Brinker, C. J.; Gong, W.; Guo, Y.; Soyez, H.; Dunn, B.; Huang, M. H.; Zink, J. I., Continuous formation of supported cubic and hexagonal mesoporous films by sol-gel dip-coating. Nature (London) 1997, 389, (6649), 364-368.

Luo, J.-Y.; Xia, Y.-Y., Effect of pore structure on the electrochemical capacitive performance of MnO2. Journal of the Electrochemical Society 2007, 154, (11), A987-A992.

Lytle, J. C.; Rhodes, C. P.; Long, J. W.; Pettigrew, K. A.; Stroud, R. M.; Rolison, D. R., The importance of combining disorder with order for Li-ion insertion into cryogenically prepared nanoscopic ruthenia. Journal of Materials Chemistry 2007, 17, (13), 1292-1299.

Ma, S.-B.; Lee, Y.-H.; Ahn, K.-Y.; Kim, C.-M.; Oh, K.-H.; Kim, K.-B., Spontaneously Deposited Manganese Oxide on Acetylene Black in an Aqueous Potassium Permanganate Solution. Journal of the Electrochemical Society 2006, 153, (1), C27-C32.

Maranzano, B. J.; Wagner, N. J.; Fritz, G.; Glatter, O., Surface charge of 3-(trimethoxysilyl) propyl methacrylate (TPM) coated Stober silica colloids by zeta-phase analysis light scattering and small angle neutron scattering. Langmuir 2000, 16, (26), 10556-10558.

May, R. A.; Kondrachova, L.; Hahn, B. P.; Stevenson, K. J., Optical Constants of Electrodeposited Mixed Molybdenum-Tungsten Oxide Films Determined by Variable-Angle Spectroscopic Ellipsometry. Journal of Physical Chemistry C 2007, 111, (49), 18251-18257.

McEvoy, T. M.; Stevenson, K. J., Spatially Resolved Imaging of Inhomogeneous Charge Transfer Behavior in Polymorphous Molybdenum Oxide. II. Correlation of Localized Coloration/Insertion Properties Using Spectroelectrochemical Microscopy. Langmuir 2005, 21, (8), 3529-3538.

McMurray, H. N.; Williams, G., Probe diameter and probe-specimen distance dependence in the lateral resolution of a scanning Kelvin probe. Journal of Applied Physics 2002, 91, (3), 1673-1679.

Medrzycka, K. B., The effect of particle concentration on zeta potential in extremely dilute solutions. Colloid and Polymer Science 1991, 269, (1), 85-90.

Miller, J. F.; Schaetzel, K.; Vincent, B., The determination of very small electrophoretic mobilities in polar and nonpolar colloidal dispersions using phase analysis light scattering. Journal of Colloid and Interface Science 1991, 143, (2), 532-54.

Miller, J. M.; Dunn, B., Morphology and Electrochemistry of Ruthenium/Carbon Aerogel Nanostructures. Langmuir 1999, 15, (3), 799-806.

Miller, J. R.; Burke, A. F., Electrochemical capacitors: challenges and opportunities for real-world applications. Electrochemical Society Interface 2008, 17, (1), 53-57.

Miller, J. R.; Simon, P., Electrochemical Capacitors for Energy Management. Science (Washington, DC, United States) 2008, 321, (5889), 651-652.

Miller, J. R.; Simon, P., Fundamentals of electrochemical capacitor design and operation. Electrochemical Society Interface 2008, 17, (1), 31-32.

Mohn, E., Kinetics of electrophoretic particle deposition and measurement of zeta potentials. Photographic Science and Engineering 1971, 15, (6), 451-455.

Morrison, I. D., Electrical charges in nonaqueous media. Colloids and Surfaces, A: Physicochemical and Engineering Aspects 1993, 71, (1), 1-37.

Murray, C. B.; Kagan, C. R.; Bawendi, M. G., Synthesis and characterization of monodisperse nanocrystals and close-packed nanocrystal assemblies. Annual Review of Materials Science 2000, 30, 545-610.

Nadal, F.; Argoul, F.; Hanusse, P.; Pouligny, B.; Ajdari, A., Electrically induced interactions between colloidal particles in the vicinity of a conducting plane. Physical Review E: Statistical, Nonlinear, and Soft Matter Physics 2002, 65, (6-1), 061409/1-061409/8.

Nadal, F.; Argoul, F.; Kestener, P.; Pouligny, B.; Ybert, C.; Ajdari, A., Electrically induced flows in the vicinity of a dielectric stripe on a conducting plate. European Physical Journal E: Soft Matter 2002, 9, (4), 387-399.

Novotny, V., Applications on nonaqueous colloids. Colloids and Surfaces 1987, 24, (4), 361-375.

Novotny, V. J., Physics of nonaqueous colloids. In Colloids Surf. Reprogr. Technol., American Chemical Society: 1982; Vol. 200, pp 281-306.

Numao, S.; Judai, K.; Nishijo, J.; Mizuuchi, K.; Nishi, N., Synthesis and characterization of mesoporous carbon nano-dendrites with graphitic ultra-thin walls and their application to supercapacitor electrodes. Carbon 2009, 47, (1), 306-312.

Obreja, V. V. N., On the performance of supercapacitors with electrodes based on carbon nanotubes and carbon activated material-A review. Physica E: Low-Dimensional Systems & Nanostructures (Amsterdam, Netherlands) 2008, 40, (7), 2596-2605.

Overbury, S. H.; Ortiz-Soto, L.; Zhu, H.; Lee, B.; Amiridis, M. D.; Dai, S., Comparison of Au catalysts supported on mesoporous titania and silica: Investigation of Au particle size effects and metal-support interactions. Catalysis Letters 2004, 95, (3-4), 99-106.

Pai, R. A.; Humayun, R.; Schulberg, M. T.; Sengupta, A.; Sun, J.-N.; Watkins, J. J., Mesoporous Silicates Prepared Using Preorganized Templates in Supercritical Fluids. Science (Washington, DC, United States) 2004, 303, (5657), 507-511.

Pandolfo, A. G.; Hollenkamp, A. F., Carbon properties and their role in supercapacitors. Journal of Power Sources 2006, 157, (1), 11-27.

Pang, S.-C.; Anderson, M. A., Novel electrode materials for electrochemical capacitors: part II. Material characterization of sol-gel-derived and electrodeposited manganese dioxide thin films. Journal of Materials Research 2000, 15, (10), 2096-2106.

Pang, S.-C.; Anderson, M. A.; Chapman, T. W., Novel electrode materials for thin-film ultracapacitors: comparison of electrochemical properties of sol-gel-derived and electrodeposited manganese dioxide. Journal of the Electrochemical Society 2000, 147, (2), 444-450.

Parfitt, G. D.; Peacock, J., Stability of colloidal dispersions in nonaqueous media. Surface and Colloid Science 1978, 10, 163-226.

Park, J.; Kang, E.; Bae, C. J.; Park, J.-G.; Noh, H.-J.; Kim, J.-Y.; Park, J.-H.; Park, H. M.; Hyeon, T., Synthesis, Characterization, and Magnetic Properties of Uniform-sized MnO Nanospheres and Nanorods. Journal of Physical Chemistry B 2004, 108, (36), 13594-13598.

Park, S.; Liang, C.; Sheng, D.; Dudney, N.; DePaoli, D., Mesoporous Carbon Materials as Electrodes for Electrochemical Double-Layer Capacitor. Materials Research Society Symposium Proceedings 2007, 973E, (Mobile Energy), No pp given, Paper #: 0973-BB07-04.

Patel, M. N.; Wang, X.; Wilson, B.; Ferrer, D.; Dai, S.; Stevenson, K. J.; Johnston Keith, P., Hybrid MnO2/ Disordered Mesoporous Carbon Nanocomposites: Synthesis and Characterization as Electrochemical Pseudocapacitor Electrodes. in prep. 2009.

Perez, M. D.; Otal, E.; Bilmes, S. A.; Soler-Illia, G. J. A. A.; Crepaldi, E. L.; Grosso, D.; Sanchez, C., Growth of Gold Nanoparticle Arrays in TiO2 Mesoporous Matrixes. Langmuir 2004, 20, (16), 6879-6886.

Portet, C.; Taberna, P. L.; Simon, P.; Flahaut, E.; Laberty-Robert, C., High power density electrodes for Carbon supercapacitor applications. Electrochimica Acta 2005, 50, (20), 4174-4181.

Portet, C.; Yushin, G.; Gogotsi, Y., Electrochemical performance of carbon onions, nanodiamonds, carbon black and multiwalled nanotubes in electrical double layer capacitors. Carbon 2007, 45, (13), 2511-2518.

Pugh, R. J.; Matsunaga, T.; Fowkes, F. M., The dispersibility and stability of carbon black in media of low dielectric constant. 1. Electrostatic and steric contributions to colloidal stability. Colloids and Surfaces 1983, 7, (3), 183-207.

Qu, D., The study of the proton diffusion process in the porous MnO2 electrode. Electrochimica Acta 2004, 49, (4), 657-665.

Ragupathy, P.; Vasan, H. N.; Munichandraiah, N., Synthesis and characterization of nano-MnO2 for electrochemical supercapacitor studies. Journal of the Electrochemical Society 2007, 155, (1), A34-A40.

Raymundo-Pinero, E.; Khomenko, V.; Frackowiak, E.; Beguin, F., Performance of Manganese Oxide/CNTs Composites as Electrode Materials for Electrochemical Capacitors. Journal of the Electrochemical Society 2005, 152, (1), A229-A235.

Rioux, R. M.; Song, H.; Hoefelmeyer, J. D.; Yang, P.; Somorjai, G. A., High-Surface-Area Catalyst Design: Synthesis, Characterization, and Reaction Studies of Platinum Nanoparticles in Mesoporous SBA-15 Silica. Journal of Physical Chemistry B 2005, 109, (6), 2192-2202.

Robel, I.; Subramanian, V.; Kuno, M.; Kamat, P. V., Quantum Dot Solar Cells. Harvesting Light Energy with CdSe Nanocrystals Molecularly Linked to Mesoscopic TiO2 Films. Journal of the American Chemical Society 2006, 128, (7), 2385-2393.

Roberts, G. S.; Sanchez, R.; Kemp, R.; Wood, T.; Bartlett, P., Electrostatic charging of nonpolar colloids by reverse micelles. Langmuir 2008, 24, (13), 6530-6541.

Rolison, D. R., Catalytic nanoarchitectures - The importance of nothing and the unimportance of periodicity. Science (Washington, DC, United States) 2003, 299, (5613), 1698-1702.

Rolison, D. R.; Long, J. W.; Lytle, J. C.; Fischer, A. E.; Rhodes, C. P.; McEvoy, T. M.; Bourg, M. E.; Lubers, A. M., Multifunctional 3D nanoarchitectures for energy storage and conversion. Chemical Society Reviews 2009, 38, (1), 226-252.

Rouquerol, F.; Rouquerol, J.; Sing, K. S. W., Adsorption by powders & porous solids: principles, methodology and applications. Academic Press: San Diego, CA, 1999.

Royall, C. P.; Leunissen, M. E.; van Blaaderen, A., A new colloidal model system to study long-range interactions quantitatively in real space. Journal of Physics: Condensed Matter 2003, 15, (48), S3581-S3596.

Ruetschi, P., Cation-vacancy model for manganese dioxide. Journal of the Electrochemical Society 1984, 131, (12), 2737-44.

Ruiz, V.; Blanco, C.; Santamaria, R.; Ramos-Fernandez, J. M.; Martinez-Escandell, M.; Sepulveda-Escribano, A.; Rodriguez-Reinoso, F., An activated carbon monolith as an electrode material for supercapacitors. Carbon 2009, 47, (1), 195-200.

Ryoo, W.; Dickson, J. L.; Dhanuka, V. V.; Webber, S. E.; Bonnecaze, R. T.; Johnston, K. P., Electrostatic Stabilization of Colloids in Carbon Dioxide: Electrophoresis and Dielectrophoresis. Langmuir 2005, 21, (13), 5914-5923.

Sainis, S. K.; Germain, V.; Mejean, C. O.; Dufresne, E. R., Electrostatic Interactions of Colloidal Particles in Nonpolar Solvents: Role of Surface Chemistry and Charge Control Agents. Langmuir 2008, 24, (4), 1160-1164.

Sanchez, C.; Boissiere, C.; Grosso, D.; Laberty, C.; Nicole, L., Design, Synthesis, and Properties of Inorganic and Hybrid Thin Films Having Periodically Organized Nanoporosity. Chemistry of Materials 2008, 20, (3), 682-737.

Sankapal, B. R.; Lux-Steiner, M. C.; Ennaoui, A., Synthesis and characterization of anatase-TiO2 thin films. Applied Surface Science 2005, 239, (2), 165-170.

Seo, W. S.; Jo, H. H.; Lee, K.; Kim, B.; Oh, S. J.; Park, J. T., Size-dependent magnetic properties of colloidal Mn3O4 and MnO nanoparticles. Angewandte Chemie, International Edition 2004, 43, (9), 1115-1117.

Shanahan, P. V.; Xu, L.; Liang, C.; Waje, M.; Dai, S.; Yan, Y. S., Graphitic mesoporous carbon as a durable fuel cell catalyst support. Journal of Power Sources 2008, 185, (1), 423-427.

Sharma, R. K.; Oh, H.-S.; Shul, Y.-G.; Kim, H., Carbon-supported, nano-structured, manganese oxide composite electrode for electrochemical supercapacitor. Journal of Power Sources 2007, 173, (2), 1024-1028.

Shevchenko, E. V.; Talapin, D. V.; Kotov, N. A.; O'Brien, S.; Murray, C. B., Structural diversity in binary nanoparticle superlattices. Nature (London, United Kingdom) 2006, 439, (7072), 55-59.

Shinomiya, T.; Gupta, V.; Miura, N., Effects of electrochemical-deposition method and microstructure on the capacitive characteristics of nano-sized manganese oxide. Electrochimica Acta 2006, 51, (21), 4412-4419.

Simon, P.; Gogotsi, Y., Materials for electrochemical capacitors. Nature Materials 2008, 7, (11), 845-854.

Smith, P. G., Jr.; Patel, M. N.; Kim, J.; Johnston, K. P.; Milner, T. E., Electrophoretic Mobility Measurement by Differential-Phase Optical Coherence Tomography. Journal of Physical Chemistry C 2007, 111, (6), 2614-2622.

Smith, P. G., Jr.; Ryoo, W.; Johnston, K. P., Electrostatically Stabilized Metal Oxide Particle Dispersions in Carbon Dioxide. Journal of Physical Chemistry B 2005, 109, (43), 20155-20165.

Smith, P. G. J. r.; Patel, M. N.; Kim, J.; Milner, T. E.; Johnston, K. P., Effect of Surface Hydrophilicity on Charging Mechanism of Colloids in Low-Permittivity Solvents. Journal of Physical Chemistry C 2007, 111, (2), 840-848.

Stathatos, E.; Lianos, P.; Falaras, P.; Siokou, A., Photocatalytically deposited silver nanoparticles on mesoporous TiO2 films. Langmuir 2000, 16, (5), 2398-2400.

Stoller, M. D.; Park, S.; Zhu, Y.; An, J.; Ruoff, R. S., Graphene-Based Ultracapacitors. Nano Letters 2008, 8, (10), 3498-3502.

Subhramannia, M.; Balan, B. K.; Sathe, B. R.; Mulla, I. S.; Pillai, V. K., Template-Assisted Synthesis of Ruthenium Oxide Nanoneedles: Electrical and Electrochemical Properties. Journal of Physical Chemistry C 2007, 111, (44), 16593-16600.

Subramanian, V.; Wolf, E.; Kamat, P. V., Semiconductor-Metal Composite Nanostructures. To What Extent Do Metal Nanoparticles Improve the Photocatalytic Activity of TiO2 Films? Journal of Physical Chemistry B 2001, 105, (46), 11439-11446.

Taberna, P. L.; Simon, P.; Fauvarque, J. F., Electrochemical characteristics and impedance spectroscopy studies of carbon-carbon supercapacitors. Journal of the Electrochemical Society 2003, 150, (3), A292-A300.

Tabor, R. F.; Eastoe, J.; Dowding, P. J.; Grillo, I.; Heenan, R. K.; Hollamby, M., Formation of Surfactant-Stabilized Silica Organosols. Langmuir 2008, 24, (22), 12793-12797.

Thomas, J. C.; Crosby, B. J.; Keir, R. I.; Hanton, K. L., Observation of Field-Dependent Electrophoretic Mobility with Phase Analysis Light Scattering (PALS). Langmuir 2002, 18, (11), 4243-4247.

Tompkins, H. G.; McGahan, W. A., Spectroscopic Ellipsometry and Reflectometry. Wiley-Interscience: 1999.

Toupin, M.; Brousse, T.; Belanger, D., Influence of Microstructure on the Charge Storage Properties of Chemically Synthesized Manganese Dioxide. Chemistry of Materials 2002, 14, (9), 3946-3952.

Toupin, M.; Brousse, T.; Belanger, D., Charge Storage Mechanism of MnO2 Electrode Used in Aqueous Electrochemical Capacitor. Chemistry of Materials 2004, 16, (16), 3184-3190.

Trau, M.; Saville, D. A.; Aksay, I. A., Field-induced layering of colloidal crystals. Science (Washington, D. C.) 1996, 272, (5262), 706-9.

Tscharnuter, W. W., Mobility measurements by phase analysis. Applied Optics 2001, 40, (24), 3995-4003.

Tulagin, V., Imaging method based on photoelectrophoresis. Journal of the Optical Society of America 1969, 59, (3), 328-331.

Uchida, H.; Patel, M. N.; May, R. A.; Gupta, G.; Stevenson, K. J.; Johnston, K. P., Perpendicularly-Oriented Mesoporous Titania Thin Films Prepared via Surfactant Assembly on Conductive Indium-Tin-Oxide / Glass Substrate. In prep.

Van der Biest, O. O.; Vandeperre, L. J., Electrophoretic deposition of materials. Annual Review of Materials Science 1999, 29, 327-352.

Vix-Guterl, C.; Frackowiak, E.; Jurewicz, K.; Friebe, M.; Parmentier, J.; Beguin, F., Electrochemical energy storage in ordered porous carbon materials. Carbon 2005, 43, (6), 1293-1302.

Wang, C. M.; Lin, S. Y., Electrochromhic properties of sputtered TiO2 thin films. Journal of Solid State Electrochemistry 2006, 10, (4), 255-259.

Wang, D.-W.; Li, F.; Liu, M.; Lu, G. Q.; Cheng, H.-M., 3D aperiodic hierarchical porous graphitic carbon material for high-rate electrochemical capacitive energy storage. Angewandte Chemie, International Edition 2008, 47, (2), 373-376.

Wang, K.; Yao, B.; Morris, M. A.; Holmes, J. D., Supercritical Fluid Processing of Thermally Stable Mesoporous Titania Thin Films with Enhanced Photocatalytic Activity. Chemistry of Materials 2005, 17, (19), 4825-4831.

Wang, X.; Liang, C.; Dai, S., Facile Synthesis of Ordered Mesoporous Carbons with High Thermal Stability by Self-Assembly of Resorcinol-Formaldehyde and Block Copolymers under Highly Acidic Conditions. Langmuir 2008, 24, (14), 7500-7505.

Wang, X.; Na, N.; Zhang, S.; Wu, Y.; Zhang, X., Rapid Screening of Gold Catalysts by Chemiluminescence-Based Array Imaging. Journal of the American Chemical Society 2007, 129, (19), 6062-6063.

Ware, B. R., Electrophoretic Light scattering. Advances in Colloid and Interface Science 1974, 4, (1), 1-44.

Williams, R. D.; Stevenson, K. J., unpublished results.

Wu, C.-W.; Ohsuna, T.; Kuwabara, M.; Kuroda, K., Formation of Highly Ordered Mesoporous Titania Films Consisting of Crystalline Nanopillars with Inverse Mesospace by Structural Transformation. Journal of the American Chemical Society 2006, 128, (14), 4544-4545.

Wu, Z.-S.; Ren, W.; Gao, L.; Zhao, J.; Chen, Z.; Liu, B.; Tang, D.; Yu, B.; Jiang, C.; Cheng, H.-M., Synthesis of graphene sheets with high electrical conductivity and good thermal stability by hydrogen arc discharge exfoliation. ACS Nano 2009, 3, (2), 411-417.

Xie, X.; Gao, L., Characterization of a manganese dioxide/carbon nanotube composite fabricated using an in situ coating method. Carbon 2007, 45, (12), 2365-2373.

Xing, W.; Qiao, S. Z.; Ding, R. G.; Li, F.; Lu, G. Q.; Yan, Z. F.; Cheng, H. M., Superior electric double layer capacitors using ordered mesoporous carbons. Carbon 2005, 44, (2), 216-224.

Xu, C.-L.; Bao, S.-J.; Kong, L.-B.; Li, H.; Li, H.-L., Highly ordered MnO2 nanowire array thin films on Ti/Si substrate as an electrode for electrochemical capacitor. Journal of Solid State Chemistry 2006, 179, (5), 1351-1355.

Yethiraj, A.; van Blaaderen, A., A colloidal model system with an interaction tunable from hard sphere to soft and dipolar. Nature (London, United Kingdom) 2003, 421, (6922), 513-517.

Zerweck, U.; Loppacher, C.; Otto, T.; Grafstroem, S.; Eng, L. M., Accuracy and resolution limits of Kelvin probe force microscopy. Physical Review B: Condensed Matter and Materials Physics 2005, 71, (12), 125424/1-125424/9.

Zhang, L. L.; Wei, T.; Wang, W.; Zhao, X. S., Manganese oxide-carbon composite as supercapacitor electrode materials. Microporous and Mesoporous Materials 2009, 123, (1-3), 260-267.

Zhang, Q.; Xu, T.; Butterfield, D.; Misner, M. J.; Ryu, D. Y.; Emrick, T.; Russell, T. P., Controlled Placement of CdSe Nanoparticles in Diblock Copolymer Templates by Electrophoretic Deposition. Nano Letters 2005, 5, (2), 357-361.

Zhao, Y.; Liu, L.; Xu, J.; Yang, J.; Yan, M.; Jiang, Z., High-performance supercapacitors of hydrous ruthenium oxide/mesoporous carbon composites. Journal of Solid State Electrochemistry 2006, 11, (2), 283-290.

Zheng, J. P.; Cygan, P. J.; Jow, T. R., Hydrous ruthenium oxide as an electrode material for electrochemical capacitors. Journal of the Electrochemical Society 1995, 142, (8), 2699-703.

Zheng, J. P.; Jow, T. R., A new charge storage mechanism for electrochemical capacitors. Journal of the Electrochemical Society 1995, 142, (1), L6-L8.

Zheng, N.; Fan, J.; Stucky, G. D., One-Step One-Phase Synthesis of Monodisperse Noble-Metallic Nanoparticles and Their Colloidal Crystals. Journal of the American Chemical Society 2006, 128, (20), 6550-6551.

Zheng, N.; Stucky, G. D., A General Synthetic Strategy for Oxide-Supported Metal Nanoparticle Catalysts. Journal of the American Chemical Society 2006, 128, (44), 14278-14280.

Ziegler, K. J.; Polyakov, B.; Kulkarni, J. S.; Crowley, T. A.; Ryan, K. M.; Morris, M. A.; Erts, D.; Holmes, J. D., Conductive films of ordered nanowires arrays. Journal of Materials Chemistry 2004, 14, (4), 585-589.

Zolfaghari, A.; Ataherian, F.; Ghaemi, M.; Gholami, A., Capacitive behavior of nanostructured MnO2 prepared by sonochemistry method. Electrochimica Acta 2007, 52, (8), 2806-2814.

Vita

Mehul Naginbhai Patel was born in Navsari, India to Naginbhai Gopalbhai and Sudhaben Naginbhai Patel on October 24th, 1981. At only six months age, he moved to the United States with his parents. After graduating from the Mississippi School for Mathematics and Science (Columbus, MS) in May, 2000, he entered Vanderbilt University (Nashville, TN). While at Vanderbilt, he conducted undergraduate research with G. Kane Jennings on preparation and characterization of partially fluorinated hexadecanethiol self-assembled monolayers. He graduated with a Bachelor of Engineering degree in Chemical Engineering, *summa cum laude*, in May, 2004. He enrolled at The University of Texas at Austin in August, 2004 for graduate study. Under the supervision of Professor Keith P. Johnston, he earned his Doctor of Philosophy in Chemical Engineering in August, 2009.

Permanent address: 102 East Mark Drive, Brandon, MS 39042

This dissertation was typed by the author.